Funded by the European Union

Thèse préparée et soutenue publiquement par

Massimo Corda

Pour obtenir le grade de Docteur en

Chimie théorique, physique, analytique

École doctorale : Sciences de la Matière, du Rayonnement et de l'Environnement

Catalyst Design and Mechanistic Insights into COx Hydrogenation to Methanol and Light Olefins

Conception de Catalyseurs et Compréhension Mécanistique de l'Hydrogénation de COx en Méthanol et Oléfines Légères

Soutenue le 13 Septembre 2024

Composition du Jury

Rapporteur	Dr. Stéphane Loridant	Directeur de Recherche, IRCELYON
Présidente et rapporteure	Pr. Anne-Cécile Roger	Professeur, Université de Strasbourg
Examinateur	Pr. Michiel Dusselier	Professeur Associé, KU Leuven
Examinateur	Dr. Andrei Khodakov	Directeur de Recherche, UCCS
Directeur de thèse	Dr. Vitaly Ordomsky	Chargé de Recherche, UCCS
Invité	Dr. Lawien Zubeir	Docteur, TNO

Contents

List of abbreviations **6**

List of figures **9**

List of tables **15**

Abstract **16**

Résumé **19**

Chapter 1 Literature review **22**

1.1. General introduction **22**

1.1.1. Greenhouse gases emissions **22**

1.1.2. Low-carbon fuels in the aviation Sector **23**

1.1.3. The TAKE-OFF project **25**

1.2. Light olefin synthesis **27**

1.3. Fischer Tropsch CO/CO_2 conversion **28**

1.4. Methanol mediated light olefin synthesis **30**

1.5. Indirect methanol-mediated light olefin synthesis **31**

1.5.1. CO_2 conversion to methanol **32**

1.5.1.1. Catalysts **35**

1.5.1.2. Mechanism of the CO_2 hydrogenation to methanol **43**

1.5.2 Methanol to Olefins (MTO) **44**

1.6. Direct methanol-mediated CO and CO_2 hydrogenation **48**

1.6.1. Catalysts **50**

1.6.2. Reaction parameters **58**

1.6.3. Mechanism **61**

1.7. Summary **65**

1.8. Objectives of this thesis **66**

1.9. References **70**

Chapter 2 Experimental details **93**

2.1. Materials **93**

2.2. Catalyst preparation **93**

2.2.1. Halogen-promoted CuO-ZnO-Al_2O_3 (CZA) catalysts **93**

2.2.2. Bifunctional OX-ZEO catalysts **94**

2.2.3. Silver-based bifunctional catalysts **98**

2.3. Characterization **99**

2.3.1. X-ray powder diffraction (XRD) **99**

2.3.2. Transmission electron microscopy (TEM) **99**

2.3.3. Scanning Electron Microscopy (SEM) 100
2.3.4. X-ray Fluorescence (XRF) 100
2.3.5. X-ray photoelectron spectroscopy (XPS) 101
2.3.6. FTIR of adsorbed CO 101
2.3.7. X-ray Absorption Spectroscopy (XAS) 102
2.3.8. Temperature Programmed Desorption (TPD) and Reduction (TPR) 103
2.3.9. Thermogravimetric analysis 104
2.3.10. Magic Angle Spinning Nuclear Magnetic Resonance (MAS-NMR) 104
2.4. Catalytic tests 105
2.4.1. Experimental set-ups 105
2.4.2. Experimental procedure of the catalytic tests 108
2.5. Temporal analysis of the products (TAP) analysis 110
2.5.1. Experiments 110
2.5.2. Kinetic evaluation 112
2.6. References 114

Chapter 3 Selective CO_2 hydrogenation to methanol by halogen deposition over a Cu-based catalyst 117
3.1. Introduction 117
3.2. Results and discussion 118
3.2.1. Halogen deposition mechanism 118
3.2.2. Catalyst characterization 121
3.2.3. Catalytic performance 126
3.2.4. Kinetic Analysis 130
3.3. Conclusions 137
3.4. References 138

Chapter 4 Decisive influence of SAPO-34 zeolite on light olefin selectivity in methanol-meditated CO_2 hydrogenation 141
4.1 Introduction 141
4.2. Results and discussion 143
4.2.1. Characterization of the methanol synthesis component 143
4.4.2. SAPO-34 characterization 149
4.2.3. CO_2 hydrogenation 154
4.2.4 Function of metal oxide 158
4.2.5. Function of SAPO-34 162
4.3. Conclusions 168
4.4. References 168

Chapter 5 Silver Metallic Nanoparticles for Direct Conversion of Carbon Monoxide to Light Olefins over Bifunctional Catalysts 175

5.1. Introduction 175

5.2. Results and discussion 176

5.2.1. CO hydrogenation over silver hybrid catalysts at steady state conditions..... 176

5.2.2. Transient behaviour of the AgZr-S34 catalyst 181

5.2.3. Catalyst structure 184

5.3. Conclusions 192

5.4. References 193

General Conclusions 197

Catalyst design 198

Mechanistic insights 199

Perspectives 201

Acknowledgements 205

List of publications 207

List of abbreviations

8MR	Eight-member ring
12MR	Twelve-member ring
AS	Acid sites
ASF	Anderson-Schulz-Flory
ASTM	American Society of Testing and Materials
ATJ	Alcohol To Jet
BET	Brunauer-Emmett-Teller
BrPh	Bromobenzene
CCUS	Carbon Capture Utilization and Storage
CHA	Chabazite
CHJ	Catalytic Hydrothermolysis Jet fuel
ClPh	Chlorobenzene
CO_x	Carbon oxides (CO or CO_2)
CZA	$CuO\text{-}ZnO\text{-}Al_2O_3$
DFT	Density Functional Theory
DME	Dimethyl Ether
DRIFTS	Diffuse Reflectance Infrared Fourier Transform Spectroscopy
EDS or EDX	Energy Dispersive X-Ray Spectroscopy
EXAFS	Extended X-ray Absorption Fine Structure
FCC	Fluidized Catalytic Cracking
FID	Flame Ionization Detector
FT	Fischer Tropsch
FTIR	Fourier Transform Infrared Spectroscopy
GC	Gas Chromatography
GHG	Greenhouse Gas
HAADF	High-Angle Annular Dark-Field imaging
HC	Hydrocarbons
HCP	Hydrocarbon pool species

HEFA	Hydroprocessed Esters and Fatty Acids
HFS-SIP	Hydroprocessed Fermented Sugars to Synthetic Isoparaffins
HTE	High-Throughput Experimentation
IATA	International Air Transportation Association
ID	Inner Diameter
Iph	Iodobenzene
LO	Light Olefins
LP	Light Paraffins
MAS-NMR	Magic Angle Spinning Nuclear Magnetic Resonance
MCP	Methylcyclopentenyl
MFC	Mass Flow Controller
MOF	Molecular Organic Framework
MS	Mass Spectrometry
MTO	Methanol To Olefins
NAP-XPS	Near Ambient Pressure X-ray Photoelectron Spectroscopy
NP	Nanoparticle
OD	Outer Diameter
OX-ZEO	Oxide-Zeolite
PAH	Polycyclic Aromatic Hydrocarbon
PVC	Poly Vinyl Chloride
RWGS	Reverse Water Gas Shift
SAF	Sustainable Aviation Fuel
SEM	Scanning Electron Microscopy
SMSI	Strong Metal-Support Interaction
SPK	Synthetic Paraffinic Kerosene
STEM	Scanning Transmission Electron Microscopy
SV	Space Velocity
TAP	Temporal Analysis of Products
TCD	Thermal Conductivity Detector
TGA	Thermogravimetric Analysis

TEM	Transmission Electron Microscopy
TPR	Temperature Programmed Reduction
TPD	Temperature Programmed Desorption
TRL	Technology Readiness Level
WGS	Water Gas Shift
WHSV	Weight Hourly Space Velocity
XANES	X-Ray Absorption Near Edge Structure
XAS	X-Ray Absorption Spectroscopy
XPS	X-ray Photoelectron Spectroscopy
XRD	X-Ray Diffraction
XRF	X-Ray Fluorescence

List of figures

Figure 1: Scheme of the TAKE-OFF SAF production pathway. 26

Figure 2: FT product weight fraction as a function of the chain growth probability. 29

Figure 3: Indirect and direct route for the CO_2 hydrogenation to light olefins. 31

Figure 4: Scheme of the MeOH Economy proposed by Olah et al. Ref[30] 33

Figure 5: Thermodynamic limitation in the MeOH synthesis process. [26] 34

Figure 6: Dependency of the selectivity to MeOH on the conversion in the CO_2 hydrogenation over In-based catalyst. Conditions: 300 °C, 5 MPa, H_2/CO_2=4. Data taken from Ref.[45,61–64,68] 38

Figure 7: CO_2 conversion (a) and MeOH selectivity (b) as a function of the temperature in the CO_2 hydrogenation to MeOH over Pd-$ZnZrO_x$ catalysts. [53] 39

Figure 8: Formate-based mechanism of the CO_2 hydrogenation to MeOH over a In_2O_3 catalyst. [92] 44

Figure 9: Scheme of the MTO reaction mechanism: initial non-autocatalytic stage; autocatalytic stage (hypercycle); coking.[93] 45

Figure 10: Evolution of HCP species inside SAPO-34 crystals of different sizes with time. (a) 5 nm; (b) 12 nm; (c) 17 nm; (d) 50 nm. The different colors represent different species: Blue: benzenic carbocations; Green: naphtalenic carbocations; Red: phenantrenic carbocations; Pink: pyrenic carbocations.[94] 46

Figure 11: Correlation of the formation rates of CH_3OH/DME (Zn–Ga–O) and C_2–C_4 olefins (Zn–Ga–O/SAPO-34) with the density of oxygen vacancies $D_{(OV)}$.[107] 52

Figure 12: Cage type of different SAPO zeolites and performance of their relative ZnAlOx/SAPO catalysts in the syngas conversion to LO. a) SAPO-35; b) SAPO-17; c) SAPO-34; d) SAPO-18; e) SAPO-11; f) SAPO-31; g) SAPO-5; h) SAPO-37. [104] 53

Figure 13: Effect of proximity between $ZnZrO_x$ and ZSM-5 components on the catalytic performance of the bifunctional catalysts in CO_2 hydrogenation: dual bed configuration (a), granules stacking with a different size (b, c), mixing of two powders by mortar mixing (d), and ball milling (e).[113] 56

Figure 14: Preparation of the core-shell ZnCrOx@SAPO-34 catalyst (a); Performance of this core-shell catalyst comparing with sole $ZnCrO_x$, $ZnCrO_x$ and SAPO separated by quartz wool, and $ZnCrO_x$ with SAPO physically mixed (b).[138] 57

Figure 15: Effect of reaction pressure on CO and CO_2 conversion and selectivity to LO in methanol-mediated hydrogenation. Data from Refs [97,115,141] 59

Figure 16: Effect of reaction temperature on the CO/CO_2 conversion (a), selectivity to CO/CO_2 (b) and CO/CO_2-free selectivity to LO in methanol-mediated CO_2 or CO hydrogenation. Ref.[97,107,110,140,141] ... 60

Figure 17: Selectivity-conversion plot for CO-free selectivity to LO in the methanol-mediated CO_2 hydrogenation based on data from Ref.[97] 61

Figure 18: Hydrocarbon distributions in the conversion of syngas, ketene, and methanol over different sites of MOR zeolites: during syngas over ZnCrOx-MOR (a, d, e); ketene conversion over MOR (b, e, f); methanol conversion over MOR (c, f, i). [129] 62

Figure 19: Proposed oxygen vacancy-assisted mechanism of methanol formation on the $ZnAl_2O_4$ surface during CO_2 hydrogenation to LO (a); in situ FTIR spectra of adsorbed species on $ZnAl_2O_4$: CO adsorption (dotted lines) and then switching to H_2/CO flow at 533 K (b,c), CO_2 adsorption (dotted lines) and then switching to H_2/CO_2 flow at 623 K (d,e). Figures from Ref.[99] 64

Figure 20: Summary of the work presented in this thesis. (MO_x stands for metal oxide)..... 67

Figure 21: Autoclave used for the synthesis of the halogen-treated CZA catalysts. 94

Figure 22: Scheme of the single fixed-bed reactor setup. 105

Figure 23: Three parallel fixed-bed reactor setup scheme. 106

Figure 24: Simplified scheme of the Avantium Flowrent High Throughput Experimentation unit with 16 parallel reactors. 108

Figure 25: Variation of the halogen loading on the catalyst surface with the increasing amount of halobenzene. 119

Figure 26: a) Scheme of the halogen deposition mechanism; b)GC-MS analysis of the liquid phases of the catalyst synthesis mixtures: CZA-Br-500 in the absence of H_2; CZA-Br-500; CZA-Br-60. 120

Figure 27: XPS Spectra related to the as-prepared catalysts. a) Cu 2p; b) Cu LMM; c) Zn 2p; d) Zn LMM; e) Br 3p; f) Cl2p; g) I 3d. 121

Figure 28: XRD patterns of the CZA and halogen-treated CZA catalysts. 122

Figure 29: STEM-HAADF (a, c, e, g) and STEM-EDS (b, d, f, h) of the studied catalysts: CZA (a, b); CZA-Br-500 (c, d) CZA-I-500 (e, f) and CZA-Cl-500 (g, h). 123

Figure 30: H_2-TPR profiles of CZA, CZA-Br-60 and CZA-Br-500 catalysts. 124

Figure 31: FTIR spectra of CO adsorbed over the reduced CZA (red) and CZA-Br-60 (blue)catalysts at 77 K. 125

Figure 32: Effect of different halogen on the catalyst activity in MeOH and CO production from CO_2 hydrogenation (Conditions: 200 °C, 20 bar, 3600 mL g_{cat}^{-1} h^{-1}). 127

Figure 33: Effect of the halogen deposition on the selectivity to MeOH during the CO_2 hydrogenation to MeOH. (Conditions: 200 °C, 20 bar, 21000-3600 mL g_{cat}^{-1} h^{1}). 127

Figure 34: Linear dependency of CO_2 conversion from the halogen concentration in the surface of the CZA catalyst. 128

Figure 35: CO_2 hydrogenation to MeOH over CZA, CZA-EtOH and CZA-Br-60. (Conditions: 200 °C, 20 bar, 21000-3600 mL g_{cat}^{-1} h^{-1}). 129

Figure 36: Parallel reactions during the CO_2 hydrogenation to MeOH, and relative kinetic equations. 130

Figure 37: Plots of the selectivity to MeOH versus the reciprocal flow rates used to calculate the kinetic constants. a) CZA; b) CZA-Br-60; c) CZA-Br-125; d) CZA-Br-250; e) CZA-Br-500. 133

Figure 38: Evaluation of the kinetic constants of the reactions occurring during the CO_2 hydrogenation over the commercial catalyst and the Br-treated catalysts (200 °C; 20 bar). a) ratio between the MEOH synthesis and RWGS constants; b) ratio between the MeOH synthesis and MeOH decomposition constant. 135

Figure 39: a) Normalized transient responses of D_2, HD, H_2 and Ar obtained upon pulsing D_2:H_2:Ar =1:1:1 mixture over the CZA, CZA-Br-60 and CZA-Br-500 catalysts at 200°C; b) evaluation of the hydrogen activation at 200 °C; c) evaluation of the CO_2 activation at 200 °C. 136

Figure 40: XRD patterns of the studied catalysts: a)ZnZrOx and InZrOx; b)ZnAlOx and ZnGaOx; c)ZnCrOx; d)ZnCeZrOx;e) MnBi/ZrO_2; f) Mn/ZrO_2 ; g) Zn/Zr-MOF-S(3.2/1.7) compared with Zr-MOF and S(3.2/1.7). 144

Figure 41 : XANES spectra of Zn-containing oxide-based samples at Zn K-edge. a)$ZnZrO_x$ and Zn/Zr-MOF; b)$ZnCeZrO_x$ and $ZnCrAlO_x$; c) $ZnAlO_x$ and $ZnGaO_x$. 145

Figure 42 : TPR profiles of the studied oxide components. 146

Figure 43 : CO_2-TPD profiles of the studied oxide components (a) and concentration of different basic sites calculated from the CO_2-TPD data (b). 147

Figure 44 : TEM images and EDX mapping of the metal oxide components of bifunctional catalysts: $ZnZrO_x$ (a), $InZrO_x$ (b), ZnO/Zr-MOF (c), $ZnGaO_x$ (d), $ZnCrAlO_x$ (e), and MnBi/ZrO_2 (f). 148

Figure 45 : XRD pattern of the studied SAPO-34 zeolites..... 150

Figure 46 : SEM images of SAPO-34 zeolites (a, b, c, d) and particle size distribution (e, f, g, h). (a, e) S(3.2/1.7); (b, f) S(3.2/0.6); (c, g) S(1.6/0.9); (d, h) S(0.5/1.1). 151

Figure 47 : NH_3-TPD profiles of SAPO-34 zeolites: (a) S(3.2/1.7); (b) S(3.2/0.6); (c) S(1.6/0.9); (d) S(0.5/1.1). 152

Figure 48 : MAS NMR spectra of different SAPO-34 samples: (a) ^{29}Si MAS NMR; (b) ^{27}Al MAS NMR; (c) ^{31}P MAS NMR. 153

Figure 49 : Selectivity to LO (a) and to CO (b) towards CO2 conversion. The catalysts mentioned are composed by different metal oxides mixed with S(3.2/1.7) in 1:1 weight ratio. 155

Figure 50 : Reaction pathway for the CO_2 hydrogenation to LO over bifunctional catalyst (a); dependences of CO-free selectivity to LO (b), LP (c), CH4 (d), and C_5+ species (e) on the hydrocarbon (HC) yield during the reaction at CO_2:H_2 = 1:3 and 375°C. The data related to bifunctional catalysts composed by different metal oxides mixed with S(3.2/1.7) in 1:1 weight ratio. 157

Figure 51 : TAP results: hydrogen activation ability of the different metal-oxide systems (a); effect of hydrogen activation ability on the CO_2 conversion and paraffin/olefin selectivity ratio (b)..... 158

Figure 52 : Ethylene model hydrogenation results: effect of water and CO_2 presence on the ethylene hydrogenation into ethane over $ZnZrO_x$ and SAPO-34 (S(3.2/1.7)). Ethylene conversion was carried out

at 375°C under 1 bar, H_2:C_2H_4 ratio of 28:1 for water addition and at H_2:CO_2:C_2H_4 ratio of 28:5:1 for CO_2 tests. 159

Figure 53 : Microkinetic models used for fitting of experimental CO_2 responses obtained aftre pulsing of CO_2:Ar =1:1 mixture over different catalysts at 375°C. 160

Figure 54: Comparison between the experimental and simulated CO_2 responses obtained after pulsing of CO_2:Ar =1:1 mixture over different catalysts at 375°C. 161

Figure 55 : Dependences of CO_2 dissociation equilibrium constant calculated by TAP on the concentration of weak and strong basic..... 162

Figure 56 : CO-free selectivity to LO towards HC yield for the $ZnZrO_x$-based catalysts mixed with SAPO-34 of different acidity and in the different weight ratios (oxide:zeolite from 1:2 to 2:1). 165

Figure 57 : Illustration of the tandem process reaction: roles of oxide and SAPO-34 components in the methanol-mediated CO_2 hydrogenation performance. 167

Figure 58: Steady state selectivities and CO conversion for different catalysts. Conditions: 375 °C; 20 bar; 4.8-0.6 NL g_{cat}^{-1} h^{-1}. 179

Figure 59: Selectivity-conversion curve: AgZr10-S34 compared to ZnZrOx-S34. 180

Figure 60: Effect of temperature on catalysis. AgZr10-S34. .Conditions: 20 bar; 1.6 NL g_{cat}^{-1} h^{-1} 180

Figure 61: Selectivity CO-free and CO and conversion versus time on stream for S-34 small and larger crystals at high conversion. a) AgZr10-S34; b) AgZr10-S34L. Conditions: 375 °C; 20 bar; 0.6 NL g_{cat}^{-1} h^{-1}. 182

Figure 62: CO conversion, CO selectivity and CO-free hydrocarbon selectivity versus time on stream for AgZr10-S34 catalysts with S-34 small crystallites at 375 °C; 20 bar; 1.6 NL g_{cat}^{-1} h^{-1}(a) and for AgNPZr12-S34 catalyst at 375 °C; 20 bar; 0.6 NL g_{cat}^{-1} h^{-1} (b) 183

Figure 63: HAADF-STEM analysis of AgZr10 component (a), and the fresh (b-d) and spent (e-h) AgZr10-S34 catalysts (b-h). Figure h shows an example of a polycrystalline nanoparticle in the AgZr10-S34 spent catalyst. 185

Figure 64: STEM-EDX mapping of the fresh AgZr10-S34 catalyst. a) HAADF-STEM; b) Ag map; c) Al map; d) Zr map; e) Si map; f) O map. 186

Figure 65: STEM-EDX mapping of the spent AgZr10-S34 catalyst. a) HAADF-STEM; b) Ag map; c) Al map; d) Zr map; e) Si map; f) O map. 186
Figure 66: XANES (a) and FT EXAFS (b) for fresh and spent silver catalysts. 187
Figure 67: SEM of zeolite used to prepare the bifunctional catalysts, and fresh and spent catalysts. a)S34; b)S34L; c) AgZr10-S34 fresh; d) AgZr10-S34 spent; e) AgZr10-S34L fresh; f) AgZr10-S34L spent. 189
Figure 68: CO FTIR spectra on spent AgZr10-S34, after treatment at 350 °C under vacuum to remove adsorbed water (red), and after a CO dose of 33 mbar (blue). 190
Figure 69: XRD of the S34 zeolite; the AgZr10 component, and the fresh and spent AgZr10-S34 catalysts. 191
Figure 70: TGA of fresh (a) and spent (b) Ag/Zr10-S-34 catalysts. 192

List of tables

Table 1: Currently available SAF production technologies, type of feedstock and maximum blend, as defined by the ASTM D7566 standard. 24

Table 2: Comparison of the performance of different catalysts in the CO_2 hydrogenation to MeOH reaction. 36

Table 3: Performance of tandem catalysts in the methanol-mediated CO hydrogenation to LO. 50

Table 4: Performance of tandem catalysts in the methanol-mediated CO_2 hydrogenation to LO. 50

Table 5: Synthesis of metal-oxide catalysts via co-precipitation. 96

Table 6: Synthesis of metal-oxide catalysts via impregnation. 97

Table 7: description of the zeolite used to prepare the bifunctional catalysts. 99

Table 8: Kinetic constants calculated for the MeOH formation, RWGS and MeOH decomposition reactions happening during the CO_2 hydrogenation to MeOH process. 132

Table 9 : Characteristics of SAPO-34 samples. 149

Table 10 : Catalytic results for the tests of $ZnZrO_x$ mixed with the SAPO-34 in different proportions. WHSV of 3000 NmL/g/h, 20 bar, and 375 °C. 165

Table 11: Catalytic performance in CO hydrogenation (375 °C, 20 bar, H_2: CO=2) at steady state. 178

Abstract

The increasing concentration of atmospheric CO_2, driven largely by the combustion of fossil fuels, presents significant environmental challenges and emphasizes the urgency for sustainable chemical processes. Concurrently, the depletion of fossil fuel reserves necessitates the exploration of alternative feedstocks for the production of industrial chemicals. One promising approach to address both issues is the catalytic conversion of CO_2 into value-added chemicals, such as methanol and light olefins, which are crucial building blocks for the chemical industry and serve as precursors to a wide array of products, including plastics, solvents, and pharmaceuticals. Additionally, methanol holds significant potential as a clean-burning fuel and energy carrier, further enhancing its value in the context of sustainable energy solutions. In addition to CO_2, CO can also be used as a sustainable feedstock, for it can be produced from biomass or waste gasification, or from CO_2 via the Reverse Water Gas Shift reaction.

This thesis will investigate three reactions, namely CO_2 hydrogenation to methanol, methanol-mediated CO and CO_2 hydrogenation to light olefins. These reactions are receiving significant attention for their contributions to the shift towards sustainable chemical production and the mitigation of carbon emissions.

Chapter 1 presents the state of the art of the three processes under study, and it presents the scope of the thesis. The experimental work is presented starting from Chapter 2, in which the catalyst synthesis, the catalytic tests and the characterization techniques are described.

In the hydrogenation of CO_2 to methanol, the selectivity of the catalyst is fundamental, as they directly influence the overall feasibility and economic viability of the process. Chapter 3 presents a work carried out to improve selectivity over the commercial $CuO\text{-}ZnO\text{-}Al_2O_3$ catalyst. The latter has been promoted with halogens (Br, Cl, I), using halobenzene precursors.

It was observed that Br allowed to improve the selectivity of 10 % compared to the pristine catalyst. The effect was observed at different amounts of halogen deposited over the catalyst surface. A kinetic analysis allowed to explain the effect of the halogen on the suppression of the Reverse Water Gas Shift reaction and of the MeOH decomposition reaction, both responsible of the parallel production of CO.

The methanol-mediated CO_2 selective hydrogenation to light olefins is performed over bifunctional catalysts containing metal oxide (methanol synthesis) and zeolite components (methanol to olefins reaction). The main challenge is to achieve high LO yield, which requires maintaining simultaneously high LO selectivity and high CO_2 conversion. Chapter 4 presents the analysis of the selectivity-conversion correlations over metal oxide-zeolite bifunctional catalysts, which allow to elucidate the functions of each catalyst component. A series of catalytic systems based on oxides of Zn, In, Mn, Cr, or Ga and different SAPO-34 zeolites were synthesized and evaluated at different CO_2 conversion levels. It was uncovered that the selectivity to LO within hydrocarbon fractions depended ultimately on the zeolite component and decreased as a function of hydrocarbon yield. The metal-oxide catalyst component was responsible for the CO_2 conversion, overall hydrocarbon and CO selectivity. The SAPO-34 morphology and acidity were identified as major descriptors of the CO-free LO selectivity in the CO_2 hydrogenation over bifunctional metal oxide -zeolite catalysts.

Also for the sustainable synthesis of light olefins from syngas, the intermediate hydrogenation of CO to methanol occurs on metal oxide catalysts, followed by the conversion of methanol to light olefins over a zeolite. In Chapter 5, the replacement of the metal oxide hydrogenation component in the hybrid bifunctional catalysts with silver supported nanoparticles. The resulting catalysts exhibited higher selectivity to light olefins and lower selectivity to methane compared to zinc-zirconia based counterparts. It was also observed that to achieve high selectivity to light olefins with hybrid zirconia-supported silver metallic

catalysts and SAPO-34 zeolite required an initial period to stabilize the size of silver metal nanoparticles.

The work reported in this thesis provided new insights into catalyst design for the COx hydrogenation to methanol or light olefins, suggesting new strategies to improve product selectivity. Additionally, the thesis advances the understanding of mechanistic aspects of CO_2 hydrogenation to methanol, and of methanol-mediated CO_2 hydrogenation to light olefins. These mechanistic studies offer a deeper comprehension of the side reaction occurring during the studied processes, defining solutions for their minimization through catalyst design.

Résumé

La concentration croissante de CO_2 atmosphérique, due en grande partie à la combustion de combustibles fossiles, présente des défis environnementaux importants et souligne l'urgence de processus chimiques durables. Parallèlement, l'épuisement des réserves de combustibles fossiles nécessite l'exploration de matières premières alternatives pour la production de produits chimiques industriels. Une approche prometteuse pour résoudre ces deux problèmes est la conversion catalytique du CO_2 en produits chimiques à valeur ajoutée, tels que le méthanol et les oléfines légères, qui sont des molécules plateforme essentiels pour l'industrie chimique et servent de précurseurs à un large éventail de produits, notamment les plastiques, les solvants et les produits pharmaceutiques. De plus, le méthanol présente un potentiel important en tant que carburant et vecteur d'énergie propre, renforçant ainsi sa valeur dans le contexte de solutions énergétiques durables. En plus du CO_2, le CO peut également être utilisé comme matière première durable, car il peut être produit à partir de la biomasse ou de la gazéification des déchets, ou à partir du CO_2 via la réaction Reverse Water Gas Shift.

Cette thèse étudiera trois réactions, notamment l'hydrogénation du CO_2 en méthanol, l'hydrogénation du CO_2 ou du CO en oléfines légères voie méthanol. Ces réactions font l'objet d'une attention particulière en raison de leur contribution à la transition vers une production chimique durable et à l'atténuation des émissions de carbone.

Le chapitre 1 présente l'état de l'art des trois procédés étudiés, ainsi que les objectifs de la thèse. Le travail expérimental est présenté à partir du chapitre 2, dans lequel sont décrits la synthèse du catalyseur, les tests catalytiques et les techniques de caractérisation.

Dans l'hydrogénation du CO_2 en méthanol, la sélectivité du catalyseur est fondamentale, car elle influence directement la faisabilité globale et la viabilité économique du procédé. Le chapitre 3 présente un travail réalisé pour améliorer la sélectivité par rapport au catalyseur

commercial CuO-ZnO-Al_2O_3. Cette dernière a été favorisée avec des halogènes (Br, Cl, I), en utilisant des halobenzènes comme précurseurs. Il a été observé que Br permettait d'améliorer la sélectivité de 10 % par rapport au catalyseur vierge. L'effet a été observé avec différentes quantités d'halogène déposées sur la surface du catalyseur. Une analyse cinétique a permis d'expliquer l'effet de l'halogène sur la suppression de la réaction Reverse Water Gas Shift et de la réaction de décomposition du MeOH, toutes deux responsables de la production parallèle de CO.

L'hydrogénation sélective du CO_2 médiée par le méthanol en oléfines légères est réalisée sur des catalyseurs bifonctionnels contenant des composants d'oxyde métallique (synthèse du méthanol) et de zéolite (réaction du méthanol en oléfines). Le principal défi est d'obtenir un rendement élevé en LO, ce qui nécessite de maintenir simultanément une sélectivité élevée en LO et une conversion élevée du CO_2. Le chapitre 4 présente l'analyse des corrélations sélectivité-conversion sur des catalyseurs bifonctionnels oxyde métallique-zéolite, qui permettent d'élucider les fonctions de chaque composant du catalyseur. Une série de systèmes catalytiques à base d'oxydes de Zn, In, Mn, Cr ou Ga et différentes zéolites SAPO-34 ont été synthétisés et évalués à différents niveaux de conversion du CO_2. Il a été découvert que la sélectivité en LO dans les fractions d'hydrocarbures dépendait du composant zéolite et diminuait en fonction du rendement en hydrocarbures. Le composant oxyde métallique du catalyseur était responsable de la conversion du CO2, de la sélectivité globale en hydrocarbures et en CO. La morphologie et l'acidité du SAPO-34 ont été identifiées comme des descripteurs majeurs de la sélectivité du LO sans CO dans l'hydrogénation du CO_2 sur des catalyseurs bifonctionnels oxyde métallique-zéolite.

Également pour la synthèse durable d'oléfines légères à partir de gaz de synthèse, l'hydrogénation intermédiaire du CO en méthanol se produit sur des catalyseurs à oxyde métallique, suivie de la conversion du méthanol en oléfines légères sur une zéolite. Au chapitre

5, le remplacement du composant d'hydrogénation d'oxyde métallique dans les catalyseurs bifonctionnels hybrides par des nanoparticules supportées par de l'argent. Les catalyseurs résultants présentaient une sélectivité plus élevée pour les oléfines légères et une sélectivité plus faible pour le méthane par rapport à leurs homologues à base de zinc-zircone. Il a également été observé que pour obtenir une sélectivité élevée pour les oléfines légères avec des catalyseurs métalliques argentés hybrides supportés par de la zircone et la zéolite SAPO-34, il fallait une période initiale nécessaire pour stabiliser la taille des nanoparticules métalliques argentées.

Les travaux rapportés dans cette thèse ont fourni de nouvelles informations sur la conception de catalyseurs pour l'hydrogénation du CO_x en méthanol ou en oléfines légères, suggérant de nouvelles stratégies pour améliorer la sélectivité des produits. De plus, la thèse fait progresser la compréhension des aspects mécanistiques de l'hydrogénation du CO_2 en méthanol et de l'hydrogénation du CO_2 en oléfines légères voie méthanol. Ces études mécanistiques offrent une compréhension plus approfondie des réactions secondaires se produisant au cours des processus étudiés, définissant des solutions pour leur minimisation grâce à la conception du catalyseur.

Chapter 1 Literature review

1.1. General introduction

1.1.1. Greenhouse gases emissions

The 21st century is marked by the concern of increasing carbon dioxide (CO_2) levels in the atmosphere and the relative impact on the Earth's climate system. This accumulation is caused by anthropogenic activities such as fossil fuel combustion, deforestation, and industrial processes. As the climate change becomes more and more evident, the need to mitigate CO_2 and greenhouse gases emissions and explore innovative approaches to manage this greenhouse gas has never been more urgent.

For this reason, on 12 December 2015 at the UN Climate Change Conference (COP21) in Paris, France, 196 Parties signed the Paris Agreement. This treaty aims to keep the increase in the global average temperature well below 2°C above pre-industrial levels, preferably limiting this increase to 1.5°C. In fact, above the 1.5°C threshold there would be a higher risk of major climate changes, including more frequent and severe droughts, heatwaves and rainfall. In alignment with this ambitious goal, the European Union introduced the "Fit for 55" package in July 2021. This comprehensive suite of legislative proposals aims to reduce the EU's greenhouse gas emissions by 55% by 2030 compared to 1990 levels, aiming for carbon neutrality by 2050.

According to recent reports from the International Energy Agency[1,2], the immediate opportunities to reduce these emissions are the energy efficiency in the industry, transport and building sector; the use of renewable energies and the behavioural changes. Moreover, four additional strategies, critical to achieve the net-zero emissions goal are the electrification of the transport, industry and buildings sectors; Carbon Capture, Utilization, and Storage (CCUS); the shift towards hydrogen and hydrogen-derived synthetic fuels (using low-carbon hydrogen and sustainable carbon sources); and the use of more sustainable alternative fuels and feedstock

such as bioenergy. Nonetheless, these last four strategies rely on technologies that are not yet commercially available, and today research is making significant efforts to bring these technologies to maturity.

The work presented in this thesis is related to two of the previously named strategies, namely CCUS and the development of H_2-based fuels. The initial role of CCUS in the emissions reduction is related to the decarbonisation of existing technologies in the power and heavy industries, but long-term goal involves the removal of carbon from the atmosphere.

In addition, the development of low-emissions fuels is particularly relevant to decarbonize some sectors that cannot rely on electricity as a power source, like for instance long-distance transport (trucks, aviation and shipping). While the technologies to directly exploit H_2 as a fuel are far from maturity, the short to medium-term alternative solution are so-called drop-in fuels. The latter are produced using green hydrogen (H_2 produced from water electrolysis) and are compatible with the existing technologies and distribution infrastructure, which consequently do not require major modifications.

1.1.2. Low-carbon fuels in the aviation Sector

As the aviation sector contributes for the 2.4% to the total GHG emissions[3], the Refuel EU Aviation initiative was presented as a part of the European Union's "Fit for 55" package, to reduce greenhouse gas emissions in the aviation sector. This initiative aims to increase the use of sustainable aviation fuels (SAF) in aviation fuel blends, starting with 2% in 2025, 5% in 2030, 20% in 2035, and 63% by 2050. Similarly, at the 77th International Aviation Transport Association (IATA) Annual General Meeting in Boston, USA, a resolution was signed by IATA member airlines to commit to the achievement of net-zero emission by 2050. The IATA identified the use of SAF as the main strategy to abate CO_2 emissions in the aviation industry.

SAF is the main term used to describe drop-in fuels for the aviation industry produced from non-fossil feedstocks. From a chemical and physical point of view, the properties of SAF and the ones of the conventional jet fuel (Jet A/ Jet A1) are almost identical, and the two types of fuel can be safely mixed to varying degrees. Today, the non-fossil fuels are blended with fossil fuels (Jet A/ Jet A1) before being employed, but tests to evaluate the feasibility of 100% SAF powered flights are underway.

To be safely employ a SAF, the fuel must comply to the specifications defined by the American Society for Testing and Materials (ASTM) D7566 "Standard Specification for Aviation Turbine Fuel Containing Synthesized Hydrocarbons". In this specification are also included 7 annexes which define the currently available pathways to produce SAF, as reported in *Table 1*.

Table 1: Currently available SAF production technologies, type of feedstock and maximum blend, as defined by the ASTM D7566 standard.

Annex	Technology Name	Feedstocks	Blending Limit
A1	Fischer-Tropsch Synthetic Paraffinic Kerosene (FT-SPK)	Biomass, municipal solid waste, agricultural residues	50 %
A2	Hydroprocessed Esters and Fatty Acids Synthetic Paraffinic Kerosene (HEFA-SPK)	Used cooking oil, animal fats, vegetable oils	50 %
A3	Synthesized Iso-Paraffins (SIP) from Hydroprocessed Fermented Sugars (HFS-SIP)	Sugarcane, sugar beet, other sugar-rich crops	10 %
A4	Fischer-Tropsch Synthetic Paraffinic Kerosene with Aromatics (FT-SPK/A)	Biomass, municipal solid waste, agricultural residues	50 %
A5	Alcohol-to-Jet Synthetic Paraffinic Kerosene (ATJ-SPK)	Biomass-derived alcohols (ethanol, iso-butanol)	50 %
A6	Catalytic Hydrothermolysis (CHJ)	Lipid-rich feedstocks such as vegetable oils, animal fats	50 %
A7	Hydroprocessed Hydrocarbons, Esters and Fatty Acids (HC-HEFA)	Oils produced from *botryococcus braunii* algae	10 %

In these technologies the CO_2 utilization is indirect: CO_2 is captured by plants and converted to sugars (biomass building blocks) through photosynthesis, and only the derived biomass is exploited for SAF production.

While biofuels production allows to reduce CO_2 emissions, it is also associated to a "food versus fuel" debate. In fact, to produce biomass for the synthesis of fuels the land use should be redefined, and resources allocated to food production should be reduced. Moreover, achieving the ambitious goals set by the Refuel EU program would be highly challenging if relying exclusively on biomass-derived feedstocks. For this reason, the development of additional pathways is needed. Power-to-liquid represents a promising candidate for SAF production: while it faces challenges like the intermittency in the generation of electricity from renewable sources and cost of production, it can rely on the abundant availability of CO_2, which is captured from industrial processes or directly from the atmosphere.

1.1.3. The TAKE-OFF project

To contribute to the research dedicated to development of new sustainable technologies, and considering the challenges set by Refuel EU, the European project TAKE-OFF aims to develop a new SAF production pathway which directly exploits CO_2 as a feedstock. The work presented in this thesis was financed by this project.

In the TAKE-OFF SAF production pathway (*Figure 1*), CO_2 captured from an industrial point-source, is hydrogenated to methanol, which in turn is converted to light olefins (LO). The used hydrogen is produced from water electrolysis, powered by renewable energies. The produced LO are then oligomerized and hydrogenated to form jet fuel range hydrocarbons (C_8-C_{16}).

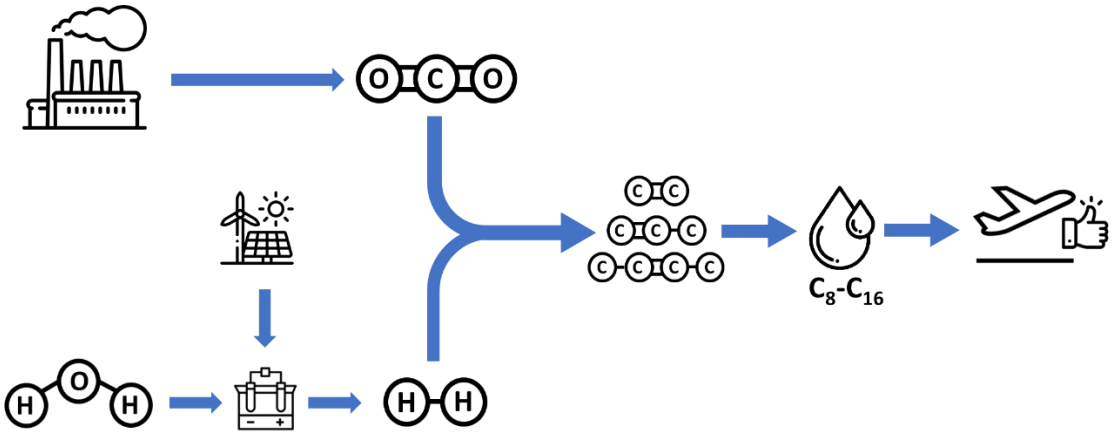

Figure 1: Scheme of the TAKE-OFF SAF production pathway.

Fischer-Tropsch is the available and certified route that can be considered as the main technology competitor for the TAKE-OFF technology. Nevertheless, this process produces a wide range of hydrocarbons (C_2 to C_{30}+), giving an overall selectivity towards the desired C_8-C_{16} fraction of 45%.[4] Based on literature reports[5–7], the TAKE-OFF technology route could achieve a higher carbon efficiency (60%).

The academic and industrial project partners work together in different aspects of the technology development: catalyst design; reactor design; demonstration of the technology under industrial-relevant conditions; emission and compliance evaluation; techno-economic and environmental assessment of jet fuels; dissemination and exploitation of the results. This thesis is related to the work devoted to the catalyst design within the project, and in particular the catalyst design for the methanol-mediated CO_2 hydrogenation to light olefins. At the same time, this thesis addresses the catalyst development for two other reactions, which are related to the light olefin synthesis pathway chosen for the project. These reactions are the CO_2 hydrogenation to methanol and CO hydrogenation to light olefins. The first one consists in the first step of the tandem CO_2 hydrogenation to light olefins, the second one is a similar process but it is based on CO, which is a product of the CO_2 hydrogenation (Reverse Water Gas Shift).

1.2. Light olefin synthesis

Light olefins (LO; ethylene, propylene and butylenes) are important feedstocks and platform molecules for the chemical industry.[8] Ethylene is the largest-volume chemical and has a broad range of applications and end-uses. It is employed in manufacturing a broad range of chemicals (i.e. ethylene glycols, ethanol, ethoxylates…),and materials (polyethylene, PVC…) employed in a multitude of sectors. Propylene is mostly consumed for manufacturing polypropylene, one of the most versatile polymers, but also for other chemicals like alcohols, propylene oxide, acrylonitrile, acrylic acid and cumene. Butylene is mostly employed in the production of gasoline additives and polybutadiene but also like a co-monomer for different sorts of polyethylene and in the production of other chemicals like butadiene and acetic acid among others. LO can be synthesized from hydrocarbon feedstocks such as oil, natural gas or shale gas. The LO synthesis technologies that involve hydrocarbon feedstocks are steam cracking of light oil and gas fractions, fluid catalytic cracking (FCC),[9,10] methane coupling[11] and direct or oxidative dehydrogenation of propane and butane[12]. Alternatively, LO can be synthesized using feedstocks like methanol, biomass or organic waste, via methanol-to-olefins (MTO)[13] or pyrolysis processes[14,15]. Finally, CO and CO_2 are interesting feedstocks for LO synthesis.

The direct conversion of CO_2 is challenging due to its high stability and chemical inertness. CO, as an alternative, is more reactive. Although CO can be produced from gasification of coal or natural gas, which are not interesting from a sustainability point of view, it can also be an indirect sustainable feedstock when produced from CO_2 through the Reverse Water Gas Shift (RWGS) reaction, or from the gasification of biomass or waste. Nonetheless, the direct CO_2 conversion might be desirable considering that a RWGS step increases the costs of the process. The technologies for LO synthesis from COx are either thermocatalytic, like the CO or CO_2-based Fischer–Tropsch (FT) synthesis[16] and the methanol-mediated CO/CO_2 hydrogenation[17], or electrocatalytic[18]. The latter pathway is very promising in terms of

selectivity to LO, but the thermocatalytic pathways are characterized by a higher Technology Readiness Level (TRL). For this reason, following in this chapter, only the two thermocatalytic pathways will be discussed: Fischer-Tropsch synthesis and methanol mediated process. In particular, the methanol-mediated CO_2 hydrogenation to LO is the LO synthesis route of interest within the TAKE-OFF project.

1.3. Fischer Tropsch CO/CO_2 conversion

The FT reaction is a polymerisation process conventionally known for the production of hydrocarbon fuels from syngas. The latter can be derived from natural gas, coal or biomass gasification through steam reforming or gasification. In the past two decades the FT process has also been studied for the production of LOs (Fischer-Tropsch to Olefins, Eq. 2). CO_2 can be used as well as a feedstock (CO_2-FT), and in this case the process involves an initial Reverse Water Gas Shift step to convert CO_2 to CO (Eq.1).

RWGS: $CO_2 + H_2 \leftrightarrow CO + H_2O$ $Eq.1$

FT to Olefins: $nCO + 2nH_2 \rightarrow C_nH_{2n} + nH_2O$ $Eq.2$

FT to Paraffins: $(2n + 1)\ H_2 + nCO \rightarrow C_nH_{2n+2} + nH_2O$ $Eq.3$

Fe, Co, Ni, and Ru-based materials are the best options for the FT process. Fe and Co are more abundant than the other three elements, and are employed in the industrialized FT processes. In particular, for the LO synthesis the best choice are the Iron catalysts. Metallic iron and iron carbides are responsible for CO dissociation and are the active phases in FT synthesis. Moreover, in the presence of the Fe catalysts, during the reaction the produced water (Eq.1) reacts rapidly with CO to produce CO_2 (Water Gas Shift, WGS) Thanks to their ability to catalyse not only FT, but also the WGS and RWGS reactions, iron-based catalysts are common for the CO_2-FT process[19,20]. The catalytic performance of iron catalysts depends on their active

phase, and to the promoter and support if present[21]. Moreover, carbon deposition is often the main cause of the loss of activity of iron-based catalysts.

FT synthesis is a complex polymerization reaction that concerns C_1 monomer species adsorbed on the surface of heterogeneous catalysts[22]. At the beginning of the reaction, CO is adsorbed on the catalyst surface followed by its direct or assisted dissociation. Thus, the formed C_1 monomers can either be hydrogenated and desorbed as CH_4 , or they can take part in chain growth phenomena to produce surface oligomers. The desorption of the surface oligomers would produce olefins or paraffins with different atoms of carbon. CO_2-FT involves the CO_2 conversion to CO at the catalyst surface prior to the polymerization mechanism. Though CO and CO_2 hydrogenation have much in common, it is rare that the catalysts showing high selectivity to LOs in FT synthesis exhibit high LO selectivity in CO_2 hydrogenation.

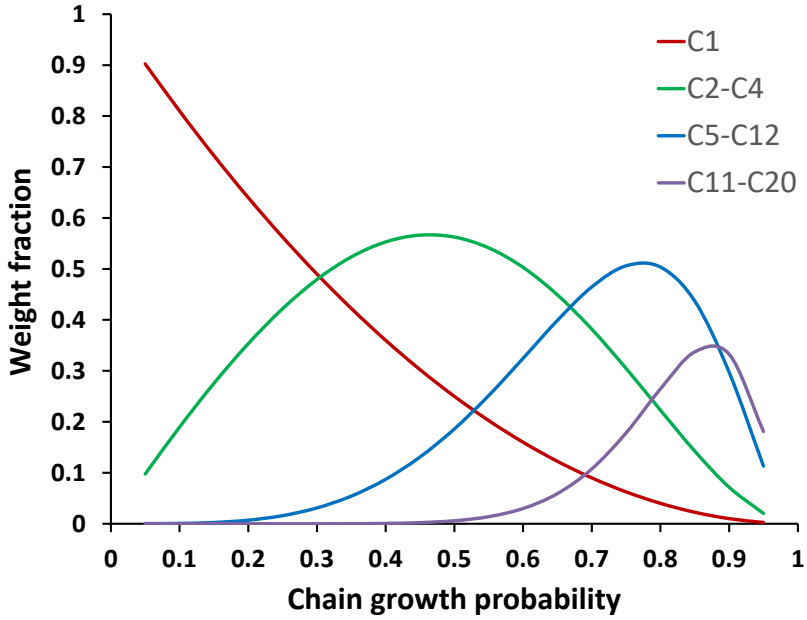

Figure 2: FT product weight fraction as a function of the chain growth probability.

The product spectrum of the FT polymerization is rather broad. Methane is an undesirable product of this reaction, while the main by-products, H_2O and CO_2, are involved in the regulation of the syngas H_2/CO ratio thanks to the WGS or RWGS reactions. Concerning the hydrocarbon fraction, it consists of a mixture of paraffins, olefins, and oxygenates. The

product distribution follows the Schulz-Flory model of linear polymerization adapted for FT synthesis by Anderson (Anderson-Schulz-Flory model[23]). According to the Anderson Schultz Flory model, the molar fraction Mn of the hydrocarbon product with a number of C atoms n depends on the chain growth probability (α), which in turn depends on the rates of chain growth r_p and chain termination r_t, according to the following equations:

$$Mn/n = (1 - \alpha)^2 \alpha^{(n-1)} \quad \text{Eq. 5}$$

$$\alpha = r_p/(r_p + r_t) \quad \text{Eq. 6}$$

Figure 2 shows the hydrocarbon distribution as a function of chain growth probability for the FT reaction. As it can be observed, FT synthesis produces always a multitude of species, that can be classified in hydrocarbons fractions (C1; C2-C4; C5-C12; C13-C20). Moreover, to maximize the production of each hydrocarbon fraction, there is a specific chain growth probability, which allows to achieve its highest theoretical selectivity. For the LO fraction (C_2-C_4) the maximum hydrocarbon selectivity (including both olefins and paraffins) is 58%,at a chain growth probability (α) of 0.46 [24]. In addition, the selectivity to CO_2 is generally around 50 %, which is corresponds to the complete reaction of the produced water with CO in the WGS reaction (Eq. 4). Considering the ASF constraint, the main challenge in FT synthesis is to reach high selectivity to specific olefins. In addition, both FT and CO_2-FT reactions are related with the synthesis of large amounts of by-products, which need to be separated. In particular, high methane production is undesirable due to the difficulties of its removal from the LO mixture. Thus, more selective routes for CO_x-to-LO process need to be developed.

1.4. Methanol mediated light olefin synthesis

The methanol-mediated route is an alternative solution to the highly selective production of hydrocarbon by-products from CO and CO_2[25]. In fact, it allows LO selectivity up to 95%

within the hydrocarbon fraction.[17] This process implies two reactions: CO or CO_2 are first hydrogenated to methanol and then methanol is converted to LOs. The COx conversion to LO can be performed with an indirect route, when the two reactions are performed separately, in two reactors and with two specific types of catalysts Alternatively, the LO synthesis can be performed directly (OX-ZEO process), in one reactor using a bifunctional catalyst that produces MeOH in-situ and converts it immediately to LO. [100] (Figure 3). . In OX-ZEO the COx conversion to MeOH involves usually metal-oxide catalysts[26], while MTO exploits mostly SAPO-34 and ZSM-5 zeolites [27].

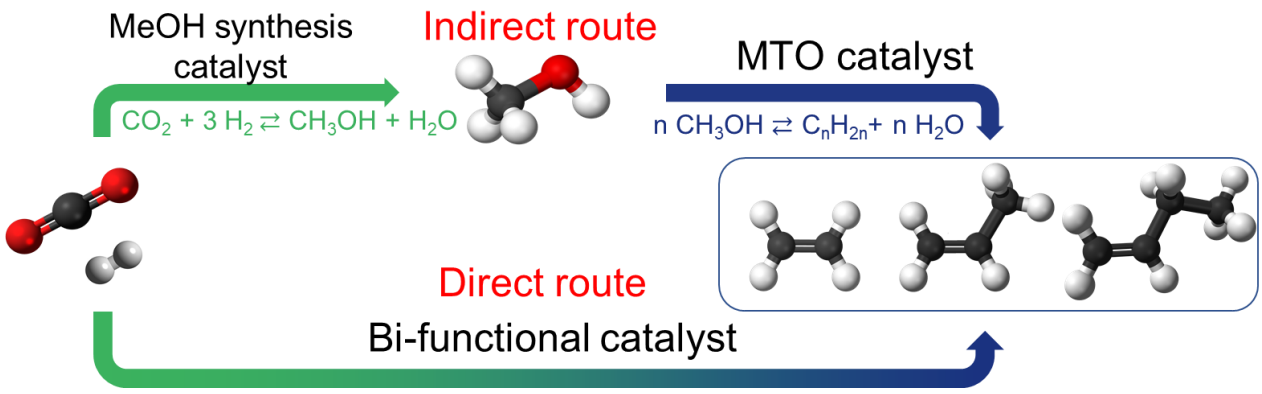

Figure 3: Indirect and direct route for the CO_2 hydrogenation to light olefins.

In the following sections, the indirect and direct routes will be presented in detail.

1.5. Indirect methanol-mediated light olefin synthesis

When the beforementioned indirect route is chosen for the LO production, the advantage is that the optimal conditions for the two steps can be selected. This is remarkable, considering that the MeOH synthesis and MTO have different operational temperatures and pressure. Moreover, in this Chapter it will be shown that while the MTO catalyst is the same in both the direct and indirect pathways, the MeOH synthesis catalyst is chosen according to the direct or indirect configuration of the process. This is due to the different temperature and pressure

conditions in the two configurations. As a result, the highest productivity could be achieved in the indirect route.

Contrarily, the disadvantages of the indirect process are the thermodynamic limitations related to the Methanol synthesis step, and the stability issues related to the MTO catalyst. Following in this Chapter these aspects will be discussed in detail. In general, the two steps of the indirect route, considered separately, are more mature compared to their combination in the direct way.

In the next two sections of this chapter the CO_2 hydrogenation to MeOH, and the Methanol To Olefins processes will be discussed.

1.5.1. CO_2 conversion to methanol

The first step of the indirect methanol mediated CO_x hydrogenation to LO is the MeOH synthesis. Methanol synthesis from CO_2 is one of the most interesting topics of study of the recent years. The reason for that is that MeOH is a versatile molecule used to produce a variety of chemicals that are currently produced from fossil feedstocks, and it can also be employed as fuel.[28] Also dimethyl ether (DME), the product of MeOH dehydration, has applications as energy carrier. The MeOH application as a fuel is facilitated by its liquid nature. Furthermore, this product can be derived from sustainable feedstocks, like biomass and CO_2.

All this considered, Olah et al. proposed a "Methanol Economy" in which this molecule is the key point for a carbon-neutral economy[29,30] (*Figure 4*). Indeed, to achieve this result, the energy used for the MeOH production has to be renewable, and the H_2 used for the CO_2 hydrogenation must be produced from water electrolysis.

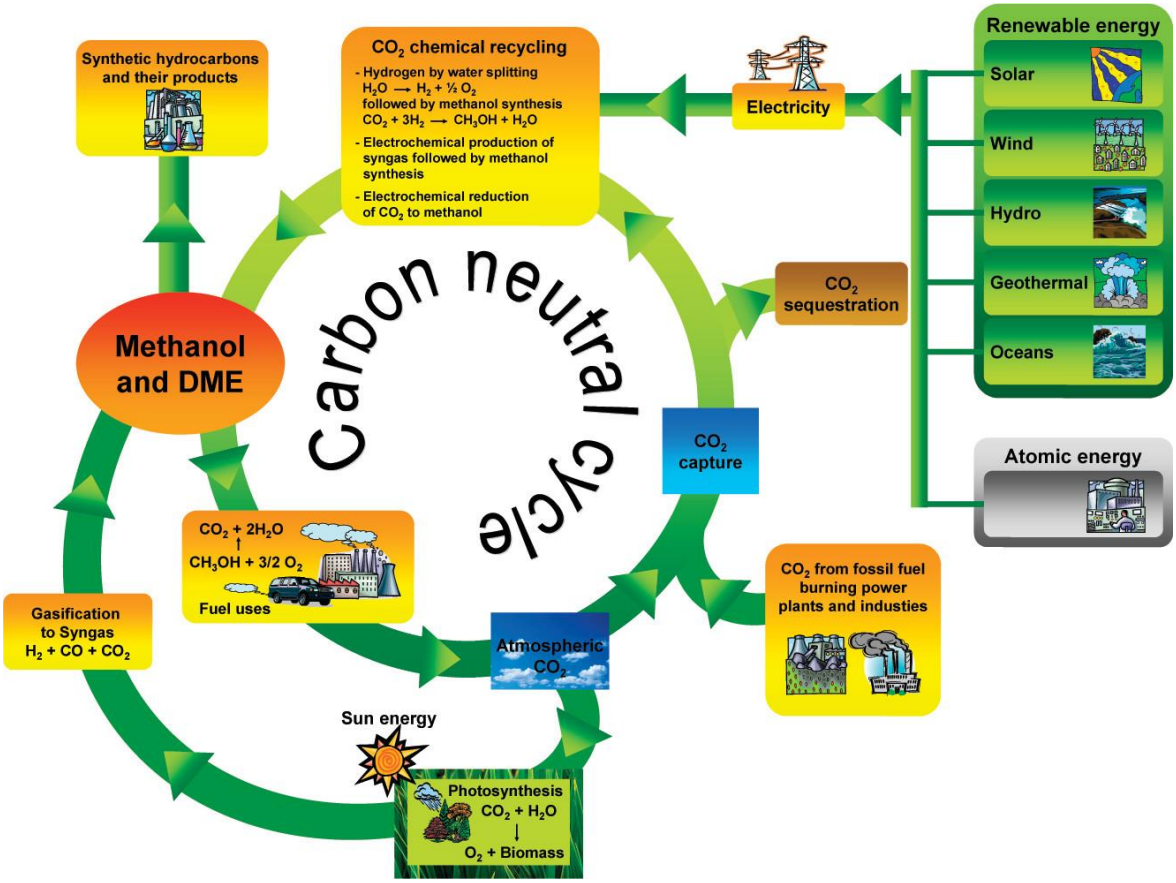

Figure 4: Scheme of the MeOH Economy proposed by Olah et al. Ref[30]

Today the industrial methanol production still involves the conversion of syngas produced from natural gas, naphtha or coal (fossil) with added CO_2 over Cu/ZnO/Al2O3 catalysts (Lurgi MegaMethanol^{TM}).

1) $CO + 2\ H_2 \rightleftharpoons CH_3OH$

Nonetheless, the research has shifted toward a more sustainable process, which converts CO_2 with green H_2. The two main reactions that occur in the CO_2 hydrogenation to MeOH conditions are:

2) $CO_2 + 3\ H_2 \rightleftharpoons CH_3OH + H_2O$

3) $CO_2 + H_2 \rightleftharpoons CO + H_2O$

Other reactions can also be present:

4) $CH_3OH \rightleftharpoons CO + 2\ H_2$

5) $CO_2 + 4\ H_2 \rightleftharpoons CH_4 + 2\ H_2O$

6) $2\ CH_3OH \rightleftharpoons CH_3OCH_3 + H_2O$

CO is the main side product of CO_2 hydrogenation, and it is produced from the RWGS reaction or from MeOH decomposition.[31] Methane can be found as a side product, produced from the complete hydrogenation of the activated CO_2.[32] Dimethyl ether (DME), can be produced especially when the catalyst shows a marked acidity, that promotes the MeOH dehydration .[33] Nonetheless, DME can be considered a valuable side product, and especially in the indirect LO synthesis, it can be used in MTO to produce olefins.[34]

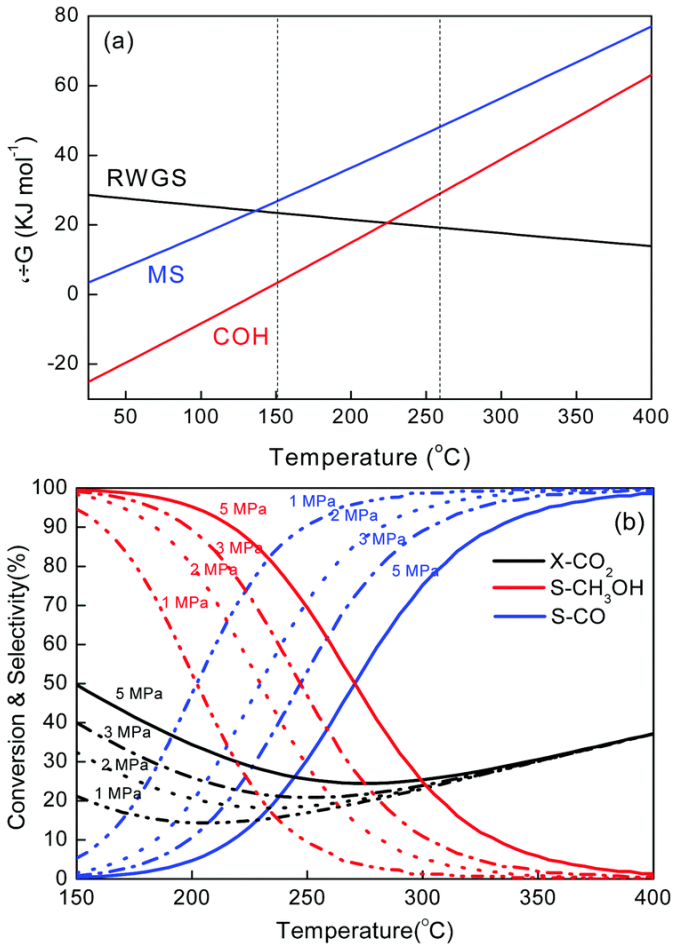

Figure 5: Thermodynamic limitation in the MeOH synthesis process. [26]

*Figure 5*a illustrates the Gibbs free energy changes for the Methanol synthesis from CO and CO_2 and for the RWGS reaction. As shown in the picture, the RWGS is an endothermic reaction, and the ΔG decreases with increasing temperature. Instead, .the CO_2 hydrogenation, as well as the CO counterpart, is an exothermal reaction. Hence, the Gibbs energy change increases with increasing temperature in both cases. Nonetheless, in the CO case the reaction is characterized by a lower ΔG, which allows to increase the temperature to higher values while keeping the MeOH synthesis as the predominant reaction. *Figure 5*b shows that the CO_2 conversion to MeOH reaction is limited by the thermodynamic equilibrium. A full conversion to MeOH is never possible. Furthermore, the CO_x hydrogenation to MeOH is associated with a decrease in the number of moles. Consequently, from a purely thermodynamic point of view, to maximize MeOH production the temperature should be lowered, and pressure should be increased. In the latter case, commonly the selected temperature is in the range of 2-5 MPa.

Together with thermodynamics, kinetics should be considered in the choice of the temperature. In fact, CO_2 is a highly stable molecule, and the thermal energy is required to overcome its activation energy. Due to that, generally the MeOH synthesis from CO_2 is performed at temperatures between 250 and 300 °C.

1.5.1.1. Catalysts

Generally, the main feature of a catalyst for the CO_2 hydrogenation to MeOH is the presence of active sites for CO_2 activation, and for the H_2 dissociative adsorption. The goal of the catalyst design is to find a material that combines these two types of sites, and reduce the number of sites that promote the side-reactions, especially the RWGS reaction, the methanol decomposition and the methanation.

The catalysts studied can be classified in these main categories: copper-based,[26,35–44] indium oxide,[45–50] mixed-oxides[51–53], noble-metal based[54–58] catalysts. The performance of different types of catalyst are reported in *Table 2*.

Table 2: Comparison of the performance of different catalysts in the CO_2 hydrogenation to MeOH reaction.

Catalyst	**P (bar)**	**T (ºC)**	**H_2:CO_2**	**WHSV NLg_{cat}^{-1} h^{-1}**	**X CO_2 (%)**	**S MeOH (%)**	**Ref.**
$Cu/ZnO/Al_2O_3$	50	180	3	15	1.7	97	59
		200	3	15	3.6	95.4	
		220	3	15	6.3	91.6	
		240	3	15	9.2	84.4	
		260	3	15	12.3	71	
$Cu-ZnO-ZrO_2$	30	220	3	3	14.9	62	60
Cu/a-ZrO2 (1% Cu)	30	180	3	1.2	1.8	100	40
$Cu/a-ZrO_2$ (15% Cu)	30	180	3	1.2	6.7	82.8	
Rh/In_2O_3	50	300	3	21	17.1	56	61
In_2O_3	50	300	3	20	3.7	100	62
Au/In_2O_3	50	300	3	21	11.7	68	62
Ni/In_2O_3	50	300	3	21	18.5	54	63
Pd/In_2O_3	50	300	3	21	18.4	72.7	64
In_2O_3/ZrO_2	50	300	3	16000	5.2	99.8	45
$ZnO-ZrO_2$	50	320	3	24	10	90	51
$Pd/ZnO/Al_2O_3$	30	180	3	3600	2.5	72.2	65
PdZn/ZnO	20	230	2	3.8	8	58	56

In_2O_3 based and mixed oxide catalysts

In_2O_3 has been identified as a highly selective catalyst for the CO_2 hydrogenation to MeOH, thanks to its ability to inhibit the RWGS reaction. Martin et al., carried out the reaction over pure or supported In_2O_3 catalysts. At 300 K 5 MPa and high space velocity, they obtained

a 100% selectivity to MeOH at a conversion of 3% for unsupported and 5% for the supported catalyst.[45]

The activity of this material is due to the formation of oxygen vacancies, which activate CO_2 and allow its hydrogenation to methanol. These vacancies are generated in the presence of hydrogen, and filled by oxygen derived from CO_2. Tsoukalou et al. [49] presented an operando study of the structural evolution of In_2O_3, using XAS and XRD to associate the catalyst structure to its performance. They observed the presence of an activation stage, in which oxygen vacancies generate, forming an In_2O_{3-x} phase: EXAFS showed a slight decrease of In–O coordination numbers, and XANES showed a partial reduction of In_2O_3. After ca. 50 h of stable MeOH synthesis, they observed a deactivation stage, due to the partial reduction of In_2O_{3-x} to metallic In.[49] With a similar work, the group also observed that the active sites in an In_2O_3:m-ZrO_2 solid solution (In-V_o-Zr) are significantly more stable than the In-V_o-In sites in the pure In_2O_3.[52] The ZrO_2-supported In_2O_3 catalyst is preferred, since the support increases the number of oxygen vacancies, facilitates CO_2 adsorption due to its higher basicity, increases the active phase dispersion, and stabilizes In_2O_3 from reduction to metallic In(0).

Despite the high selectivity to MeOH, a weak point of In-based catalyst is the low H_2 dissociation ability, which leads to generally low conversion at relatively high temperatures. To solve this issue, In_2O_3 has been promoted with different metals (Au[62], Ni[46], Pd[50,64,66], Pt[67,68], Rh[61]). This solution allows to enhance H_2 activation and consequently to increase the concentration of oxygen vacancies and thus improves the catalyst performance. It should be noted that the selectivity to MeOH in the CO_2 hydrogenation is a function of the conversion. Figure 6 shows the decrease in MeOH selectivity with increasing CO_2 conversion: the high selectivity to MeOH is only observed when the conversion is lower than 5%.

Moreover, a possible weak point is the need to operate in the upper limit of the conventional MeOH synthesis temperature range: the indium-based catalysts are normally active around 300 °C.

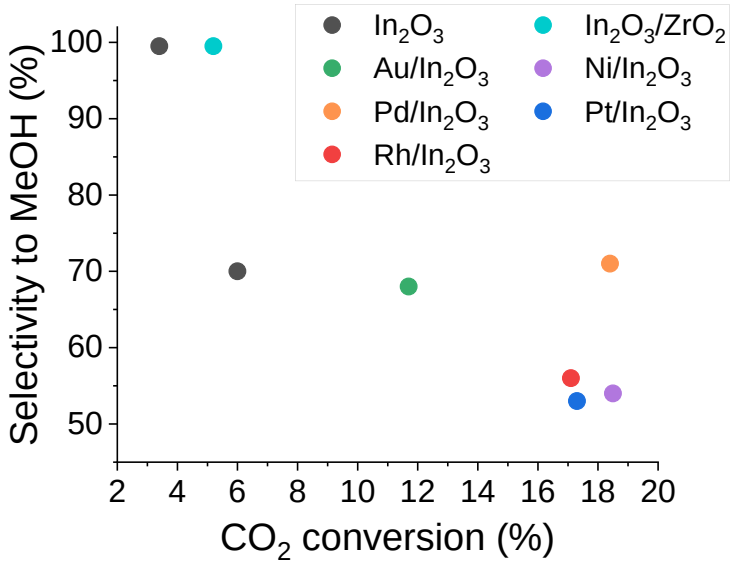

Figure 6: Dependency of the selectivity to MeOH on the conversion in the CO_2 hydrogenation over In-based catalyst. Conditions: 300 °C, 5 MPa, H_2/CO_2=4. Data taken from Ref.[45,61–64,68]

Similar to In_2O_3-ZrO_2, other mixed oxides have been reported in the literature. An interesting catalyst is ZnO–ZrO_2: Wang et al showed that at a Zn/(Zn+Zr) molar ratio of 13% this catalyst can attain a CO_2 conversion of 10% and a methanol selectivity of 90% (5.0 MPa, H_2/CO_2 = 3:1, 320°C, GHSV = 24,000 ml g_{cat}^{-1} h^{-1}).[51] In this catalyst, H_2 is adsorbed and dissociated on the Zn sites, and CO_2 is adsorbed on the coordination unsaturated Zr sites. Similar to In-based catalysts, it was observed that adding atomically dispersed Pd up to 0.8 at.% to the catalyst increases MeOH yield compared to the pure ZnO-ZrO_2 catalyst.[53] Other types of MZrOx solid-solutions that allow to achieve good results are GaZrOx and CdZrOx which exhibit methanol selectivity of ca. 80% at a conversion of 4.3–12.4%.[69]

As already pointed out for the In-based catalysts, also $ZnZrO_x$ shows good activity in the MeOH synthesis at temperatures around 300 °C, and a decrease of the MeOH selectivity with increasing conversion (Figure 7).

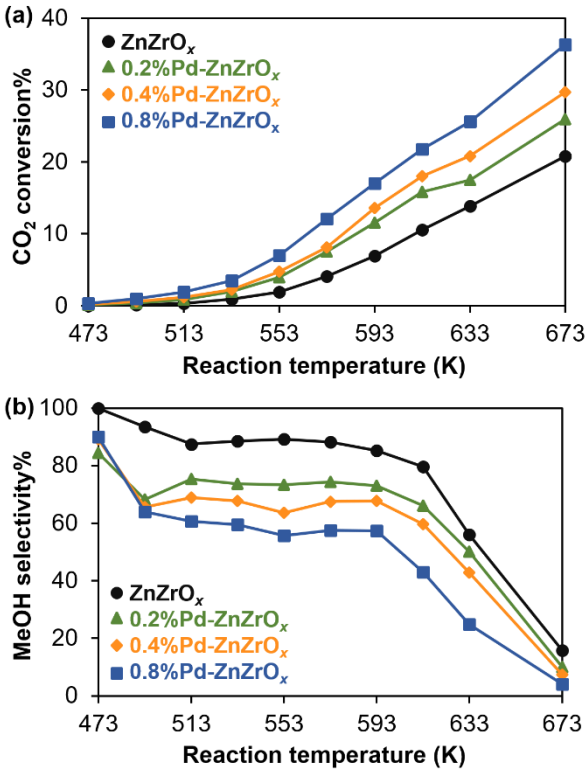

Figure 7: CO_2 conversion (a) and MeOH selectivity (b) as a function of the temperature in the CO_2 hydrogenation to MeOH over Pd-$ZnZrO_x$ catalysts. [53]

Noble metal-based catalysts

The main noble metal that has been studied for the CO_2 hydrogenation to MeOH is Pd. In particular, the Pd/ZnO catalyst attracted significant attention. The catalyst is generally a good RWGS catalyst, but if reduced at temperatures above 300 °C it modifies, forming a PdZn alloy that shows good activity in the MeOH synthesis reaction.[56] This different activity has been explained by the fact that the PdZn alloy stabilizes formate species produced in its surface from the CO_2 hydrogenation, which can then go further allowing to produce methanol. On the contrary, in the absence of the alloy, Pd decomposes the surface formate to CO and water,

promoting the RWGS.[70] Other than Pd/ZnO[56,65], alternative supports have been studied, like Ga_2O_3[71–73], CeO_2[74,75], mesoporous SiO_2[76], and CNTs[77].

Another noble metal that has been studied for the MeOH synthesis is gold. In a work presented by Hartadi et al, the Au/Al_2O_3, Au/TiO_2, Au/ZnO, and Au/ZrO_2 systems were compared. Among the these catalysts, Au/ZnO is the one that shows the highest selectivity (56%).[58] Moreover, it was observed that its performance was influenced by the AuNP particle size: the methanol selectivity increased from 56% (2 nm) to ca. 85% (7 nm).

As previously mentioned, noble metals are used to improve the activity In_2O_3 and $ZnZrO_x$ catalyst, which show generally show high MeOH selectivity. The Ag/In_2O_3 catalyst presented by Rui et al. showed a MeOH productivity 20 times higher than Ag/ZnO and other supports.[62] In the case of Ag, the data in the literature is poor. Already in 1993, Baiker et al compared the performances of Cu/ZrO_2, Ag/ZrO_2, and Au/ZrO_2 in the CO_2 hydrogenation to MeOH. While Au/ZrO_2 showed a significant activity to the RWGS reaction, Cu/ZrO_2 and Ag/ZrO_2 showed similar and good selectivity to methanol (ca. 80 % at 210 °C, 1.7 MPa, H_2:CO_2=3:1).[78] Another work on Ag-based catalysts was presented by Grabowski et al., who studied the CO_2 hydrogenation over Ag/ZrO_2 and Ag/ZrO_2/ZnO catalysts. They proposed that Ag^+ species were the MeOH synthesis sites, while Ag(0) leads to CO production. In fact, the rate of methanol formation is proportional to the content of Ag^+ species, and also to the content of the t-ZrO_2 phase. Interestingly, they observed that the formation of oxygen vacancies stabilizes the Ag^+ sites and the thermodynamically unstable tetragonal ZrO_2. On the contrary, The ZnO addition did not influence the methanol space time yield and was then considered non necessary.[79]

Copper-based catalysts

Among the catalysts known for the CO_2 hydrogenation to MeOH, copper can be considered the best metal choice for the catalyst development, providing at the same time

excellent performance and economic advantages. In fact, Cu-based catalysts show high activity at relatively low temperatures (200-250 °C), and most importantly, among the elements present in the Earth crust, Cu is the 25th most abundant one. This makes its use cheaper (compared to noble metals and indium) and sustainable. On the contrary, the high activity in CO_2 hydrogenation that distinguish the Cu-based catalysts leads to the disadvantage of the relatively high production of CO. Even so, the advantages of using this metal are confirmed by the fact that only Cu-ZnO-Al_2O_3 is used as a catalyst in the industrial synthesis of MeOH from CO_2.[26,80]

For the MeOH synthesis, Cu catalysts are always combined to other promoters or supports: the most diffused additive to Cu catalysts is ZnO which increases significantly the catalyst activity. Other components that can be frequently found in the literature are Al_2O_3 and ZrO_2, used either as promoters or supports. In the commercial CuO-ZnO-Al_2O_3 catalyst, Al_2O_3 acts as a structural promoter to increase the distribution of Cu, total surface area and the mechanical stability of catalyst.

Active sites in Cu-based catalysts

Concerning the active sites of Cu-based catalysts for the CO_2 hydrogenation to MeOH there is still a debate regarding their nature.

Different works showed that the activity of the CZA catalyst is due to the presence of steps at the surface of metallic Cu NPs.[35,81] According to Behrens et al, these steps can be stabilized by bulk defects like stacking faults or twin boundaries terminating at the surface.[81] Moreover, the presence of $Zn^{\delta+}$ in the steps further strengthens the binding of the intermediates and increases the activity of the catalyst. In particular, Strong Metal-Support Interaction (SMSI) leads to partial coverage of the Cu with ZnO_x, and a substitution of Zn into the Cu steps.

Alternatively, the catalyst activity has been explained with the reduction of ZnO, and the incorporation of Zn in the Cu particles forming CuZn alloys.[82] Nonetheless, Kattel et al

compared the activity of ZnCu and ZnO/Cu, observing that under the reaction conditions Zn in ZnCu is oxidized to ZnO, allowing ZnCu to reach the activity of ZnO/Cu.[83]

Furthermore, several works present the Cu^+ species as the active site for the reaction[84–88]. Zhang et al. observed a linear relationship between the MeOH production rate and the apparent $Cu^+/(Cu^+ + Cu^0)$ ratio in $Cu/CeZrO_x$ catalysts.[84] Specifically, they proposed a RWGS + CO hydrogenation mechanism, and they attributed the improved methanol production to a stronger interaction between Cu^+ and CO. The same result was presented by Yu et al, whose work showed that the stabilization of Cu^+ species in Cu/SiO_2 catalysts prevents CO desorption and promotes its further hydrogenation to MeOH.[85] The enhancement of the MeOH selectivity due to Cu^+ species has been associated to the formate pathway by Fernández-Villanueva et al.[86]. Their DFT study focused on the CO_2 hydrogenation to methanol over a Cu-MgO-based catalyst suggests that Cu^+ ions facilitate the stabilization of monodentate formate intermediates, while the bidentate formate formation leads to methane and CO. Moreover, hydroxyl groups and surface water stabilize the catalyst and promote the activation of CO_2 on the Cu^+ sites. Zhao et al studied atomically dispersed Cu over ZrO_2 and they observed that the active sites for the MeOH production are the $Cu^{\delta+}$ sites.[40] Increasing the copper loading above 8 wt. % produced large particles of Cu^0 which did not have CO_2 activation ability. Finally, Nakamura et al attributed role of ZnO in Cu/ZnO catalysts to the stabilization of Cu^+ on the Cu surface.[89]

While significant effort has been dedicated to determining the nature of the active sites for MeOH synthesis, insufficient evidence is available to clarify the differences between the sites responsible for MeOH synthesis and those participating in the RWGS reaction or secondary CH_3OH transformations to CO[26,90]. Ortner et al studied the selectivity-conversion correlations related to the CO_2 hydrogenation to MeOH over a CZA catalyst, combined with a kinetic analysis.[31]Their work identified two different types of active sites, for the MeOH synthesis from CO_2 and the MeOH decomposition sites, which is influent in the CO production.

Moreover, they showed that by saturating the MeOH decomposition sites with water, the selectivity to MeOH could be improved.

1.5.1.2. Mechanism of the CO_2 hydrogenation to methanol

The main mechanism proposed for the CO_2 hydrogenation to MeOH over Cu catalyst is the formate-based one (*Figure 8*). This important intermediate (HCOO*) forms from the adsorption of CO_2 on the surface (forming a CO_2* species), followed by its the direct hydrogenation by H* species. The latter form by the dissociative adsorption of H_2. The hydrogenation of HCOO* preferentially leads to the formation of HCOOH*which is then further hydrogenated to CH_3O_2*, which subsequently forms CH_2O* by splitting off its OH group. CH_3O* is the final intermediate before CH_3OH* is formed. This model was presented by Grabow, Mavrikakis, based on a DFT study.[91] In their work, a microkinetic model was fitted to experimental methanol synthesis rate data published in the literature, related to a commercial $Cu/ZnO/Al_2O_3$ catalyst. The model showed a good fit to the experimental data.

Alternatively, it was proposed that CO_2 was converted to CO via the RWGS reaction: CO_2* is hydrogenated to form a hydrocarboxyl (COOH*) intermediate that by further hydrogenation splits into CO* and H_2O. Once CO* is produced, it is hydrogenated to produce a formyl group (HCO*). The latter is then progressively hydrogenated to formaldehyde (CH_2O*), methoxy groups (CH_3O*) and finally CH_3OH.[83]

The formate pathway was presented also in the case of other catalyst like In_2O_3 [47,49], MoS_2[59], and $ZnO\text{-}ZrO_2$[51].

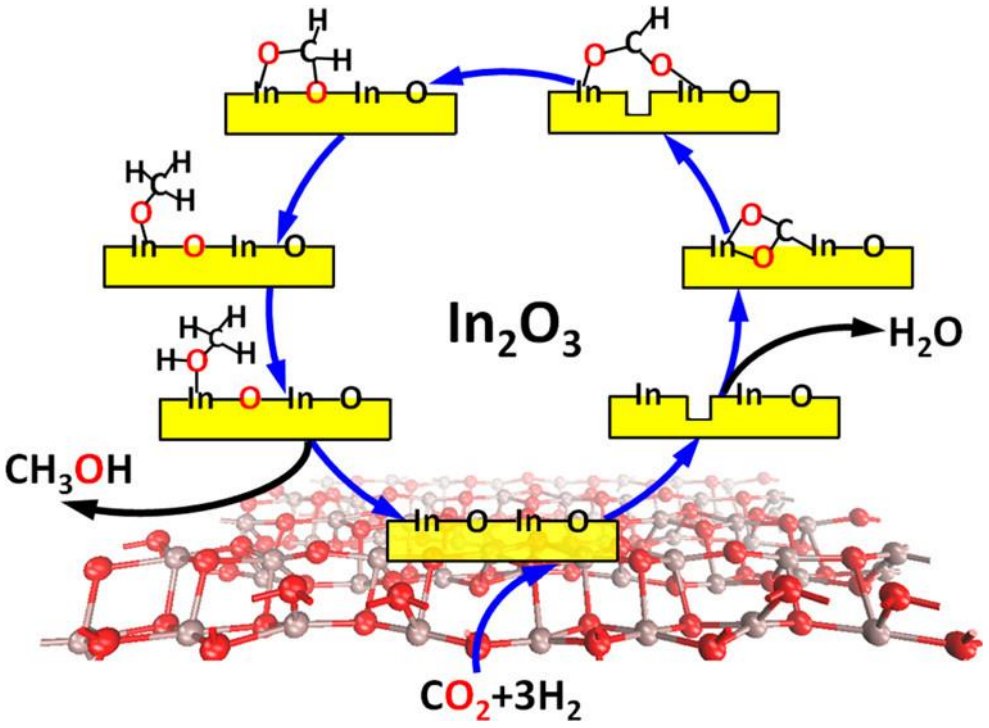

Figure 8: Formate-based mechanism of the CO_2 hydrogenation to MeOH over a In_2O_3 catalyst. [92]

1.5.2 Methanol to Olefins (MTO)

The Methanol to Olefins process (MTO), to date, this is the only process used for the industrial production of LOs that uses a feedstock that does not originate from oil. The main strength of the MTO process is its high MeOH conversion and selectivity to light olefins.

The two most studied catalysts for this reaction are the zeolites ZSM-5 and SAPO-34. The latter are the only ones exploited in MTO industrial plants.[59] Generally, SAPO-34 shows complete methanol conversion and total LO selectivity around 80-85 %.[60–63]. This high selectivity is due to the material mild acidity, and to the shape selectivity effect generated by the eight-membered ring pore openings that characterize SAPO-34 framework. On the other hand, the presence of small pores causes fast catalyst deactivation. In the case of ZSM-5, the pore openings are made of medium size ten-membered rings. On the one hand, ZSM-5 shows

lower total LO selectivity compared to SAPO-34; on the other hand, it allows to maximize the selectivity to propene (up to 50 %) and it shows a slower deactivation than SAPO-34.[64–66]

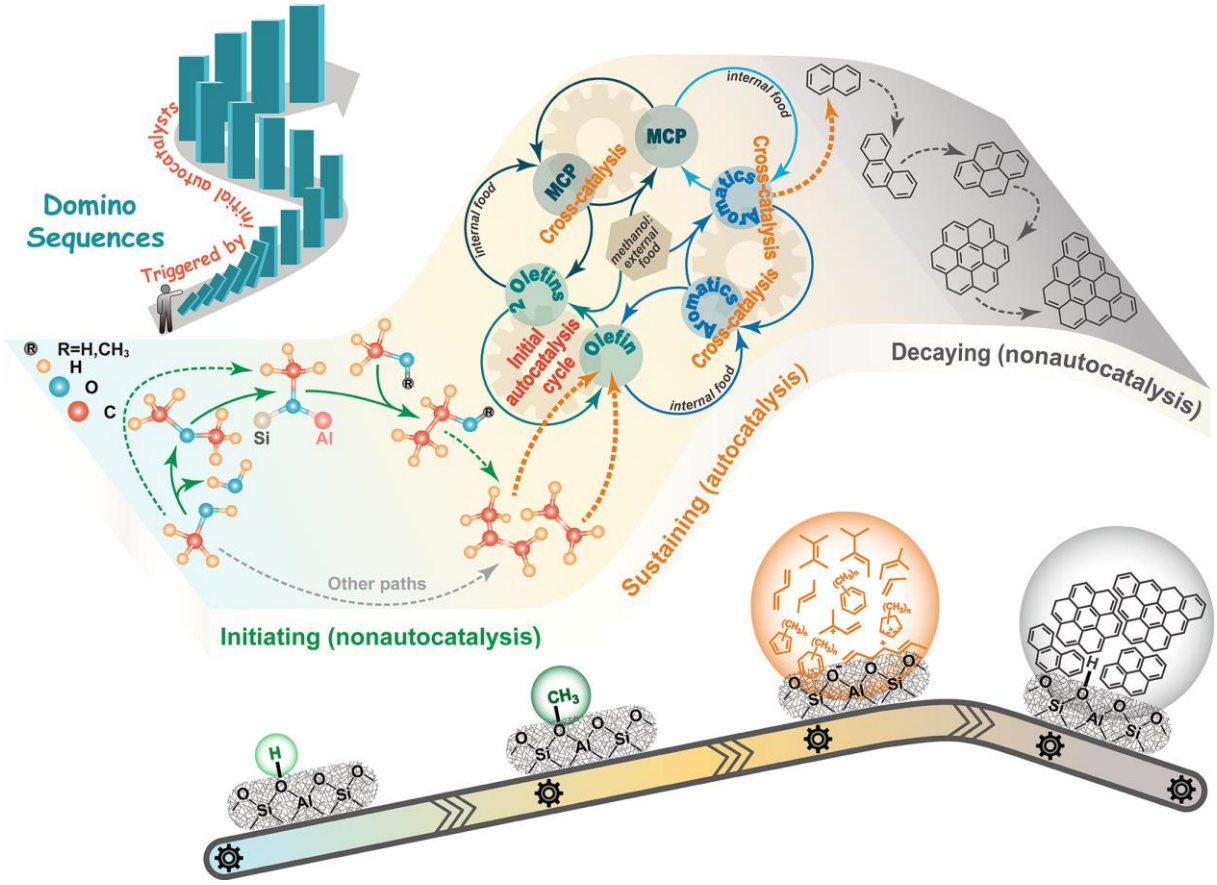

Figure 9: Scheme of the MTO reaction mechanism: initial non-autocatalytic stage; autocatalytic stage (hypercycle); coking.[93]

From the mechanistic point of view, there is an agreement on the definition of MTO as an autocatalytic reaction. First, MeOH is converted to LO inside the zeolite cages via the formation of methoxy groups on the zeolite surface and following C-C coupling. Second, the produced LO further react to form the so-called hydrocarbon pool species (HCPs), which can be described as polyalkylbenzenes or higher olefins. Finally, the HCPs contribute to the LO production (*Figure 9*). The mechanism can be described by two cycles: the first one is called olefinic cycle and consists of the cracking of higher olefins to produce mostly propylene; the second one is the aromatic cycle, based on the formation of aromatic species, which are mainly related to the ethylene production. A third cycle, based on Methylcyclopentenyl (MCP) cations,

was described by Zhang and co-workers[67]. The MCP species can be considered as bridge between the two main cycles. In fact, MCP can yield the olefins inside the zeolite cages. In turn, aromatic species can be produced from MCP.[68]

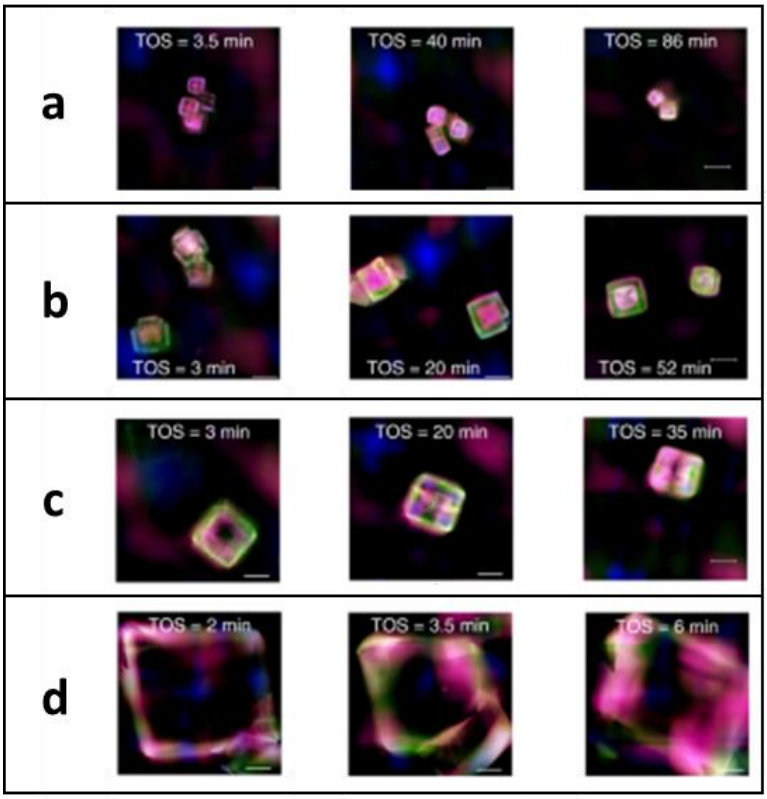

Figure 10: Evolution of HCP species inside SAPO-34 crystals of different sizes with time. (a) 5 nm; (b) 12 nm; (c) 17 nm; (d) 50 nm. The different colors represent different species: Blue: benzenic carbocations; Green: naphtalenic carbocations; Red: phenantrenic carbocations; Pink: pyrenic carbocations.[94]

The HCP mechanism is also linked with the main weak point of MTO catalysts, the coke deposition and pore occlusion. The nature of coke species and the mechanism for coke expansion inside SAPO-34 zeolite was studied by Wang[61] and colleagues. A two-phase deactivation mechanism was defined. First, polycyclic aromatic hydrocarbons (PAHs) form inside the zeolite cages. The largest possible one is pyrene due to the shape selectivity of the CHA cages. Then, a cage-passing growth phenomenon allows the expansion of the coke through the cross-link of PAH. Other studies on deactivation phenomena for the SAPO-34 catalysts were presented by Gao[69] et al. and Yang[70] et al. In particular, their work helped to

better localize the regions of the crystals affected by coke deposition and to classify the HCP species formed inside the cages. For nanoparticles with a diameter around 5 nm, both groups of carbon species observed at an initial stage in which HCPs appear in the centre of the crystal, followed by the expansion of these deposits to the external region. Furthermore, Gao et al. performed MTO on SAPO-34 catalyst with increasing crystal size (5 μm, 13 μm, 17 μm, 50 μm). According to their work, [69] after the catalyst deactivation, the distribution of HCPs and coke around the zeolite improves with decreasing the crystallite size, while for bigger crystals the formation of these carbon species occurs only in the external region of the zeolite (*Figure 10*).

Yang et al. studied the long-term effects of MTO conversion on SAPO-34 zeolite. They observed that coke formation causes a reversible expansion of the SAPO-34 unit cell. In fact, the ^{31}P MAS NMR spectra of deactivated samples were different from the fresh sample: the signal at -30.1 ppm., related to the tetrahedrally coordinated P (IV) atoms, was shifted to high fields. After the catalyst regeneration, the signal returned to the value of the fresh sample. In addition, the reversible expansion of the SAPO-34 unit cell was confirmed by the Rietveld refinements of the XRD patterns of deactivated and fresh samples, and by DFT calculations. Bhan's group presented a solution to increase the catalyst lifetime. They showed that H_2 cofeeding at high partial pressures allows to increase the cumulative turnover capacity towards hydrocarbons up to more than 70 times. This beneficial contribution of H_2 was confirmed by the absence of improvement when He was substituted to H_2 at the same experimental conditions.

The different stability of the two types of MTO catalyst, SAPO-34 and ZSM-5, influences the choice of the reactor type for the MTO process. The MTO process developed by UOP exploits SAPO-34, which deactivates relatively fast: the reactor chosen is a fluidized bed reactor in a reaction-regeneration layout. This choice is due to the fact that this

configuration allows to continuously regenerate the catalyst. The latter, in fact, can be transported from the reactor and regenerator and vice versa thanks to its fluidized nature. On the other hand, the Lürgi process uses the ZSM-5 catalyst: its higher resistance to carbon deposition allows to use a fixed bed reactor. [71]

1.6. Direct methanol-mediated CO and CO_2 hydrogenation

As previously mentioned, the MeOH synthesis and MTO can be combined to produce LO in one single process. This synthesis pathway was initially presented for the CO conversion to LO by Bao[25] and Wang[95], then it was studied for the conversion of CO_2.

In general, the methanol-mediated process can be considered as a combination of the following reactions:

1) $CO_2 + 3\ H_2 \rightleftharpoons CH_3OH + H_2O$

2) $CO + 2\ H_2 \rightleftharpoons CH_3OH$

3) $2\ CH_3OH \rightleftharpoons CH_3OCH_3 + H_2O$

4) $n\ CH_3OH/\ \frac{n}{2} CH_3OCH_3 \rightleftharpoons C_nH_{2n} + n/\frac{n}{2}\ H_2O$

The following side reactions also take place:

5) $CO_2 + H_2 \rightleftharpoons 2CO + H_2O$

6) CO_2 (or CO) + 4(or 3) $H_2 \rightleftharpoons CH_4$ + 2(or 1) H_2O

7) $CO_2/CO + H_2 \rightleftharpoons C^{5+} + H_2O$

8) $CH_3OH\ /\ CH_3OCH_3 \rightleftharpoons C^{5+} + H_2O$

9) $C_nH_{2n} + H_2 \rightleftharpoons C_nH_{2n+2}$

In this process, CO_2 is converted over a bi-functional catalyst, which is of the Oxide-Zeolite (OX-ZEO) type. For the latter, the methanol synthesis is typically ascribed to oxides of Zn, In, and Cu supported on ZrO_2, Cr_2O_3 or Ga_2O_3, while for the MTO the active phase is mostly SAPO-34 (*Table 3*and *Table 4*).

Interestingly, inside the hydrocarbon fraction the LO selectivity can reach up to ~90 %. This because, compared to FT synthesis, the MTO process does not have ASF type product distribution. In addition, methane production is low. On the contrary, the main side processes of the methanol-mediated CO_x hydrogenation to LO are the water-gas-shift reaction (WGS) in case of CO as a source and the reversible WGS (RWGS) reaction when CO_2 is used. [96] While the selectivity to CO in CO_2 conversion cannot go above 50%, the selectivity to CO in CO_2 hydrogenation can be as high as 90%.[97] At the same time, despite such a high yield of CO_2 or CO, the separation of carbon oxides and their recycling might increase the carbon efficiency of the process. Moreover, the addition of CO into the CO_2+H_2 inlet mixture and CO_2 to CO+H_2 is known to reduce the rate of RWGS and WGS reactions.[98,99]

The reaction conditions of this tandem process are a compromise between the different conditions related to the two original reactions: methanol synthesis is usually carried out at temperatures around 200-300°C and pressures of 3-5 MPa; MTO, instead, is performed at higher temperatures, 400-500°C, and lower pressure, atmospheric pressure. As a result, the CO and CO_2 tandem hydrogenation is generally performed at the temperature of 350-400°C, at which the production of the methanol intermediate would be reduced, and pressures up to 5 MPa, which significantly higher than the MTO conditions. Nonetheless, this process takes advantage of the combination of methanol synthesis and MTO. In fact, on the one hand, at high temperatures thermodynamics limits the CO_2 hydrogenation to methanol; on the other hand, the MTO step is favoured. So, the consumption of MeOH in the second sub-reaction shifts the equilibrium of the first one, and even with low MeOH production the LO production is possible.[97]

Table 3 shows the performance of recently published data for the CO hydrogenation to LO, while Table 4 presents the data for the CO_2 counterpart. It can be observed that the LO selectivity within the produced hydrocarbon (COx-free selectivity) is generally between 60 to

90%. This value depends on the selected catalyst, temperature, pressure and space velocity. Unquestionably, from the selectivity point of view, the results achievable with FT (60 wt%) are outperformed by the methanol-mediated pathway.

Table 3: Performance of tandem catalysts in the methanol-mediated CO hydrogenation to LO.

Catalyst	P (bar)	T (ºC)	H_2:CO	WHSV NL g_{cat}^{-1} h^{-1}	X_{CO} (%)	S_{CO2} (%)	CO_2-free S_{LO} (%)	Ref.
$ZnCrO_x$-AlPO-18	40	390	1	1200*	25.3	48	83	[100]
$ZrCeZnO_x$-SAPO-34	25	400	2	3.9	24.1	44.8	80.2	[101]
ZnO-ZrO_2-SAPO-34	30	400	2	3.6	25	41	75	[102]
$ZrCeZnO_x$-SAPO-34	10	400	2	3.9	12.6	44.6	82	[103]
ZnAlO-SAPO-34	30	400	2	3.0	24	44	80.6	[104]
Mn-Ga-SAPO-34	25	400	2	4.875	8.6	44.5	68.3	[105]
CrMnGa-SAPO-34	30	400	2	3.0	37.6	46.2	87.4	[106]

* – GHSV, h^{-1}

Table 4: Performance of tandem catalysts in the methanol-mediated CO_2 hydrogenation to LO.

Catalyst	P (bar)	T (ºC)	H_2:CO_2	WHSV NLg_{cat}^{-1} h^{-1}	X_{CO2} (%)	S_{CO} (%)	CO-free S_{LO} (%)	Ref.
$ZnGa_2O_4$-SAPO	30	370	3	5.4	13	48	86	[107]
In_2O_3-ZrO_2-SAPO	20	400	3	2.16	36.2	43	86.5	[98]
ZnO/Y_2O_3-SAPO-34	40	390	4	1.8	27.6	85	83.9	[108]
Cu-CeO_2-SAPO-34	20	396	3	5.8	15.2	57	63.1	[109]
NiCu/CeO_2-SAPO-34	20	375	3	12	15	65	77	[110]
$ZnAl_2O_4$-SAPO-34	30	370	3	15.9	15	49	87	[99]
$InCrO_x$-SAPO-34	35	350	3	1.14	33.6	55	75	[111]
In_2O_3-SAPO-34	30	350	3	9	14.1	60.9	76.9	[112]
$ZnZrO_x$&Bio-ZSM-5	30	380	3	2.0	10	82	60	[113]
ZnO/ZrO_2-MnSAPO-34	20	380	3	4800*	21.3	42.2	61.7	[114]
Mn_2O_3/ZnO-SAPO-34	30	380	3	3.6	29.8	55.1	80.2	[115]

* – GHSV, h^{-1}

1.6.1. Catalysts

Considering that the methanol-mediated route exploits bifunctional catalysts, the selectivity to LO depends on the combination of properties of two different type of catalyst. In fact, even though the commercial CuO-ZnO-Al_2O_3 catalyst is an optimal catalyst for methanol synthesis due to its activity and good selectivity at moderate temperatures of 200-300°C, it is

not suitable for the tandem process due to its high hydrogenation activity and hence higher methane and paraffin production at 350-400°C.[95] The same can be said for the Pd-based catalysts.[116] Cu-based systems have been studied in the methanol-mediated CO_x hydrogenation to LO but Zn- and In-based systems allow to obtain better LO selectivity. For this reason, the optimal choice for the tandem CO_2 hydrogenation to LO are ZnO- and In_2O_3-based catalysts. The activation of hydrogen by dissociation is found to occur on the -Zn-O-, -In-O-, or -Ga-O- domains[99,107]. It should be pointed out that a higher fraction of such fragments may lead to over-hydrogenation (formation of paraffins or methane).

In case of the CO conversion, In_2O_3 catalysts are not suitable due to their reducibility to metallic In in the presence of CO[117]. In the metallic state, In produces methane. Contrarily, for the CO conversion, MnO_2 or its mixture with oxides like Ga_2O_3 are active and selective to LO.[118,119] The chromium-based systems were also considered for this process. Recently Zhang[106] et al. showed that Cr addition enhances the catalyst performance thanks to an increase in the CO activation ability and the reducibility of mixed oxide catalysts. However, the toxicity of chromium makes this additive not desirable for the large-scale applications.

An important parameter for CO_x chemisorption and activation is the concentration of oxygen vacancies[99,107,120,121]: *Figure 11* shows the increase of LO selectivity over ZnGaOx-SAPO or MeOH/DME over ZnGaOx with increasing oxygen vacancies[76] . Dang et al. [120] studied the effect of zirconia on the In-based catalysts for CO_2 hydrogenation. In the studied catalysts, the presence of the $In_{1-x}Zr_xO_y$ mixed oxide enhances sharply the CO_2 chemisorption and stabilizes the reaction intermediates. This effect is due to the fact that such phase contains a large number of oxygen vacancies. Moreover, a reduction of the RWGS reaction activity and, hence, CO formation rate were observed. A linear dependence of site-time yields of both methanol and LO on the density of oxygen vacancies was found for the ZnCeZrO/SAPO-34 catalyst. Again, according to the authors, the vacancies activated CO_2 and stabilized the

methanol synthesis intermediates. In the case of CO hydrogenation, a sharp increase in oxygen vacancy number allowed the authors to obtain the LO already at atmospheric pressure and a relatively low temperature (300°C).[122]

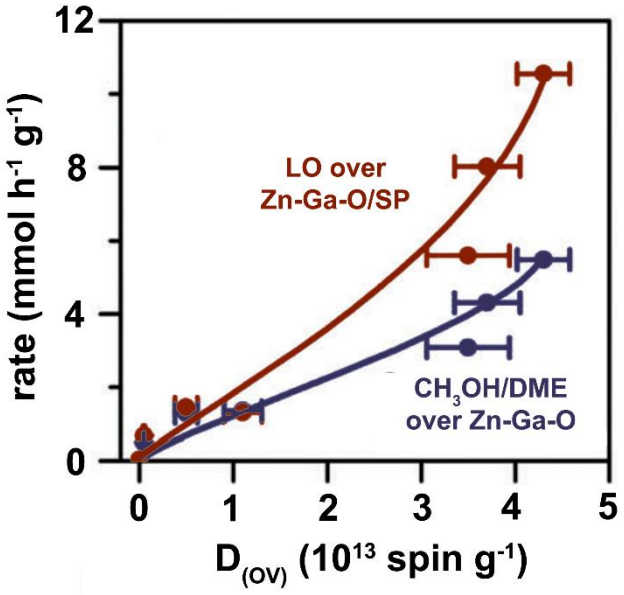

Figure 11: Correlation of the formation rates of CH_3OH/DME (Zn–Ga–O) and C_2–C_4 olefins (Zn–Ga–O/SAPO-34) with the density of oxygen vacancies $D_{(OV)}$.[107]

Interestingly, Zhu et al. proposed a MnO_2 catalyst that can provide both CO activation and further hydrogenation. [119]

For the second step of the process, MTO, the choice of zeolite can affect significantly the catalyst performance. In the tandem process, SAPO-34 is the most frequently chosen material, since the cage size of this zeolite allows to achieve the highest LO yield among all the studied systems.[114,123–126] *Figure 12* shows the analysis of the effect of SAPO types (SAPO-35, SAPO-17, SAPO-34, SAPO-18, SAPO-11, SAPO-31, SAPO-5 and SAPO-37) on the selectivity of CO hydrogenation, performed by Wang et al. [104] It can be observed that SAPO-34 possesses the highest selectivity towards LO fraction.

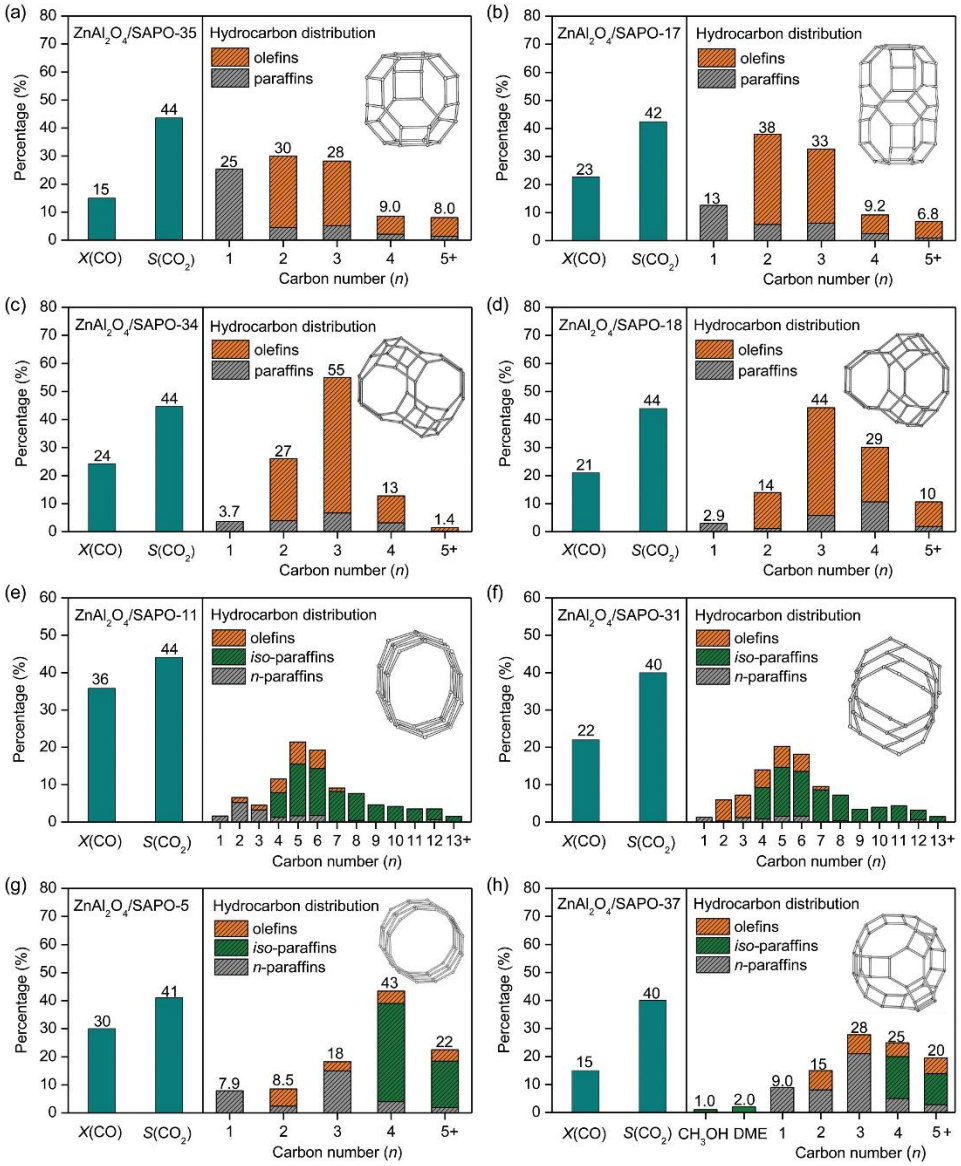

Figure 12: Cage type of different SAPO zeolites and performance of their relative ZnAlOx/SAPO catalysts in the syngas conversion to LO. a) SAPO-35; b) SAPO-17; c) SAPO-34; d) SAPO-18; e) SAPO-11; f) SAPO-31; g) SAPO-5; h) SAPO-37. [104]

Hierarchical SAPO-34 porosity improved mass-transfer inside zeolite phase. Nitric acid treatment of SAPO increased the catalyst porosity and reduced its acidity, which prevents coking. This change in properties resulted in an enhanced LO selectivity.[127] Moreover, the preparation of SAPO-34 with an hierarchical structure allowed an increase of the catalyst stability.[102] It was established that of such porosity in combination of high hydrogen pressure prevented the formation of polyaromatics, i.e. coke.

The ZSM-5 zeolite is often employed in the CO_x tandem hydrogenation to aromatics[128], due to its bigger pores. Nonetheless, hierarchical porosity can be considered an important factor to achieve high LO selectivity with this zeolite type, like it has been reported for a $ZnZrO_x$-ZSM-5 catalyst. [113] ZSM-5 with an hierarchical structure derived by a biomass template provided a ~65% CO-free selectivity to LO and only less than 1% of aromatics.[113]

Bao's group studied the behaviour of different types of MOR zeolite cages. While larger 12MR channels facilitate the formation of a broad range of hydrocarbons from methane to C_{5+}, smaller-sized "side pockets" 8MR selectively produce ethylene.[129] It was observed that blocking the access to the 12MR pores (hence MOR with only (MR pores available) allowed to achieve a higher selectivity to ethylene (>80%), while in the case of SAPO-34 the selectivity was only 20-30%.

Recently, Wang et al. observed that the use of H-RUB-13 zeolite provided a shift to propylene-butylene fraction in the product distribution compared to SAPO-34. This was explained by a change in hydrocarbon pool mechanism from aromatic to olefinic cycle.[130]

To control the light olefins selectivity, the most relevant SAPO-34 properties are the Brønsted acidity and the zeolite morphology. For the first parameter, a moderate acid strength is optimal for the conversion of MeOH/DME to LO. On the contrary, the strong Brønsted acid sites promote hydrogen transfer reactions, which lead to the formation of paraffins. For SAPO-34, NH_3-TPD exhibits two main peaks: the first desorption peak, at around 200 °C, is related to medium strength acid sites; the second one, generally found at 300-400 °C, is assigned to stronger sites. Luo et al have observed that the zeolite in the OX-ZEO catalyst shows a reduction of the intensity of the second peak, and a shift towards lower temperatures, compare to the pure phase. [120,121] This observation has been explained as an effect of the intimate contact between the two components.[121] Liu et al. studied the CO hydrogenation to LOs over a Zn-ZrO_2/SSZ-13 bifunctional catalyst. The effect of the variation of the zeolite acidity was studied, by

gradually increasing the H^+ content from NaSSZ-13 up to HSSZ-13 through an ion exchange method. Initially, they increased the Brønsted acid site concentration up to 0.10 mmol g^{-1}, and they observed an improvement in LO selectivity. Above this value, instead, they recorded a reduction of LO selectivity. From the paraffins selectivity point of view, they observed a continuous increase in Brønsted acid site concentration.[131] Similarly, Jiao et al evaluated the acid strength effect on the olefins/paraffins ratio in the C_2-C_4 fraction. A C_2-C_4 olefins/paraffins ratio of 0.9 was associated to a peak at 395 ° in the NH_3-TPD profile. Differently, when the NH_3-TPD peak shifted to 350 °C, the ratio increased to 4.7.[25] A way to control the acid sites concentration in the zeolite is modification of its composition, either by controlling the Si content, or introducing a transition metal (i.e. Mn, Zn, Zr). The addition of transition metals and decrease in Al/Si ratio promote the reduction of the strength and density of acid sites in SAPO.34 zeolites. As a consequence, an improvement in LO selectivity has been observed.[99,114,132]

The proximity of the OX-ZEO components is another feature that impacts the activity and selectivity of the catalysts in the CO_x tandem hydrogenation to LO. The diffusion from oxide to zeolite of the methanol produced in-situ may play an important role in both primary and secondary hydrogenation reactions. The local methanol concentration can be influenced by the proximity of the components, which should be optimal in order to achieve the best LO yields.[133] The proximity control, and hence the regulation of the diffusion of reaction intermediates, can be achieved in different ways.

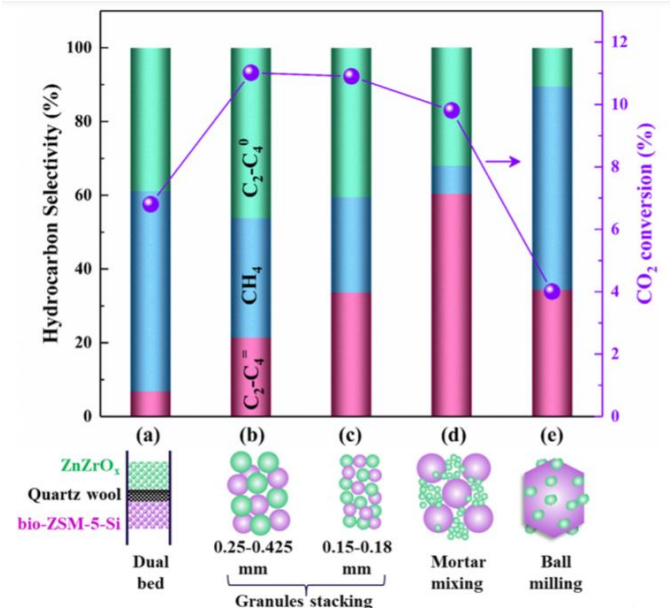

Figure 13: Effect of proximity between $ZnZrO_x$ and ZSM-5 components on the catalytic performance of the bifunctional catalysts in CO_2 hydrogenation: dual bed configuration (a), granules stacking with a different size (b, c), mixing of two powders by mortar mixing (d), and ball milling (e).[113]

The first approach consists in mixing the two catalyst components in different ways. This affects the distance between MeOH synthesis and MTO sites.[25,97,113,115] It was proven that a dual-bed layout promotes the methane production and RWGS[97,115,134,135]. Moreover, it was observed that if the two layers are in contact, methane production is reduced, and increasing the number of alternated oxide and zeolite layers the selectivity to C_2-C_4 hydrocarbons increases even further.[134,135]In general, grinding and physically mixing the components in a mortar is the best procedure to prepare selective and active tandem catalysts. A severe mixing through ball milling can affect negatively the performance (*Figure 13*).[113] Recently, it was shown that In- and Zn-species are mobile in the LO synthesis reaction conditions. This can lead to the blocking of the Bronsted acid sites and hence to the breaking of the components cooperative behavior.[136] This phenomenon is more likely to happen in the case of elevated proximity between the components. Ding et al studied the effects of components proximity in $ZnCrO_x$-SAPO-34 and MnO_x-SAPO-34. in the first case, the proximity had to be properly tuned to avoid nanoscale

interactions, while in the MnO_x-SAPO-34 catalyst the Mn migration was not recorded, and the nanoscale contact allowed to achieve the highest activity and selectivity possible.[137]

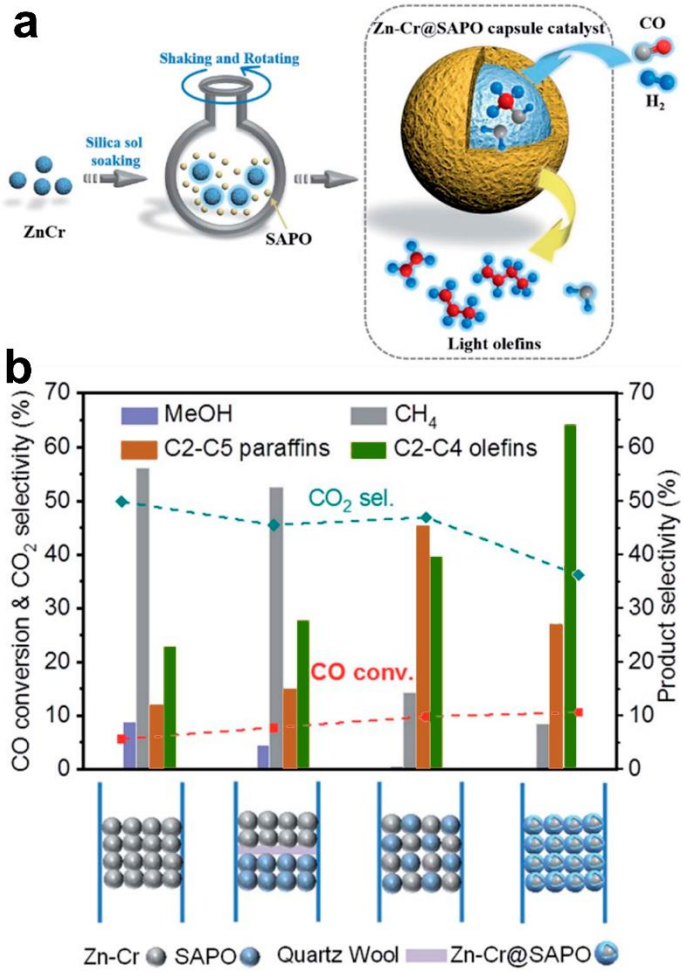

Figure 14: Preparation of the core-shell ZnCrOx@SAPO-34 catalyst (a); Performance of this core-shell catalyst comparing with sole $ZnCrO_x$, $ZnCrO_x$ and SAPO separated by quartz wool, and $ZnCrO_x$ with SAPO physically mixed (b).[138]

The alternative way to tune the proximity is the preparation of Oxide@zeolite core-shell structures. Such design should increase the extent of methanol transformation to LO and suppress the further hydrogenation of the latter products to paraffins. Tan et al. obtained core-shell by covering Zn-Cr granules by SAPO-34 crystallites, and the activity and selectivity of this catalyst was higher than in the case of a regular mixture of Zn-Cr and SAPO-34 (*Figure 14*). [138] The advantage of core-shell catalyst lies in the fast diffusion of methanol and water from the oxide surface to SAPO-34 channels, which limits the WGS reaction and promotes the LO synthesis. Synthesized LOs have less chances to undergo secondary hydrogenation to light

paraffins on the oxide surface due to the protection of the latter by the SAPO shell. A similar effect of zeolite shell protection from secondary processes was observed in the case of a CuZnZr@SAPO-34 catalyst.[139]

Long-term studies have shown that the tandem catalysts are characterized by high stability. This can be considered one of the main benefits of direct LO synthesis from CO_x, compared to the conventional MTO process, where the catalyst regeneration should be done cyclically due to the zeolite coking and consequent pore blocking. The presence of hydrogen and produced water in the reaction mixture facilitates the removal of carbon species from the zeolite. For example, after 124 h of activity in the CO_2 hydrogenation over $ZnGa_2O_4$/SAPO-34 at 400°C, the conversion decreased of 5%, while the selectivity to LO remained constant.[107] Similar behaviours were observed over other catalysts, which worked without noticeable conversion and selectivity changes for a long period of time.[25,113,120,127,138,140]

1.6.2. Reaction parameters

Most of reactions taking part in the methanol-mediated LO synthesis from CO_x, except for WGS or RWGS, are characterized by a volume reduction. Therefore, a pressure increase should improve the conversion to hydrocarbons or oxygenates and should not influence the CO or CO_2 production. The experimental data published in several works agree with this statement (*Figure 15*): CO_2 conversion progressively grows with the pressure increase. Moreover, on the one hand the selectivity to CO decreases due to a greater production of hydrocarbons; on the other hand, the pressure increase may promote the olefin secondary hydrogenation to paraffins (*Figure 15*a),[97,115] As a result, pressures in the range of 20-30 bar are optimal for balance the two phenomena and enable a high olefin selectivity.

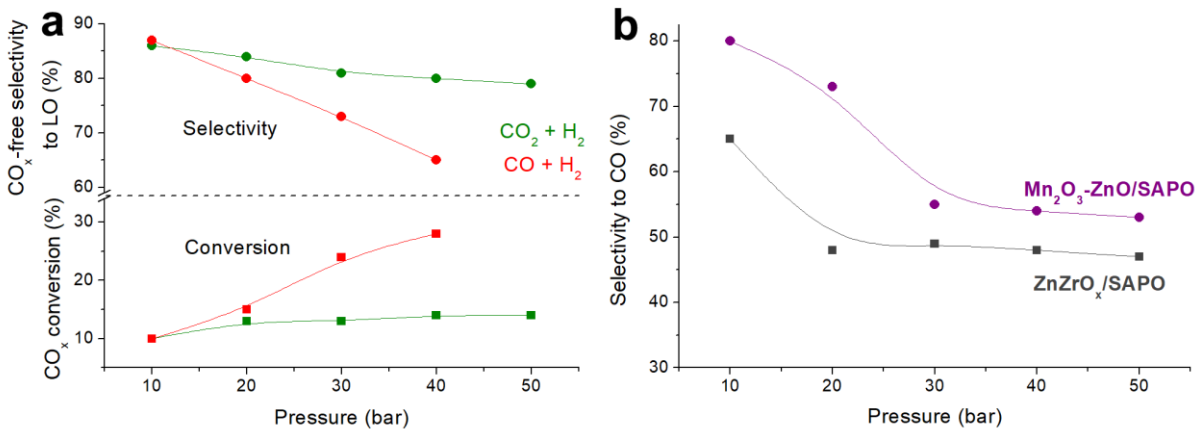

Figure 15: Effect of reaction pressure on CO and CO_2 conversion and selectivity to LO in methanol-mediated hydrogenation. Data from Refs [97,115,141]

Along with the pressure, the temperature is a key parameter to control the catalyst performance. In general, higher temperature results in better conversion but in the case of CO_2 hydrogenation, RWGS is predominant, and for both CO and CO_2 conversions, the light olefin secondary hydrogenation intensifies. (*Figure 16*). According to the information found in the literature, to obtain the highest LO selectivity the appropriate temperature range is around 370-390°C (*Figure 16*c). Wang[122,130] et al. studied a bifunctional catalyst composed by a Zinc-Cerium-Zirconium oxide solid solution and SAPO-34, achieving at 300 °C a good selectivity to LO and low CO and CH_4 selectivities. A similar result was obtained at 350°C for the CO_2 hydrogenation. The authors ascribed low WGS/RWGS activity to structure of the oxide phase, which increases the formation energy of carboxylate species, which are responsible for both CO and CO_2 production. Raveendra et al showed that an increase in temperature above 400 °C caused the decrease in LO selectivity and a growth of CH_4 and LP production.[142] An increase of the activity in methanation above 400 °C were also obtained for Zn-Cr-SAPO-34 catalyst.[138]

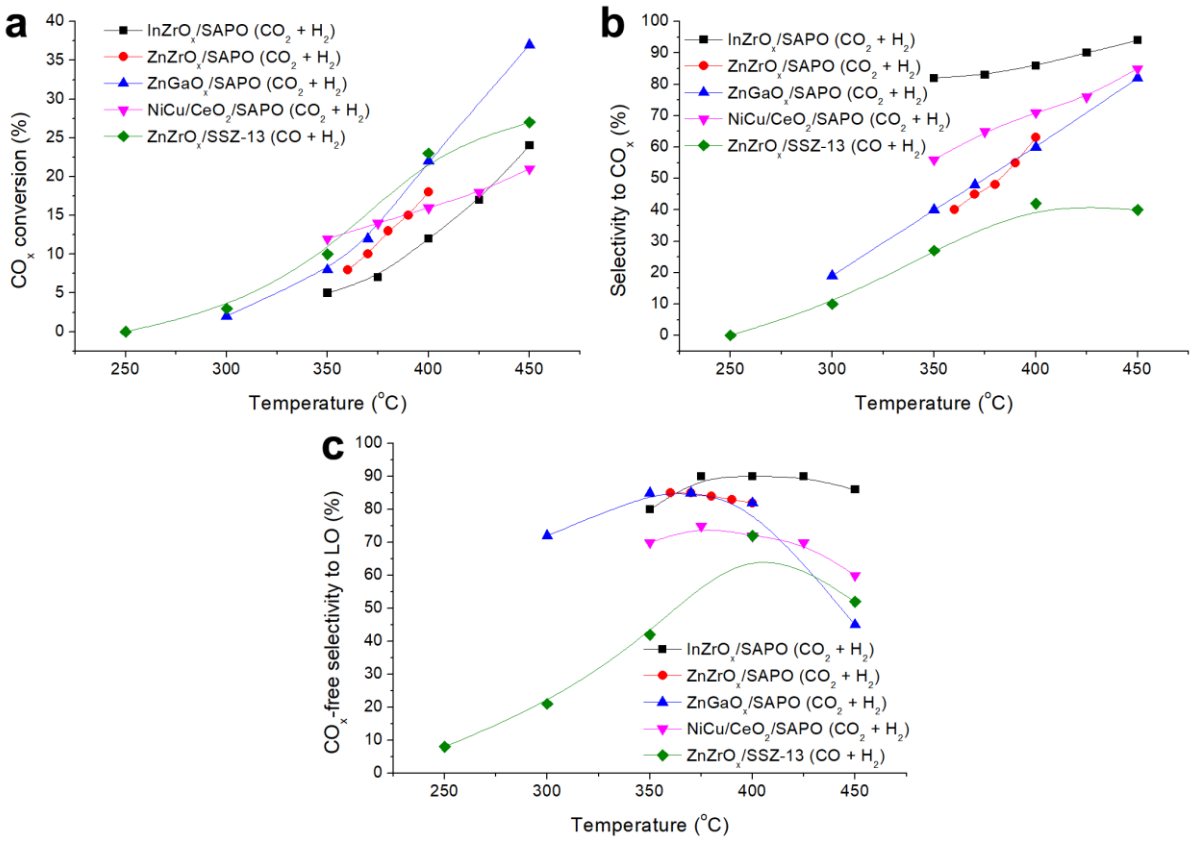

Figure 16: Effect of reaction temperature on the CO/CO_2 conversion (a), selectivity to CO/CO_2 (b) and CO/CO_2-free selectivity to LO in methanol-mediated CO_2 or CO hydrogenation. Ref.[97,107,110,140,141]

Finally, the third reaction parameter that affects the performance is the space velocity (SV). An increase in SV leads to a reduction of the conversion. [110] As a consequence, the higher the SV the higher the LO selectivity in both CO and CO_2 hydrogenation (*Figure 17*).[97,138] In fact, a faster flow decreases the contact time of the reagents and it should reduce the side reactions such as LO hydrogenation or methanation.

Nonetheless, in a work presented by Numpilai et al., the best LO yield (7.31%) in CO_2 methanol-mediated hydrogenation was obtained at the low SV of 1500 ml g^{-1} h^{-1}, despite the lowest olefin-to-paraffin ratio observed at this space velocity. [143] Sedighi and Mohammadi studied a CuCe/SAPO-34 catalyst and defined different space velocities for different purposes:

to achieve the highest LO selectivity it was proposed a SV of 17330 ml g^{-1} h^{-1}, while to obtain the best and LO yield they used a SV of 5400 ml g^{-1} h^{-1}. [109]

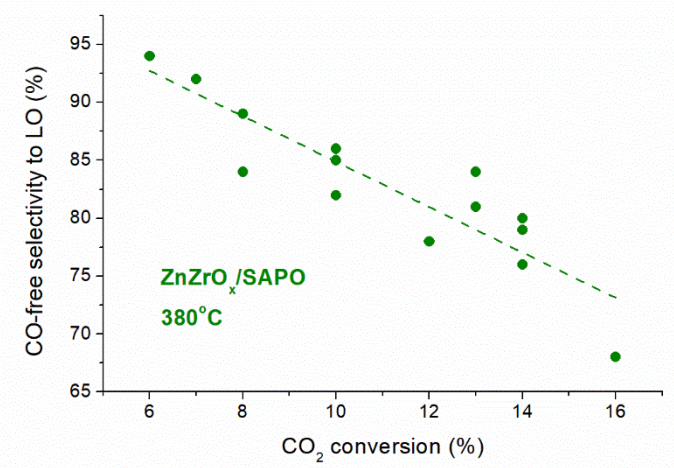

Figure 17: Selectivity-conversion plot for CO-free selectivity to LO in the methanol-mediated CO_2 hydrogenation based on data from Ref.[97]

1.6.3. Mechanism

1.6.3.1. Tandem CO hydrogenation to light olefins

The first mechanism proposed for the syngas hydrogenation to LO involved a ketene-intermediate.[25] Thanks to *in situ* NAP-XPS , it was observed that the reduced surface of zinc-chromium spinel activated CO, forming CO_2 and a single carbon atom C*. The hydrogenation of the latter surface species generates the very reactive CH_2* species, which in turn can react with CO forming the ketene CH_2CO. A further polymerization to higher hydrocarbons, similar to the FT mechanism, is not possible due to the polymerization inhibition effect caused by the ketene. To confirm the ketene-based mechanism, the authors did two tests, feeding either gas-phase CH_2CO or MeOH over the OX-ZEO catalyst at 400 °C: in the first case, the product selectivity was similar to the CO hydrogenation reaction; in the second case they observed a significant production of CO, derived from MeOH decomposition. A similar result was obtained from the same group in a work in which the product distribution of CO hydrogenation to LO over $ZnCrO_x$-Mordenite was compared to the ketene and the methanol conversion over

the pure mordenite[129] (*Figure 18*). Again, both syngas and ketene conversion gave a similar product distribution, with ethylene being the main product, while methanol produced a broader range of products. Further studies showed that the confinement effect in the different MOR types of cage plays an important role in ketene reactions. Larger 12MR channels allow longer contact time of ketene , which results in the production of a broader range of hydrocarbons and coking. The 8MR channels, instead, provide confinement which leads to the formation of stable acylium ions from ketene protonation. These ions then participate in catalytic reactions.[144]

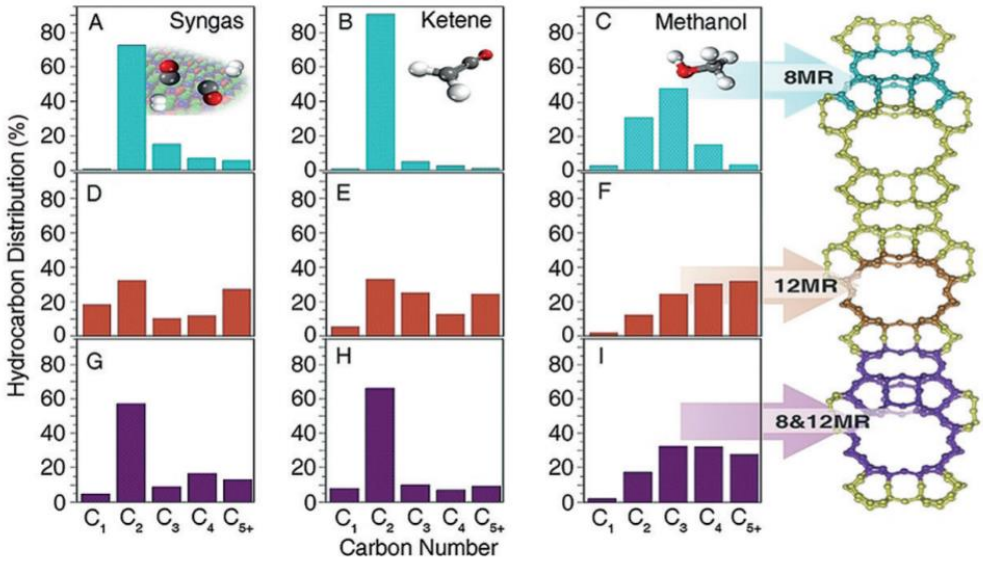

Figure 18: Hydrocarbon distributions in the conversion of syngas, ketene, and methanol over different sites of MOR zeolites: during syngas over ZnCrOx-MOR (a, d, e); ketene conversion over MOR (b, e, f); methanol conversion over MOR (c, f, i). [129]

A mechanism proposed as an alternative to the ketene-mediated route involves the formaldehyde intermediate. A combination of time-resolved DRIFTS and *in-situ* XPS was used by Wang et al.[122] to define this mechanism. They proposed that formaldehyde HCO* and H_2CO* species form on the catalyst surface after the CO adsorption and protonation. The lattice oxygen can convert these species to HCOO* or H_2COO*, which in turn can be hydrogenated to methoxy CH_3O* species. Finally, methoxy species form methanol, which can move to the zeolite and undergoes the MTO mechanism. A possible production of CH_4 can happen when

the hydrogenation of methoxy species breaks the C−O bond. Not only formate groups can form in the surface of the catalyst. The reaction between the adsorbed CO and hydroxyls OH* formed after water dissociation can form carboxylate COOH* groups. The latter can be hydrogenated to $COOH_2$* and afterwards can decompose into CO_2 and H_2. Formate and methoxy-species were identified by in situ DRIFTS in the work of Luo et al.[121] According to this work, oxygen vacancies activate CO molecules which can be hydrogenated to produce formate intermediates.

1.6.3.2. Tandem CO_2 hydrogenation to light olefins

For the CO_2 hydrogenation case, in 2017 a mechanism was proposed for the reaction catalysed by zinc-zirconia oxide mixed with SAPO-34, based on the formation of formate and methoxy groups[97]. This work proved the tandem nature of this process: ZnO-ZrO_2 and SAPO-34 were tested separately and it was observed that while the oxide produced only methanol, SAPO-34 was not active. Thanks to operando DRIFTS and MS analysis, the presence of both HCOO* and CH_3O* species were detected on the oxide surface in the absence of SAPO-34, while HCOO* was the prevalent species in the bifunctional catalyst. This observation proposed that during the tandem reaction CH_3O* produced MeOH which then moved to the zeolite to form olefins.

The same mechanism was proposed for the reaction performed over the Zn-Ga-O and Zn-Ce-Zr-O systems.[107,130,145] The initiation of the reaction has been attributed to the presence of oxygen vacancies by Liu et al[99], in the case of a $ZnAl_2O_4$-SAPO-34 catalyst (*Figure 19*). According to this work, CO_2 adsorption on the oxide surface forms a monodentate carbonate (CO_2*). The hydrogenation of the latter produces first HCOO* with water elimination, then CH_3O* and finally methanol. The authors proposed as well a mechanism for the hydrogen dissociation on the oxide surface. In detail, H^+ and H^- pair are formed, and HCOO* or CO_2* are hydrogenated by H-. After the MeOH production, this molecule interacts with the Brønsted

acid sites of zeolite and undergoes the hydrocarbon-pool mechanism that takes to the LO production.[130]

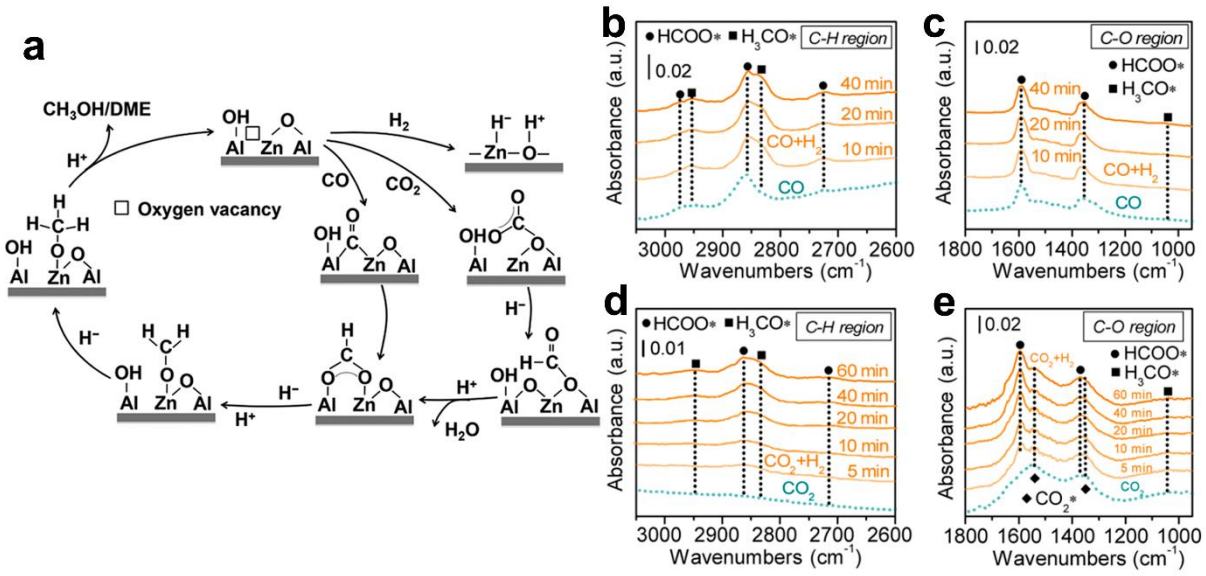

Figure 19: Proposed oxygen vacancy-assisted mechanism of methanol formation on the $ZnAl_2O_4$ surface during CO_2 hydrogenation to LO (a); in situ FTIR spectra of adsorbed species on $ZnAl_2O_4$: CO adsorption (dotted lines) and then switching to H_2/CO flow at 533 K (b,c), CO_2 adsorption (dotted lines) and then switching to H_2/CO_2 flow at 623 K (d,e). Figures from Ref.[99]

Wang[111] et al. studied In-based catalysts for CO_2 hydrogenation to LO and proposed the mechanism not only for the direct process but also for side reactions such as methanation and RWGS. Their work combined DFT with DRIFTS and MS analysis and showed that after the formation of H_3CO* through the formate mechanism already described, it might be protonated to methanol or hydrogenated to methane by breaking the C−O bond. The RWGS reaction, instead, instead of a formate intermediate has a carboxylate one, COOH*, which is formed after hydrogenation of adsorbed CO_2, then hydrogenated again to form $COOH_2$* and then decomposed to CO and H_2O. In this study, the authors also showed that the methanation process is inhibited by the addition of Ce or Cr to indium oxide. This is due to the much higher free energy barriers for the CH_3O* hydrogenation to CH_4 compared to pristine In_2O_3. At the same time, the RWGS activity was enhanced by the addition of Cr due to a stronger electron interaction between the catalyst surface and COOH* species.

1.7. Summary

The increasing levels of atmospheric CO_2 due to anthropogenic activities necessitate the development of viable technologies for its utilization, transforming a major environmental pollutant into useful products. The research on solutions to this issue is therefore both timely and essential.

Sustainable Aviation Fuels are the short-term solution for the abatement of CO_2 emission in the aviation industry. The SAF production technologies available today rely on biomass feedstocks, and have the disadvantages of a limited biomass availability, high land exploitation, and competition with food supply. These disadvantages are accentuated by the fact that the demand of SAF is expected to increase to meet the 2050 targets. For this reason, the development of Power-to-SAF technologies is necessary.

The TAKE-OFF project contributes to respond to this need, and aims to develop a new technology to produce SAF from CO_2. Even though Fischer-Tropsch allows to produce e-fuels from CO_2, the TAKE-OFF technology exploits an alternative pathway that involves the conversion of CO_2 to light olefins via methanol, followed by their oligomerization and hydrogenation to C_6-C_{12} hydrocarbons. This allows to achieve a higher carbon efficiency compared to the FT technology.

Within this project, this thesis contributes to the development of new catalyst for the methanol-mediated (tandem) CO_2 hydrogenation to LO, along with the CO_2 hydrogenation to methanol and the tandem CO hydrogenation to LO. The target molecules of this work not only are interesting within the project, but are key platform molecule for the chemical industry.

The methanol-mediated LO synthesis, especially from CO_2, is a potential sustainable pathway for the industrial production of this class of hydrocarbons. If this process reached a technological maturity, it would contribute in the future to reduce CO_2 emission in the

production of such valuable chemicals. Again, the FT process is an alternative pathway for the LO synthesis, but the methanol-mediated route has the advantage of reducing the selectivity to methane, and in general to obtain higher selectivity to LO.

Considering the two steps of the tandem reaction independently, for the MeOH synthesis the Cu-based catalysts are the most active, and allow to operate at milder conditions compared to the more selective In_2O_3 and $ZnO\text{-}ZrO_2$ catalysts. CO is the main side-product of this reaction, and the selectivity to MeOH at high conversion could be improved. For the Cu-based catalyst, not only the nature of the active sites for the MeOH synthesis is still under debate, but also the nature of the sites involved in the RWGS or MeOH decomposition that are responsible for CO production is still not clear. A better knowledge of the nature of these sites can allow to improve the selectivity to MeOH during the process, with a consequent increase in the catalyst activity.

Concerning the MTO process, the catalyst currently known allow to obtain high LO yields. The catalyst choice should be done depending on the desired olefins: SAPO-34 for ethylene-propylene and ZSM-5 for propylene. The main challenge for this reaction is to improve the catalyst stability to coking.

Concerning the direct methanol-mediated CO_x hydrogenation to LO, further studies are needed to increase the single-pass LO yield and to develop new catalytic systems making them more suitable to obtain particular olefins and to reduce the WGS/RWGS activity.

1.8. Objectives of this thesis

Considering the information presented in this Chapter, this thesis aims to tackle the urgent challenge of developing efficient and sustainable catalytic processes for the hydrogenation of CO_2 and CO into valuable chemicals, specifically light olefins and methanol. These chemicals

are crucial for numerous industrial applications, including the production of plastics, and fuels, like SAF.

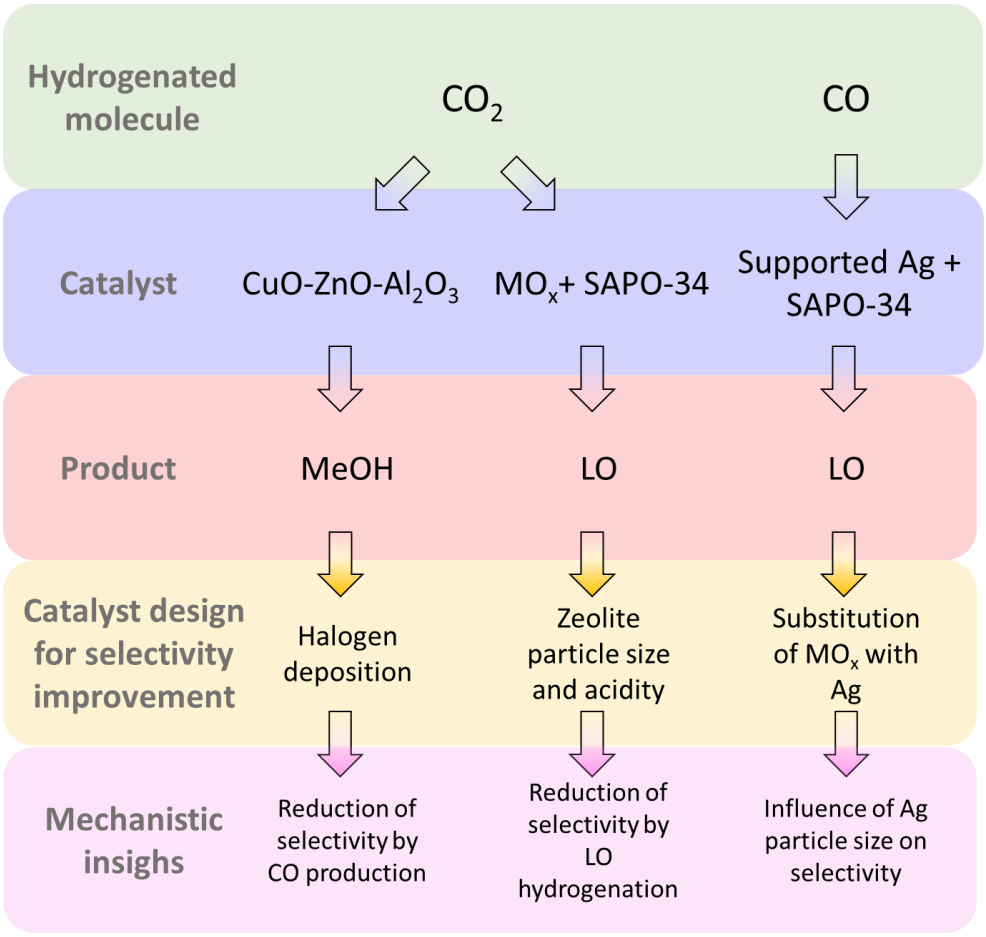

Figure 20: Summary of the work presented in this thesis. (MO_x stands for metal oxide).

The general goal of this thesis is on improving the performance and selectivity of catalysts used in these hydrogenation processes. To address these objectives, the strategic approach involves a combination of catalyst design and mechanistic studies. The Catalyst design involves the synthesis via simple and scalable methods, a variety of characterization techniques, and performance testing. The mechanistic studies are conducted to understand the underlying principles governing catalyst performance. The second chapter of this thesis will describe the experimental details of the work: the catalyst synthesis procedure, the catalytic experiments, and the characterization experiments, while the following chapters will present the results obtained.

The first area of research investigates the improvement of the commercial of CuO-ZnO-Al_2O_3 catalysts for methanol production. Even though this catalyst is commonly used in the industrial methanol production, in the CO_2 hydrogenation the undesired parallel production of CO, which reduces the overall efficiency of methanol synthesis, can still be reduced to improve the catalyst performance. The third chapter will be focused on the catalyst design for the CO_2 conversion to MeOH. By introducing halogen promoters into the CZA system, this work aims to improve the selectivity to methanol and reduce the production of unwanted CO. Moreover, the second objective of this chapter is to explain the observed selectivity-conversion correlations.

Secondly, this thesis delves into the methanol-mediated CO_2 hydrogenation to light olefins over bifunctional catalysts. In particular, this work aims to examine the roles of metal oxides and the SAPO-34 zeolite in this process. In particular, this work aims to better understand how to improve both components, thereby improving the yield and selectivity of light olefins. This investigation includes a detailed study of the catalytic mechanisms at play, providing insights that could direct the design of more efficient catalysts. The fourth chapter will present the work carried out to achieve this objective.

In parallel, the thesis aims to develop a novel catalyst for the methanol-mediated CO hydrogenation to LO. CO is a more reactive CO_2 derivate, produced via the Reverse Water Gas Shift reaction, and it is the main by-product of the methanol-mediated CO_2 hydrogenation to LO. The catalyst developed herein incorporates silver in a bifunctional material, with the goal of improving the selectivity of the hydrogenation process. The challenge addressed here is to tune the silver hydrogenation activity to achieve superior catalytic performance. Moreover, as it was observed that the selectivity to LO changed with time on stream, the second objective was to explain this phenomenon through the evaluation of the catalyst structural modifications. This work is presented in the fifth Chapter of this thesis.

At the end of this manuscript, the general conclusion of this work will be drawn, and new perspectives for future research will be evaluated, offering new ideas for the advancement in the LO production from CO_2. The outcomes of this research have the potential to advance technologies for CO_2 utilization, providing environmentally friendly and economically viable pathways for the production of essential chemicals, thereby addressing both environmental and industrial challenges.

1.9. References

(1) IEA. Net Zero Roadmap: A Global Pathway to Keep the 1.5 °C Goal in Reach, 2023. https://www.iea.org/reports/net-zero-roadmap-a-global-pathway-to-keep-the-15-0c-goal-in-reach.

(2) IEA. Net Zero by 2050, 2021. https://www.iea.org/reports/net-zero-by-2050.

(3) Calvin, K.; Dasgupta, D.; Krinner, G.; Mukherji, A.; Thorne, P. W.; Trisos, C.; Romero, J.; Aldunce, P.; Barrett, K.; Blanco, G.; Cheung, W. W. L.; Connors, S.; Denton, F.; Diongue-Niang, A.; Dodman, D.; Garschagen, M.; Geden, O.; Hayward, B.; Jones, C.; Jotzo, F.; Krug, T.; Lasco, R.; Lee, Y.-Y.; Masson-Delmotte, V.; Meinshausen, M.; Mintenbeck, K.; Mokssit, A.; Otto, F. E. L.; Pathak, M.; Pirani, A.; Poloczanska, E.; Pörtner, H.-O.; Revi, A.; Roberts, D. C.; Roy, J.; Ruane, A. C.; Skea, J.; Shukla, P. R.; Slade, R.; Slangen, A.; Sokona, Y.; Sörensson, A. A.; Tignor, M.; Van Vuuren, D.; Wei, Y.-M.; Winkler, H.; Zhai, P.; Zommers, Z.; Hourcade, J.-C.; Johnson, F. X.; Pachauri, S.; Simpson, N. P.; Singh, C.; Thomas, A.; Totin, E.; Arias, P.; Bustamante, M.; Elgizouli, I.; Flato, G.; Howden, M.; Méndez-Vallejo, C.; Pereira, J. J.; Pichs-Madruga, R.; Rose, S. K.; Saheb, Y.; Sánchez Rodríguez, R.; Ürge-Vorsatz, D.; Xiao, C.; Yassaa, N.; Alegría, A.; Armour, K.; Bednar-Friedl, B.; Blok, K.; Cissé, G.; Dentener, F.; Eriksen, S.; Fischer, E.; Garner, G.; Guivarch, C.; Haasnoot, M.; Hansen, G.; Hauser, M.; Hawkins, E.; Hermans, T.; Kopp, R.; Leprince-Ringuet, N.; Lewis, J.; Ley, D.; Ludden, C.; Niamir, L.; Nicholls, Z.; Some, S.; Szopa, S.; Trewin, B.; Van Der Wijst, K.-I.; Winter, G.; Witting, M.; Birt, A.; Ha, M.; Romero, J.; Kim, J.; Haites, E. F.; Jung, Y.; Stavins, R.; Birt, A.; Ha, M.; Orendain, D. J. A.; Ignon, L.; Park, S.; Park, Y.; Reisinger, A.; Cammaramo, D.; Fischlin, A.; Fuglestvedt, J. S.; Hansen, G.; Ludden, C.; Masson-Delmotte, V.; Matthews, J. B. R.; Mintenbeck, K.; Pirani, A.; Poloczanska, E.;

Leprince-Ringuet, N.; Péan, C. *IPCC, 2023: Climate Change 2023: Synthesis Report. Contribution of Working Groups I, II and III to the Sixth Assessment Report of the Intergovernmental Panel on Climate Change [Core Writing Team, H. Lee and J. Romero (Eds.)]*. *IPCC, Geneva, Switzerland.*, First.; Intergovernmental Panel on Climate Change (IPCC), 2023. https://doi.org/10.59327/IPCC/AR6-9789291691647.

(4) Cinti, G.; Baldinelli, A.; Di Michele, A.; Desideri, U. Integration of Solid Oxide Electrolyzer and Fischer-Tropsch: A Sustainable Pathway for Synthetic Fuel. *Appl. Energy* **2016**, *162*, 308–320. https://doi.org/10.1016/j.apenergy.2015.10.053.

(5) Gao, J.; Jia, C.; Liu, B. Direct and Selective Hydrogenation of CO_2 to Ethylene and Propene by Bifunctional Catalysts. *Catal. Sci. Technol.* **2017**, *7* (23), 5602–5607. https://doi.org/10.1039/c7cy01549f.

(6) Babu, B. H.; Lee, M.; Hwang, D. W.; Kim, Y.; Chae, H.-J. An Integrated Process for Production of Jet-Fuel Range Olefins from Ethylene Using Ni-AlSBA-15 and Amberlyst-35 Catalysts. *Appl. Catal. Gen.* **2017**, *530*, 48–55. https://doi.org/10.1016/j.apcata.2016.11.020.

(7) Saavedra Lopez, J.; Dagle, R. A.; Dagle, V. L.; Smith, C.; Albrecht, K. O. Oligomerization of Ethanol-Derived Propene and Isobutene Mixtures to Transportation Fuels: Catalyst and Process Considerations. *Catal. Sci. Technol.* **2019**, *9* (5), 1117–1131. https://doi.org/10.1039/C8CY02297F.

(8) Chernyak, S. A.; Corda, M.; Dath, J.-P.; Ordomsky, V. V.; Khodakov, A. Y. Light Olefin Synthesis from a Diversity of Renewable and Fossil Feedstocks: State-of the-Art and Outlook. *Chem. Soc. Rev.* **2022**, *51* (18), 7994–8044. https://doi.org/10.1039/D1CS01036K.

(9) Akah, A.; Williams, J.; Ghrami, M. An Overview of Light Olefins Production via Steam Enhanced Catalytic Cracking. *Catal. Surv. Asia* **2019**, *23* (4), 265–276. https://doi.org/10.1007/s10563-019-09280-6.

(10) Rahimi, N.; Karimzadeh, R. Catalytic Cracking of Hydrocarbons over Modified ZSM-5 Zeolites to Produce Light Olefins: A Review. *Appl. Catal. Gen.* **2011**, *398* (1–2), 1–17. https://doi.org/10.1016/j.apcata.2011.03.009.

(11) Gambo, Y.; Jalil, A. A.; Triwahyono, S.; Abdulrasheed, A. A. Recent Advances and Future Prospect in Catalysts for Oxidative Coupling of Methane to Ethylene: A Review. *J. Ind. Eng. Chem.* **2018**, *59*, 218–229. https://doi.org/10.1016/j.jiec.2017.10.027.

(12) Sattler, J. J. H. B.; Ruiz-Martinez, J.; Santillan-Jimenez, E.; Weckhuysen, B. M. Catalytic Dehydrogenation of Light Alkanes on Metals and Metal Oxides. *Chem. Rev.* **2014**, *114* (20), 10613–10653. https://doi.org/10.1021/cr5002436.

(13) Yarulina, I.; Chowdhury, A. D.; Meirer, F.; Weckhuysen, B. M.; Gascon, J. Recent Trends and Fundamental Insights in the Methanol-to-Hydrocarbons Process. *Nat. Catal.* **2018**, *1* (6). https://doi.org/10.1038/s41929-018-0078-5.

(14) Eschenbacher, A.; Varghese, R. J.; Abbas-Abadi, M. S.; Geem, K. M. V. Maximizing Light Olefins and Aromatics as High Value Base Chemicals via Single Step Catalytic Conversion of Plastic Waste. *Chem. Eng. J.* **2022**, *428*, 132087. https://doi.org/10.1016/j.cej.2021.132087.

(15) Shang, J.; Fu, G.; Cai, Z.; Feng, X.; Tuo, Y.; Zhou, X.; Yan, H.; Peng, C.; Jin, X.; Liu, Y.; Chen, X.; Yang, C.; Chen, D. Regulating Light Olefins or Aromatics Production in Ex-Situ Catalytic Pyrolysis of Biomass by Engineering the Structure of Tin Modified ZSM-5 Catalyst. *Bioresour. Technol.* **2021**, *330*, 124975. https://doi.org/10.1016/j.biortech.2021.124975.

(16) Torres Galvis, H. M.; Bitter, J. H.; Khare, C. B.; Ruitenbeek, M.; Dugulan, A. I.; de Jong, K. P. Supported Iron Nanoparticles as Catalysts for Sustainable Production of Lower Olefins. *Science* **2012**, *335* (6070), 835–838. https://doi.org/10.1126/science.1215614.

(17) Zhou, W.; Cheng, K.; Kang, J.; Zhou, C.; Subramanian, V.; Zhang, Q.; Wang, Y. New Horizon in C1 Chemistry: Breaking the Selectivity Limitation in Transformation of Syngas and Hydrogenation of CO2 into Hydrocarbon Chemicals and Fuels. *Chem. Soc. Rev.* **2019**, *48* (12), 3193–3228. https://doi.org/10.1039/c8cs00502h.

(18) Nitopi, S.; Bertheussen, E.; Scott, S. B.; Liu, X.; Engstfeld, A. K.; Horch, S.; Seger, B.; Stephens, I. E. L.; Chan, K.; Hahn, C.; Nørskov, J. K.; Jaramillo, T. F.; Chorkendorff, I. Progress and Perspectives of Electrochemical CO_2 Reduction on Copper in Aqueous Electrolyte. *Chem. Rev.* **2019**, *119* (12), 7610–7672. https://doi.org/10.1021/acs.chemrev.8b00705.

(19) Wei, J.; Ge, Q.; Yao, R.; Wen, Z.; Fang, C.; Guo, L.; Xu, H.; Sun, J. Directly Converting CO_2 into a Gasoline Fuel. *Nat. Commun.* **2017**, *8* (May), 1–8. https://doi.org/10.1038/ncomms15174.

(20) Panzone, C.; Philippe, R.; Chappaz, A.; Fongarland, P.; Bengaouer, A. Power-to-Liquid Catalytic CO_2 Valorization into Fuels and Chemicals: Focus on the Fischer-Tropsch Route. *J. CO_2 Util.* **2020**, *38*, 314–347. https://doi.org/10.1016/j.jcou.2020.02.009.

(21) Zhai, P.; Li, Y.; Wang, M.; Liu, J.; Cao, Z.; Zhang, J.; Xu, Y.; Liu, X.; Li, Y.-W.; Zhu, Q.; Xiao, D.; Wen, X.-D.; Ma, D. Development of Direct Conversion of Syngas to Unsaturated Hydrocarbons Based on Fischer-Tropsch Route. *Chem* **2021**, *7* (11), 3027–3051. https://doi.org/10.1016/j.chempr.2021.08.019.

(22) Schulz, H. Principles of Fischer–Tropsch Synthesis—Constraints on Essential Reactions Ruling FT-Selectivity. *Catal. Today* **2013**, *214*, 140–151. https://doi.org/10.1016/j.cattod.2013.05.009.

(23) Anderson, R.B.; Schultz, J.F.; Hofer, L.J.E.; Storch, H. H. Physical Chemistry of the Fischer-Tropsch Synthesis. In *US Bureau of Mines Bulletin, 580*; 1959.

(24) Chakkingal, A.; Pirro, L.; Costa da Cruz, A. R.; Barrios, A. J.; Virginie, M.; Khodakov, A. Y.; Thybaut, J. W. Unravelling the Influence of Catalyst Properties on Light Olefin Production via Fischer–Tropsch Synthesis: A Descriptor Space Investigation Using Single-Event MicroKinetics. *Chem. Eng. J.* **2021**, *419*, 129633. https://doi.org/10.1016/j.cej.2021.129633.

(25) Jiao, F.; Li, J. J.; Pan, X.; Xiao, J.; Li, H.; Ma, H.; Wei, M.; Pan, Y.; Zhou, Z.; Li, M.; Miao, S.; Li, J. J.; Zhu, Y.; Xiao, D.; He, T.; Yang, J.; Qi, F.; Fu, Q.; Bao, X. Selective Conversion of Syngas to Light Olefins. *Science* **2016**, *351* (6277), 1065–1068. https://doi.org/10.1126/science.aaf1835.

(26) Zhong, J.; Yang, X.; Wu, Z.; Liang, B.; Huang, Y.; Zhang, T. State of the Art and Perspectives in Heterogeneous Catalysis of CO_2 Hydrogenation to Methanol. *Chem. Soc. Rev.* **2020**, *49* (5), 1385–1413. https://doi.org/10.1039/C9CS00614A.

(27) Yang, M.; Fan, D.; Wei, Y.; Tian, P.; Liu, Z. Recent Progress in Methanol-to-Olefins (MTO) Catalysts. *Adv. Mater.* **2019**, *31* (50), 1902181. https://doi.org/10.1002/adma.201902181.

(28) Goeppert, A.; Czaun, M.; Jones, J.-P.; Surya Prakash, G. K.; Olah, G. A. Recycling of Carbon Dioxide to Methanol and Derived Products – Closing the Loop. *Chem Soc Rev* **2014**, *43* (23), 7995–8048. https://doi.org/10.1039/C4CS00122B.

(29) Olah, G. A.; Prakash, G. K. S.; Goeppert, A. Anthropogenic Chemical Carbon Cycle for a Sustainable Future. *J. Am. Chem. Soc.* **2011**, *133* (33), 12881–12898. https://doi.org/10.1021/ja202642y.

(30) Olah, G. A.; Goeppert, A.; Prakash, G. K. S. Chemical Recycling of Carbon Dioxide to Methanol and Dimethyl Ether: From Greenhouse Gas to Renewable, Environmentally

Carbon Neutral Fuels and Synthetic Hydrocarbons. *J. Org. Chem.* **2009**, *74* (2), 487–498. https://doi.org/10.1021/jo801260f.

(31) Ortner, N.; Zhao, D.; Mena, H.; Weiß, J.; Lund, H.; Bartling, S.; Wohlrab, S.; Armbruster, U.; Kondratenko, E. V. Revealing Origins of Methanol Selectivity Loss in CO_2 Hydrogenation over CuZn-Containing Catalysts. *ACS Catal.* **2023**, *13* (1), 60–71. https://doi.org/10.1021/acscatal.2c04480.

(32) Rui, N.; Shi, R.; Gutiérrez, R. A.; Rosales, R.; Kang, J.; Mahapatra, M.; Ramírez, P. J.; Senanayake, S. D.; Rodriguez, J. A. CO_2 Hydrogenation on ZrO_2 /Cu(111) Surfaces: Production of Methane and Methanol. *Ind. Eng. Chem. Res.* **2021**, *60* (51), 18900–18906. https://doi.org/10.1021/acs.iecr.1c03229.

(33) Cara, C.; Secci, F.; Lai, S.; Mameli, V.; Skrodczky, K.; Russo, P. A.; Ferrara, F.; Rombi, E.; Pinna, N.; Mureddu, M.; Cannas, C. On the Design of Mesostructured Acidic Catalysts for the One-Pot Dimethyl Ether Production from CO_2. *J. CO_2 Util.* **2022**, *62*, 102066. https://doi.org/10.1016/j.jcou.2022.102066.

(34) Li, Y.; Zhang, M.; Wang, D.; Wei, F.; Wang, Y. Differences in the Methanol-to-Olefins Reaction Catalyzed by SAPO-34 with Dimethyl Ether as Reactant. *J. Catal.* **2014**, *311*, 281–287. https://doi.org/10.1016/j.jcat.2013.12.004.

(35) Van Den Berg, R.; Prieto, G.; Korpershoek, G.; Van Der Wal, L. I.; Van Bunningen, A. J.; Lægsgaard-Jørgensen, S.; De Jongh, P. E.; De Jong, K. P. Structure Sensitivity of Cu and CuZn Catalysts Relevant to Industrial Methanol Synthesis. *Nat. Commun.* **2016**, *7*. https://doi.org/10.1038/ncomms13057.

(36) Lam, E.; Larmier, K.; Wolf, P.; Tada, S.; Safonova, O. V.; Copéret, C. Isolated Zr Surface Sites on Silica Promote Hydrogenation of CO_2 to CH_3OH in Supported Cu Catalysts. *J. Am. Chem. Soc.* **2018**, *140* (33), 10530–10535. https://doi.org/10.1021/jacs.8b05595.

(37) Lam, E.; Noh, G.; Chan, K. W.; Larmier, K.; Lebedev, D.; Searles, K.; Wolf, P.; Safonova, O. V.; Copéret, C. Enhanced CH_3OH Selectivity in CO_2 Hydrogenation Using Cu-Based Catalysts Generated via SOMC from Ga III Single-Sites. *Chem. Sci.* **2020**, *11* (29), 7593–7598. https://doi.org/10.1039/D0SC00465K.

(38) Laudenschleger, D.; Ruland, H.; Muhler, M. Identifying the Nature of the Active Sites in Methanol Synthesis over $Cu/ZnO/Al_2O_3$ Catalysts. *Nat. Commun.* **2020**, *11* (1), 3898. https://doi.org/10.1038/s41467-020-17631-5.

(39) Beck, A.; Zabilskiy, M.; Newton, M. A.; Safonova, O.; Willinger, M. G.; van Bokhoven, J. A. Following the Structure of Copper-Zinc-Alumina across the Pressure Gap in Carbon Dioxide Hydrogenation. *Nat. Catal.* **2021**, *4* (6), 488–497. https://doi.org/10.1038/s41929-021-00625-x.

(40) Zhao, H.; Yu, R.; Ma, S.; Xu, K.; Chen, Y.; Jiang, K.; Fang, Y.; Zhu, C.; Liu, X.; Tang, Y.; Wu, L.; Wu, Y.; Jiang, Q.; He, P.; Liu, Z.; Tan, L. The Role of Cu_1–O_3 Species in Single-Atom Cu/ZrO2 Catalyst for CO_2 Hydrogenation. *Nat. Catal.* **2022**, *5* (9), 818–831. https://doi.org/10.1038/s41929-022-00840-0.

(41) Divins, N. J.; Kordus, D.; Timoshenko, J.; Sinev, I.; Zegkinoglou, I.; Bergmann, A.; Chee, S. W.; Widrinna, S.; Karslıoğlu, O.; Mistry, H.; Lopez Luna, M.; Zhong, J. Q.; Hoffman, A. S.; Boubnov, A.; Boscoboinik, J. A.; Heggen, M.; Dunin-Borkowski, R. E.; Bare, S. R.; Cuenya, B. R. Operando High-Pressure Investigation of Size-Controlled CuZn Catalysts for the Methanol Synthesis Reaction. *Nat. Commun.* **2021**, *12* (1), 1435. https://doi.org/10.1038/s41467-021-21604-7.

(42) Wu, C.; Lin, L.; Liu, J.; Zhang, J.; Zhang, F.; Zhou, T.; Rui, N.; Yao, S.; Deng, Y.; Yang, F.; Xu, W.; Luo, J.; Zhao, Y.; Yan, B.; Wen, X.-D.; Rodriguez, J. A.; Ma, D. Inverse ZrO2/Cu as a Highly Efficient Methanol Synthesis Catalyst from CO_2 Hydrogenation. *Nat. Commun.* **2020**, *11* (1), 5767. https://doi.org/10.1038/s41467-020-19634-8.

(43) Wang, Y.; Kattel, S.; Gao, W.; Li, K.; Liu, P.; Chen, J. G.; Wang, H. Exploring the Ternary Interactions in Cu–ZnO–ZrO 2 Catalysts for Efficient CO_2 Hydrogenation to Methanol. *Nat. Commun.* **2019**, *10* (1). https://doi.org/10.1038/s41467-019-09072-6.

(44) Zhou, H.; Chen, Z.; López, A. V.; López, E. D.; Lam, E.; Tsoukalou, A.; Willinger, E.; Kuznetsov, D. A.; Mance, D.; Kierzkowska, A.; Donat, F.; Abdala, P. M.; Comas-Vives, A.; Copéret, C.; Fedorov, A.; Müller, C. R. Engineering the Cu/Mo_2CTx (MXene) Interface to Drive CO_2 Hydrogenation to Methanol. *Nat. Catal.* **2021**, *4* (10), 860–871. https://doi.org/10.1038/s41929-021-00684-0.

(45) Martin, O.; Martín, A. J.; Mondelli, C.; Mitchell, S.; Segawa, T. F.; Hauert, R.; Drouilly, C.; Curulla-Ferré, D.; Pérez-Ramírez, J. Indium Oxide as a Superior Catalyst for Methanol Synthesis by CO_2 Hydrogenation. *Angew. Chem. - Int. Ed.* **2016**, *55* (21), 6261–6265. https://doi.org/10.1002/anie.201600943.

(46) Frei, M. S.; Mondelli, C.; García-Muelas, R.; Morales-Vidal, J.; Philipp, M.; Safonova, O. V.; López, N.; Stewart, J. A.; Ferré, D. C.; Pérez-Ramírez, J. Nanostructure of Nickel-Promoted Indium Oxide Catalysts Drives Selectivity in CO_2 Hydrogenation. *Nat. Commun.* **2021**, *12* (1), 1960. https://doi.org/10.1038/s41467-021-22224-x.

(47) Dang, S.; Qin, B.; Yang, Y.; Wang, H.; Cai, J.; Han, Y.; Li, S.; Gao, P.; Sun, Y. Rationally Designed Indium Oxide Catalysts for CO_2 Hydrogenation to Methanol with High Activity and Selectivity. *Sci. Adv.* **2020**, *6* (25). https://doi.org/10.1126/sciadv.aaz2060.

(48) Wang, J.; Zhang, G.; Zhu, J.; Zhang, X.; Ding, F.; Zhang, A.; Guo, X.; Song, C. CO 2 Hydrogenation to Methanol over In_2O_3 -Based Catalysts: From Mechanism to Catalyst Development. *ACS Catal.* **2021**, *11* (3), 1406–1423. https://doi.org/10.1021/acscatal.0c03665.

(49) Tsoukalou, A.; Abdala, P. M.; Stoian, D.; Huang, X.; Willinger, M.-G.; Fedorov, A.; Müller, C. R. Structural Evolution and Dynamics of an In_2O_3 Catalyst for CO_2 Hydrogenation to Methanol: An Operando XAS-XRD and In Situ TEM Study. *J. Am. Chem. Soc.* **2019**, *141* (34), 13497–13505. https://doi.org/10.1021/jacs.9b04873.

(50) Araújo, T. P.; Mondelli, C.; Agrachev, M.; Zou, T.; Willi, P. O.; Engel, K. M.; Grass, R. N.; Stark, W. J.; Safonova, O. V.; Jeschke, G.; Mitchell, S.; Pérez-Ramírez, J. Flame-Made Ternary Pd-In_2O_3-ZrO_2 Catalyst with Enhanced Oxygen Vacancy Generation for CO_2 Hydrogenation to Methanol. *Nat. Commun.* **2022**, *13* (1). https://doi.org/10.1038/s41467-022-33391-w.

(51) Wang, J.; Li, G.; Li, Z.; Tang, C.; Feng, Z.; An, H.; Liu, H.; Liu, T.; Li, C. A Highly Selective and Stable ZnO-ZrO $_2$ Solid Solution Catalyst for CO $_2$ Hydrogenation to Methanol. *Sci. Adv.* **2017**, *3* (10). https://doi.org/10.1126/sciadv.1701290.

(52) Tsoukalou, A.; Abdala, P. M.; Armutlulu, A.; Willinger, E.; Fedorov, A.; Müller, C. R. Operando X-Ray Absorption Spectroscopy Identifies a Monoclinic ZrO_2:In Solid Solution as the Active Phase for the Hydrogenation of CO_2 to Methanol. *ACS Catal.* **2020**, *10* (17), 10060–10067. https://doi.org/10.1021/acscatal.0c01968.

(53) Lee, K.; Anjum, U.; Araújo, T. P.; Mondelli, C.; He, Q.; Furukawa, S.; Pérez-Ramírez, J.; Kozlov, S. M.; Yan, N. Atomic Pd-Promoted ZnZrOx Solid Solution Catalyst for CO_2 Hydrogenation to Methanol. *Appl. Catal. B Environ.* **2022**, *304* (December 2021). https://doi.org/10.1016/j.apcatb.2021.120994.

(54) Quilis, C.; Mota, N.; Pawelec, B.; Millán, E.; Navarro Yerga, R. M. Intermetallic PdZn/TiO2 Catalysts for Methanol Production from CO_2 Hydrogenation: The Effect of ZnO Loading on PdZn-ZnO Sites and Its Influence on Activity. *Appl. Catal. B Environ.* **2023**, *321*. https://doi.org/10.1016/j.apcatb.2022.122064.

(55) Zaman, S. F.; Ojelade, O. A.; Alhumade, H.; Mazumder, J.; Mohamed, H. O.; Castaño, P. Elucidating the Promoting Role of Ca on PdZn/CeO_2 Catalyst for CO_2 Valorization to Methanol. *Fuel* **2023**, *343*. https://doi.org/10.1016/j.fuel.2023.127927.

(56) Bowker, M.; Lawes, N.; Gow, I.; Hayward, J.; Esquius, J. R.; Richards, N.; Smith, L. R.; Slater, T. J. A.; Davies, T. E.; Dummer, N. F.; Kabalan, L.; Logsdail, A.; Catlow, R. C.; Taylor, S.; Hutchings, G. J. The Critical Role of βPdZn Alloy in Pd/ZnO Catalysts for the Hydrogenation of Carbon Dioxide to Methanol. *ACS Catal.* **2022**, *12* (9), 5371–5379. https://doi.org/10.1021/acscatal.2c00552.

(57) Gutterød, E. S.; Lazzarini, A.; Fjermestad, T.; Kaur, G.; Manzoli, M.; Bordiga, S.; Svelle, S.; Lillerud, K. P.; Skúlason, E.; Øien-ØDegaard, S.; Nova, A.; Olsbye, U. Hydrogenation of CO_2 to Methanol by Pt Nanoparticles Encapsulated in UiO-67: Deciphering the Role of the Metal-Organic Framework. *J. Am. Chem. Soc.* **2020**, *142* (2), 999–1009. https://doi.org/10.1021/jacs.9b10873.

(58) Hartadi, Y.; Widmann, D.; Behm, R. J. CO_2 Hydrogenation to Methanol on Supported Au Catalysts under Moderate Reaction Conditions: Support and Particle Size Effects. *ChemSusChem* **2015**, *8* (3), 456–465. https://doi.org/10.1002/cssc.201402645.

(59) Hu, J.; Yu, L.; Deng, J.; Wang, Y.; Cheng, K.; Ma, C.; Zhang, Q.; Wen, W.; Yu, S.; Pan, Y.; Yang, J.; Ma, H.; Qi, F.; Wang, Y.; Zheng, Y.; Chen, M.; Huang, R.; Zhang, S.; Zhao, Z.; Mao, J.; Meng, X.; Ji, Q.; Hou, G.; Han, X.; Bao, X.; Wang, Y.; Deng, D. Sulfur Vacancy-Rich MoS_2 as a Catalyst for the Hydrogenation of CO_2 to Methanol. *Nat. Catal.* **2021**, *4* (3), 242–250. https://doi.org/10.1038/s41929-021-00584-3.

(60) Wang, Y.; Kattel, S.; Gao, W.; Li, K.; Liu, P.; Chen, J. G.; Wang, H. Exploring the Ternary Interactions in Cu–ZnO–ZrO_2 Catalysts for Efficient CO_2 Hydrogenation to Methanol. *Nat. Commun.* **2019**, *10* (1), 1166. https://doi.org/10.1038/s41467-019-09072-6.

(61) Wang, J.; Sun, K.; Jia, X.; Liu, C. CO_2 Hydrogenation to Methanol over Rh/In_2O_3 Catalyst. *Catal. Today* **2021**, *365*, 341–347. https://doi.org/10.1016/j.cattod.2020.05.020.

(62) Rui, N.; Zhang, F.; Sun, K.; Liu, Z.; Xu, W.; Stavitski, E.; Senanayake, S. D.; Rodriguez, J. A.; Liu, C.-J. Hydrogenation of CO_2 to Methanol on a $Au^{\delta+}$–In_2O_{3-x} Catalyst. *ACS Catal.* **2020**, *10* (19), 11307–11317. https://doi.org/10.1021/acscatal.0c02120.

(63) Jia, X.; Sun, K.; Wang, J.; Shen, C.; Liu, C. jun. Selective Hydrogenation of CO_2 to Methanol over Ni/In_2O_3 Catalyst. *J. Energy Chem.* **2020**, *50*, 409–415. https://doi.org/10.1016/j.jechem.2020.03.083.

(64) Rui, N.; Wang, Z.; Sun, K.; Ye, J.; Ge, Q.; Liu, C. CO_2 Hydrogenation to Methanol over Pd/In_2O_3: Effects of Pd and Oxygen Vacancy. *Appl. Catal. B Environ.* **2017**, *218*, 488–497. https://doi.org/10.1016/j.apcatb.2017.06.069.

(65) Xu, J.; Su, X.; Liu, X.; Pan, X.; Pei, G.; Huang, Y.; Wang, X.; Zhang, T.; Geng, H. Methanol Synthesis from CO_2 and H_2 over $Pd/ZnO/Al_2O_3$: Catalyst Structure Dependence of Methanol Selectivity. *Appl. Catal. Gen.* **2016**, *514*, 51–59. https://doi.org/10.1016/j.apcata.2016.01.006.

(66) Frei, M. S.; Mondelli, C.; García-Muelas, R.; Kley, K. S.; Puértolas, B.; López, N.; Safonova, O. V.; Stewart, J. A.; Curulla Ferré, D.; Pérez-Ramírez, J. Atomic-Scale Engineering of Indium Oxide Promotion by Palladium for Methanol Production via CO_2 Hydrogenation. *Nat. Commun.* **2019**, *10* (1), 3377. https://doi.org/10.1038/s41467-019-11349-9.

(67) Sun, K.; Shen, C.; Zou, R.; Liu, C. jun. Highly Active Pt/In_2O_3-ZrO_2 Catalyst for CO_2 Hydrogenation to Methanol with Enhanced CO Tolerance: The Effects of ZrO_2. *Appl. Catal. B Environ.* **2023**, *320*. https://doi.org/10.1016/j.apcatb.2022.122018.

(68) Han, Z.; Tang, C.; Wang, J.; Li, L.; Li, C. Atomically Dispersed Ptn+ Species as Highly Active Sites in Pt/In_2O_3 Catalysts for Methanol Synthesis from CO_2 Hydrogenation. *J. Catal.* **2021**, *394*, 236–244. https://doi.org/10.1016/j.jcat.2020.06.018.

(69) Wang, J.; Tang, C.; Li, G.; Han, Z.; Li, Z.; Liu, H.; Cheng, F.; Li, C. High-Performance $M_a ZrO_x$ (M_a = Cd, Ga) Solid-Solution Catalysts for CO_2 Hydrogenation to Methanol. *ACS Catal.* **2019**, *9* (11), 10253–10259. https://doi.org/10.1021/acscatal.9b03449.

(70) Bahruji, H.; Bowker, M.; Hutchings, G.; Dimitratos, N.; Wells, P.; Gibson, E.; Jones, W.; Brookes, C.; Morgan, D.; Lalev, G. Pd/ZnO Catalysts for Direct CO_2 Hydrogenation to Methanol. *J. Catal.* **2016**, *343*, 133–146. https://doi.org/10.1016/j.jcat.2016.03.017.

(71) Collins, S. E.; Chiavassa, D. L.; Bonivardi, A. L.; Baltanás, M. A. Hydrogen Spillover in Ga_2O_3–Pd/SiO_2 Catalysts for Methanol Synthesis from CO_2/H_2. *Catal. Lett.* **2005**, *103* (1–2), 83–88. https://doi.org/10.1007/s10562-005-6507-5.

(72) Zhou, X.; Qu, J.; Xu, F.; Hu, J.; Foord, J. S.; Zeng, Z.; Hong, X.; Edman Tsang, S. C. Shape Selective Plate-Form Ga_2O_3 with Strong Metal–Support Interaction to Overlying Pd for Hydrogenation of CO_2 to CH_3OH. *Chem. Commun.* **2013**, *49* (17), 1747. https://doi.org/10.1039/c3cc38455a.

(73) Chiavassa, D. L.; Collins, S. E.; Bonivardi, A. L.; Baltanás, M. A. Methanol Synthesis from CO_2/H_2 Using Ga_2O_3–Pd/Silica Catalysts: Kinetic Modeling. *Chem. Eng. J.* **2009**, *150* (1), 204–212. https://doi.org/10.1016/j.cej.2009.02.013.

(74) Ojelade, O. A.; Zaman, S. F.; Daous, M. A.; Al-Zahrani, A. A.; Malik, A. S.; Driss, H.; Shterk, G.; Gascon, J. Optimizing Pd:Zn Molar Ratio in $PdZn/CeO_2$ for CO_2 Hydrogenation to Methanol. *Appl. Catal. Gen.* **2019**, *584*, 117185. https://doi.org/10.1016/j.apcata.2019.117185.

(75) Malik, A. S.; Zaman, S. F.; Al-Zahrani, A. A.; Daous, M. A.; Driss, H.; Petrov, L. A. Development of Highly Selective $PdZn/CeO_2$ and Ca-Doped $PdZn/CeO_2$ Catalysts for

Methanol Synthesis from CO_2 Hydrogenation. *Appl. Catal. Gen.* **2018**, *560*, 42–53. https://doi.org/10.1016/j.apcata.2018.04.036.

(76) Koizumi, N.; Jiang, X.; Kugai, J.; Song, C. Effects of Mesoporous Silica Supports and Alkaline Promoters on Activity of Pd Catalysts in CO_2 Hydrogenation for Methanol Synthesis. *Catal. Today* **2012**, *194* (1), 16–24. https://doi.org/10.1016/j.cattod.2012.08.007.

(77) Wang, J.; Lu, S.; Li, J.; Li, C. A Remarkable Difference in CO_2 Hydrogenation to Methanol on Pd Nanoparticles Supported inside and Outside of Carbon Nanotubes. *Chem. Commun.* **2015**, *51* (99), 17615–17618. https://doi.org/10.1039/C5CC07079A.

(78) Baiker, A.; Kilo, M.; Maciejewski, M.; Menzi, S.; Wokaun, A. Hydrogenation of CO2 Over Copper, Silver and Gold/Zirconia Catalysts: Comparative Study of Catalyst Properties and Reaction Pathways. In *Studies in Surface Science and Catalysis*; Elsevier, 1993; Vol. 75, pp 1257–1272. https://doi.org/10.1016/S0167-2991(08)64449-3.

(79) Grabowski, R.; Słoczyński, J.; Śliwa, M.; Mucha, D.; Socha, R. P.; Lachowska, M.; Skrzypek, J. Influence of Polymorphic ZrO_2 Phases and the Silver Electronic State on the Activity of Ag/ZrO_2 Catalysts in the Hydrogenation of CO_2 to Methanol. *ACS Catal.* **2011**, *1* (4), 266–278. https://doi.org/10.1021/cs100033v.

(80) Navarro-Jaén, S.; Virginie, M.; Bonin, J.; Robert, M.; Wojcieszak, R.; Khodakov, A. Y. Highlights and Challenges in the Selective Reduction of Carbon Dioxide to Methanol. *Nat. Rev. Chem.* **2021**, *5* (8), 564–579. https://doi.org/10.1038/s41570-021-00289-y.

(81) Behrens, M.; Studt, F.; Kasatkin, I.; Kühl, S.; Hävecker, M.; Abild-Pedersen, F.; Zander, S.; Girgsdies, F.; Kurr, P.; Kniep, B.-L.; Tovar, M.; Fischer, R. W.; Nørskov, J. K.; Schlögl, R. The Active Site of Methanol Synthesis over $Cu/ZnO/Al_2O_3$ Industrial Catalysts. *Science* **2012**, *336* (6083), 893–897. https://doi.org/10.1126/science.1219831.

(82) Kuld, S.; Conradsen, C.; Moses, P. G.; Chorkendorff, I.; Sehested, J. Quantification of Zinc Atoms in a Surface Alloy on Copper in an Industrial-Type Methanol Synthesis Catalyst. *Angew. Chem. Int. Ed.* **2014**, *53* (23), 5941–5945. https://doi.org/10.1002/anie.201311073.

(83) Kattel, S.; Ramírez, P. J.; Chen, J. G.; Rodriguez, J. A.; Liu, P. *Active Sites for CO_2 Hydrogenation to Methanol on Cu/ZnO Catalysts*; 2017; Vol. 355, p 24. https://www.science.org.

(84) Zhang, J.; Sun, X.; Wu, C.; Hang, W.; Hu, X.; Qiao, D.; Yan, B. Engineering Cu^{+}/CeZrO Interfaces to Promote CO_2 Hydrogenation to Methanol. *J. Energy Chem.* **2023**, *77*, 45–53. https://doi.org/10.1016/j.jechem.2022.10.034.

(85) Yu, J.; Yang, M.; Zhang, J.; Ge, Q.; Zimina, A.; Pruessmann, T.; Zheng, L.; Grunwaldt, J.-D.; Sun, J. Stabilizing Cu^{+} in Cu/SiO_2 Catalysts with a Shattuckite-Like Structure Boosts CO_2 Hydrogenation into Methanol. *ACS Catal.* **2020**, *10* (24), 14694–14706. https://doi.org/10.1021/acscatal.0c04371.

(86) Fernández-Villanueva, E.; Lustemberg, P. G.; Zhao, M.; Soriano Rodriguez, J.; Concepción, P.; Ganduglia-Pirovano, M. V. Water and Cu^{+} Synergy in Selective CO_2 Hydrogenation to Methanol over Cu-MgO-Al_2O_3 Catalysts. *J. Am. Chem. Soc.* **2024**, *146* (3), 2024–2032. https://doi.org/10.1021/jacs.3c10685.

(87) Liu, Y.-M.; Liu, J.-T.; Liu, S.-Z.; Li, J.; Gao, Z.-H.; Zuo, Z.-J.; Huang, W. Reaction Mechanisms of Methanol Synthesis from CO/CO_2 Hydrogenation on $Cu_2O(111)$: Comparison with Cu(111). *J. CO2 Util.* **2017**, *20*, 59–65. https://doi.org/10.1016/j.jcou.2017.05.005.

(88) Dasireddy, V. D. B. C.; Likozar, B. The Role of Copper Oxidation State in $Cu/ZnO/Al_2O_3$ Catalysts in CO_2 Hydrogenation and Methanol Productivity. *Renew. Energy* **2019**, *140*, 452–460. https://doi.org/10.1016/j.renene.2019.03.073.

(89) Nakamura, J.; Nakamura, I.; Uchijima, T.; Kanai, Y.; Watanabe, T.; Saito, M.; Fujitani, T. Methanol Synthesis over a Zn-Deposited Copper Model Catalyst. *Catal. Lett.* **1995**, *31* (4), 325–331. https://doi.org/10.1007/BF00808596.

(90) Beck, A.; Newton, M. A.; Van De Water, L. G. A.; Van Bokhoven, J. A. The Enigma of Methanol Synthesis by Cu/ZnO/Al $_2$ O $_3$ -Based Catalysts. *Chem. Rev.* **2024**, *124* (8), 4543–4678. https://doi.org/10.1021/acs.chemrev.3c00148.

(91) Grabow, L. C.; Mavrikakis, M. Mechanism of Methanol Synthesis on Cu through CO $_2$ and CO Hydrogenation. *ACS Catal.* **2011**, *1* (4), 365–384. https://doi.org/10.1021/cs200055d.

(92) Ye, J.; Liu, C.; Mei, D.; Ge, Q. Active Oxygen Vacancy Site for Methanol Synthesis from CO $_2$ Hydrogenation on In $_2$ O $_3$ (110): A DFT Study. *ACS Catal.* **2013**, *3* (6), 1296–1306. https://doi.org/10.1021/cs400132a.

(93) Lin, S.; Zhi, Y.; Chen, W.; Li, H.; Zhang, W.; Lou, C.; Wu, X.; Zeng, S.; Xu, S.; Xiao, J.; Zheng, A.; Wei, Y.; Liu, Z. Molecular Routes of Dynamic Autocatalysis for Methanol-to-Hydrocarbons Reaction. *J. Am. Chem. Soc.* **2021**, *143* (31), 12038–12052. https://doi.org/10.1021/jacs.1c03475.

(94) Gao, M.; Li, H.; Liu, W.; Xu, Z.; Peng, S.; Yang, M.; Ye, M.; Liu, Z. Imaging Spatiotemporal Evolution of Molecules and Active Sites in Zeolite Catalyst during Methanol-to-Olefins Reaction. *Nat. Commun.* **2020**, *11* (1), 3641. https://doi.org/10.1038/s41467-020-17355-6.

(95) Cheng, K.; Gu, B.; Liu, X.; Kang, J.; Zhang, Q.; Wang, Y. Direct and Highly Selective Conversion of Synthesis Gas into Lower Olefins: Design of a Bifunctional Catalyst Combining Methanol Synthesis and Carbon-Carbon Coupling. *Angew. Chem.* **2016**, *128* (15), 4803–4806. https://doi.org/10.1002/ange.201601208.

(96) Ratnasamy, C.; Wagner, J. P. Water Gas Shift Catalysis. *Catal. Rev.* **2009**, *51* (3), 325–440. https://doi.org/10.1080/01614940903048661.

(97) Li, Z.; Wang, J.; Qu, Y.; Liu, H.; Tang, C.; Miao, S.; Feng, Z.; An, H.; Li, C. Highly Selective Conversion of Carbon Dioxide to Lower Olefins. *ACS Catalysis*. American Chemical Society December 1, 2017, pp 8544–8548. https://doi.org/10.1021/acscatal.7b03251.

(98) Tan, L.; Zhang, P.; Cui, Y.; Suzuki, Y.; Li, H.; Guo, L.; Yang, G.; Tsubaki, N. Direct CO2 Hydrogenation to Light Olefins by Suppressing CO By-Product Formation. *Fuel Process. Technol.* **2019**, *196*, 106174. https://doi.org/10.1016/j.fuproc.2019.106174.

(99) Liu, X.; Wang, M.; Yin, H.; Hu, J.; Cheng, K.; Kang, J.; Zhang, Q.; Wang, Y. Tandem Catalysis for Hydrogenation of CO and CO_2 to Lower Olefins with Bifunctional Catalysts Composed of Spinel Oxide and SAPO-34. *ACS Catal.* **2020**, *10* (15), 8303–8314. https://doi.org/10.1021/acscatal.0c01579.

(100) Su, J.; Zhou, H.; Liu, S.; Wang, C.; Jiao, W.; Wang, Y.; Liu, C.; Ye, Y.; Zhang, L.; Zhao, Y.; Liu, H.; Wang, D.; Yang, W.; Xie, Z.; He, M. Syngas to Light Olefins Conversion with High Olefin/Paraffin Ratio Using ZnCrOx/AlPO-18 Bifunctional Catalysts. *Nat. Commun.* **2019**, *10* (1), 1297. https://doi.org/10.1038/s41467-019-09336-1.

(101) Meng, F.; Li, X.; Zhang, P.; Yang, L.; Liu, S.; Li, Z. A Facile Approach for Fabricating Highly Active ZrCeZnOx in Combination with SAPO-34 for the Conversion of Syngas into Light Olefins. *Appl. Surf. Sci.* **2021**, *542*, 148713. https://doi.org/10.1016/J.APSUSC.2020.148713.

(102) Wang, M.; Wang, Z.; Liu, S.; Gao, R.; Cheng, K.; Zhang, L.; Zhang, G.; Min, X.; Kang, J.; Zhang, Q.; Wang, Y. Synthesis of Hierarchical SAPO-34 to Improve the Catalytic Performance of Bifunctional Catalysts for Syngas-to-Olefins Reactions. *J. Catal.* **2021**, *394*, 181–192. https://doi.org/10.1016/J.JCAT.2020.08.020.

(103) Meng, F.; Li, X.; Zhang, P.; Yang, L.; Yang, G.; Ma, P.; Li, Z. Highly Active Ternary Oxide ZrCeZnOx Combined with SAPO-34 Zeolite for Direct Conversion of Syngas into Light Olefins. *Catal. Today* **2021**, *368* (September 2019), 118–125. https://doi.org/10.1016/j.cattod.2020.03.023.

(104) Wang, M.; Kang, J.; Xiong, X.; Zhang, F.; Cheng, K.; Zhang, Q.; Wang, Y. Effect of Zeolite Topology on the Hydrocarbon Distribution over Bifunctional ZnAlO/SAPO Catalysts in Syngas Conversion. *Catal. Today* **2021**, *371*, 85–92. https://doi.org/10.1016/J.CATTOD.2020.07.076.

(105) Yang, G.; Meng, F.; Zhang, P.; Yang, L.; Li, Z. Effects of Preparation Method and Precipitant on Mn-Ga Oxide in Combination with SAPO-34 for Syngas Conversion into Light Olefins. *New J. Chem.* **2021**, *45* (18), 7967–7976. https://doi.org/10.1039/d1nj00443c.

(106) Zhang, P.; Meng, F.; Yang, L.; Yang, G.; Liang, X.; Li, Z. Syngas to Olefins over a CrMnGa/SAPO-34 Bifunctional Catalyst: Effect of Cr and Cr/Mn Ratio. *Ind. Eng. Chem. Res.* **2021**. https://doi.org/10.1021/acs.iecr.1c02150.

(107) Liu, X.; Wang, M.; Zhou, C.; Zhou, W.; Cheng, K.; Kang, J.; Zhang, Q.; Deng, W.; Wang, Y. Selective Transformation of Carbon Dioxide into Lower Olefins with a Bifunctional Catalyst Composed of ZnGa 2 O 4 and SAPO-34. *Chem. Commun.* **2018**, *54* (2), 140–143. https://doi.org/10.1039/C7CC08642C.

(108) Li, J.; Yu, T.; Miao, D.; Pan, X.; Bao, X. Carbon Dioxide Hydrogenation to Light Olefins over ZnO-Y_2O_3 and SAPO-34 Bifunctional Catalysts. *Catal. Commun.* **2019**, *129*, 105711. https://doi.org/10.1016/j.catcom.2019.105711.

(109) Sedighi, M.; Mohammadi, M. CO_2 Hydrogenation to Light Olefins over Cu-CeO_2/SAPO-34 Catalysts: Product Distribution and Optimization. *J. CO_2 Util.* **2020**, *35*, 236–244. https://doi.org/10.1016/j.jcou.2019.10.002.

(110) Ghasemi, M.; Mohammadi, M.; Sedighi, M. Sustainable Production of Light Olefins from Greenhouse Gas CO_2 over SAPO-34 Supported Modified Cerium Oxide. *Microporous Mesoporous Mater.* **2020**, *297*, 110029.

(111) Wang, S.; Wang, P.; Qin, Z.; Yan, W.; Dong, M.; Li, J.; Wang, J.; Fan, W. Enhancement of Light Olefin Production in CO_2 Hydrogenation over In2O3-Based Oxide and SAPO-34 Composite. *J. Catal.* **2020**, *391*, 459–470. https://doi.org/10.1016/j.jcat.2020.09.010.

(112) Lu, S.; Yang, H.; Zhou, Z.; Zhong, L.; Li, S.; Gao, P.; Sun, Y. Effect of In2O3 Particle Size on CO_2 Hydrogenation to Lower Olefins over Bifunctional Catalysts. *Chin. J. Catal.* **2021**, *42* (11), 2038–2048. https://doi.org/10.1016/S1872-2067(21)63851-2.

(113) Li, W.; Wang, K.; Zhan, G.; Huang, J.; Li, Q. Design and Synthesis of Bioinspired ZnZrOx&Bio-ZSM-5 Integrated Nanocatalysts to Boost CO_2 Hydrogenation to Light Olefins. *ACS Sustain. Chem. Eng.* **2021**, *9* (18), 6446–6458. https://doi.org/10.1021/acssuschemeng.1c01384.

(114) Tong, M.; Gapu Chizema, L.; Chang, X.; Hondo, E.; Dai, L.; Zeng, Y.; Zeng, C.; Ahmad, H.; Yang, R.; Lu, P. Tandem Catalysis over Tailored ZnO-ZrO_2/MnSAPO-34 Composite Catalyst for Enhanced Light Olefins Selectivity in CO2 Hydrogenation. *Microporous Mesoporous Mater.* **2021**, *320*, 111105. https://doi.org/10.1016/j.micromeso.2021.111105.

(115) Mou, J.; Fan, X.; Liu, F.; Wang, X.; Zhao, T.; Chen, P.; Li, Z.; Yang, C.; Cao, J. CO2 Hydrogenation to Lower Olefins over Mn_2O_3-ZnO/SAPO-34 Tandem Catalysts. *Chem. Eng. J.* **2021**, *421*, 129978. https://doi.org/10.1016/j.cej.2021.129978.

(116) Ruiz Esquius, J.; Bahruji, H.; Bowker, M.; Hutchings, G. J. Identification of C_2 –C_5 Products from CO_2 Hydrogenation over PdZn/TiO_2 –ZSM-5 Hybrid Catalysts. *Faraday Discuss.* **2021**, *230*, 52–67. https://doi.org/10.1039/D0FD00135J.

(117) Araújo, T. P.; Shah, A.; Mondelli, C.; Stewart, J. A.; Curulla Ferré, D.; Pérez-Ramírez, J. Impact of Hybrid CO_2-CO Feeds on Methanol Synthesis over In_2O_3-Based Catalysts. *Appl. Catal. B Environ.* **2021**, *285*, 119878. https://doi.org/10.1016/J.APCATB.2021.119878.

(118) Zhang, P.; Meng, F.; Li, X.; Yang, L.; Ma, P.; Li, Z. Excellent Selectivity for Direct Conversion of Syngas to Light Olefins over a Mn–Ga Oxide and SAPO-34 Bifunctional Catalyst. *Catal. Sci. Technol.* **2019**, *9* (20), 5577–5581. https://doi.org/10.1039/C9CY01348B.

(119) Zhu, Y.; Pan, X.; Jiao, F.; Li, J.; Yang, J.; Ding, M.; Han, Y.; Liu, Z.; Bao, X. Role of Manganese Oxide in Syngas Conversion to Light Olefins. *ACS Catal.* **2017**, *7* (4), 2800–2804. https://doi.org/10.1021/acscatal.7b00221.

(120) Dang, S.; Gao, P.; Liu, Z.; Chen, X.; Yang, C.; Wang, H.; Zhong, L.; Li, S.; Sun, Y. Role of Zirconium in Direct CO_2 Hydrogenation to Lower Olefins on Oxide/Zeolite Bifunctional Catalysts. *J. Catal.* **2018**, *364*, 382–393. https://doi.org/10.1016/j.jcat.2018.06.010.

(121) Luo, Y.; Wang, S.; Guo, S.; Yuan, K.; Wang, H.; Dong, M.; Qin, Z.; Fan, W.; Wang, J. Conversion of Syngas into Light Olefins over Bifunctional ZnCeZrO/SAPO-34 Catalysts: Regulation of the Surface Oxygen Vacancy Concentration and Its Relation to the Catalytic Performance. *Catal. Sci. Technol.* **2021**, *11* (1), 338–348. https://doi.org/10.1039/d0cy01759k.

(122) Wang, S.; Wang, P.; Shi, D.; He, S.; Zhang, L.; Yan, W.; Qin, Z.; Li, J.; Dong, M.; Wang, J.; Olsbye, U.; Fan, W. Direct Conversion of Syngas into Light Olefins with Low CO_2 Emission. *ACS Catal.* **2020**, *10* (3), 2046–2059. https://doi.org/10.1021/acscatal.9b04629.

(123) Zhang, Z.; Huang, Y.; Ma, H.; Qian, W.; Zhang, H.; Ying, W. Syngas-to-Olefins over MOF-Derived ZnZrOx and SAPO-34 Bifunctional Catalysts. *Catal. Commun.* **2021**, *152*, 106292. https://doi.org/10.1016/J.CATCOM.2021.106292.

(124) Ni, Y.; Liu, Y.; Chen, Z.; Yang, M.; Liu, H.; He, Y.; Fu, Y.; Zhu, W.; Liu, Z. Realizing and Recognizing Syngas-to-Olefins Reaction via a Dual-Bed Catalyst. *ACS Catal.* **2019**, *9* (2), 1026–1032. https://doi.org/10.1021/acscatal.8b04794.

(125) Numpilai, T.; Kahadit, S.; Witoon, T.; Ayodele, B. V.; Cheng, C. K.; Siri-Nguan, N.; Sornchamni, T.; Wattanakit, C.; Chareonpanich, M.; Limtrakul, J. CO_2 Hydrogenation to Light Olefins Over In_2O_3/SAPO-34 and Fe-Co/K-Al_2O_3 Composite Catalyst. *Top. Catal.* **2021**, *64* (5–6), 316–327. https://doi.org/10.1007/s11244-021-01412-5.

(126) Yang, M.; Li, B.; Gao, M.; Lin, S.; Wang, Y.; Xu, S.; Zhao, X.; Guo, P.; Wei, Y.; Ye, M.; Tian, P.; Liu, Z. High Propylene Selectivity in Methanol Conversion over a Small-Pore SAPO Molecular Sieve with Ultra-Small Cage. *ACS Catal.* **2020**, *10* (6), 3741–3749. https://doi.org/10.1021/acscatal.9b04703.

(127) Dang, S.; Li, S.; Yang, C.; Chen, X.; Li, X.; Zhong, L.; Gao, P.; Sun, Y. Selective Transformation of CO_2 and H_2 into Lower Olefins over In_2O_3-ZnZrOx/SAPO-34 Bifunctional Catalysts. *ChemSusChem* **2019**, *12* (15), 3582–3591. https://doi.org/10.1002/cssc.201900958.

(128) Wang, T.; Yang, C.; Gao, P.; Zhou, S.; Li, S.; Wang, H.; Sun, Y. ZnZrOx Integrated with Chain-like Nanocrystal HZSM-5 as Efficient Catalysts for Aromatics Synthesis from CO_2 Hydrogenation. *Appl. Catal. B Environ.* **2021**, *286*, 119929. https://doi.org/10.1016/j.apcatb.2021.119929.

(129) Jiao, F.; Pan, X.; Gong, K.; Chen, Y.; Li, G.; Bao, X. Shape-Selective Zeolites Promote Ethylene Formation from Syngas via a Ketene Intermediate. *Angew. Chem. Int. Ed.* **2018**, *57* (17), 4692–4696. https://doi.org/10.1002/anie.201801397.

(130) Wang, S.; Zhang, L.; Zhang, W.; Wang, P.; Qin, Z.; Yan, W.; Dong, M.; Li, J.; Wang, J.; He, L.; Olsbye, U.; Fan, W. Selective Conversion of CO_2 into Propene and Butene. *Chem* **2020**, *6* (12), 3344–3363. https://doi.org/10.1016/J.CHEMPR.2020.09.025.

(131) Liu, X.; Zhou, W.; Yang, Y.; Cheng, K.; Kang, J.; Zhang, L.; Zhang, G.; Min, X.; Zhang, Q.; Wang, Y. Design of Efficient Bifunctional Catalysts for Direct Conversion of Syngas into Lower Olefins: Via Methanol/Dimethyl Ether Intermediates. *Chem. Sci.* **2018**, *9* (20), 4708–4718. https://doi.org/10.1039/c8sc01597j.

(132) Sun, Q.; Wang, N.; Fan, Q.; Zeng, L.; Mayoral, A.; Miao, S.; Yang, R.; Jiang, Z.; Zhou, W.; Zhang, J.; Zhang, T.; Xu, J.; Zhang, P.; Cheng, J.; Yang, D. C.; Jia, R.; Li, L.; Zhang, Q.; Wang, Y.; Terasaki, O.; Yu, J. Subnanometer Bimetallic Platinum–Zinc Clusters in Zeolites for Propane Dehydrogenation. *Angew. Chem. - Int. Ed.* **2020**, *59* (44), 19450–19459. https://doi.org/10.1002/anie.202003349.

(133) Jiang, H.; Hou, Z.; Luo, Y. A Kinetic View on Proximity-Dependent Selectivity of Carbon Dioxide Reduction on Bifunctional Catalysts. *ACS Catal.* **2020**, *10* (22), 13518–13523. https://doi.org/10.1021/acscatal.0c03414.

(134) L'hospital, V.; Coudercy, C.; Pinard, L.; Rousseau, J.; Loridant, S.; Le Valant, A. Syngas Conversion into Light Hydrocarbons over Bifunctional Catalyst: Effect of the Density of Contact between Cu-ZnO-Al_2O_3 and SAPO-34. *Appl. Catal. Gen.* **2022**, *643*, 118757. https://doi.org/10.1016/j.apcata.2022.118757.

(135) Coudercy, C.; L'hospital, V.; Checa, R.; Le Valant, A.; Afanasiev, P.; Loridant, S. On the Reaction Mechanism of MnO_x/SAPO-34 Bifunctional Catalysts for the Conversion of Syngas to Light Olefins. *Catal. Sci. Technol.* **2021**, *11* (24), 7844–7849. https://doi.org/10.1039/D1CY01673C.

(136) Wang, Y.; Wang, G.; Wal, L. I.; Cheng, K.; Zhang, Q.; Jong, K. P.; Wang, Y. Visualizing Element Migration over Bifunctional Metal-Zeolite Catalysts and Its Impact on

Catalysis. *Angew. Chem. Int. Ed.* **2021**, *60* (32), 17735–17743. https://doi.org/10.1002/anie.202107264.

(137) Ding, Y.; Jiao, F.; Pan, X.; Ji, Y.; Li, M.; Si, R.; Pan, Y.; Hou, G.; Bao, X. Effects of Proximity-Dependent Metal Migration on Bifunctional Composites Catalyzed Syngas to Olefins. *ACS Catal.* **2021**, *11* (15), 9729–9737. https://doi.org/10.1021/acscatal.1c01649.

(138) Tan, L.; Wang, F.; Zhang, P.; Suzuki, Y.; Wu, Y.; Chen, J.; Yang, G.; Tsubaki, N. Design of a Core–Shell Catalyst: An Effective Strategy for Suppressing Side Reactions in Syngas for Direct Selective Conversion to Light Olefins. *Chem. Sci.* **2020**, *11* (16), 4097–4105. https://doi.org/10.1039/C9SC05544D.

(139) Chen, J.; Wang, X.; Wu, D.; Zhang, J.; Ma, Q.; Gao, X.; Lai, X.; Xia, H.; Fan, S.; Zhao, T.-S. S. Hydrogenation of CO2 to Light Olefins on CuZnZr@(Zn-)SAPO-34 Catalysts: Strategy for Product Distribution. *Fuel* **2019**, *239*, 44–52. https://doi.org/10.1016/j.fuel.2018.10.148.

(140) Gao, J.; Jia, C.; Liu, B. Direct and Selective Hydrogenation of CO_2 to Ethylene and Propene by Bifunctional Catalysts. *Catal. Sci. Technol.* **2017**, *7* (23), 5602–5607. https://doi.org/10.1039/c7cy01549f.

(141) Liu, X.; Zhou, W.; Yang, Y.; Cheng, K.; Kang, J.; Zhang, L.; Zhang, G.; Min, X.; Zhang, Q.; Wang, Y. Design of Efficient Bifunctional Catalysts for Direct Conversion of Syngas into Lower Olefins via Methanol/Dimethyl Ether Intermediates. *Chem. Sci.* **2018**, *9* (20), 4708–4718. https://doi.org/10.1039/C8SC01597J.

(142) Raveendra, G.; Li, C.; Liu, B.; Cheng, Y.; Meng, F.; Li, Z. Synthesis of Lower Olefins from Syngas over Zn/Al_2O_3 –SAPO-34 Hybrid Catalysts: Role of Doped Zr and Influence of the Zn/Al_2O_3 Ratio. *Catal. Sci. Technol.* **2018**, *8* (14), 3527–3538. https://doi.org/10.1039/C8CY00574E.

(143) Numpilai, T.; Wattanakit, C.; Chareonpanich, M.; Limtrakul, J.; Witoon, T. Optimization of Synthesis Condition for CO_2 Hydrogenation to Light Olefins over In_2O_3 Admixed with SAPO-34. *Energy Convers. Manag.* **2019**, *180*, 511–523. https://doi.org/10.1016/j.enconman.2018.11.011.

(144) Chen, W.; Li, G.; Yi, X.; Day, S. J.; Tarach, K. A.; Liu, Z.; Liu, S. Bin; Edman Tsang, S. C.; Góra-Marek, K.; Zheng, A. Molecular Understanding of the Catalytic Consequence of Ketene Intermediates under Confinement. *J. Am. Chem. Soc.* **2021**. https://doi.org/10.1021/jacs.1c08036.

(145) Peng, Y.; Wang, L.; Luo, Q.; Cao, Y.; Dai, Y.; Li, Z.; Li, H.; Zheng, X.; Yan, W.; Yang, J.; Zeng, J. Molecular-Level Insight into How Hydroxyl Groups Boost Catalytic Activity in CO_2 Hydrogenation into Methanol. *Chem* **2018**, *4* (3), 613–625. https://doi.org/10.1016/J.CHEMPR.2018.01.019.

Chapter 2 Experimental details

2.1. Materials

The commercial MeOH synthesis catalyst (66% CuO; 25% ZnO; 9% Al_2O_3; CZA) and ZrO_2 (Surface area 90 m^2 g^{-1}; Total pore volume (Hg) 0.32 cm^3 g^{-1}) were purchased from Alfa Aesar. Chlorobenzene (99.5%), Bromobenzene (99%), Iodobenzene (98%), $Zn(NO_3)_2$ $6H_2O$ (99%) and $ZrO(NO_3)_2$ xH_2O (99.5%) were purchased from Thermo Fisher Scientific. $AgNO_3$ (≥99.0 %), trisodium citrate ($Na_3C_6H_5O_7$, ≥99.0 %), H_2O_2 (30%), $NaBH_4$ (≥98.0 %), $In(NO_3)_3 \cdot xH_2O$ (99.9 %), $Al(NO_3)_3$ $9H_2O$ (≥98%), $Cr(NO_3)_3$ $9H_2O$ (≥99.99%), $Ce(NO_3)_3$ $6H_2O$ (99%), $Ga(NO_3)_3$ xH_2O (99.9 %), $Mn(NO_3)_2 \cdot 4H_2O$ (≥99.9%) $Bi(NO_3)_3$ $5H_2O$ (≥98.0%), NH_4HCO_3 (≥99.0%) and absolute ethanol were purchased from Aldrich. Zr-MOF (MOF-801-P; $Zr_6O_4(OH)_4(fumarate)_6$; Surface area 990 m^2 g^{-1}; 99%) was purchased from Nanoshel. All the chemicals were used as received without any further purification. CO_2 (99.995%), CO (≥ 99,997 %), H2 (>99.999 %), and N2 (>99.999 %) were purchased from Air Liquide.

2.2. Catalyst preparation

2.2.1. Halogen-promoted CuO-ZnO-Al_2O_3 (CZA) catalysts

In order to obtain the halogen-modified catalysts, 200 mg of CZA catalysts was treated with a solution of 500 µmol of halobenzene in 5 mL of ethanol in an autoclave (*Figure 21*) pressurized with 20 bar of H_2. The synthesis was performed at 120 °C for 1 h. After the treatment, the catalyst was separated from the supernatant and washed three times with 15 mL of ethanol. Finally, the catalyst was dried overnight at 80 °C.



Figure 21: Autoclave used for the synthesis of the halogen-treated CZA catalysts.

The catalyst was treated with bromobenzene (ClPh), bromobenzene (BrPh), or iodobenzene (IPh), and the products were named CZA-X (X= Cl, Br, I). For the Br-treated CZA, different amounts of BrPh were used: 500 µmol; 250 µmol; 125 µmol; 60 µmol. The Br-treated catalysts were named respectively CZA-Br-500; CZA-Br-250; CZA-Br-125; CZA-Br-6. Before the reaction, the catalysts were pressed into pellets, which in turn were crushed, ground and sieved to obtain 125-300 µm pellets.

2.2.2. Bifunctional OX-ZEO catalysts

The OX-ZEO bi-functional catalysts were prepared by physically mixing a metal oxide and a zeolite phase. To obtain the bifunctional catalysts, the components were mixed in an agate mortar, then pressed into the pellets, grinded and sieved to obtain 125-300 µm pellets. The resulting bifunctional catalysts were named as Ox-S(X/Y) where Ox is the metal oxide and S(X/Y) refers to the SAPO-34 type.

Several catalysts were prepared for different purposes: to evaluate the selectivity-conversion correlations, the catalysts were prepared by modifying the metal oxide was while maintaining the same zeolite; to evaluate the zeolite effect on the performance, the same metal-oxide was used while the zeolite was changed; to evaluate the oxide/zeolite ratio effect, both phases were kept identical, but their ratio was modified.

2.2.2.1. Synthesis of the metal oxide phases

The bifunctional catalysts synthesized in this work consist of a metal-oxide which is responsible for methanol production, and a zeolite component for MTO. For the metal oxides, six catalysts were synthesized by co-precipitation and were abbreviated as $M_1M_2O_x$, where M_n stands for Zn, In, Ga, Cr, Al, Ce and Zr. The metal oxide composition and co-precipitation techniques for the were taken from the literature [1–4]. In a general co-precipitation synthesis, the metal nitrate precursors were mixed in 150 ml of water, and the system was heated to a desired temperature under stirring. Then, a water solution of NH_4HCO_3 or glucose was added drop-wise until the formation of a precipitate. After ageing the mixture for a certain time, the precipitate was washed with distilled water, dried at 100°C and finally calcined . The details related to each synthesis are reported in Table 5.

Table 5: Synthesis of metal-oxide catalysts via co-precipitation.

Catalyst	Composition	Precipitation agent	Temperature (°C)	Time (h)	Calcination
$ZnZrO_x$	Zn/(Zn+Zr)= 13 mol.%	NH_4HCO_3	70	4	500°C, 5 h
$InZrO_x$	In/(In+Zr)= 13 mol.%	NH_4HCO_3	70	4	500°C, 5 h
$ZnCrAlO_x$	Zn:Cr:Al = 5:1.4:1.4	NH_4HCO_3	70	4	500°C, 1 h
$ZnAlO_x$	Zn:Al = 1:2	NH_4HCO_3	70	4	500°C, 5 h
$ZnCeZrO_x$	Zn:Ce:Zr = 0.5:0.2:1.8	Glucose	RT 80	2 8	300°C, 1 h 500°C, 3 h
$ZnGaO_x$	Zn:Ga = 1:2	NH_4HCO_3	70	4	500°C, 5 h

In addition, the ZnO/Zr-MOF, Mn-, and Bi-Mn-based catalysts were prepared by incipient wetness impregnation and abbreviated as X/Sup where X is metal (or metal oxide), and Sup is support. For ZnO/Zr-MOF, a Zr-based MOF-801-P (Nanoshel) was used as support, and the Zn concentration was 13 at. % (same used for $ZnZrO_x$). For Mn-, and Bi-Mn-based catalysts, ZrO_2 (Alfa Aesar, 90 m^2/g specific surface area) was used as support and selected amounts of metal nitrate solutions were added dropwise. In case of the Bi-containing sample, a HNO_3 aqueous solution was used to dissolve the metal nitrate. Then the samples were dried at 110°C and calcined. The molar ratios of the metals were Bi:Mn:Zr = 1:1:2 and Mn:Zr = 1:3. The details related to each synthesis are reported in *Table 6*.

The reason for selection of Zn/Zr-MOF was to synthesize more disperse Zn species over Zr-based matrix. Mn-based catalysts were chosen to expand the diversity of different oxide active sites since these metal-oxide systems are known as hydrogenation catalysts including MeOH synthesis.

Table 6: Synthesis of metal-oxide catalysts via impregnation.

Catalyst	Composition	Calcination
ZnO/Zr-MOF	Zn/(Zn+Zr)= 13 mol.%	300°C, 3 h
Mn/ZrO_2	Mn:Zr = 1:3	400°C, 3 h
$Bi\text{-}Mn/ZrO_2$	Bi:Mn:Zr = 1:1:2	400°C, 3 h

2.2.2.2. SAPO-34 zeolites

For the preparation of OX-ZEO catalysts, four different commercial SAPO-34 zeolites were used. The samples with different morphologies and acidity were provided by ACS Materials, USA (Si/(Si+Al+P)=0.12, Si/Al=0.25), NanKai University Catalyst Co., Ltd, Tianjin, China (Si/(Si+Al+P)=0.12, 0.06 and Si/Al=0.25 and 0.12 respectively) and UOP. The zeolite samples in the manuscript are labelled as S(crystallite size/acid density). The average zeolite crystallite size was calculated from SEM analysis, while the density of acid sites was evaluated from NH_3 TPD.

2.2.3. Silver-based bifunctional catalysts

The bifunctional catalysts were composed by a supported Ag catalyst mixed with a commercial SAPO-34 (S34) component. To prepare the bifunctional catalyst, the Ag-based component was physically mixed with S34 in a mortar. Different supported Ag catalyst were prepared, and different zeolites were used to prepare the bifunctional catalysts.

2.2.3.1. Supported Ag catalysts preparation

Silver catalysts were prepared either by a wet impregnation method, using a silver nitrate solution, or by a sol deposition method, involving the deposition of silver nanoparticles on ZrO_2.

In the wet impregnation procedure, in a beaker a calculated amount of $AgNO_3$ was added to ZrO_2 in order to obtain a 10 wt.% Ag loading, together with 10 mL H_2O. The samples are labelled AgZr10, where X stands for the weight content of silver (in wt.%) in the catalysts. The samples were kept under stirring at 70 °C until complete evaporation of the solvent. Then, the samples were dried overnight in an oven and calcined at 350 °C for 3 h. The Ag-S34 catalyst was also prepared in the same way, using SAPO-34 as the support, and an amount of $AgNO_3$ necessary to obtain an Ag loading of 3.3 wt. %.

Silver nanoparticles (AgNPs) were synthesized using a modified literature procedure.[26] Silver nitrate (0.05 M, 1 mL), trisodium citrate (75 mM, 10 mL), and H_2O_2 (30 wt %, 1.2 mL) were dissolved in 34 mL H_2O under active stirring. To reduce silver, sodium borohydride ($NaBH_4$, 100 mM, 5 mL) was quickly added to the prepared solution and stirred for 30 min, forming a dark yellow stable sol with a silver content of 0.01 wt%. Then, the nanoparticles were deposited on zirconia by adding the sol in a beaker containing ZrO_2, and keeping the system under stirring until complete evaporation of the liquid phase. Afterwards, the samples were

calcined at 350°C in air and then washed in water. The subsequent elemental analysis showed zero sodium content in the catalysts after washing.

2.2.3.2. Zeolite components

The zeolite component of the Ag-based bifunctional catalysts corresponds either to the S(1.6/0.9) or to S(3.2/1.7) presented in section 2.2.3.2. **Zeolite components**. In this case, the zeolites were renamed respectively S34 and S34L (L= large), referring to the zeolite crystal size.

Table 7: description of the zeolite used to prepare the bifunctional catalysts.

Zeolite	Crystallite size (µm)	Acid density (mmol/g)	BET surface area (m^2/g)	Pore volume (cm^3/g)	Supplier
S34	1.6	0.95	438	0.26	NanKai
S34L	3.2	1.67	>550	0.27	ACS Materials

2.3. Characterization

2.3.1. X-ray powder diffraction (XRD)

The X-ray powder diffraction analysis were conducted using a Bruker AXS D8 diffractometer with Cu Kα radiation (λ =0.1538 nm). The XRD patterns were collected in the 8 – 80° (2θ) range, with the 0.02° step size and 1 s step time.

2.3.2. Transmission electron microscopy (TEM)

The TEM analysis of the samples were realized on Thermo Fisher Scientific Tecnai G2-20 microscope operation at 200 kV and equipped with LaB_6 filament. The catalysts were placed on holey carbon Cu grids (200 mesh) by dry powder deposition. Morphology investigation was

performed in bright field imaging conditions using parallel illumination mode. EDS maps were collected in hyperspectral mode with 17 ms dwell time per pixel with frames of about 512x512 pixels in continuous scanning mode over 5-10 minutes until significant signal to nose ratio has been achieved.

Scanning transmission electron microscopy (STEM) was performed on a TITAN Themis 300 S/TEM microscope equipped with a probe aberration corrector and a monochromator, allowing spatial resolution of 70 pm and energy resolution of 150 meV, a super-X windowless 4 quadrant SDD (silicon drift detector) detection system for STEM-EDX mapping, and several annular dark field detectors. Measurements were performed with a spot size of about 500 pm, a semi convergence angle between 20 mrad, and a probe current of approximately 100 pA. The collection angles were selected between 50 and 200 mrad for HAADF images.

2.3.3. Scanning Electron Microscopy (SEM)

Scanning electron microscopy was performed on a Jeol JSM-7800F (JEOL Ltd., Tokyo, Japan) scanning electron microscope with a Schottky field emission gun (FEG) electron source operating between 5 and 30 kV high tension. The analyses were conducted on carbon coated samples, at high tension of 5 kV and working distance of 15 mm.

2.3.4. X-ray Fluorescence (XRF)

Elemental analysis was performed with the use of an energy dispersive micro-XRay Fluorescence spectrometer M4 TORNADO (Bruker). This instrument is equipped with 2 anodes a Rhodium X-ray tube 50 kV/600 mA (30 W) and a Tungsten X-Ray tube 50 kV/700 mA (35 W). For sample characterization, the X-rays Rhodium with a polycapillary lens

enabling excitation of an area of 200 μm was used. The detector used was a Silicon-Drift-Detector Si(Li) with <145 eV resolution at 100000 cps (Mn Kα) and cooled with a Peltier cooling (253°K). The measurement was done under vacuum (20 mbar). The elements, that can be measured by this instrument unit range from sodium (Na) to uranium (U). Quantitative analysis was done using fundamental parameter (FP) (standardless). As elements are present in stoichiometric compounds, its formula was used for quantification of the weight percent of each element. For each sample 36 points (of 200 μm) were analyzed.

2.3.5. X-ray photoelectron spectroscopy (XPS)

X-ray photoelectron spectra were recorded on a Kratos Axis Supra photoelectron spectrometer. A monochromatic Al Ka X-ray source (1486.7 eV, 120 W) with hybrid (magnetic/electrostatic) optics was used. All of the spectra were acquired at normal emission with the analyzer in the fixed analyzer transmission mode. A pass energy of 160 eV was employed to record the survey spectra and a pass energy of 20 eV was used for the high-resolution spectra. All of the spectra were acquired under charge neutralization conditions, with the samples isolated from the instrument ground to prevent differential charging and charge neutralization provided using a low-energy electron gun within the field of the magnetic lens. Spectra were analyzed using CasaXPS. The adventitious carbon located at 284.8 eV was used to calibrate the XPS spectra.

2.3.6. FTIR of adsorbed CO

The FTIR spectra of adsorbed CO were recorded on a Thermo Scientific Is 50 equipped with a KBr beam splitter and a mercury cadmium tellure (MCT) detector. For the analyses presented in Chapter 3 (Cu-based catalysts), the samples were diluted with γ-Al_2O_3 in a 1:2 ratio to increase transmittance, then pressed (1 ton/cm^2) into a self-supported wafer (2.01 cm^2,

10 mg.cm^{-2}). For the analyses presented in Chapter 5 (Ag-based catalyst), the catalyst was used without dilution. The sample was then placed in a quartz sample holder, and introduced in a quartz cell equipped with KBr windows. The vertically mobile quartz holder allowed to position the sample in the infrared beam for spectroscopy acquisitions or in the furnace for thermal treatments. The cell was connected to a vacuum line for evacuation ($P_{residual} \simeq 10^{-6}$ Torr) and for the introduction of probes molecules into the infrared cell. All IR were recorded between 400 and 4000 cm^{-1} with 2 cm^{-1} resolutions and 64 scans and were normalized to a disc of 5 mg.cm^{-2}. Each Cu-based catalyst (Chapter 3) was reduced under 150 mbar of H_2 100% under static condition at 250°C over night. Hydrogen was then evacuated under high vacuum for 2 hours at 250°C. After cooling the measurement cell at 77 K with liquid Nitrogen, Carbon Monoxide (100%) was added by successive doses until saturation. For the Ag-based catalyst (Chapter 5) adsorbed water was removed from the sample by heating at 350°C under vacuum for 1h. Then, Carbon Monoxide (100%) was added by successive doses.

2.3.7. X-ray Absorption Spectroscopy (XAS)

XAS studies at the Zn-K edge were performed at the Super XAS beamline from SLS synchrotron in PSI (Villigen, Switzerland). For *ex-situ* investigation, the pellets of the catalysts mixed with cellulose were prepared by grinding in agate mortar and pelletizing at 1 bar. The incident photon beam was selected by a Si(111) channel-cut monochromator from the polychromatic beam coming from 2.9 T super bend magnet. The EXAFS spectra were analyzed using the Demeter software package and fitted to the Fourier transformed, k^3-weighted signal. Calibration was realized using Zn foil standard.

2.3.8. Temperature Programmed Desorption (TPD) and Reduction (TPR)

For NH_3-TPD, CO_2-TPD and TPR measurements, the Micromeritics Autochem II 2920 system was used.

In case of NH_3-TPD, the samples were first treated for 1h at 375°C under Ar 40 mL/min with a heating rate of 10°C/min, then cooled down to 100°C. Then, a 10% NH_3/Ar mixture was flowed at 100°C during 30 min. TPD was carried out at heating under Ar 30 mL/min flow from 100 to 800°C with a heating rate of 10°C/min. The desorbed ammonia was quantified with a mass-spectrometer, pre-calibrated by the injections of NH_3 with a loop.

For CO_2-TPD, the sample were first treated for 1h at 375°C under Ar 40 mL/min, with a heating rate of 10°C/min. Afterwards, the system was cooled down to 40°C. A 5% CO_2/He mixture (30 mL/min) was flowed at 40°C for 30 min, then the system was purged for 1h under He 50 mL/min. TPD was performed under He 30 mL/min, heating to 700°C with a heating rate of 10°C/min. The desorbed CO_2 was quantified with a mass-spectrometer, pre-calibrated by the injections of CO_2 with a loop.

For TPR, the sample was initially pre-treated for 1h at 375°C under Ar flow of 50 mL/min and then cooled to room temperature. The analysis was done with a 5% H_2/Ar flow of 50 mL/min and a heating rate of 10°C/min up to 900°C. For the CZA-based catalysts the procedure was different: the catalysts were pre-treated at room temperature under an Ar flow of 50 mL/min for 30 min. Then TPR was performed under a 10 % H_2/Ar flow of 50 mL/min and a heating rate of 5°C/min up to 400 °C.

2.3.9. Thermogravimetric analysis

Thermogravimetric analysis was performed using an SDT Q600 V20.9 Build 20 Thermogravimetric Analyzer (TGA) & Differential Scanning Calorimeter (DSC). 10 mg of the sample were analyzed, heating with ramp of 5 °C/min until 900 °C under air flow.

2.3.10. Magic Angle Spinning Nuclear Magnetic Resonance (MAS-NMR)

The ^{31}P MAS-NMR experiments were acquired at 161.9 MHz on a Bruker AVANCE III 9.4 T spectrometer equipped with a Bruker 4 mm MAS probe operating at a spinning frequency (n_{rot}) of 12.5 kHz. The ^{31}P MAS-NMR spectra were recorded with a pulse length of 3.6 µs (p/2 flip angle), 8 transients, and a rd of 150 s. The ^{29}Si MAS-NMR experiments were acquired at 79.5 MHz on a Bruker AVANCE III 9.4 T spectrometer equipped with a Bruker 7.0 mm MAS probe operating at a spinning frequency (n_{rot}) of 5 kHz. The ^{29}Si MAS-NMR spectra were recorded with a pulse length of 5 µs (p/2 flip angle), 1024 transients and a rd of 60 s. ^{27}Al MAS-NMR spectra were recorded at 208.5 MHz, on a 18.8 T Bruker AVANCE NEO spectrometer equipped with a Bruker 3.2 mm CP-MAS probe operating at a n_{rot} of 22 kHz.^{27}Al (I = 5/2) MAS-NMR spectra were obtained with a pulse length of 1 µs (~ p/10 flip angle), 1024 transients, and a rd of 1 s.

2.4. Catalytic tests

2.4.1. Experimental set-ups

To perform the catalytic experiments, three different set-ups were used: one single fixed-bed reactor set-up, one three parallel fixed-bed reactor set-up and an Avantium Flowrence High Throughput Experimentation unit.

2.4.1.1. Single fixed-bed reactor set-up

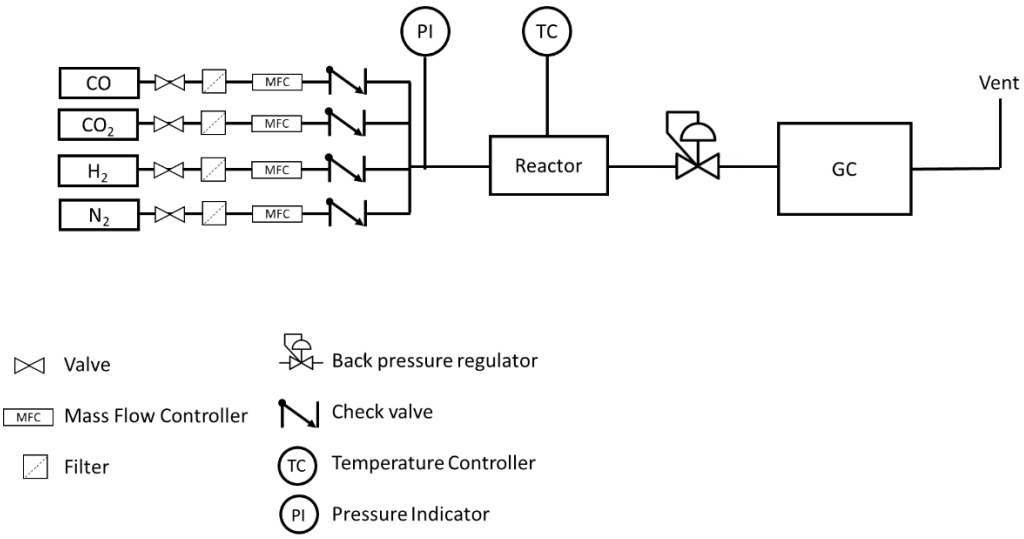

Figure 22: Scheme of the single fixed-bed reactor setup.

The single fixed-bed reactor set-up was built specifically to carry out the work of this thesis. A scheme of the set-up is represented in Figure 22. N_2, H_2, CO_2 and CO coming from the gas lines were filtered and each gas flow was regulated by a mass-flow controller (MFC) provided by Brooks. A non-return valve was placed after each MFC. The gases were then mixed and fed through the reactor placed in a copper made oven connected to a temperature controller. To make sure that the catalyst bed was placed in the isothermal zone of the oven, a 1/8“ OD and 2 mm ID reactor was used for catalyst amounts ≤ 150 mg, while a 1/4“ OD and 3.9 mm ID reactor was used for higher catalyst amounts. The pressure was controlled with a back-pressure

regulator placed after the reactor. The reactor outlet was heated above 100 °C to avoid the condensation of liquid products, and the gaseous products were analyzed online using an on-line gas chromatographer (GC). H_2, N_2, CO and CO_2 were separated with a ShinCarbon ST column (1mm ID; 2m length) and analyzed by a thermal conductivity detector (TCD). CH_4, DME, MeOH, light olefins, light paraffins and C_5+ species were separated with a CP-PoraPlotQ column (0.53 mm ID; 25 m length) and analyzed with a flame ionization detector (FID).

2.4.1.2. Three parallel fixed-bed reactors set-up

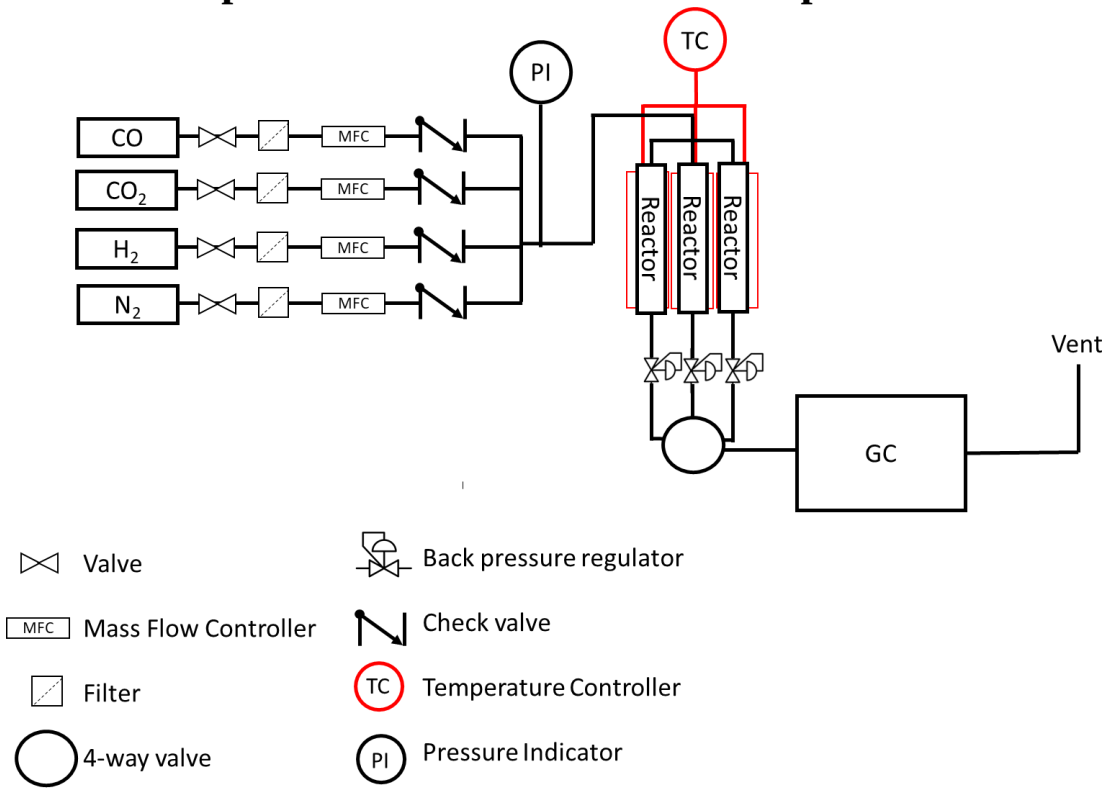

Figure 23: Three parallel fixed-bed reactor setup scheme.

The in-house built three parallel fixed-bed reactor setup scheme was similar to the single-reactor set-up (Figure 23). The main difference was that gas feed was split into three lines of capillaries with ultra-small inner diameter, each one connected to one of the reactors. Each reactor was placed in an oven connected to a temperature controller that allowed to control the three ovens at the same time. Three back-pressure valves were placed after the reactors, and

the outlet gas mixtures (heated to 80-110°C) went to the GC sequentially, through a multi-way valve. The GC characteristics and analysis type were identical to the ones of the single reactor set-up.

2.4.1.3. Avantium Flowrence High Throughput Experimentation Unit

The HTE unit used to carry out the experiments of this thesis belonged to the Realcat platform of the University of Lille. In the Avantium Flowrence unit, represented in Figure 24, the feed gases were mixed and homogeneously split into 16 reactors. The latter were divided in four different ovens. The reactors consist in a stainless-steel tube (inner diameter of 2.0 mm and length of 15 cm). The outlet of the 16 reactors were connected to a 16 ways-valve system that allowed the sequential analysis of the products coming from each reactor. The reaction products were analyzed online with GC. Permanent gases (He, H_2, N_2, CH_4, and CO) were separated by a Hayesep Q/Molecular Sieve column and determined by a thermal conductivity detector (TCD); CO_2 and CH_4 were separated by a PPQ/PPQ column and analyzed by a TCD detector; DME, MeOH, light olefins, light paraffins and C_5+ species were separated by a CP-Sil5/CP-Sil5 column and analyzed by a flame ionization detector (FID).

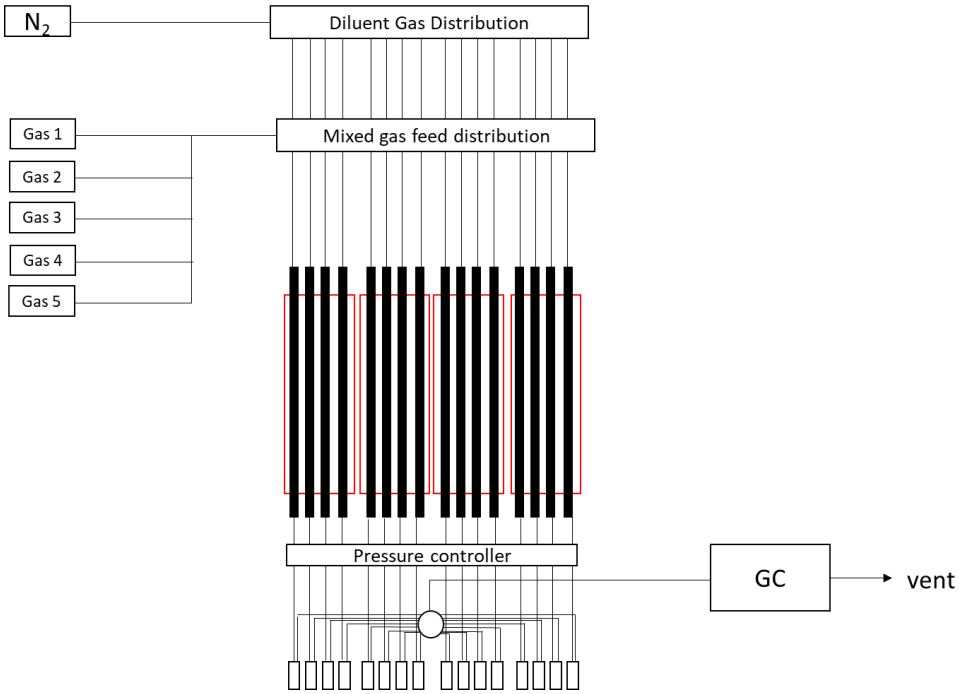

Figure 24: Simplified scheme of the Avantium Flowrent High Throughput Experimentation unit with 16 parallel reactors.

2.4.2. Experimental procedure of the catalytic tests

The CO_2 hydrogenation to Methanol reaction was performed in the single fixed-bed reactor setup and in the Avantium Flowrence unit.

In a general experiment, the reactor was loaded with SiC, to position the catalytic bed in the isothermal zone of the reactor, and 100 mg of the catalyst. Prior to the CO_2 hydrogenation reaction, all catalysts were activated in H_2 (7 mL/min) under atmospheric pressure at 250 °C for 1 h. After activation, the system was cooled down to room temperature and then pressurized with $N_2/H_2/CO_2$ (0.8:3:1) to 20 bar. Following, the temperature was increased to 200 °C at a rate of 5 °C/min. To be able to compare the catalysts at a similar conversion, the weight hourly space velocity WHSV was varied in the range 3.6–21 L $g_{cat}^{-1} \cdot h^{-1}$.

The MeOH decomposition experiments was performed in the single reactor fixed-bed reactor setup at 200 °C, 1 bar and a WHSV of 3.6 L g_{cat}^{-1} h^{-1}. MeOH vapors were fed to the

reactor flowing N_2 in a MeOH containing volume connected to the setup. The space velocity was controlled through the nitrogen flow.

The CO_2 hydrogenation to light olefins were performed in the three parallel reactor setup and in the Avantium Flowrence unit. The reactors were loaded with SiC to position the catalyst bed in the isothermal zone of the oven, and with 150 mg of catalyst. Prior to the reaction, all catalysts were activated in a nitrogen flow of 5 mL/min at 300 °C, at 1 bar for 1 h and then cooled down to 100 °C. After the activation, the pressure was increased up to 20 bar in $N_2/H_2/CO_2$ (1:1:3) and the temperature was raised to 375 °C at 5 °C/ min. Different WHSV values (1−3 NL/g·h) were used to test the catalysts.

Ethylene model hydrogenation tests were realized in the 3 parallel reactor set-up. 21 mg of ZnZrOx and 100 mg of SAPO-34 were put in separate reactors on the layer of SiC and a third reactor with only SiC was used as a reference. Different amounts of the samples were used for the similar conversion level. Ethylene:H_2 ratio of ~25:1 was set and the temperature was increased to 375ºC at 1 bar. In order to check the effect of CO_2, additional flow of this gas was provided for the CO_2/ethylene ratio of ~6:1. For the H_2O-test, the flow of ethylene and hydrogen was passed through the bottle of water at room temperature for the partial pressure of ~0.03 bar.

The CO hydrogenation reaction was performed in all the three set-ups already presented in this chapter. The tests were performed with a $N_2/H_2/CO$ (1:2:1) feed, at 375 °C and 20 bar. The weight hourly space velocity WHSV was varied between 4.8 and 0.6 L $g_{cat}^{-1} \cdot h^{-1}$.

The CO_x conversion, product selectivity and product yield were calculated using respectively Eq.1, Eq. 2 and Eq. 3:

$$X\ CO_x = \frac{\sum_{i=1}^{n} x_i C_{i,out}}{(\sum_{i=1}^{n} x_i C_{i,out}) + C_{COx,out}} \cdot 100 \qquad \text{Eq.1}$$

$$S\ product\ j = \frac{x C_{j,out}}{\sum_{i=1}^{n} x_i C_{i,out}} \cdot 100 \qquad \text{Eq.2}$$

$$Y\ product\ j = \frac{S_j * X_{COx}}{100} \quad \text{Eq.3}$$

Where X COx is the CO_2 or CO conversion; S is the selectivity; x$C_{i/j,out}$ is the molar concentration at the outlet of product i/j multiplied by a stoichiometry factor; $C_{COx,out}$ is the molar concentration of CO_2 or CO at the outlet.

To calculate the production rate of a generic product (MeOH or CO), Eq.4 was used:

$$r_{product,i} = \frac{F_{CO_2,in} * X_{CO_2} * S_{product,i}}{m_{cat}} \quad \text{Eq.4}$$

Where $F_{CO2,in}$ is the flow of CO_2 at the inlet, and m_{cat} is the mass of catalyst.

For the ethylene hydrogenation model reaction the equation used to calculate conversion, selectivity, yield and production rate are the same as for the CO_x hydrogenation.

Carbon balance was 95-105% for the high throughput tests and 98-102% for laboratory tests. Eq.5 was used to calculate this value:

$$\text{Carbon balance} = \frac{(\sum_{i=1}^{n} x_i C_{i,\ out}) + C_{COx,\ out}}{C_{COx,\ in}} * 100$$

Where x$C_{i/j,out}$ is the molar concentration at the outlet of product i multiplied by a stoichiometry factor; $C_{COx,out}$ is the molar concentration of CO_2 or CO at the outlet; $C_{COx,in}$ is the molar concentration of CO_2 or CO at the inlet.

2.5. Temporal analysis of the products (TAP) analysis

The TAP analysis was performed at the Leibniz Institute for Catalysis (LIKAT, Rostock, Germany) in collaboration with Prof. Evgenii Kondratenko.

2.5.1. Experiments

Mechanistic and kinetic aspects of CO_2 and D_2-H_2 interactions with the developed catalysts were investigated in the temporal analysis of the product reactor (TAP-2) system, described in detail in Refs. [5–7]. In these experiments, each catalyst (15 mg, 250-350 μm fraction)

was loaded in an in-house-developed quartz-tube reactor within its isothermal zone and fixed between two layers of quartz particles of the same size.

For the analyses presented in Chapter 3, prior to pulse experiments described below, the catalysts were treated in a flow H_2 (7 ml/min) at 250 °C for 1 hour. For the analyses presented in Chapter 4, prior to pulse experiments described below, the catalysts were treated in a flow of CO_2 (1.94 ml/min) and H_2 (4.5 ml/min) at 375 °C for 3 hours. After the pre-treatment the reactor was evacuated to ca. 10^{-5} Pa.

Transient experiments were performed at the same temperature in the single pulse mode using CO_2/Ar = 1:1 (the total pulse size was below 10^{15} molecules) or H_2/D_2/Ar = 1:1:1 (the total pulse size was 3-6·10^{15} molecules) mixtures. The analyses presented in Chapter 3 were carried out at 200 °C; the analyses presented in Chapter 4 were carried out at 375 °C. H_2 (Air Liquide, 5.0), D_2 (CK Special Gases Limited, 2.8), CO_2 (Air Liquide, 4.5) and Ar (Air Liquide, 5.0) were applied for preparing these mixtures without additional purification. The hydrogen isotopic exchange experiments were performed with the overall pulse size of 3-6·10^{15} molecules. The total pulse size of the CO_2/Ar = 1:1 mixture was below 10^{15} molecules to ensure Knudsen diffusion regime. Under such conditions, the mass transport can be quantitatively described by the Knudsen diffusion, and any collisions between gas-phase species are suppressed. In this way, only heterogeneous reaction steps could be analyzed. The gas composition at the reactor outlet was quantitatively analyzed by a quadrupole mass spectrometer (HAL RC 301 Hiden Analytical). The following m/z signals were used for identification of different compounds: 44 (CO_2), 32 (O_2), 28 (CO_2, CO), 4 (D_2), 3 (HD), 2 (H_2) and 40 (Ar). The pulses with each mixture were repeated 10 times for each m/z and averaged to improve the signal-to-noise ratio. The concentrations of the feed components and the reaction products were calculated from the ratio of the area of signal recorded at the respective m/z to the area of Ar used as an inert standard. The fragmentation patterns and sensitivity factors

required for these calculations were determined separately upon pulsing the same mixtures in the reactor filled only with quartz particles.

2.5.2. Kinetic evaluation

The CO_2 pulse experiments were kinetically evaluated through fitting of CO_2 transient responses to different microkinetic models. The mathematic routine has been described in Ref.[8,9]. The TAP reactor was considered as a one pseudo-homogeneous reactor system and divided into three different zones: upstream inert zone, catalyst zone and downstream inert zone.

The mass balances for gas-phase and surface species outside the catalyst layer were described using equations 5 and 6, respectively:

$$\frac{\partial C_i}{\partial t} = D_{Knudsen}^{eff} \times \frac{\partial^2 C_i}{\partial x^2} \quad \text{Eq. 5}$$

$$\theta_i = 0 \quad \text{Eq. 6}$$

where C_i is the concentration of CO_2 or Ar, θ_i is the fraction of adsorbed species i, t is the time and x - the coordinate along the reactor.

In the catalyst zone, the reaction term was included in the mass balances for gas-phase (equation 7) and surface species (equation 8):

$$\frac{\partial C_i}{\partial t} = D_{Knudsen}^{eff} \times \frac{\partial^2 C_i}{\partial x^2} + \sum_j \rho_{cat} \nu_{ij} r_j \quad \text{Eq. 7}$$

$$\frac{\partial \theta_i}{\partial t} = \sum_j \frac{\nu_{ij} r_j}{C_{total}} \quad \text{Eq. 8}$$

With $r_j = k_j \prod_l C_l^{n_l} \prod_m \theta_m^{n_m}$ and $0 \leq n_l \leq 1$, $0 \leq n_m \leq 2$, ν_{ij} - stoichiometric coefficient of species i in reaction j, ρ_{cat} - density of the catalyst and C_{total}.- concentration of adsorption centers.

The following boundary conditions are applied for solving these partial differential equations:

i) C_i at the reactor outlet is equal to 0 for all species due to low amounts of pulsed molecules and low pressure in the analytic chamber;

ii) $\partial C_i/\partial x$ at the reactor inlet is equal to 0 for $t \geq t_{open}$ (t_{open} – opening time of pulse valve). This means that the gradient of concentration is equal to zero when the pulse valve is closed;

iii) Only for pulsed molecules, the concentration gradient for a certain time interval ($t_{open} \sim 10$ ms) is describing the inlet pulse as a linear decline to 0 at $t = t_{open}$: $\partial C_i/\partial x = \partial C_i/\partial x|_{t = 0}$, $(t < t_{open})$

The resulting system of partial differential equations was solved applying a FORTRAN-program which uses the numerical routine PDEONE[10]. The search for kinetic parameters was performed in a wide range of possible values (10^{-4} to 10^{8}) using first a genetic algorithm to find good starting values and then the Nelder-Mead simplex algorithms[11]. The quality of fits was characterized by an objective function defined as the sum of squares of the shortest deviation between the respective points of the experimental data and simulated data. Moreover, the fitting for each catalyst was repeated at least 10 times. Typically, the same solution with the lowest residuum was obtained several times. A sensitivity analysis was applied to check the significance of the parameters derived using the best kinetic model. To this end, each parameter was varied until the objective function changed by 10%. Thus, if the change in the parameter is larger than 10%, this parameter does not significantly contribute to the goodness of the fit. To check if the parameters correlate, the Jacobi-matrix approach was applied.

2.6. References

(1) Jiao, F.; Li, J.; Pan, X.; Xiao, J.; Li, H.; Ma, H.; Wei, M.; Pan, Y.; Zhou, Z.; Li, M.; Miao, S.; Li, J.; Zhu, Y.; Xiao, D.; He, T.; Yang, J.; Qi, F.; Fu, Q.; Bao, X. Selective Conversion of Syngas to Light Olefins. *Science* **2016**, *351* (6277), 1065–1068. https://doi.org/10.1126/science.aaf1835.

(2) Liu, X.; Wang, M.; Yin, H.; Hu, J.; Cheng, K.; Kang, J.; Zhang, Q.; Wang, Y. Tandem Catalysis for Hydrogenation of CO and CO_2 to Lower Olefins with Bifunctional Catalysts Composed of Spinel Oxide and SAPO-34. *ACS Catal.* **2020**, *10* (15), 8303–8314. https://doi.org/10.1021/acscatal.0c01579.

(3) Li, Z.; Wang, J.; Qu, Y.; Liu, H.; Tang, C.; Miao, S.; Feng, Z.; An, H.; Li, C. Highly Selective Conversion of Carbon Dioxide to Lower Olefins. *ACS Catal.* **2017**, *7* (12), 8544–8548. https://doi.org/10.1021/acscatal.7b03251.

(4) Wang, S.; Zhang, L.; Zhang, W.; Wang, P.; Qin, Z.; Yan, W.; Dong, M.; Li, J.; Wang, J.; He, L.; Olsbye, U.; Fan, W. Selective Conversion of CO_2 into Propene and Butene. *Chem* **2020**, *6* (12), 3344–3363. https://doi.org/10.1016/j.chempr.2020.09.025.

(5) Morgan, K.; Maguire, N.; Fushimi, R.; Gleaves, J. T.; Goguet, A.; Harold, M. P.; Kondratenko, E. V.; Menon, U.; Schuurman, Y.; Yablonsky, G. S. Forty Years of Temporal Analysis of Products. *Catal. Sci. Technol.* **2017**, *7* (12), 2416–2439. https://doi.org/10.1039/C7CY00678K.

(6) Gleaves, J. T.; Yablonskii, G. S.; Phanawadee, P.; Schuurman, Y. TAP-2: An Interrogative Kinetics Approach. *Appl. Catal. Gen.* **1997**, *160* (1), 55–88. https://doi.org/10.1016/S0926-860X(97)00124-5.

(7) Perezramirez, J.; Kondratenko, E. Evolution, Achievements, and Perspectives of the TAP Technique. *Catal. Today* **2007**, *121* (3–4), 160–169. https://doi.org/10.1016/j.cattod.2007.01.001.

(8) Rothaemel, M.; Baerns, M. Modeling and Simulation of Transient Adsorption and Reaction in Vacuum Using the Temporal Analysis of Products Reactor. *Ind. Eng. Chem. Res.* **1996**, *35* (5), 1556–1565. https://doi.org/10.1021/ie950379b.

(9) Soick, M.; Wolf, D.; Baerns, M. Determination of Kinetic Parameters for Complex Heterogeneous Catalytic Reactions by Numerical Evaluation of TAP Experiments. *Chem. Eng. Sci.* **2000**, *55* (15), 2875–2882. https://doi.org/10.1016/S0009-2509(99)00553-9.

(10) Sincovec, R. F.; Madsen, N. K. Software for Nonlinear Partial Differential Equations. *ACM Trans. Math. Softw.* **1975**, *1* (3), 232–260. https://doi.org/10.1145/355644.355649.

(11) Gao, F.; Han, L. Implementing the Nelder-Mead Simplex Algorithm with Adaptive Parameters. *Comput. Optim. Appl.* **2012**, *51* (1), 259–277. https://doi.org/10.1007/s10589-010-9329-3.

Chapter 3

Selective CO_2 hydrogenation to methanol by halogen deposition over a Cu-based catalyst

3.1. Introduction

Among the possible products of CO_2 conversion, MeOH is an important platform-molecule used as a precursor for a variety of chemicals, and it is also employed as fuel. [1]

Cu-based catalysts have emerged as the most promising candidates for CO_2 hydrogenation to methanol. On the one hand, Cu is the 25th most abundant element in the Earth crust, which makes its use cheaper (compared to noble metals and indium) and sustainable. On the other hand, Cu based catalysts show high activity at relatively low temperatures (200-250 °C). The possibility to operate under reduced temperature and pressure conditions can lead to significant energy savings and reduced costs, making the process more attractive for large-scale implementation. As a matter of fact, Cu-ZnO-Al_2O_3 is the only catalyst used in the industrial synthesis of MeOH from CO_2. [1,2]

Despite its good performance in the CO_2 hydrogenation to MeOH, the industrial catalyst can be improved to reduce the unwanted parallel CO production. Previous studies have demonstrated promising results with halogen-promoted catalysts, achieving notable reductions in CO selectivity. Gao et al. treated Cu/Zn/Al hydrotalcite with NaF and then calcined the sample to obtain a fluorine modified CZA catalyst[3]. They observed an increase of selectivity to MeOH due to the increase of CuO, which is easily reducible. Moreover, the CO_2 conversion decreased due to a lower content of copper surface area. Similarly, Dybbert et al. treated a Cu/ZnO catalysts with fluorine through a oxidative fluorination route.[4] In this case, they observed better selectivity to MeOH due to the presence of a Cu/ZnO_{1-x}/Zn_xF_{2x} active phase.[5]

Chen et al, instead, modified a CuZnZr catalyst with $CuBr_2$, obtaining high methanol selectivity (97.1%) at a CO_2 conversion of 10.7%. In this work it was observed that the presence of a CuBr phase reduces the activity of the catalyst in the reverse water-gas shift reaction.[6]

In this context, our work aims to explore the effects of various halogen as promoters on the commercial CZA catalyst, used in the industry for CO_2 hydrogenation to MeOH. Our group studied already the effect of halogen deposition on the surface of different types of catalysts using halobenzenes.[7–10] This treatment allows the deposition of Cl, Br and I on the CZA catalyst by a simple modification of the commercial catalyst surface. This strategy can be used to selectively poison the active sites responsible for unwanted parallel reactions. The CO_2 hydrogenation to MeOH reaction was performed over these catalysts, and the halogen effect on the selectivity to MeOH was explained. Through the combination of characterization and a kinetic study, we investigated the influence of Br on reducing the selectivity to CO.

3.2. Results and discussion

3.2.1. Halogen deposition mechanism

The CZA catalyst was treated with different halobenzenes (BrPh, ClPh, and IPh) dissolved in ethanol at 120 °C, in an autoclave pressurized with 20 bar of H_2. The presence of the halogens on the catalyst surface was confirmed by XRD and XPS analysis (*Figure 25*).

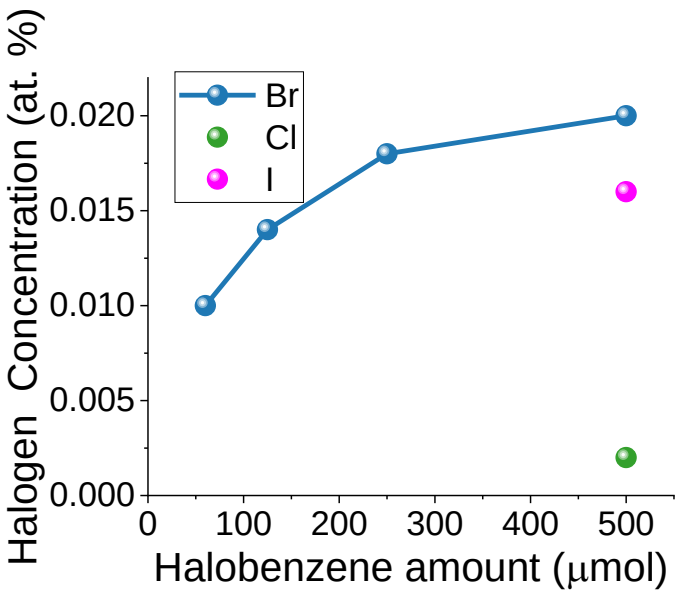

Figure 25: Variation of the halogen loading on the catalyst surface with the increasing amount of halobenzene.

To vary the bromine concentration in the surface of the catalyst, several CZA-based catalysts have been synthesized, reducing progressively the BrPh amount (respectively 500, 250, 125 and 60 µmol of BrPh). With XRF, it was confirmed that a lower amount of BrPh is associated with a lower amount of Br on the surface of CZA (Figure 26a). Moreover, based on the surface concentration of Br, Cl, and I using the same amount of halobenzene, it was observed that Chlorobenzene was less reactive than Iodobenzene and Bromobenzene.

To define the mechanism of the halogen deposition, the liquid phase of the synthesis mixture was analyzed by GC-MS (Figure 26b). The chromatogram recorded after the synthesis of the CZA-Br-500 catalyst shows that the liquid phase contained ethanol, unreacted bromobenzene, and benzene. Indeed, Benzene is the product of the decomposition of BrPh on the surface of the catalyst, and this reaction allows the deposition of the halogen. In the case of CZA-Br-60 synthesis, the unreacted bromobenzene and the benzene peaks were characterized by lower intensities due to the lower content of the halogen precursor. To assess the role of H_2 in the reaction, the CZA-Br-500 catalyst has been synthesized without adding 20 bar of H_2. It

was observed that without the presence of H_2 in the system, no products of decomposition of bromobenzene were detected. Consequently, H_2 was crucial for the deposition of Br on the catalyst surface.

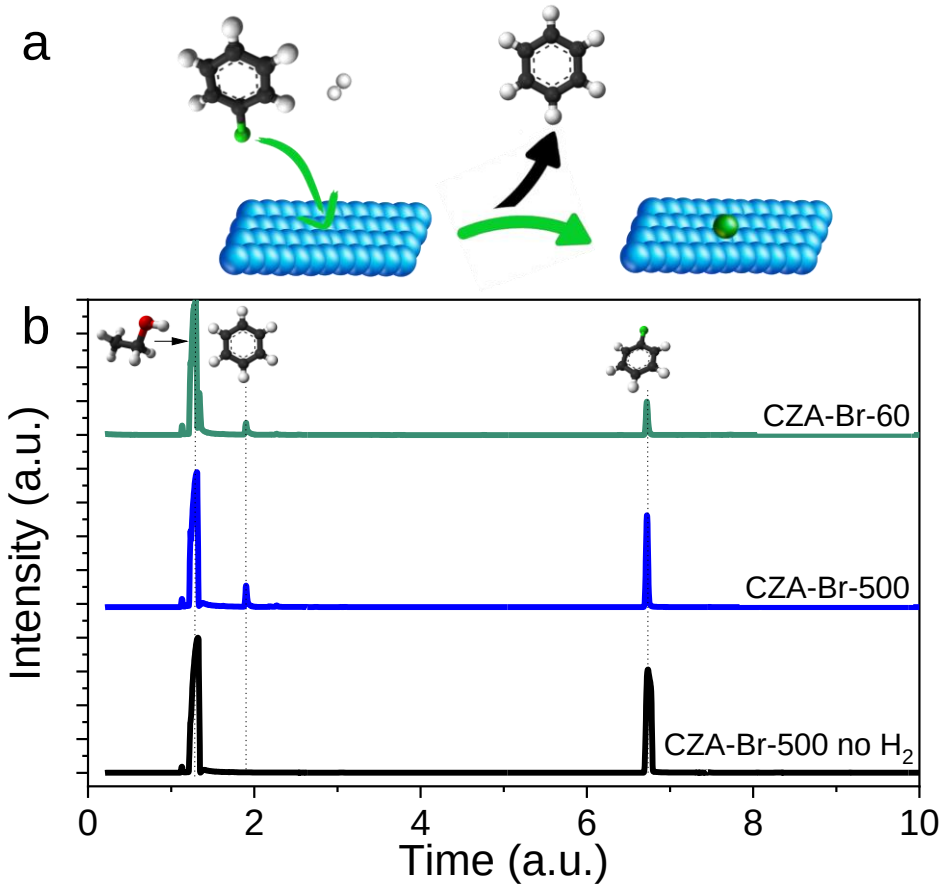

Figure 26: a) Scheme of the halogen deposition mechanism; b)GC-MS analysis of the liquid phases of the catalyst synthesis mixtures: CZA-Br-500 in the absence of H_2; CZA-Br-500; CZA-Br-60.

3.2.2. Catalyst characterization

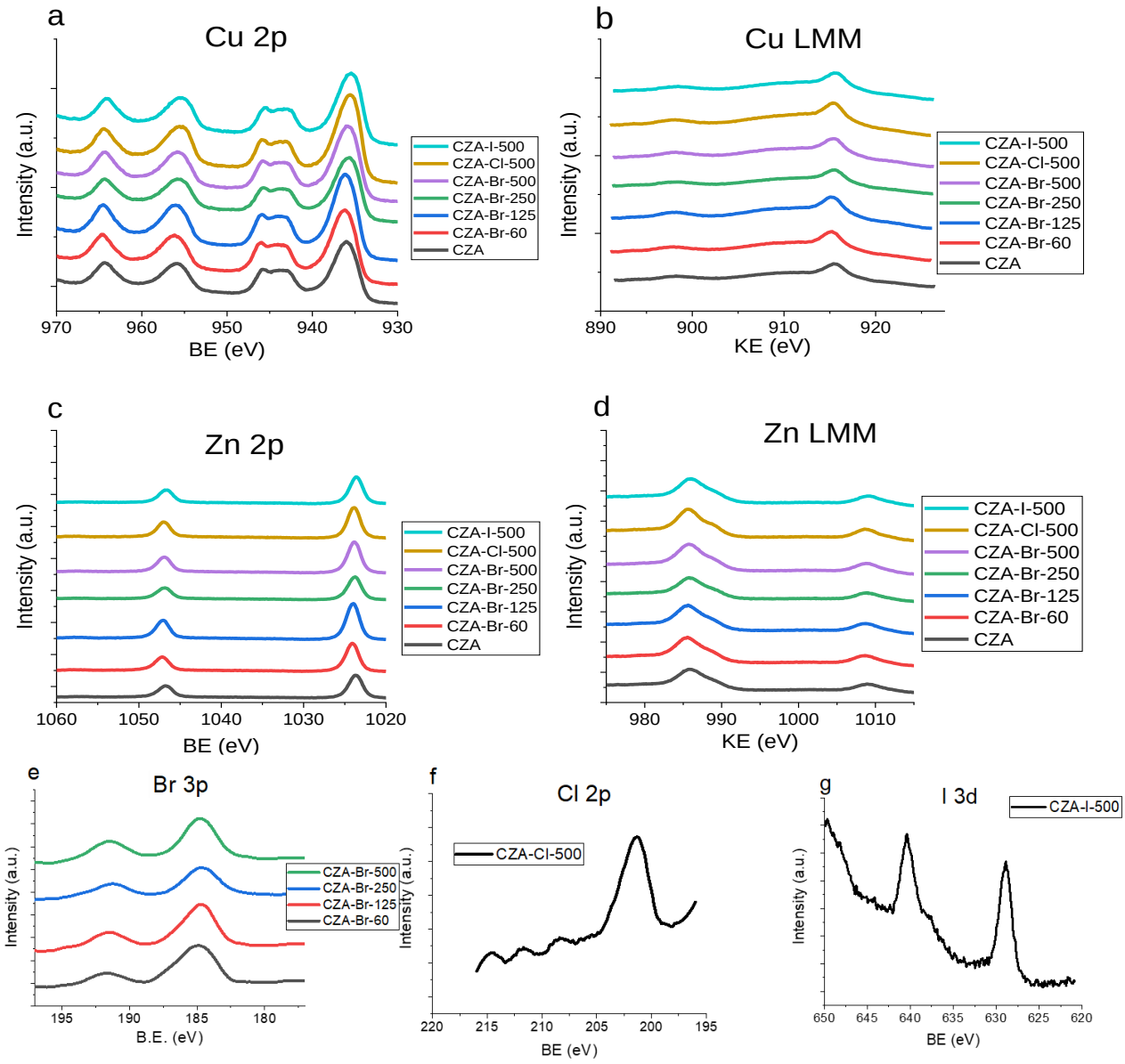

Figure 27: XPS Spectra related to the as-prepared catalysts. a) Cu 2p; b) Cu LMM; c) Zn 2p; d) Zn LMM; e) Br 3p; f) Cl2p; g) I 3d.

The XPS spectra of the as-synthesized catalysts are reported in Figure 27. The Cu 2p spectra of all the catalyst showed the presence of Cu^{2+}, confirmed by the presence of satellite peaks, and by the calculated Cu $2p_{3/2}$ – Cu $L_3M_{4,5}M_{4,5}$ modified auger parameter which was 1851.5 eV typical of CuO[11]. The Br3p spectra of the CZA-Br-X catalysts confirmed the

presence of Br for each treated catalyst (Figure 27e). Similarly, the I3d and Cl2p spectra confirmed respectively the presence of Cl in CZA-Cl-500 (Figure 27f), and I in CZA-I-500 (Figure 27g).

The XRD analysis showed that the pristine CZA catalysts and the Cl-, Br- and I-containing CZA catalyst were a combination of CuO, ZnO and Al_2O_3 phases (Figure 28). A minor presence of Malachite ($Cu_2CO_3(OH)_2$) was also observed in all the catalysts. All the patterns showed broad peaks, due both to the overlapping of the signals of the three main components, and to the small size of the particles. Moreover, the halogen-CZA XRD patterns were similar to the one of CZA, and no new peaks were detected, showing that the treatment with halogens did not affect the structure of the CZA catalyst.

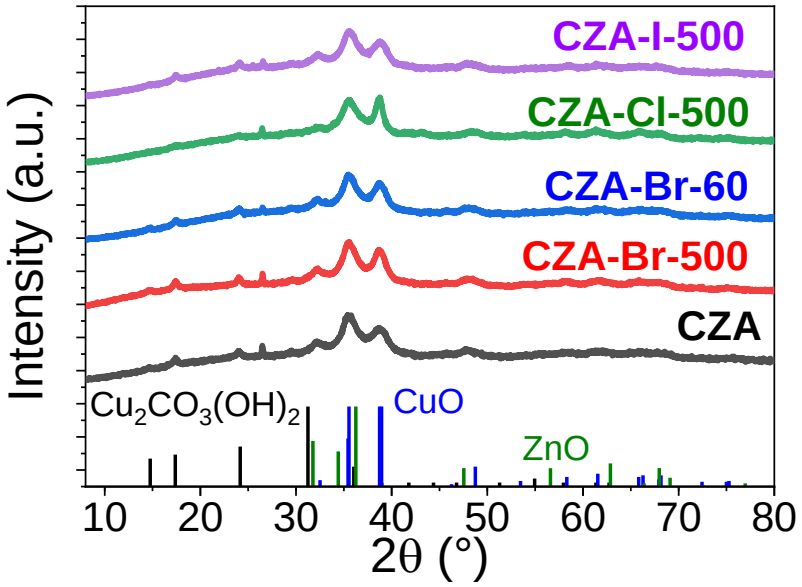

Figure 28: XRD patterns of the CZA and halogen-treated CZA catalysts.

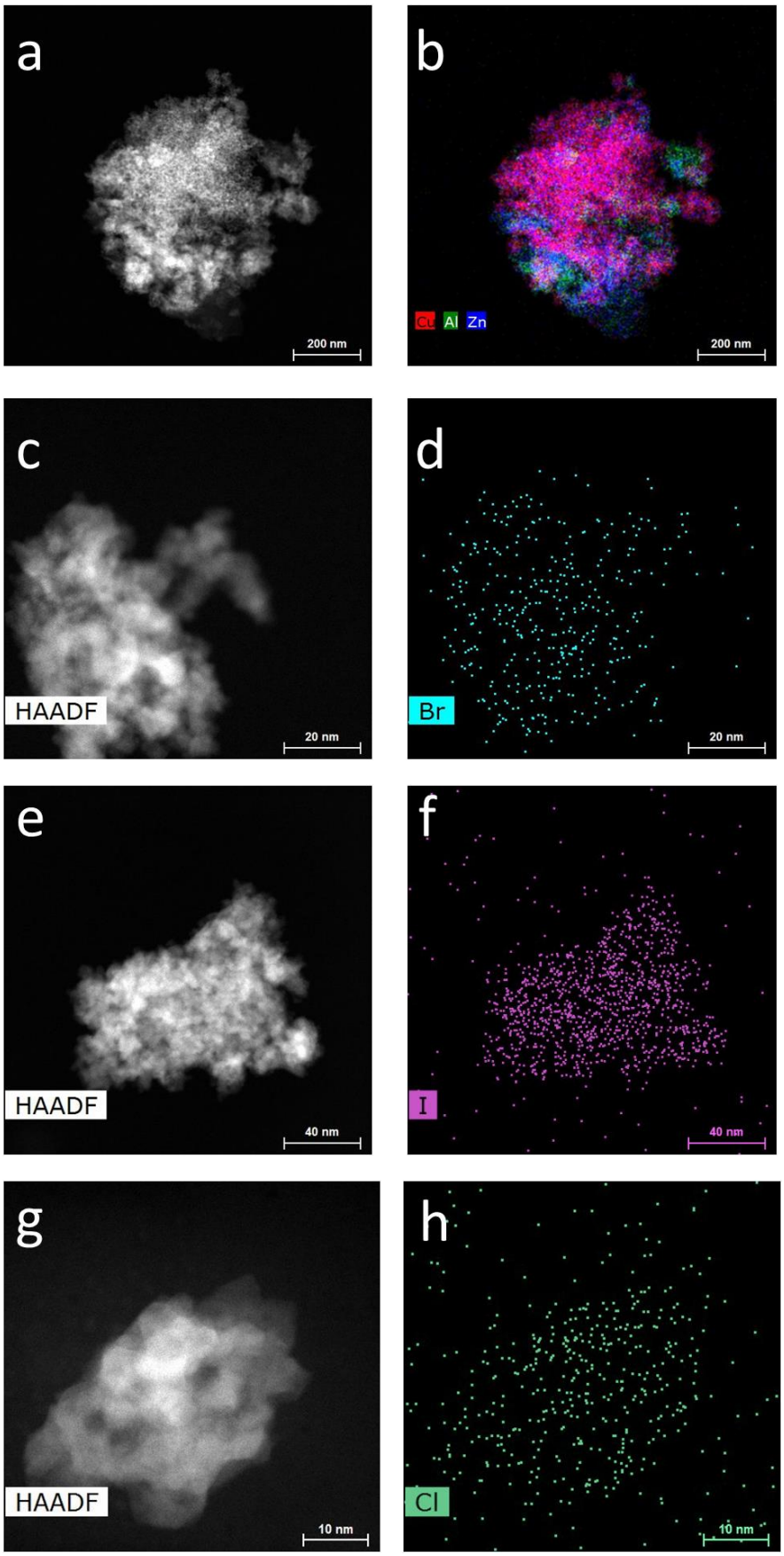

Figure 29: STEM-HAADF (a, c, e, g) and STEM-EDS (b, d, f, h) of the studied catalysts: CZA (a, b); CZA-Br-500 (c, d) CZA-I-500 (e, f) and CZA-Cl-500 (g, h).

The catalysts were analyzed with HAADF-STEM and HAADF-EDS to determine the morphology and the components distribution. The commercial CZA catalyst was an agglomeration of very small nanoparticles. ZnO was homogeneously dispersed around the main phase, CuO. Al_2O_3, on the contrary, was distributed heterogeneously, forming isolated aggregates. HAADF-EDS verified the deposition of the halogens on the surface of the CZA-X-500 catalysts, and to detect any preferential interaction of the halogens with a specific component of the mixed oxide catalyst (Figure 29). For the three CZA-X-500 catalysts, the dispersion of the halogen all over the catalyst surface was observed. Figure 29d shows the Br dispersion over the CZA-Br-500 sample , and Figure 29f shows the I distribution over the CZA-I-500 sample. In the case of CZA-Cl-500, the detection of Chlorine was not simple due to a very low Cl kα signal (Figure 29h).

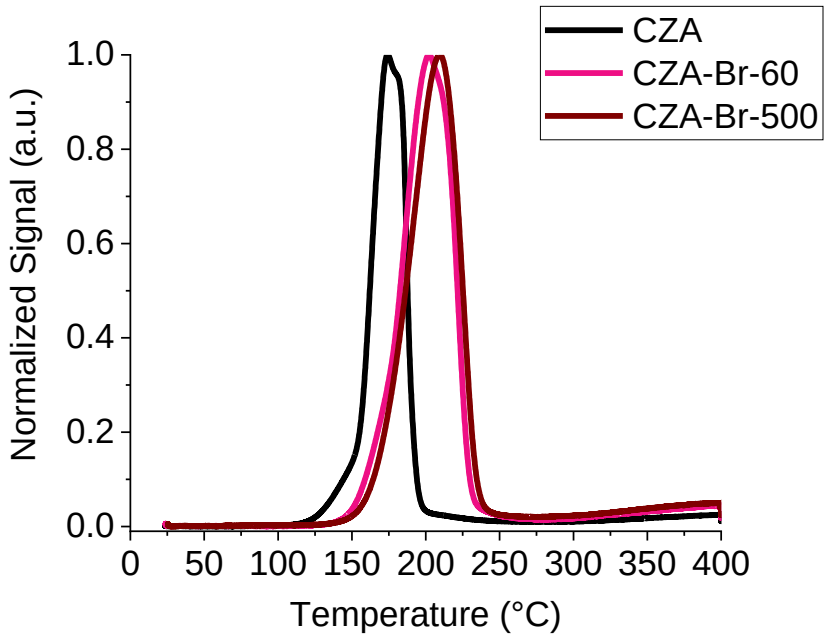

Figure 30: H_2-TPR profiles of CZA, CZA-Br-60 and CZA-Br-500 catalysts.

The TPR analysis of the commercial and Br-treated CZA catalyst presented an asymmetric reduction peak in the range of 100–250 °C (Figure 30). This peak is attributed to the reduction of highly dispersed CuO particles[12]. It can be observed that the reduction of the bromine containing catalyst happened at relatively higher temperatures. Hence, it can be stated that the interaction of Bromine with CuO can slightly lower the reducibility of CuO particles. A similar result was observed with fluorine-treated Cu/ZnO catalysts, in which a higher Fluorine content caused an increase in the reduction temperature of the catalyst.[5]

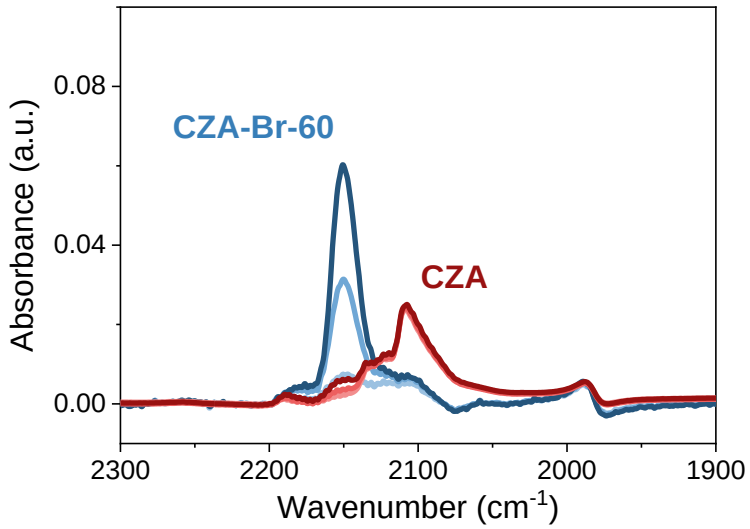

Figure 31: FTIR spectra of CO adsorbed over the reduced CZA (red) and CZA-Br-60 (blue)catalysts at 77 K.

FTIR spectroscopy of adsorbed CO was used to understand the surface modification of the CZA catalyst due to the presence of the halogen. The CO absorption was performed at room at 77 K, over the reduced CZA catalyst and CZA-Br-60 catalysts. Figure 31 shows the IR spectra measured during progressive CO dosage at 77 K. The main peaks detected are to be found at 2187 cm^{-1}, 2148 cm^{-1}, and 2108 cm^{-1}. The most intense peak for the CZA catalyst was the one at 2108 cm^{-1}, while two very weak signals at 2150 and 2187 cm^{-1} were observed. Instead, in the spectra related to the CZA-Br-60 catalyst an intense peak at 2150 cm^{-1} could be

observed. Based on the work of Mintova's group[13], we attributed the band at 2108 cm^{-1} to the Cu(0)-CO mono-carbonyl complexes, and the signal at 2150 cm^{-1} can be attributed to Cu^{+}-CO mono-carbonyl complexes. Even though Mintova's group[13] reported that the band associated to this second type of complex is found at 2140 cm^{-1}, Nielsen et al. observed that the interaction of Br with copper can cause a blue shift in the CO-Cu^{+} band[14]. The signal at 2187 cm^{-1} can finally be attributed to the CO adsorption on Zn^{2+} [15]. Hence, for the Br-treated catalyst, the presence of Br produces a higher concentration of Cu^{+} sites on the catalyst surface, and this could be the reason why the MeOH selectivity is improved. In Chapter 1 it has been reported that Cu^{+} has been presented by several authors as the active sites for the MeOH synthesis.

3.2.3. Catalytic performance

To assess the halogen effect in the CZA-catalyzed CO_2 hydrogenation to methanol, the CZA catalyst was compared to halogen-treated ones. Concerning the catalyst activity, the deposition of the three halogens generated a decrease in MeOH and CO production. In Figure 32 it can be observed that among the CZA-X-500 catalysts, CZA-Br-500 was the less active and CZA-Cl-500 the most active one. At the same time, the CO production rate for Cl and I was higher than in the case of Br. Moreover, in Figure 32 it can be observed that the methanol productivity was function of the content of Br: the lower the amount of Br on the catalyst surface, the higher the MeOH production. Contrarily, the CO production is affected by the amount of surface Br to a minor extent, and its values are significantly lower compared to the starting catalyst.

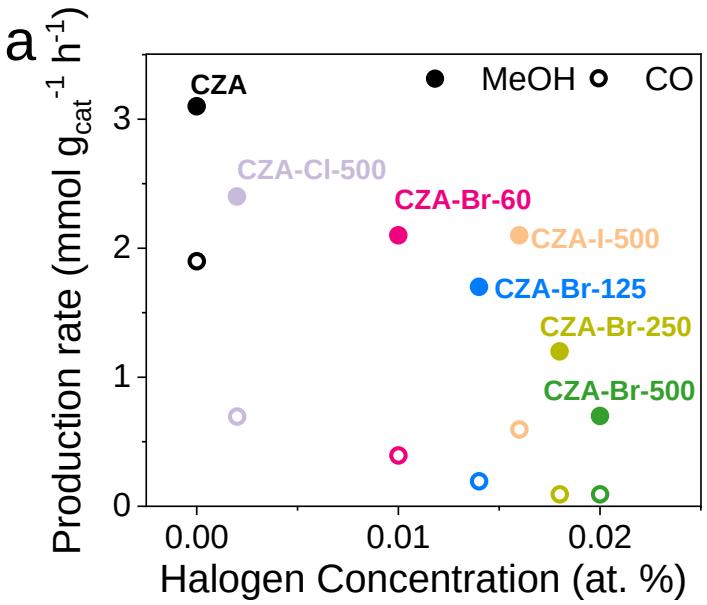

Figure 32: Effect of different halogen on the catalyst activity in MeOH and CO production from CO_2 hydrogenation (Conditions: 200 °C, 20 bar, 3600 mL g_{cat}^{-1} h^{-1}).

It must be taken in consideration that the selectivity to MeOH increases with decreasing CO_2 conversion. Hence, the results obtained with the halogen-treated catalysts were compared with the ones obtained with the pristine CZA at the same conversions (Figure 33).

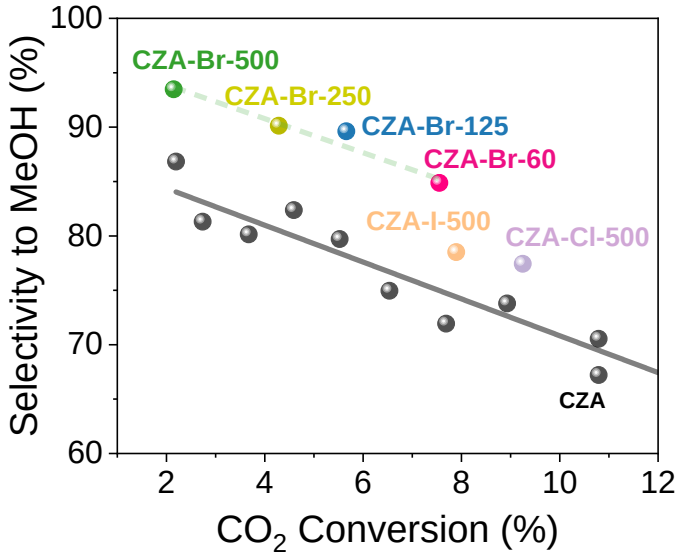

Figure 33: Effect of the halogen deposition on the selectivity to MeOH during the CO_2 hydrogenation to MeOH. (Conditions: 200 °C, 20 bar, 21000-3600 mL g_{cat}^{-1} h^{1}).

It was observed that chlorine did not affect significantly the selectivity to MeOH. This could be explained by the negligible concentration of Chlorine on the catalyst surface (Figure *25*). Bromine and Iodine, instead, were present at concentrations ten times higher than the Chlorine counterpart (around 0.02 at. %). However, iodine had a minor effect on the selectivity to MeOH and Bromine had the major one, with an increase in selectivity of 10%. Interestingly, the 10% increase in the selectivity to MeOH (with respect to the pristine CZA catalyst) did not change with the Br amount (Figure 33).

The CO_2 conversion has a linear dependency to the Br concentration on the catalyst surface (Figure 34). At the same time, the 10% increase in the selectivity to MeOH showed in Figure 33 does not change with the Br amount due to the fact that Br poisons more significantly the sites responsible for CO production.

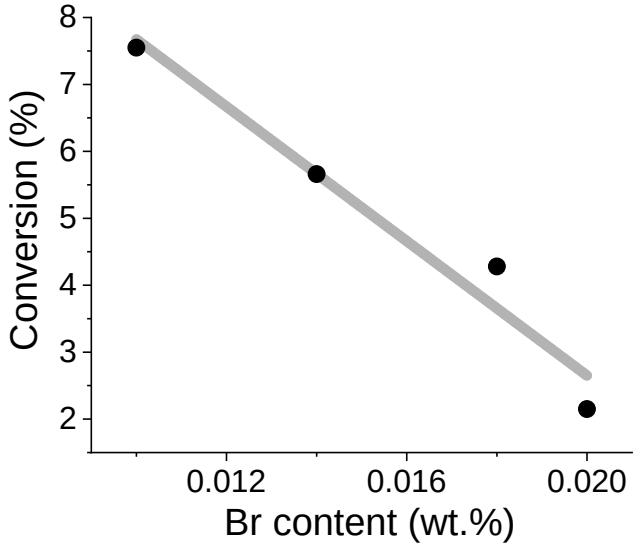

Figure 34: Linear dependency of CO_2 conversion from the halogen concentration in the surface of the CZA catalyst.

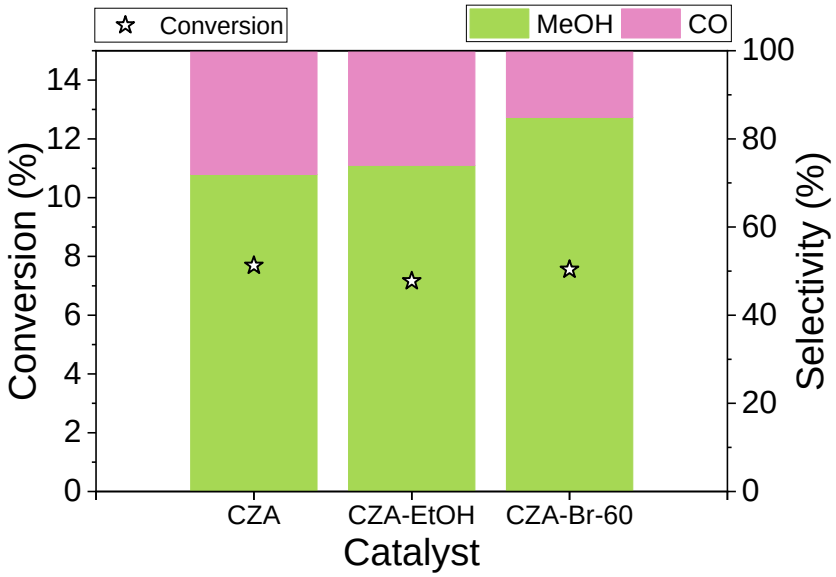

Figure 35: CO_2 hydrogenation to MeOH over CZA, CZA-EtOH and CZA-Br-60. (Conditions: 200 °C, 20 bar, 21000-3600 mL g_{cat}^{-1} h^{-1}).

It is important to point out that the solvent used to for the halogen deposition treatment does not have an effect on the selectivity to MeOH. To verify this, the treatment of the CZA catalyst was performed in the absence of bromobenzene, and the catalyst (CZA-EtOH) was tested in the CO_2 hydrogenation to methanol. Figure 35 reports the comparison of the performance of the CZA, CZA-EtOH and CZA-Br-60 catalysts at a CO_2 conversion of 7 %. It is clear that while the CZA-EtOH catalyst shows the same selectivity to MeOH as the starting catalyst, in the presence of Br the selectivity improves.

3.2.4. Kinetic Analysis

The increase in selectivity to CO with increasing conversion might be attributed to two different reactions: RWGS and MeOH decomposition (Figure 36).

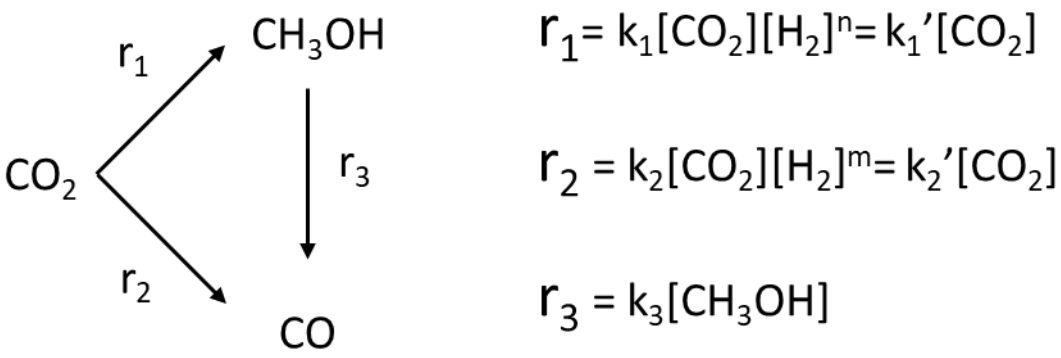

Figure 36: *Parallel reactions during the CO_2 hydrogenation to MeOH, and relative kinetic equations.*

The Kondratenko's group confirmed with a recent work that at relatively low temperatures the CH_3OH decomposition to CO over CuZn-based catalysts is the main contribute to the loss of CH_3OH selectivity with increasing CO_2 conversion.[16] Indeed, with increasing conversion both CZA and the Br-containing catalysts showed a decrease in MeOH selectivity and an increase of CO production. To understand the bromine influence in the two CO production pathways, the kinetic constants of the three reactions were calculated according to a model similar to what reported by Khodakov et al. for the production of COx during propane oxidative dehydrogenation[17].

The equations of the rates of the reactions considered in the model are reported in Figure 36.

The rate of CO_2 consumption and the rate of MeOH production can be expressed as a combination of these three equations:

Eq.1 $-Q\frac{d[CO_2]}{dV} = r_1 + r_2 = (k_1' + k_2')[CO_2]$ CO2 consumption

Eq.2 $Q\ \frac{d[CH_3OH]}{dV} = r_1 - r_3 = k_1' [CO_2] - k_3 [CH_3OH]$ MeOH production

Where Q is the gas flow rate.

Expressing Eq. 1 and Eq. 2 in their exponential form, one can obtain the following equations:

Eq.3 $[CO_2] = [CO_2]_0 \exp(-(k_1' + k_2')\tau)$

Eq.4 $[CH_3OH] = [CO_2]_0 \frac{k_1'}{k_3 - (k_1' + k_2')}(\exp(-(k_1' + k_2')\tau) - \exp(-k_3\tau))$

Where τ is the residence time ($\tau = (V/Q)$).

The selectivity to MeOH S_{CH3OH} can be expressed as

Eq.5 $S_{CH3OH} = \frac{[CH_3OH]}{[CO_2]_0 - [CO_2]}$

And substituting Eq.3 and Eq.4 in Eq. 5, and considering that

$e^x = \sum_{n=0}^{\infty} \frac{x^n}{n!} \approx 1 + x$

one obtains

Eq. 6 $S_{CH3OH} = \frac{[CH_3OH]}{(k_1' + k_2')\tau[CO_2]_0} = \frac{k_1'}{k_1' + k_2'} \left(1 - \frac{k_1' + k_2' + k_3}{2}\tau\right)$

By plotting the Selectivity to MeOH as a function of the reciprocal flow rate ($1/Q = V/\tau$) one can obtained the values of k_1' and k_2' from the intercept, and the k_3 value from the intercept. k_1' can be calculated from the value of the methanol production rate at zero CO_2 conversion ($\tau \rightarrow 0$).

The plots used for the calculation of the kinetic constants are reported in Figure 37 and the results of the calculation are reported in Table 8.

Table 8: Kinetic constants calculated for the MeOH formation, RWGS and MeOH decomposition reactions happening during the CO_2 hydrogenation to MeOH process.

Catalyst	**Br content (at.%)**	**k_1'(mL/min)**	**k_2' (mL/min)**	**k_3 (mL/min)**
CZA	0.000	0.300	0.077	0.399
CZA-Br-60	0.010	0.186	0.016	0.225
CZA-Br-125	0.014	0.136	0.010	0.075
CZA-Br-250	0.018	0.109	0.008	0.042
CZA-Br-500	0.020	0.059	0.003	0.033

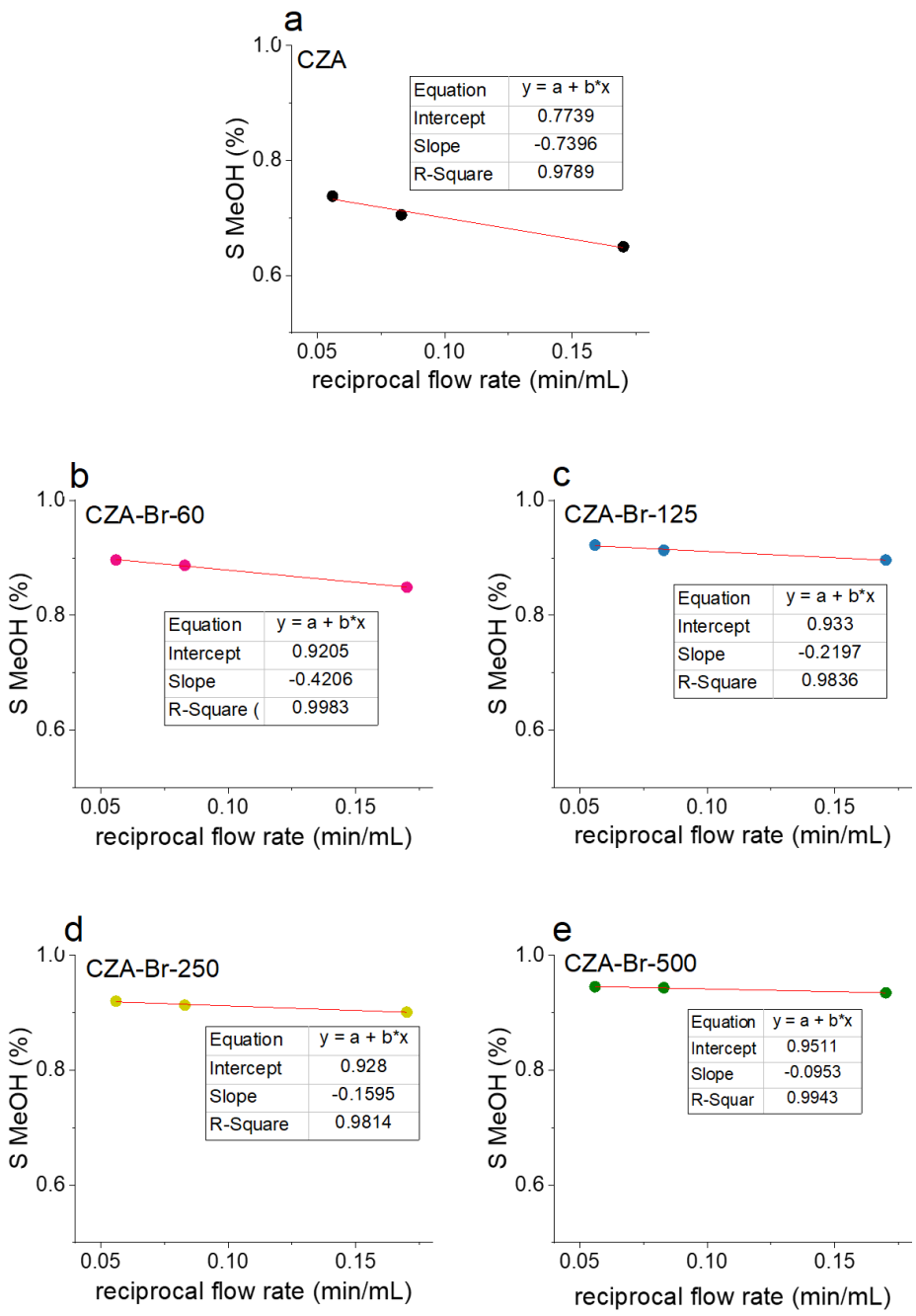

Figure 37: Plots of the selectivity to MeOH versus the reciprocal flow rates used to calculate the kinetic constants. a) CZA; b) CZA-Br-60; c) CZA-Br-125; d) CZA-Br-250; e) CZA-Br-500.

From the values of k_1' it can be stated that Bromine is a poison for the active site of MeOH production from CO_2. In fact, increasing the content of bromine, the kinetic constant is reduced up to 4.5 times. Nonetheless, the catalyst with a bromine content of 0.010 at. % showed a kinetic constant comparable to the one of the pristine CZA catalyst. Interestingly, the kinetic constant k_2'related to the RWGS reaction was affected to a higher extent by the presence of the Br. In fact, at a bromine concentration of 0.020 at.% the kinetic constant reduced ca. 25 times compared to the starting commercial catalyst. Moreover, calculating the ratio k_1'/k_2' it can be observed that in the presence of Br the MeOH formation is prevalent compared to the RWGS reaction (Figure 38a).

Also for the MeOH decomposition kinetic constant k_3, it was observed a decrease with increasing bromine content (Table 8). Likewise, in Figure 37 it can be clearly seen that the slope of the linear fit decreases with increasing Br content in the catalyst. The MeOH formation and the MeOH decomposition reaction rates depend from the concentration of CO_2 and of MeOH respectively. Nonetheless, the k_1'/k_3 ratio was calculated to compare the different bromine-based catalysts (Figure 38b). Interestingly, it was observed that below a Br concentration of 0.014 at.% the k_1'/k_3 ratio was almost the same as the CZA catalyst, while at higher Br contents it could be observed a suppression of the MeOH decomposition reaction. This suggests that only relatively high content of Br can suppress the MeOH decomposition reaction, and that in the presence of Br the produced CO is generated from the methanol decomposition reaction rather than from RWGS.

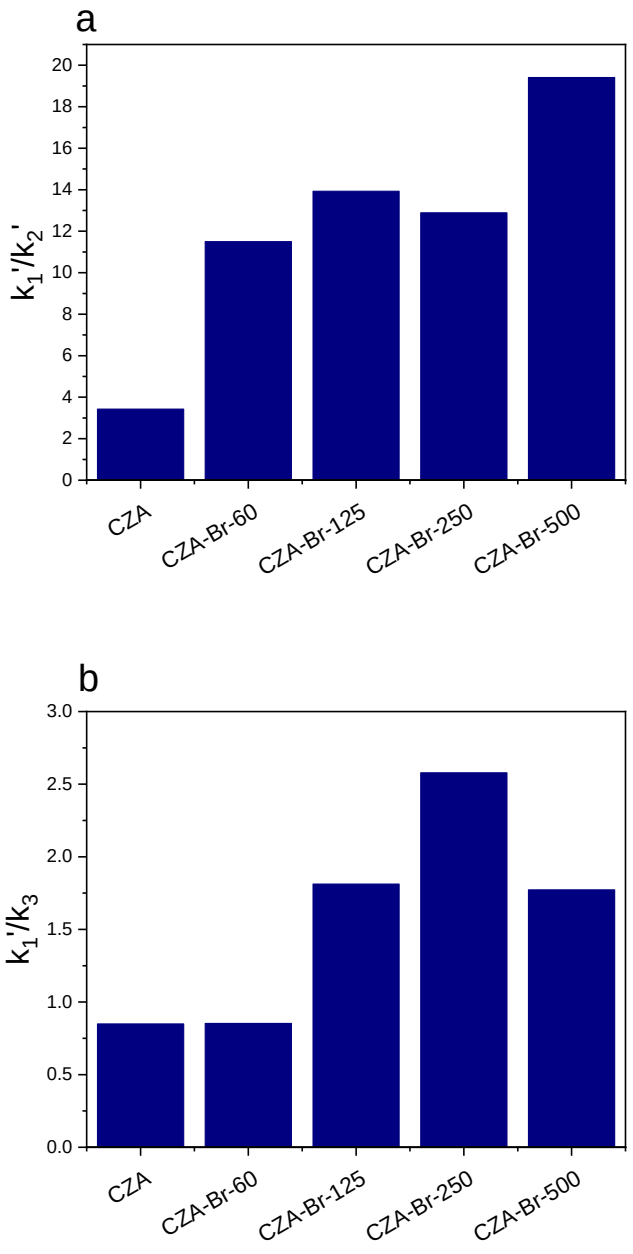

Figure 38: Evaluation of the kinetic constants of the reactions occurring during the CO_2 hydrogenation over the commercial catalyst and the Br-treated catalysts (200 °C; 20 bar). a) ratio between the MEOH synthesis and RWGS constants; b) ratio between the MeOH synthesis and MeOH decomposition constant.

Hydrogen isotopic exchange experiments (TAP) were performed to study the ability to activate hydrogen of the CZA, CZA-Br-60 and CZA-Br-500 catalysts. The normalized transient responses of D_2, HD, H_2 and Ar obtained upon pulsing D_2:H_2:Ar =1:1:1 mixture over different catalysts at 200°C are shown in Figure 39a. Here, the activity in H_2 activation is represented by

the ratio between the concentration of HD and the concentration of D_2 at the reactor outlet (Figure 39b).

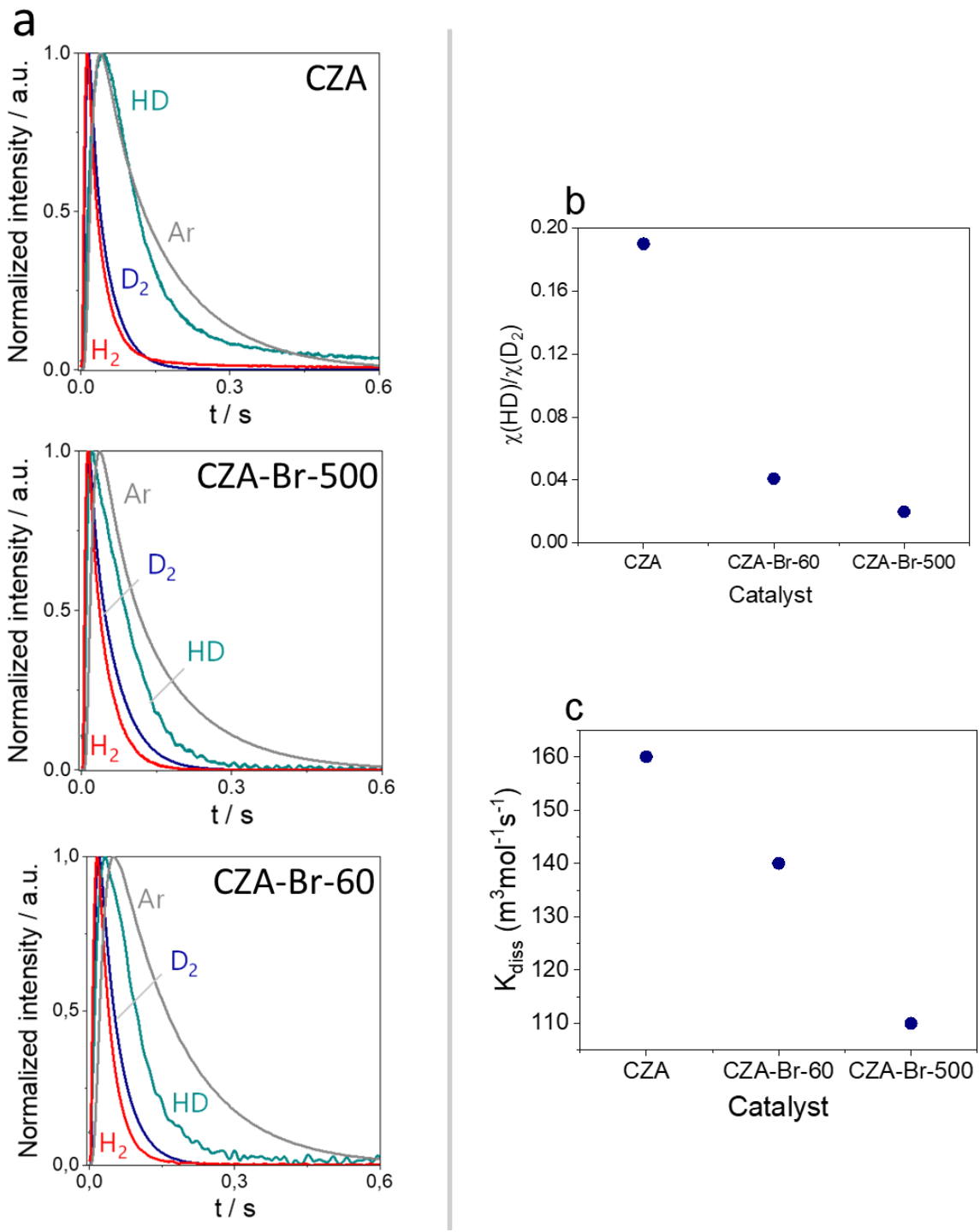

Figure 39: a) Normalized transient responses of D_2, HD, H_2 and Ar obtained upon pulsing D_2:H_2:Ar =1:1:1 mixture over the CZA, CZA-Br-60 and CZA-Br-500 catalysts at 200°C; b) evaluation of the hydrogen activation at 200 °C; c) evaluation of the CO_2 activation at 200 °C.

From the TAP experiments it was observed that the CZA catalyst has the higher H_2 activation activity, and this parameter decreases in the increasing concentration of Br. TAP CO_2 pulse experiments were also performed to study the influence of Br in the activation of CO_2, which was possible thanks to a microkinetic analysis of the experimental results. The analysis was carried out using a model that considers a reversible non-dissociative CO_2 adsorption followed by reversible dissociation of adsorbed CO_2 to adsorbed CO and O. Taking the constant of CO_2 dissociation to evaluate CO_2 activation (Figure 39b), it can be clearly seen that in the presence of Br the constant is reduced, and the higher the Br amount in the catalyst the lower the CO_2 activation. Generally, the results of TAP experiments to evaluate both H_2 and CO_2 activation are both consistent with the catalytic results shown in Figure 32.

3.3. Conclusions

Halobenzenes can be used to deposit halogen in the surface of Cu-based catalysts. In this way, the performance of the catalyst in the CO_2 hydrogenation to MeOH can be improved. Chlorine and Iodine do not affect significantly the selectivity to MeOH, while Bromine allows to improve it of 10 %. The content of Bromine influences the activity of the catalyst: the higher the Br concentration in the catalyst surface, the lower the catalyst activity. The increase in methanol selectivity was attributed to two phenomena. First, Br deactivates significantly the active sites responsible for the RWGS reaction, while the active sites for the MeOH synthesis can be preserved by reducing the Br amount. Second, the MeOH decomposition active sites are affected by the presence of Br: at high Br content the catalyst activity towards MeOH decomposition is much lower compared to that of the commercial catalyst.

3.4. References

(1) Zhong, J.; Yang, X.; Wu, Z.; Liang, B.; Huang, Y.; Zhang, T. State of the Art and Perspectives in Heterogeneous Catalysis of CO_2 Hydrogenation to Methanol. *Chem. Soc. Rev.* **2020**, *49* (5), 1385–1413. https://doi.org/10.1039/C9CS00614A.

(2) Navarro-Jaén, S.; Virginie, M.; Bonin, J.; Robert, M.; Wojcieszak, R.; Khodakov, A. Y. Highlights and Challenges in the Selective Reduction of Carbon Dioxide to Methanol. *Nat. Rev. Chem.* **2021**, *5* (8), 564–579. https://doi.org/10.1038/s41570-021-00289-y.

(3) Gao, P.; Li, F.; Zhang, L.; Zhao, N.; Xiao, F.; Wei, W.; Zhong, L.; Sun, Y. Influence of Fluorine on the Performance of Fluorine-Modified Cu/Zn/Al Catalysts for CO_2 Hydrogenation to Methanol. *J. CO_2 Util.* **2013**, *2*, 16–23. https://doi.org/10.1016/j.jcou.2013.06.003.

(4) Dybbert, V.; Fehr, S. M.; Klein, F.; Schaadt, A.; Hoffmann, A.; Frei, E.; Erdem, E.; Ludwig, T.; Hillebrecht, H.; Krossing, I. Oxidative Fluorination of Cu/ZnO Methanol Catalysts. *Angew. Chem.* **2019**, *131* (37), 13069–13073. https://doi.org/10.1002/ange.201811267.

(5) Krossing, I.; Fehr, S. M.; Nguyen, K.; Njel, C. Enhancement of Methanol Synthesis by Oxidative Fluorination of Cu/ZnO Catalysts-Insights from Surface Analyses. *ACS Catal.* **2021**, *11* (21), 13223–13235. https://doi.org/10.1021/acscatal.1c03735.

(6) Chen, S.; Zhang, J.; Song, F.; Zhang, Q.; Yang, G.; Zhang, M.; Wang, X.; Xie, H.; Tan, Y. Induced High Selectivity Methanol Formation during CO_2 Hydrogenation over a $CuBr_2$-Modified CuZnZr Catalyst. *J. Catal.* **2020**, *389*, 47–59. https://doi.org/10.1016/j.jcat.2020.05.023.

(7) Zhou, Y.; Trentesaux, M.; Marinova, M.; Chernyak, S.; Morin, J. C.; Dubois, M.; Eyley, S.; Thielemans, W.; Martin-Diaconescu, V.; Khodakov, A.; Zaffran, J.; Ordomsky, V. Identifying Metal-Halogen Bonding for Hydrogen-Induced Acid Generation in Bifunctional Catalysis. *ACS Catal.* **2023**, *13* (9), 6351–6364. https://doi.org/10.1021/acscatal.3c00845.

(8) Wu, D.; Zhang, S.; Hernández, W. Y.; Baaziz, W.; Ersen, O.; Marinova, M.; Khodakov, A. Y.; Ordomsky, V. V. Dual Metal-Acid Pd-Br Catalyst for Selective Hydrodeoxygenation of 5-Hydroxymethylfurfural (HMF) to 2,5-Dimethylfuran at Ambient Temperature. *ACS Catal.* **2021**, *11* (1), 19–30. https://doi.org/10.1021/acscatal.0c03955.

(9) Wu, D.; Wang, Q.; Safonova, O. V.; Peron, D. V.; Zhou, W.; Yan, Z.; Marinova, M.; Khodakov, A. Y.; Ordomsky, V. V. Lignin Compounds to Monoaromatics: Selective Cleavage of C−O Bonds over a Brominated Ruthenium Catalyst. *Angew. Chem. - Int. Ed.* **2021**, *60* (22), 12513–12523. https://doi.org/10.1002/anie.202101325.

(10) Wu, D.; Hernández, W. Y.; Zhang, S.; Vovk, E. I.; Zhou, X.; Yang, Y.; Khodakov, A. Y.; Ordomsky, V. V. In Situ Generation of Brønsted Acidity in the Pd-I Bifunctional Catalysts for Selective Reductive Etherification of Carbonyl Compounds under Mild Conditions. *ACS Catal.* **2019**, *9* (4), 2940–2948. https://doi.org/10.1021/acscatal.8b04925.

(11) Biesinger, M. C. Advanced Analysis of Copper X-ray Photoelectron Spectra. *Surf. Interface Anal.* **2017**, *49* (13), 1325–1334. https://doi.org/10.1002/sia.6239.

(12) Kamsuwan, T.; Guntida, A.; Praserthdam, P.; Jongsomjit, B. Differences in Deterioration Behaviors of Cu/ZnO/Al_2O_3 Catalysts with Different Cu Contents toward Hydrogenation of CO and CO_2. *ACS Omega* **2022**, *7* (29), 25783–25797. https://doi.org/10.1021/acsomega.2c03068.

(13) Kharchenko, A.; Zholobenko, V.; Vicente, A.; Fernandez, C.; Vezin, H.; De Waele, V.; Mintova, S. Formation of Copper Nanoparticles in LTL Nanosized Zeolite: Spectroscopic

Characterization. *Phys. Chem. Chem. Phys.* **2018**, *20* (4), 2880–2889. https://doi.org/10.1039/C7CP07650A.

(14) Nielsen, N. D.; Smitshuysen, T. E. L.; Damsgaard, C. D.; Jensen, A. D.; Christensen, J. M. Characterization of Oxide-Supported Cu by Infrared Measurements on Adsorbed CO. *Surf. Sci.* **2021**, *703*, 121725. https://doi.org/10.1016/j.susc.2020.121725.

(15) Schumann, J.; Kröhnert, J.; Frei, E.; Schlögl, R.; Trunschke, A. IR-Spectroscopic Study on the Interface of Cu-Based Methanol Synthesis Catalysts: Evidence for the Formation of a ZnO Overlayer. *Top. Catal.* **2017**, *60* (19–20), 1735–1743. https://doi.org/10.1007/s11244-017-0850-9.

(16) Ortner, N.; Zhao, D.; Mena, H.; Weiß, J.; Lund, H.; Bartling, S.; Wohlrab, S.; Armbruster, U.; Kondratenko, E. V. Revealing Origins of Methanol Selectivity Loss in CO_2 Hydrogenation over CuZn-Containing Catalysts. *ACS Catal.* **2023**, *13* (1), 60–71. https://doi.org/10.1021/acscatal.2c04480.

(17) Khodakov, A.; Yang, J.; Su, S.; Iglesia, E.; Bell, A. Structure and Properties of Vanadium Oxide-Zirconia Catalysts for Propane Oxidative Dehydrogenation. *J. Catal.* **1998**, *177* (2), 343–351. https://doi.org/10.1006/jcat.1998.2143.

Chapter 4

Decisive influence of SAPO-34 zeolite on light olefin selectivity in methanol-meditated CO_2 hydrogenation

4.1 Introduction

As already discussed in Chapter 1, the LO synthesis from CO_2 is a sustainable alternative pathway for the production of this high demand platform molecules. There are two main routes for the direct synthesis of LO from CO_2. The first one is based on Fischer-Tropsch synthesis (FTS), which involves a two-step: first, the reverse water-gas-shift (RWGS) reaction, i.e., CO_2 conversion to CO, and then CO is hydrogenated to hydrocarbons via FTS. Nonetheless, the selectivity to LO in the FTS-based route is limited by Anderson-Schultz-Flory kinetics; ~60% of light olefins in the hydrocarbon fraction being the upper limit. Moreover, a significant amount of methane is produced which is a highly undesirable product. The second pathway is the "tandem" methanol-mediated CO_2 hydrogenation.

To produce LO directly from CO_2 via the in-situ production of MeOH, bifunctional catalysts are used, which contain both methanol synthesis and methanol-to-olefins (MTO) components.[1] The active species in the bifunctional catalysts used for the methanol synthesis are metal oxides such as ZnO, Cr_2O_3, In_2O_3 or Ga_2O_3, while the acid sites of zeolite (mostly SAPO-34) are responsible for MTO. Because of their strong hydrogenation activity, copper-based systems show noticeably lower LO selectivity than the counterparts containing zinc or indium oxides.[2] At the same time, the zeolite acid sites may be involved in the hydrogen transfer reactions.[3]

The main challenge in the CO_2 hydrogenation to LO is to achieve high target product yield, which requires maintaining high LO selectivity at high CO_2 conversion. Hence, a better understanding of how to control these two parameters is important: the analysis of the correlation between selectivity and conversion comes in help, as it allows to interpret the reaction mechanism, and to understand how to improve the selectivity and yield of target products.[4–6]

The work presented in this chapter has two objectives: the first one is to analyze and understand the selectivity-conversion correlations for CO_2 hydrogenation to LO; the second one is to elucidate the role of each component of the bifunctional catalysts in this reaction. To achieve our objectives, we carried out a comprehensive analysis of metal oxide catalysts with diverse elemental compositions and phases. These oxide catalysts were subsequently mixed with four distinct SAPO-34 zeolites. The CO_2 conversion at a fixed temperature was variated by changing the space velocity, pressure and catalyst composition. Ethylene hydrogenation was used as a model reaction to identify the role of the two components of the bifunctional catalysts in secondary LO reactions. The Temporal Analysis of Products (TAP) provided mechanistic and kinetic insights into activation (adsorption/desorption/dissociation) of H_2 and CO_2 over metal-oxide catalysts. Our findings revealed that the CO-free LO selectivity was exclusively influenced by the zeolite, whereas the overall rate of CO_2 hydrogenation and CO selectivity were primarily governed by the metal oxide component.

4.2. Results and discussion

4.2.1. Characterization of the methanol synthesis component

The XRD patterns of the calcined catalysts are given in Figure 40. Only broad signals attributed to the cubic ZrO_2 phase was detected in $ZnZrO_x$ and $InZrO_x$ (Figure 40a). No distinct patterns attributed to Zn and In were detected. This suggests that the Zn or In cations are uniformly distributed within the zirconia lattice. Such structures commonly occur in the catalysts prepared by co-precipitation and corresponds to the solid solution of Zn and In in zirconia[7]. The crystallite size of the ZrO_2 phase in these two samples calculated using the Scherrer equation was about ~4-6 nm. In the $ZnAlO_x$ and $ZnGaO_x$ catalysts, the $ZnAl_2O_4$ and $ZnGa_2O_4$ spinel structures were respectively detected (Figure 40b). In the case of ZnAlOx the crystallite size of the spinel structure was smaller compared to ZnGaOx. The $ZnCrAlO_x$ and $ZnCeZrO_x$ catalysts showed the presence of ZnO, $ZnAl_2O_4$ and $ZnCr_2O_4$ in the first case (Figure 40c), and of ZnO and $Zr_{0.86}Ce_{0.14}O_2$ in the second case (Figure 40d). They exhibited broad XRD peaks corresponding to crystallites of ~3-4 nm. The Mn/ZrO_2 catalyst showed the peaks of monoclinic Baddeleyite-like ZrO_2 phase corresponding to the zirconia support and those of pyrolusite MnO_2(Figure 40e). In $MnBi/ZrO_2$, cubic Bi_2O_3 oxide and mixed bismuth-manganese cubic $Bi_{12}MnO_{20}$ oxide were identified along with monoclinic ZrO_2 (Figure 40f). Finally, after the impregnation with Zn, the Zr-MOF structure changed significantly, and the Zn/Zr-MOF showed a prevalently amorphous structure. The latter catalyst was analyzed directly as mixed with the zeolite component. It can be observed from Figure 40g that the main observable signals belong to the zeolite, while the diffraction pattern of the MOF support is barely noticeable.

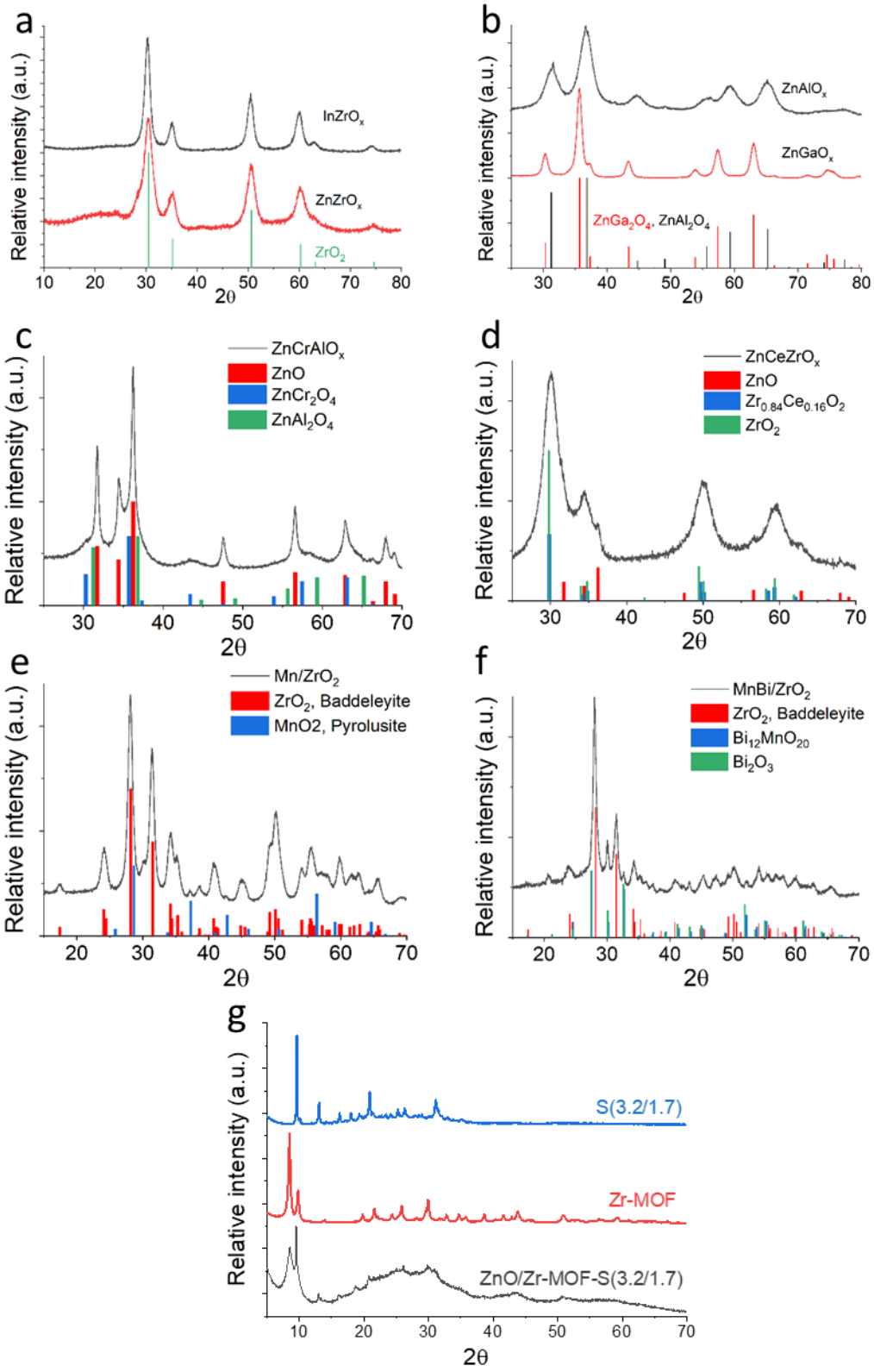

Figure 40: XRD patterns of the studied catalysts: a)ZnZrOx and InZrOx; b)ZnAlOx and ZnGaOx; c)ZnCrOx; d)ZnCeZrOx;e) MnBi/ZrO_2; f) Mn/ZrO_2 ; g) Zn/Zr-MOF-S(3.2/1.7) compared with Zr-MOF and S(3.2/1.7).

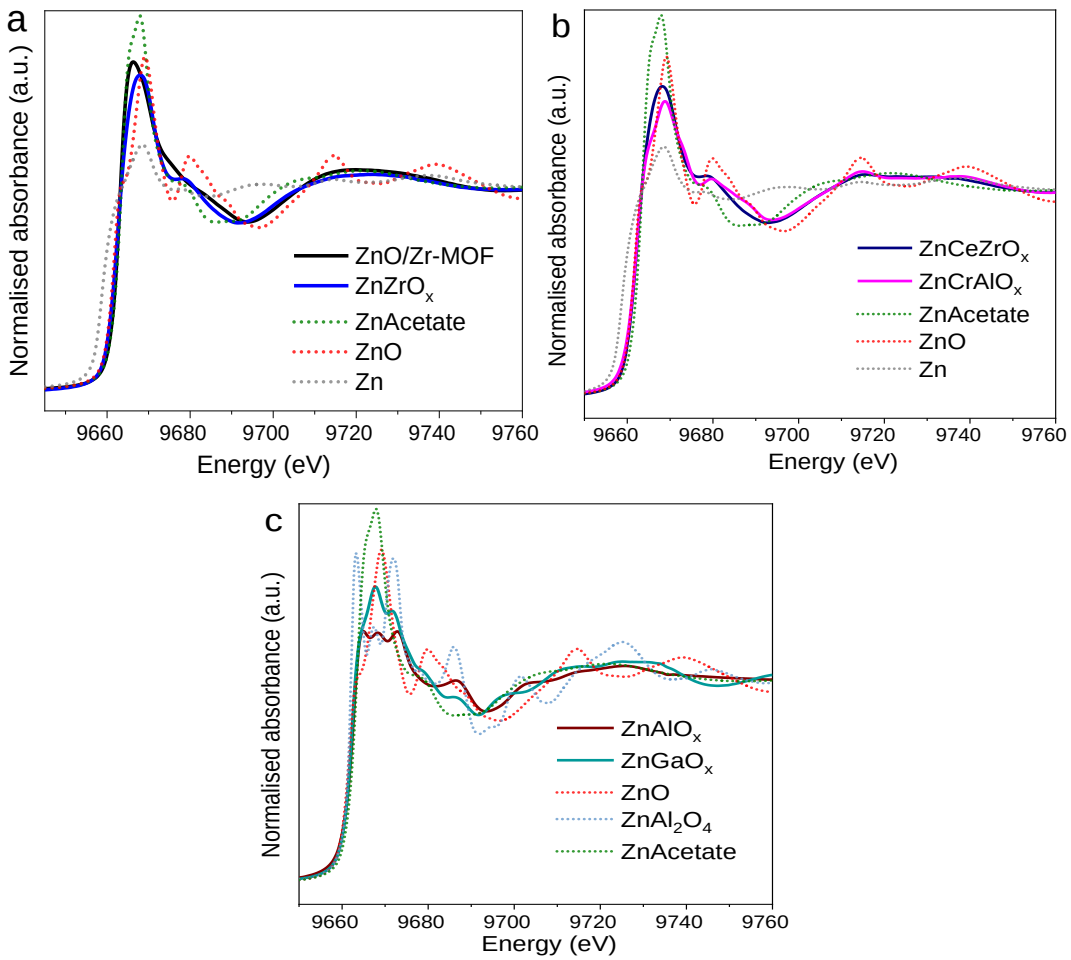

Figure 41 : XANES spectra of Zn-containing oxide-based samples at Zn K-edge. a)$ZnZrO_x$ and Zn/Zr-MOF; b)$ZnCeZrO_x$ and $ZnCrAlO_x$; c) $ZnAlO_x$ and $ZnGaO_x$.

The XANES spectra for the Zn-based catalysts and of some reference Zn compounds are given in Figure 41. The XANES spectra at Zn K-edge are consistent with the XRD data. The $ZnZrO_x$ and ZnO/Zr-MOF are characterized by the XANES spectra similar to that of isolated zinc cations in organic salts. The main peak at 9669 eV corresponds to the transition from Zn 1s to Zn 4p+O 2p hybridized states of the conduction band.[8] The XANES spectra of $ZnCeZrO_x$ and $ZnCrAlO_x$ are similar to that of ZnO. Note however that the spectrum of $ZnCrAlO_x$ contains a component at 9672 eV typical of Zn in the spinel structure. This correlates with the XRD patterns, which are indicative of the presence of both ZnO and $ZnCr_2O_4$ phases. In the XANES spectra of $ZnAlO_x$ and $ZnGaO_x$, the white line consists of three components showing the presence of both spinel and ZnO.

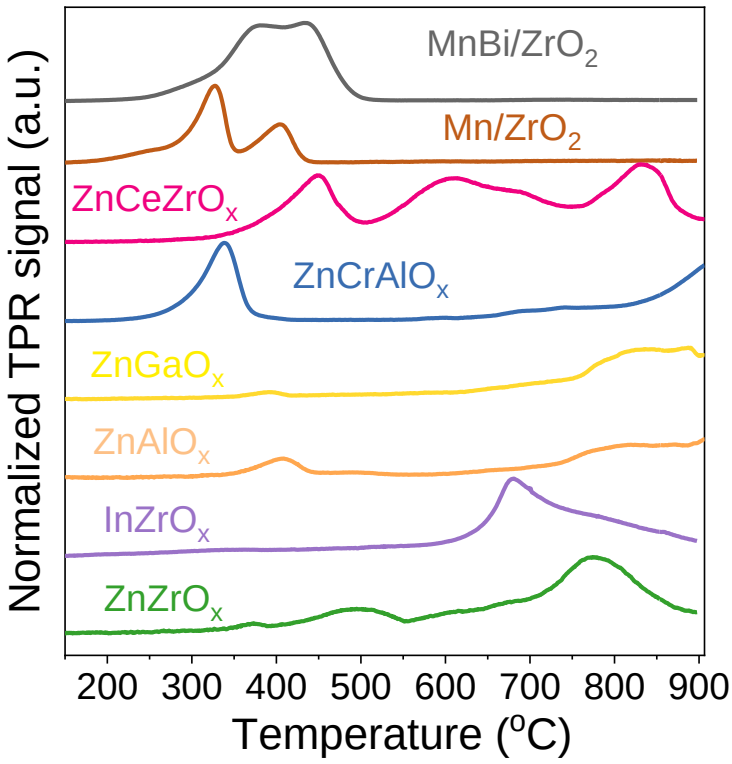

Figure 42 : TPR profiles of the studied oxide components.

The TPR results are presented in Figure 42. The profiles of H_2 consumption over $ZnZrO_x$, $InZrO_x$, $ZnGaO_x$ and $ZnAlO_x$ contain weak low-temperature peaks, which correspond to the surface oxide reduction and formation of oxygen vacancies.[9] The main reduction peaks of $ZnZrO_x$ and $InZrO_x$ appear at elevated temperatures, which confirms high dispersion and strong interaction of Zn and In cations within the zirconia matrix. XRD and XANES suggest the presence of spinel-type oxides in the $ZnGaO_x$ and $ZnAlO_x$ samples, which may explain their difficult reduction. In opposite to these systems, because of the presence of zinc oxide clusters, $ZnCeZrO_x$ and $ZnCrAlO_x$ start to reduce at a temperature below 500 °C. In Mn/ZrO_2, Mn oxide is reduced in three steps occurring at 245, 327 and 405 °C. The first weak peak can be assigned to the reduction of either residual nitrate or weakly-bonded MnO_2. The main two peaks could relate to the reduction of MnO_2 to Mn_2O_3 and then to Mn_3O_4.[10] In the $Mn\text{-}Bi/ZrO_2$ catalyst, two peaks are shifted to higher temperatures due to the presence of Bi oxide. The peaks overlap because of the simultaneous reduction of Bi_2O_3, MnO_2 and mixed Bi-Mn oxide.

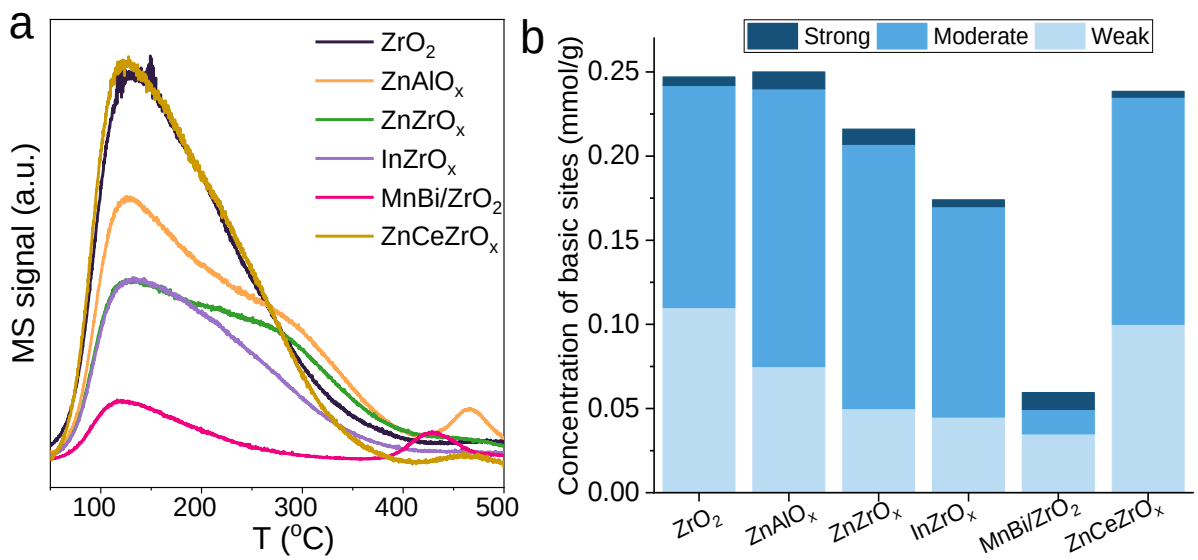

Figure 43 : CO_2-TPD profiles of the studied oxide components (a) and concentration of different basic sites calculated from the CO_2-TPD data (b).

The signals in the CO_2-TPD patterns of the metal oxide catalysts can be divided into three main groups: below ~200ºC, between 200-380ºC and above 380 °C (Figure 43a). According to the literature, they correspond to CO_2 desorption from weak, moderate and strong basic sites, respectively.[11] Pure zirconia and $ZnCeZrO_x$ show very intense low-temperature CO_2-TPD peaks, while the $ZnAlO_x$ and $ZnZrO_x$ samples demonstrate noticeable shoulders at 200-380°C, which correspond to moderate basicity. Strong basic sites were found in $ZnAlO_x$ and $MnBi/ZrO_2$. The amounts of weak, moderate, and strong basic sites calculated from CO_2-TPD profiles are displayed in Figure 43b.

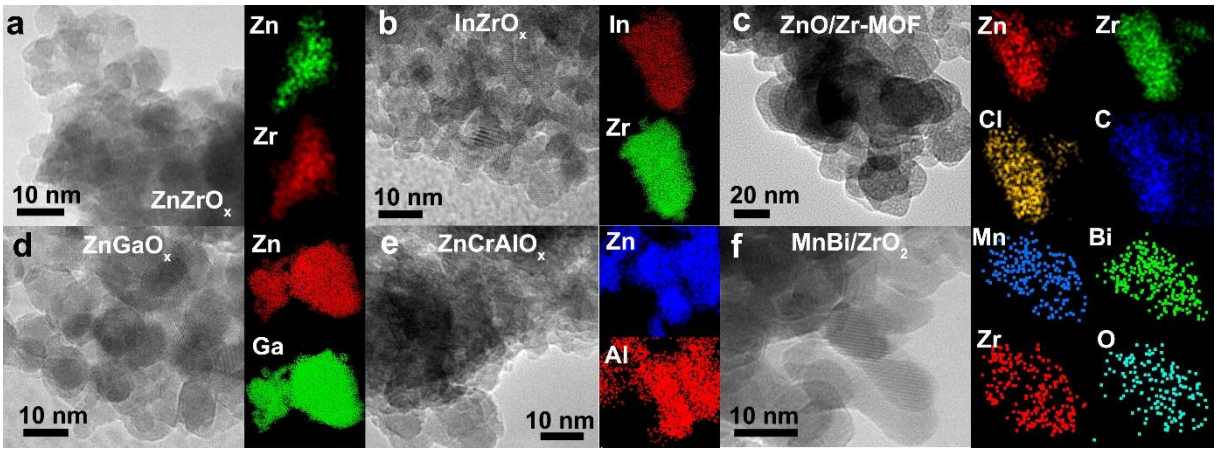

Figure 44 : TEM images and EDX mapping of the metal oxide components of bifunctional catalysts: $ZnZrO_x$ (a), $InZrO_x$ (b), ZnO/Zr-MOF (c), $ZnGaO_x$ (d), $ZnCrAlO_x$ (e), and $MnBi/ZrO_2$ (f).

The TEM analysis allowed to evaluate the nanoparticle morphology in both impregnated and co-precipitated catalysts (Figure 44). The size of particles was in the range of 5-20 nm, which correlates with the XRD data. Uniform metal distribution was detected by EDX in the $ZnZrO_x$, InZrOx, ZnO/Zr-MOF and spinel $ZnGaO_x$ catalysts, while Bi and Mn separate localizations were observed in $BiMn/ZrO_2$. In ZnO/Zr-MOF, noticeable carbon and chlorine signals were detected which originated from the MOF incomplete decomposition (Figure 44c). Chlorine presence can be due to the use of zirconium chloride for MOF synthesis. Since halogens are catalytic poisons, this may explain the low CO_2 conversion over ZnO/Zr-MOF that will be presented further in this chapter. Also, in the $ZnCrAlO_x$ sample EDX showed a non-uniform distribution of Zn over alumina.

4.4.2. SAPO-34 characterization

The properties of the four chosen SAPO-34 zeolites are given in Table 9.

Table 9 : Characteristics of SAPO-34 samples.

Zeolite	Crystal size (µm)	Acid density (mmol/g)	Fraction of strong acid sites*	BET surface area, (m^2/g)	Pore volume (cm^3/g)	Supplier
S(3.2/1.7)	3.2	1.67	0.74	>550	0.27	ACS Materials
S(3.2/0.6)	3.2	0.61	0.62	445	0.22	NanKai
S(1.6/0.9)	1.6	0.95	0.63	438	0.26	NanKai
S(0.5/1.1)	0.5	1.14	0.50	-	-	UOP

*The density of strong acid sites was obtained by integrating the NH_3 TPD peaks at temperatures >280°C

The XRD patterns of SAPO-34 samples are shown in Figure 45. The most intense diffraction peaks for all the samples can be attributed to the SAPO-34 chabazite-type crystalline phase[12–14]. Interestingly, the XRD peaks are slightly broader in S(1.6/0.9) and S(0.5/1.1) samples, indicating a smaller zeolite crystallite size. Moreover, XRD patterns of S(1.6/0.9) and S(0.5/1.1) exhibit additional low intense peaks, which were attributed to the presence of minor amounts of AlPO-34 phase[14]. AlPO-34 has a chabazite-like structure but does not contain hydroxyl groups with strong acidity. Thus, is not expected to contribute to the reaction. Moreover, the S(0.5/1.1) sample also displays a broad band at 25 ° which is characteristic of a large fraction of amorphous phase.

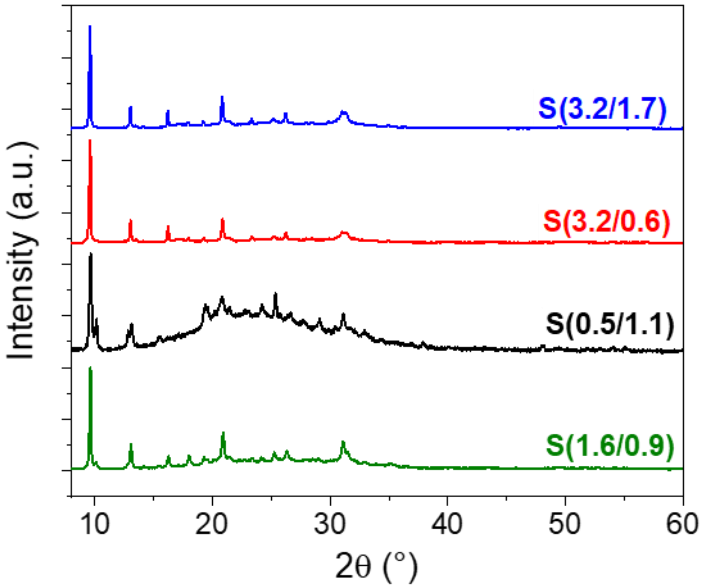

Figure 45 : XRD pattern of the studied SAPO-34 zeolites.

The XRD data are consistent with the SEM results. The representative SEM images of SAPO-34 zeolites are shown in Figure 46a-d, while the histograms of crystallite size are given in Figure 46e-h. Similar crystalline morphology with ~3.15-3.16 µm cubic particles was observed for S(3.2/1.7) and S(3.2/0.6) (Figure 46a,e and Figure 46b,f, respectively). Please observe that even though the particle size is similar, Table 9 shows that S(3.2/0.6) has a decreased BET surface area and porosity compared to S(3.2/1.7). This can be due to partial plugging of micropores of S(3.2/06).

The crystallite size for S(1.6/0.9) was about 1.58 µm (Figure 46c,g), while very small (< 1 µm) crystallites were detected for S(0.5/1.1) samples with an average size of 0.46 µm (Figure 46d,h). Moreover, SEM images of S(0.5/1.1) display agglomerates of submicronic SAPO-34 crystallites together with a large amount of amorphous phase.

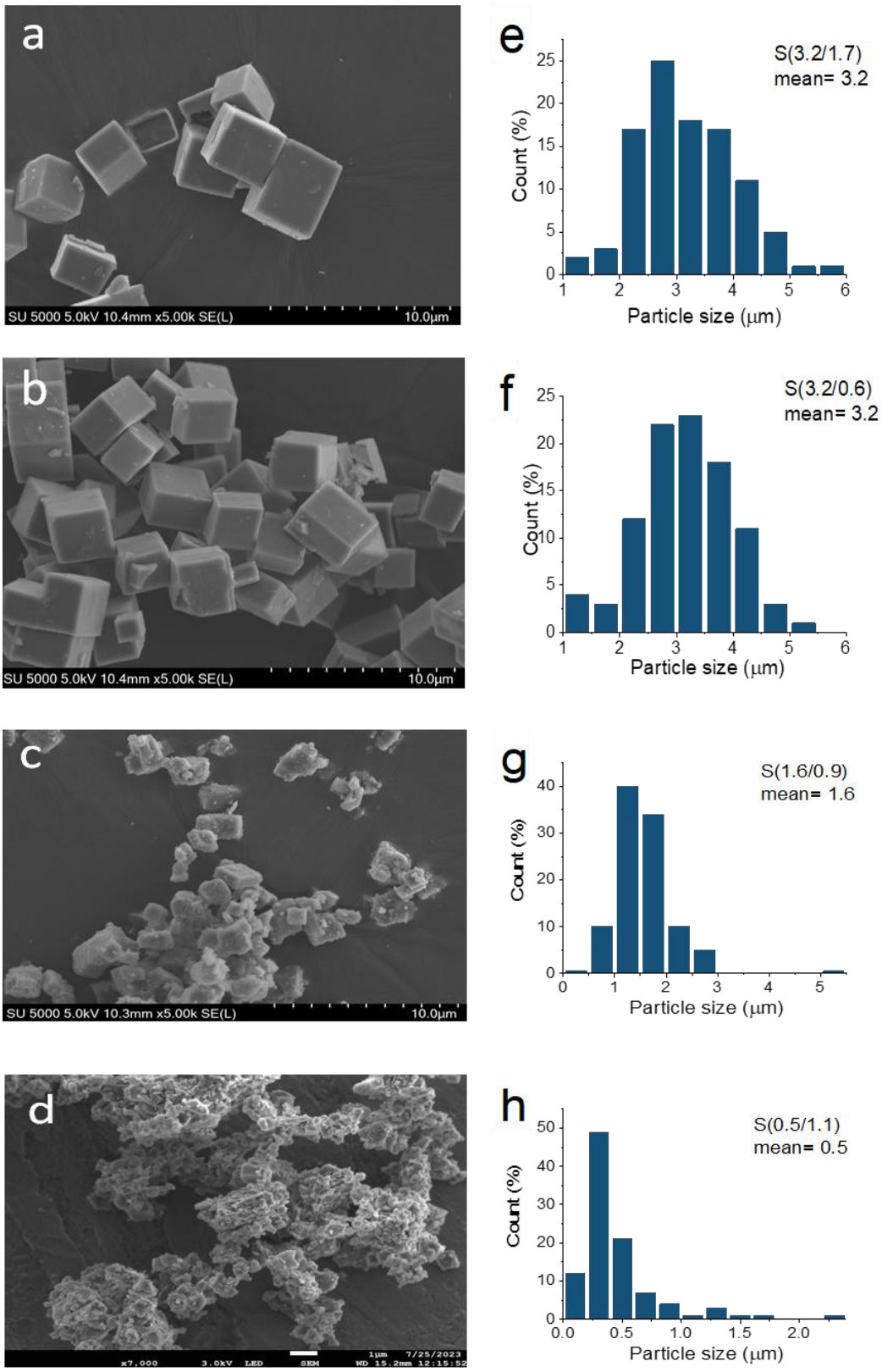

Figure 46 : SEM images of SAPO-34 zeolites (a, b, c, d) and particle size distribution (e, f, g, h). (a, e) S(3.2/1.7); (b, f) S(3.2/0.6); (c, g) S(1.6/0.9); (d, h) S(0.5/1.1).

The acidity of SAPO-34 zeolites was studied by NH_3-TPD. The total amount of acid sites and fraction of strong acid sites calculated from integration of the TPD profiles is given in Table 9**.** The TPD profiles (Figure 47) show peaks in two main regions: at 150-300°C which corresponds to the ammonia desorption from weak acid sites (AS), while the peaks in the 300−500 °C range are assigned to the desorption from strong AS[15]. The SAPO-34 samples differ from each other by the total amount of AS, while the ratio between strong and weak AS remains almost the same, with an exception of S(3.2/1.7), where the fraction of strong AS is notably higher. The highest amount of strong acid sites was detected in S(3.2/1.7) followed by S(0.5/1.1) and S(1.6/0.9) sample. The smallest amount of acid sites was observed in S(3.2/0.6).

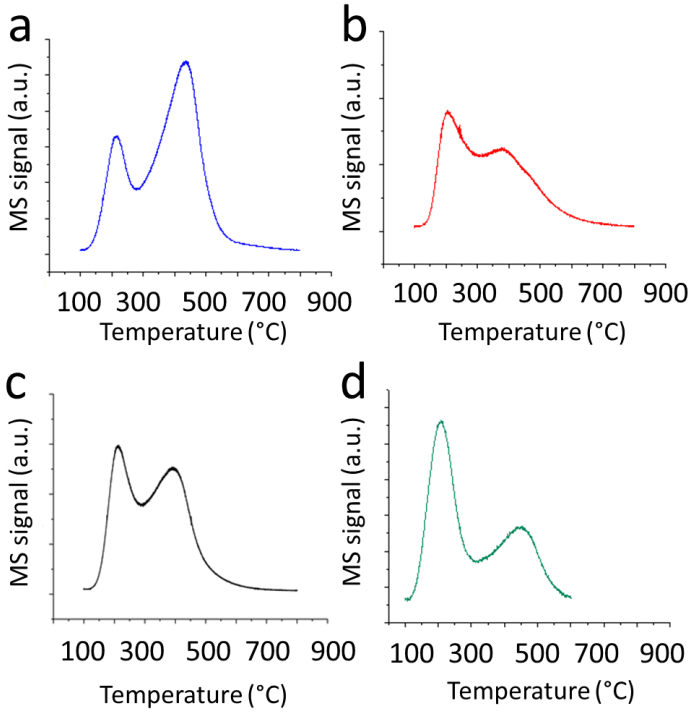

Figure 47 : NH_3-TPD profiles of SAPO-34 zeolites: (a) S(3.2/1.7); (b) S(3.2/0.6); (c) S(1.6/0.9); (d) S(0.5/1.1).

The ^{29}Si MAS NMR spectra of all SAPO-34 samples (Figure 48a) show the main peak near -89.8 ppm, which corresponds to the isolated silicon atoms surrounded by aluminum through the OH bridges[16]. The peaks at -93.5 (3Al), 99.0 (2Al), and -104.5 (1Al) are related to

the silicon atoms bonded via oxygen with one, two, and three other silicon atoms, respectively[17,18]. The peaks at -109.7 and -113.3 ppm correspond to the silicon bonded with other silicon atoms. The peak (or shoulder) at ~83 ppm can be assigned with the defective or hydrated Si. Spectra for S(3.2/1.7) and S(3.2/0.6) look similar and contain silicon in all the above-mentioned configurations. S(0.5/1.1) shows a slightly more intensive component of hydrated/defective Si, while the intensity of the other peaks is lower than those for S(3.2/1.7) and S(3.2/0.6). In S(1.6/0.9), most Si atoms are either in an isolated configuration or in a defective state.

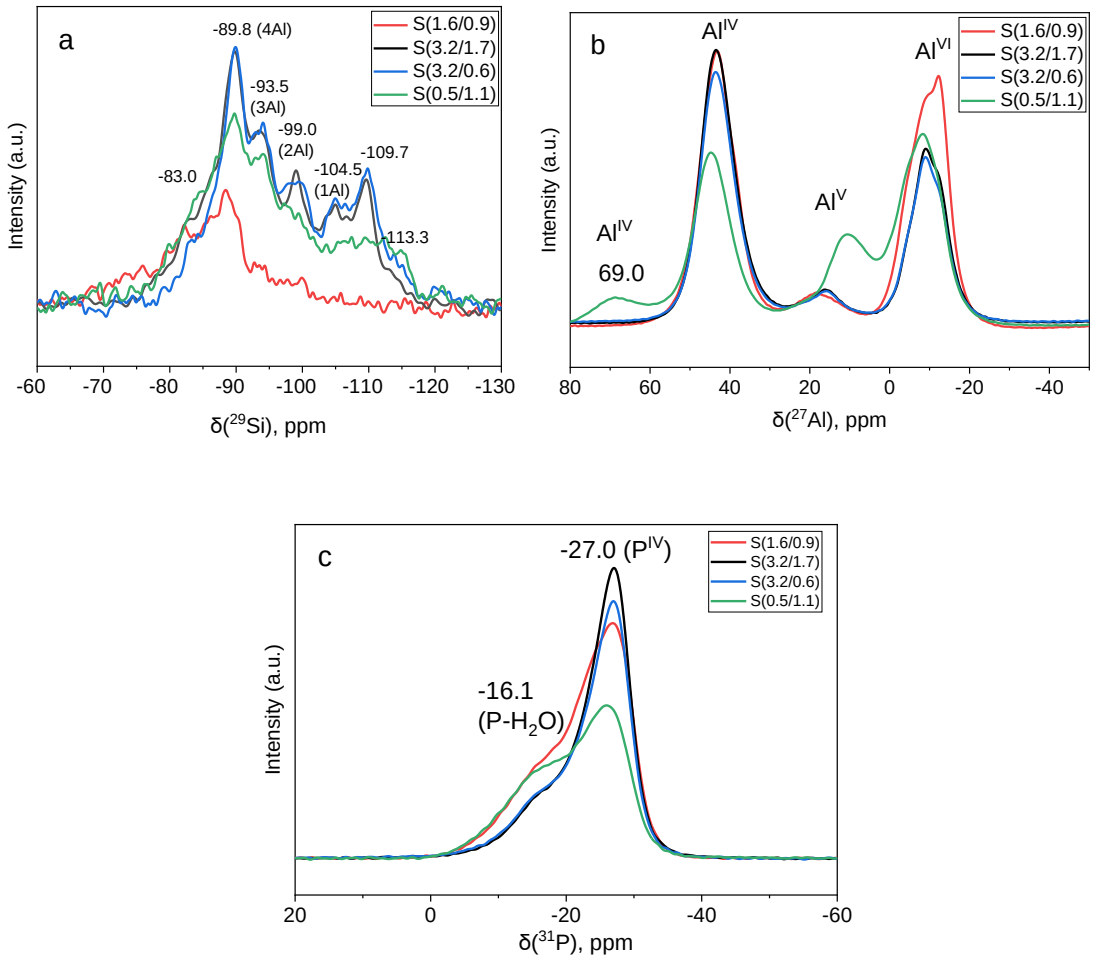

Figure 48 : MAS NMR spectra of different SAPO-34 samples: (a) [29] Si MAS NMR; (b) ^{27}Al MAS NMR; (c) ^{31}P MAS NMR.

The ^{27}Al NMR spectra of all the samples (Figure 48b) show a peak in the region from -9 to -12.5 ppm which corresponds to the octahedral coordination of Al in the SAPO-34 zeolite extra-framework species[19]. The intensity of this peak is higher for S(1.6/0.9), which indicates its higher hydration degree. A peak at ~40 ppm is assigned with the tetrahedral Al atoms in the SAPO zeolite structure and that at ~18 ppm is usually ascribed to the penta-coordinated ones. The spectrum shape of S(0.5/1.1) sharply differs from those of other samples and shows the strong additional components at 10 and 69 ppm. The peak at 10 ppm may correspond to either ^{V}Al in SAPO-34 structure or to ^{VI}Al in the alumina while that at 69 ppm – to the ^{IV}Al in Al-enriched materials where the aluminum atoms are coordinated by other Al in the first coordination shell[20–22]. As a result, most likely two different phases present in this sample: SAPO-34 and Al-enriched one, possibly small amounts AlPO-34 also detected by XRD.

The ^{31}P NMR spectra (Figure 48c) display the main peak at -27 ppm, which corresponds to a single P(4A1) environment, while the shoulder at -16.1 has been assigned to the P-OH fragments. [19,23]

The simultaneous presence of defective silicon, octahedral aluminum, and hydrated phosphorus sites is evidence of the greater defectivity of S(1.6/0.9) and S(0.5/1.1). Lower Si content, absence of silicon islands and a high fraction of defects result in the reduced acidity of S(1.6/0.9).

4.2.3. CO_2 hydrogenation

Initially, to evaluate the selectivity-conversion correlations, and as a consequence to identify general trends in the CO_2 hydrogenation to LO, the bifunctional catalysts studied were composed by a variable metal-oxide phase, mixed with the same SAPO-34 zeolite (S(3.2/1.7)).

The weight ratio of 1:1 was used for most of experiments. The catalytic performance was measured at 375°C, pressure of 20-30 bar and WHSV of 1-3 NL/g_{cat}/h.

Pure zirconia was tested in the same conditions mixed with SAPO-34 but the conversion was ~3% with >90% of CO selectivity. Such low activity in hydrogenation despite the high CO_2 dissociation ability is caused by the absence of a hydrogenation component (Zn or In oxide or metallic particle).

The determined dependences of the selectivity to LO and CO on the CO_2 conversion measured for S(3.2/1.7)-derived metal oxide catalysts are shown in Figure 49.

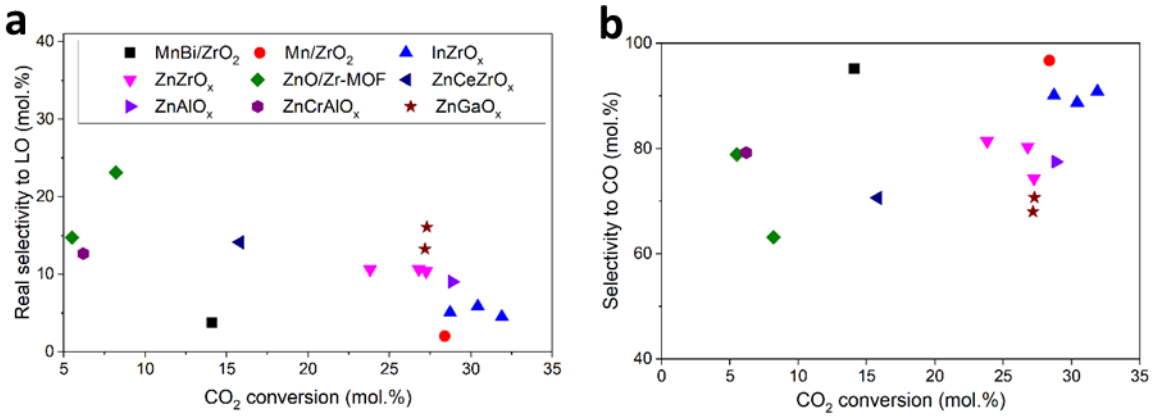

Figure 49 : Selectivity to LO (a) and to CO (b) towards CO2 conversion. The catalysts mentioned are composed by different metal oxides mixed with S(3.2/1.7) in 1:1 weight ratio.

Only very rough trends were observed: higher conversion slightly increases S_{CO}, but slightly decreases S_{LO}. The scattering of the data was high. Previously, a slight decrease in LO selectivity with an increase in CO_2 conversion has been observed in the CO hydrogenation to LO over metal-oxide-zeolite bifunctional catalysts[24,25].

The reason why the trends in Figure 49 are not straightforward can be explained by considering the main reaction steps of the methanol-mediated CO_2 hydrogenation to LO: (1) reversible synthesis of MeOH from CO_2, (2) RWGS as a side process, and (3) MeOH conversion to hydrocarbons (Figure 50a). Moreover, at low temperatures (~200°C), CO can also be produced by the decomposition of methanol. This reaction pathway, however, might be less influent at high reaction temperatures. [26] To put it in another way, the CO_2 conversion value includes also the produced CO, which does not take part in the hydrocarbon production. As a result, it might be more interesting to evaluate the selectivity/conversion correlation considering only the CO_2 molecules converted to hydrocarbons, hence the total hydrocarbon yield.

Figure 50b,c shows the dependences of the CO-free selectivity to LO and LP fractions on the CO_2-related yield of hydrocarbons. Again, the data used were related to the catalysts prepared mixing S(3.2/1.7) with the different metal oxides. It is clearly seen that the CO-free selectivity to LO decreases when the yield of HC increases. At the same time, the CO-free selectivity to LP increases with increasing the HC yield. It is worth noting that there were no dependences of methane and C_{5+} selectivity on the HC yield (Figure 50d,e).

In general, a decrease in the CO-free LO selectivity with the CO_2 or CO conversion can be attributed to secondary LO transformation to LP.[27] In the present study, a similar dependence of LO selectivity on HC yield was established for the numerous catalysts of different structures and compositions. Increasing hydrocarbon yield results in the secondary LO-to-LP transformation and, hence, limits the maximum LO yield.

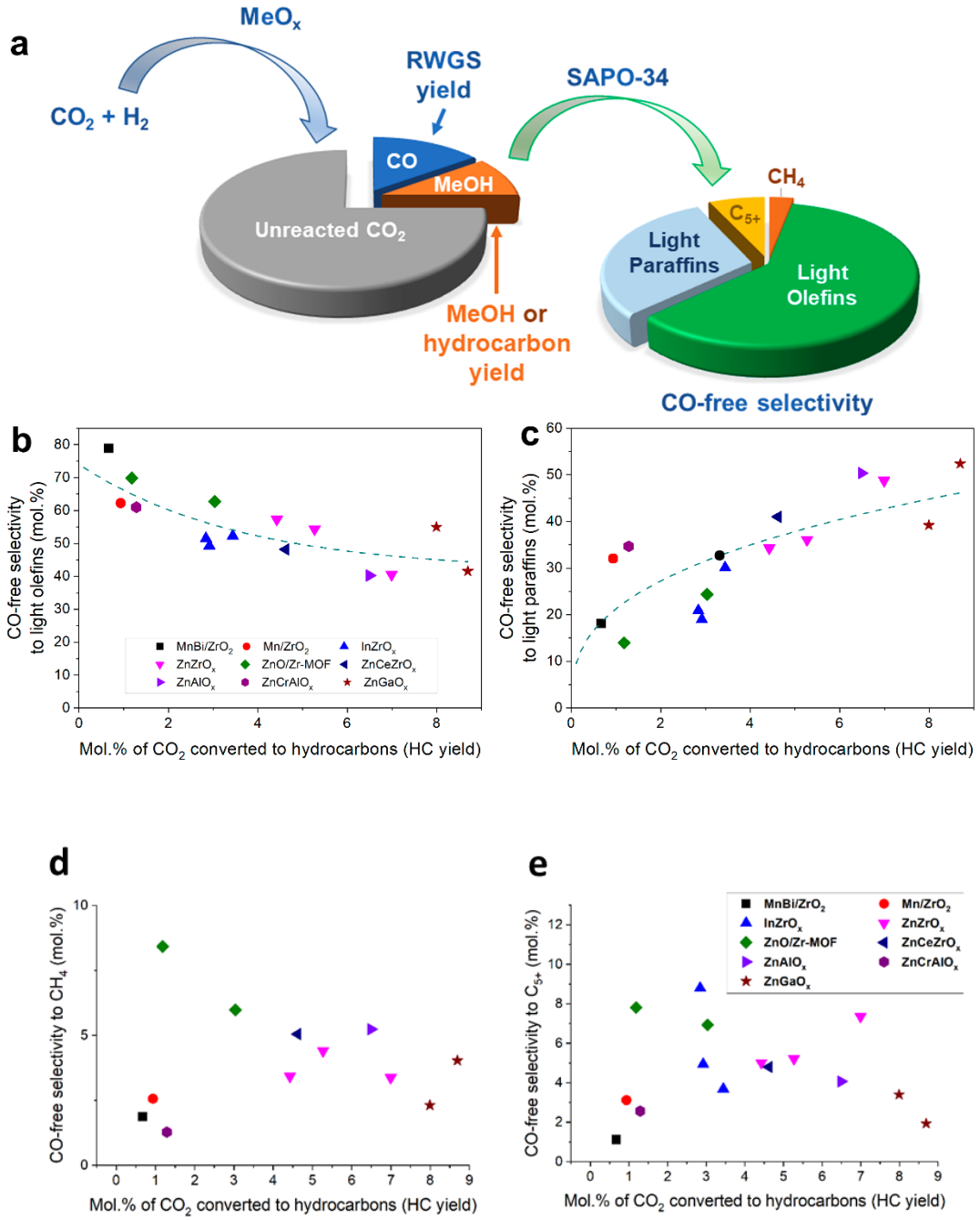

Figure 50 : Reaction pathway for the CO_2 hydrogenation to LO over bifunctional catalyst (a); dependences of CO-free selectivity to LO (b), LP (c), CH4 (d), and C_5+ species (e) on the hydrocarbon (HC) yield during the reaction at CO_2:H_2 = 1:3 and 375°C. The data related to bifunctional catalysts composed by different metal oxides mixed with S(3.2/1.7) in 1:1 weight ratio.

4.2.4 Function of metal oxide

Figure 50b suggests that the choice of metal oxide in bifunctional catalysts does not strongly affect the selectivity to LO. To confirm this, we analyzed mechanistic and kinetic aspects of H_2 and CO_2 activation over metal-oxide catalysts using temporal analysis of products (TAP) operating with sub-millisecond resolution[28]. When a mixture of H_2 and D_2 was pulsed, HD was detected at the reactor outlet. This was due to the catalysts action in breaking H-H and D-D bonds and form a new H-D bond. Although the catalysts differ in their ability to activate hydrogen as reflected by the ratio of HD/D_2 (Figure 51a), no obvious effect of this catalyst property on the paraffin/olefin ratio determined from CO_2 hydrogenation tests could be established (Figure 51b). Furthermore, no obvious trend was observed between relative HD content and CO_2 conversion (Figure 51b). Thus, it can be proposed that the catalyst ability to activate hydrogen is not a determining factor for both methanol synthesis rate and secondary LO conversion.

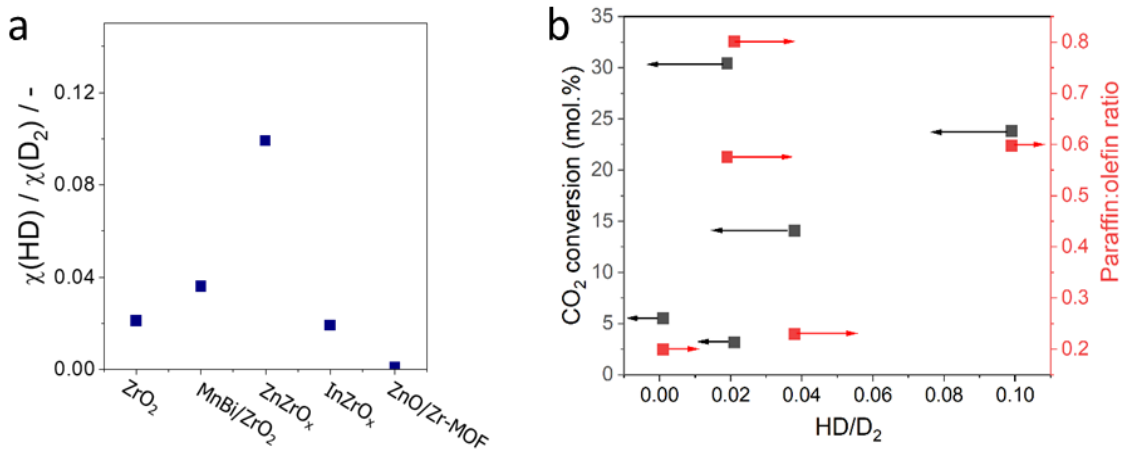

Figure 51 : TAP results: hydrogen activation ability of the different metal-oxide systems (a); effect of hydrogen activation ability on the CO_2 conversion and paraffin/olefin selectivity ratio (b).

It was previously shown that water could be a poison for the direct olefin hydrogenation over zinc oxide.[29] Since both methanol production and MTO process imply the release of substantial amounts of water, LO secondary hydrogenation could be strongly inhibited in the conditions of the tandem process. In addition to water, the presence of CO_2 can be also crucial for the LO secondary hydrogenation. To prove this suggestion, we investigated ethylene hydrogenation over $ZnZrO_x$ and S(3.2/1.7) in the absence and in the presence of added water or CO_2. In the absence of water and CO_2, ethylene conversion occurs over both metal-oxide catalyst and zeolite but the hydrogenation rate over the former is much higher than that over the latter (Figure 52). In addition to ethane, the conversion of ethylene on SAPO-34 also led to the production of C_{3+} hydrocarbons from the oligomerization of ethylene and the isomerization/cracking of long chain olefins.[24,30]

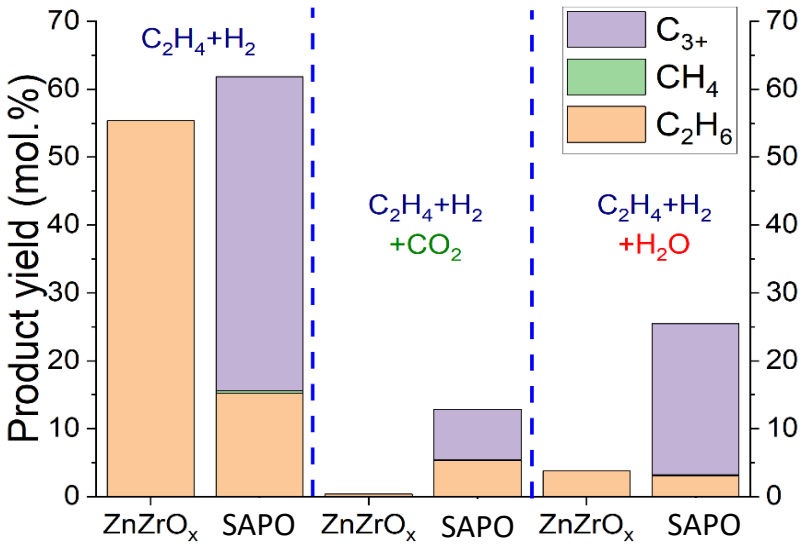

Figure 52 : Ethylene model hydrogenation results: effect of water and CO_2 presence on the ethylene hydrogenation into ethane over $ZnZrO_x$ and SAPO-34 (S(3.2/1.7)). Ethylene conversion was carried out at 375°C under 1 bar, H_2:C_2H_4 ratio of 28:1 for water addition and at H_2:CO_2:C_2H_4 ratio of 28:5:1 for CO_2 tests.

When ethylene was hydrogenated in the presence of CO_2, a sharp decrease in the conversion was observed. The CO_2 inhibiting effect was more pronounced (almost complete

inhibition) over $ZnZrO_x$ than over S(3.2/1.7). The inhibition can be attributed to the blockage of active hydrogenation sites because of the formation of surface carbonates on the $ZnZrO_x$ surface. On the contrary, the conversion of ethylene on zeolite was affected to a lesser extent by the presence of CO_2 in the feed. Indeed, ethylene conversion involves AS on the zeolite, which are less sensitive to CO_2. The addition of water vapor also inhibited ethylene hydrogenation on both oxide and zeolite. Previously it was shown that water molecules are strongly adsorbed on the zinc oxide forming the hydroxyl groups and blocking hydrogen activation sites. [29]

TAP demonstrates that the hydrogen activation capability has no observable impact on CO_2 conversion and the ratio of paraffin to olefin selectivity (Figure 51). The ability of different metal-oxide components to activate CO_2 was found to relate to their basicity. This can be illustrated by the microkinetic analysis of CO_2 responses from TAP tests.

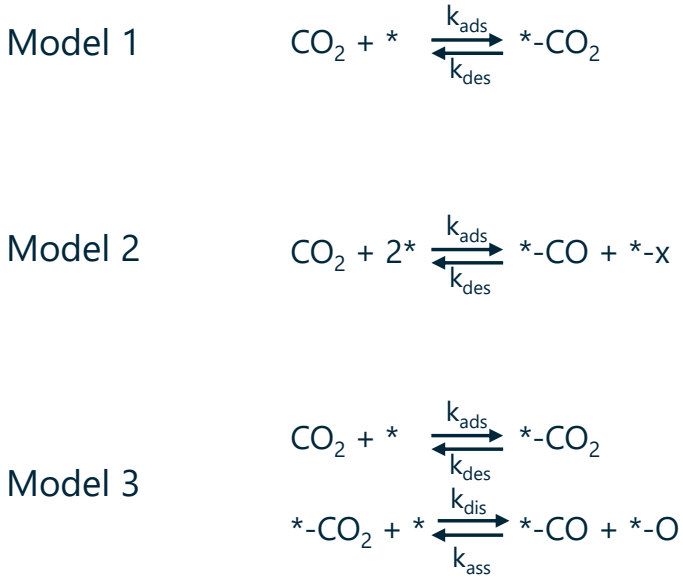

Figure 53 : Microkinetic models used for fitting of experimental CO_2 responses obtained aftre pulsing of CO_2:Ar =1:1 mixture over different catalysts at 375°C.

Three models were used to explain the experimental results (Figure 53**)**. The model considering a reversible non-dissociative CO_2 adsorption followed by reversible dissociation of

adsorbed CO_2 to adsorbed CO and O (model 3 in Figure 53) describes the CO_2 activation over ZrO_2, $ZnZrO_x$, $MnBi/ZrO_2$ and $InZrO_x$ (Figure 54).

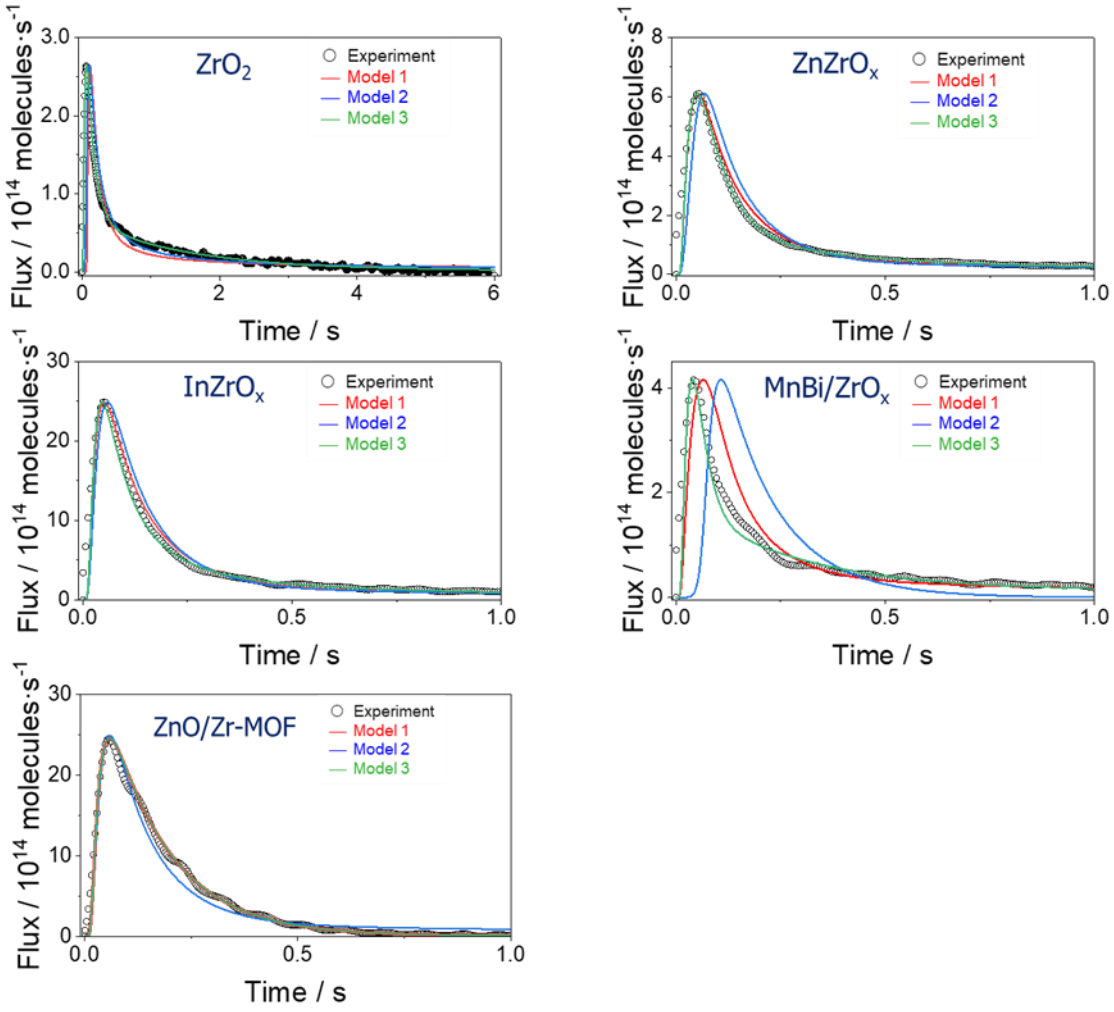

Figure 54: Comparison between the experimental and simulated CO_2 responses obtained after pulsing of CO_2:Ar =1:1 mixture over different catalysts at 375°C.

A comparison of kinetic and characterization results indicates a key role of weak basic sites in the CO_2 dissociation. The higher their concentration, the higher the equilibrium constant of dissociation of adsorbed CO_2 species (Figure 55). Strong basic sites are detrimental to this process. Formation of stable surface carbonate species over strong basic sites inhibits the CO_2 dissociation and blocks the active sites decreasing the hydrogenation activity of the catalyst.

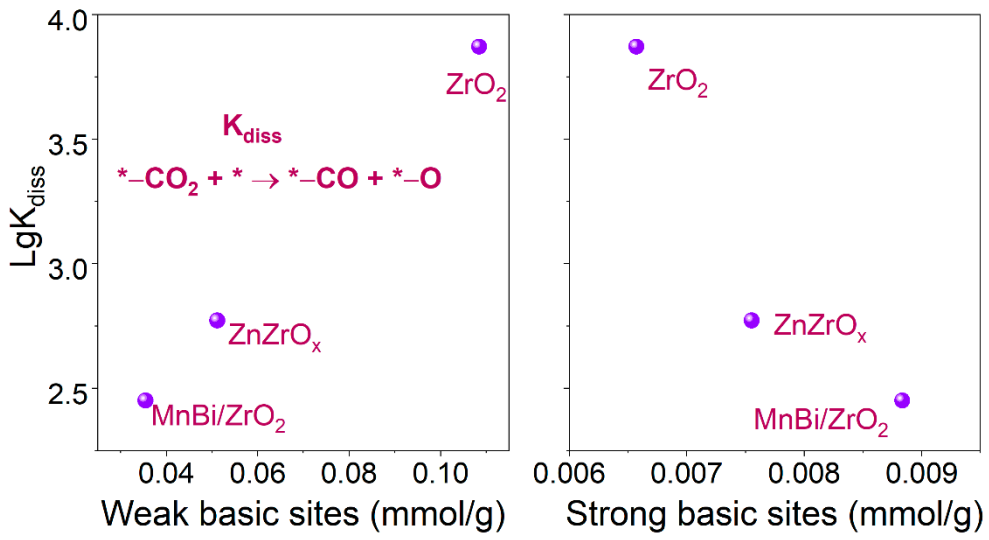

Figure 55 : Dependences of CO_2 dissociation equilibrium constant calculated by TAP on the concentration of weak and strong basic.

Thus, the presence of water and, more significantly, CO_2 in the reaction mixture of OX-ZEO process completely inhibit the activity of metal-oxide catalyst in LO hydrogenation. Hence, in the tandem process, LO secondary conversion to LP mostly occurs on the acid sites of zeolite.

4.2.5. Function of SAPO-34

In the MTO process, LO-to-LP transformations are determined by the hydrogen transfer over acid sites and may include either methanol interaction with LO and formaldehyde or olefins interaction with each other with the formation of paraffins and aromatics/coke[3] (Equations 1 and 2, respectively). The reaction in Equation 2 is more probable in the CO_2 hydrogenation over bifunctional catalysts because of the extremely low methanol concentration in the reaction mixture compared to olefins.

$$C_nH_{2n} + CH_3OH \rightleftharpoons C_nH_{2n+2} + CH_2O \quad (1)$$

$$C_nH_{2n} + C_mH_{2m} \rightleftharpoons C_nH_{2n+2} + C_mH_{2m-2} \quad (2)$$

Equation 2 can also explain the decrease in LO selectivity with an increase in HC yield (Figure 50b). The increase in the partial pressure of the hydrocarbons in the reaction mixture results in a higher probability of their interaction with each other and, therefore, in enhanced hydrogen transfer.

Considering that the metal-oxide component of a bifunctional catalyst does not noticeably affect the LO/LP selectivity, it can be proposed therefore that the structure of zeolite is the most crucial factor for the final CO-free LO selectivity.

Table 10 and Figure 56 show a decrease in LO selectivity with an increase in HC yield for bifunctional catalysts having different weight metal oxide/zeolite ratios and those prepared using SAPO-34 zeolites with different acidity and crystallite size. Let us first discuss the effect of zeolite crystallite size on LO selectivity. At the same HC yield (which corresponds to the same conversion of CO_2 to methanol), catalysts prepared using zeolite with smaller crystallites (S(1.6/0.9) and S(0.5/1.1)) exhibit higher CO-free LO selectivity. The slope of selectivity-conversion curve was also flatter for those samples than for the S(3.2/1.7) and S(3.2/0.6) derived catalysts with larger zeolite crystallites. Thus, the selectivity to LP increases with an increase in the zeolite crystallite sizes. Similar phenomena such as an increase in LO selectivity on smaller SAPO-34 crystallites were previously observed for the MTO process[2,31–34].

The decrease in selectivity towards LO coincides with a concurrent increase in selectivity towards LP as a function of CO_2 conversion to hydrocarbons. In large crystallites, the LO secondary reactions are more likely to be controlled by diffusion limitations. The increase in LO intrapore residence time in larger zeolite crystallites enhances their secondary reactions leading to LP. In smaller zeolite crystallites, LO have a high probability to escape from the pores without subsequent conversion to LP.

Table 10 also shows a somewhat lower CO selectivity on the bifunctional catalysts prepared from S(1.6/0.9) zeolite compared to the ones prepared with S(3.2/1.7). CO is mostly produced by RWGS, though some contribution of methanol decomposition to the CO generation cannot be excluded. Lower CO selectivity over S (1.6/0.9) derived samples can be attributed to smaller zeolite crystallites facilitating diffusion of intermediate methanol from metal oxide to zeolite and thus, hindering methanol decomposition.

The zeolite acidity stands as the second parameter of SAPO-34 that holds the potential to influence the selectivity towards LO. According to the MTO mechanism based on the olefin cycle, the branched unsaturated C_{5+} hydrocarbons are the precursors for the light olefins[35]. Reducing the number of strong acid sites can partially inhibit the cracking of C_{5+} olefins to LO giving higher C_{5+} selectivity. This suggests that zeolite with a smaller density of strong Bronsted AS might be more attractive for the direct hydrogenation of CO_2 to LO than zeolite with high acid site density. Though zeolite acidity can potentially affect the LO selectivity, it does not seem to be the most influential parameter. Indeed, bifunctional catalysts prepared from S(3.2/1.7) and S(3.2/0.6) have rather low LO selectivity (Figure 56). Note that the zeolites used for the catalyst preparation have similar larger crystallites but different acidity. The identical logic applies to the catalysts obtained from zeolites S(1.6/0.9) and S(0.5/1.1). Both these zeolites have small crystallite sizes but rather different acidity. Note that their catalytic performance is similar. Consequently, within the bifunctional catalysts utilized for CO_2 hydrogenation to LO, the influence of zeolite crystallite sizes in controlling LO selectivity surpasses that of zeolite acidity, encompassing both weak and strong acid site densities. Please be aware that the interaction between zeolite crystallinity, which tends to be more pronounced in larger crystallites, and acidity cannot be entirely ruled out. In fact, smaller and less well-crystallized zeolites could exhibit weaker acid sites compared to their highly crystallized counterparts.

The ratio of metal oxide to zeolite in the bifunctional catalyst also has a strong impact on the reaction rate and LO selectivity. An increase in the zeolite fraction in the bifunctional catalyst decreases the CO_2 conversion and the selectivity to CO, but at the same time it increases the selectivity to LO measured at the same conversion. Indeed, the RWGS reaction producing CO from CO_2 principally occurs on the metal oxide. A smaller amount of metal oxide in the bifunctional catalyst lowers the RWGS and CO selectivity.

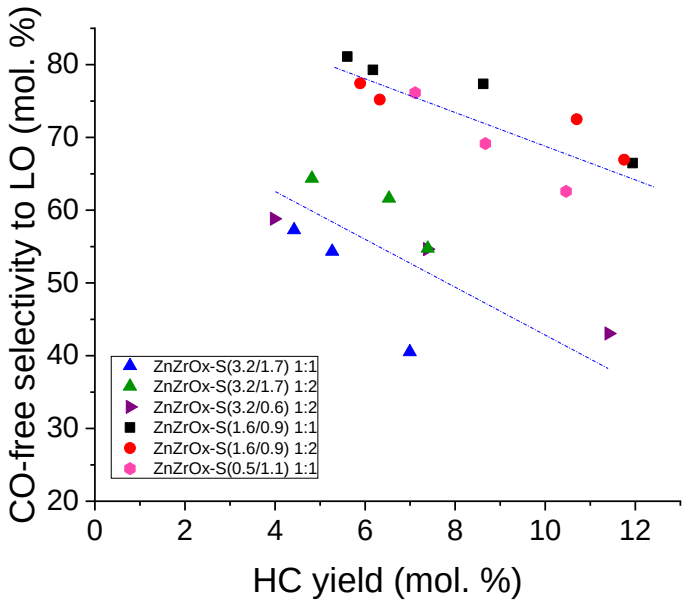

Figure 56 : CO-free selectivity to LO towards HC yield for the $ZnZrO_x$-based catalysts mixed with SAPO-34 of different acidity and in the different weight ratios (oxide:zeolite from 1:2 to 2:1).

Table 10 : Catalytic results for the tests of $ZnZrO_x$ mixed with the SAPO-34 in different proportions. WHSV of 3000 NmL/g/h, 20 bar, and 375 °C.

Catalyst	**X_{CO2} (mol.%)**	**S(CO) (mol.%)**	**CO-free selectivity (mol.%)**				**O/P ratio**
			S(CH_4)	S(LO)	S(LP)	S(C_{5+})	
$ZnZrO_x$-S(3.2/1.7) 1:1	23.8	81.4	3.4	57.3	34.3	5.0	1.7
$ZnZrO_x$-S(1.6/0.9) 1:1	23.9	54.7	1.4	72.4	21.1	7.3	3.4

$ZnZrO_x$- S(3.2/1.7) 1:2	19.4	74.5	2.3	64.4	29.5	2.8	2.2
$ZnZrO_x$- S(1.6/0.9) 1:2	17.6	50.6	1.1	77.4	17.7	3.5	4.4

Our results suggest a strong influence of SAPO-34 zeolite on the dependence of LO selectivity as a function of the HC yield. We can conclude that metal-oxide is not involved in the LO-to-LP conversion under the conditions of CO_2 hydrogenation. This suggestion has been confirmed by the following experiments:

1) In the presence of CO_2 and water, ethylene hydrogenation over metal oxide was inhibited much more strongly than over the zeolite. These phenomena have been demonstrated by model C_2H_4 + H_2 hydrogenation experiments (Figure 52). The participation of metal oxide in the secondary LO reactions could be less significant than zeolite.
2) TAP results showed no clear relation between the hydrogen activation ability and the selectivity towards different hydrocarbon fractions.
3) The variation of the SAPO-34 crystallite size, acidity and ratio of metal oxide to SAPO-34 zeolite in a bifunctional catalyst strongly affects the selectivity-HC yield dependence.

The scheme in Figure 57 summarizes the roles of the metal oxide and zeolite components in the bifunctional catalyst in direct CO_2 hydrogenation to LO. Metal oxide determines the total CO_2 conversion and MeOH/CO production ratio regulating the CO_2 adsorption and dissociation as well as activation of hydrogen. These processes are set by the amount of oxygen vacancies for CO_2 activation and by the presence of M-O surface bonds for that of hydrogen, as well as by the proximity of both sites[8,36]. According to what already

reported in Chapter 1, this process goes through the formate-based mechanism where CO_2 (activated by oxygen vacancies) is hydrogenated first to formate species and then to methoxy fragments. Zeolite itself does not convert CO_2 but coupling methanol synthesis with MTO increases the total conversion.

A key step in bifunctional catalysis is a transfer of reaction intermediates from metal oxide and zeolite. Methanol can decompose over the metal oxide,[26] while methanol conversion over zeolites thermodynamically drives the process to hydrocarbon formation route. Furthermore, recent studies showed that simple physical mortar mixing is enough to achieve maximum selectivity to hydrocarbons in the CO_2 hydrogenation.[37]

Two descriptors determine the CO-free LO selectivity over metal oxide-SAPO-34 zeolite bifunctional catalysts: zeolite morphology and acidity. First, the LO selectivity in the CO_2 hydrogenation strongly depends on the SAPO-34 zeolite morphology: larger size of zeolite crystallites promotes hydrogen transfer and lowers the CO-free LO selectivity. The results are to some extent similar to those previously reported for CO hydrogenation to LO over bifunctional metal oxide-zeolite catalysts.[25] The decrease in CO-free LO selectivity with the HC yield is explained by the secondary hydrogen transfer reactions over zeolite acid sites. These reactions are getting more significant at higher LO concentration, longer LO residence time and higher density of acid sites within the larger zeolite crystallites.

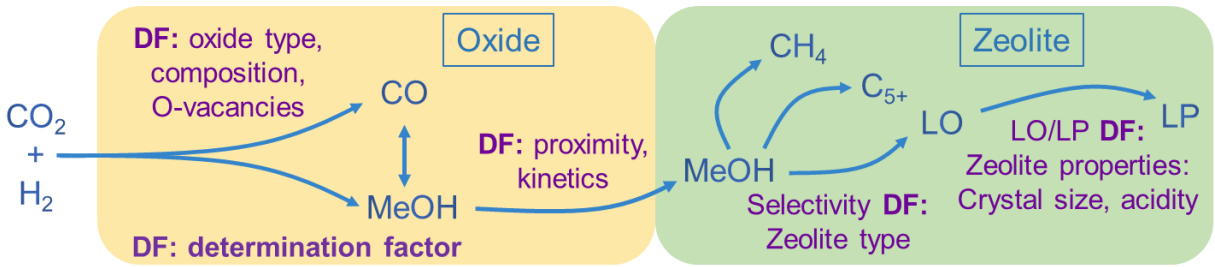

Figure 57 : Illustration of the tandem process reaction: roles of oxide and SAPO-34 components in the methanol-mediated CO_2 hydrogenation performance.

4.3. Conclusions

A series of metal oxide zeolite bifunctional for CO_2 hydrogenation to LO catalysts with various chemical and phase composition were synthesized and their structure was characterized by XRD, TEM and XAS. Despite the differences, the catalysts mixed with SAPO-34 showed an obvious dependence of CO-free selectivity to LO on the hydrocarbon yield. This selectivity-HC yield trend is principally affected by zeolite component in the bifunctional catalysts and is almost independent on the metal oxide.

Catalytic and characterization data allowed the functions of each component in the bifunctional catalysts to be identified. It was concluded that the metal-oxide was responsible for the overall CO_2 conversion and for the selectivity to CO and the overall hydrocarbon selectivity. At the same time, no noticeable effect of metal oxides with different structure and chemical composition on the LO CO-free selectivity was observed.

The zeolite choice is the crucial factor which determines the CO-free LO selectivity in CO_2 hydrogenation over metal oxide zeolite bifunctional catalysts: hydrogen transfer processes occur mainly on strong acid sites and set the resulting olefin to paraffin ratio. We identified two descriptors affecting the CO-free LO selectivity: zeolite morphology and acidity. The reduction in zeolite crystallite size and in acid site density result in a deceleration of secondary LO reactions taking place within the zeolite pores. As a result, this leads to an increased selectivity towards LO. Hence, this investigation underscores the potential of methanol-mediated CO_2 hydrogenation and emphasizes the essential role played by zeolites in achieving elevated selectivity towards light olefins.

4.4. References

(1) Liu, Y.; Deng, D.; Bao, X. Catalysis for Selected C1 Chemistry. *Chem* **2020**, *6* (10), 2497–2514. https://doi.org/10.1016/j.chempr.2020.08.026.

(2) Chernyak, S. A.; Corda, M.; Dath, J.-P.; Ordomsky, V. V.; Khodakov, A. Y. Light Olefin Synthesis from a Diversity of Renewable and Fossil Feedstocks: State-of the-Art and Outlook. *Chem. Soc. Rev.* **2022**, *51* (18), 7994–8044. https://doi.org/10.1039/D1CS01036K.

(3) Müller, S.; Liu, Y.; Kirchberger, F. M.; Tonigold, M.; Sanchez-Sanchez, M.; Lercher, J. A. Hydrogen Transfer Pathways during Zeolite Catalyzed Methanol Conversion to Hydrocarbons. *J. Am. Chem. Soc.* **2016**, *138* (49), 15994–16003. https://doi.org/10.1021/jacs.6b09605.

(4) Labinger, J. A. Oxidative Coupling of Methane: An Inherent Limit to Selectivity? *Catal. Lett.* **1988**, *1* (11), 371–375. https://doi.org/10.1007/BF00766166.

(5) Hájek, J.; Wärnå, J.; Murzin, D. Yu. Liquid-Phase Hydrogenation of Cinnamaldehyde over a Ru−Sn Sol−Gel Catalyst. 2. Kinetic Modeling. *Ind. Eng. Chem. Res.* **2004**, *43* (9), 2039–2048. https://doi.org/10.1021/ie034081u.

(6) Barrios, A. J.; Peron, D. V.; Chakkingal, A.; Dugulan, A. I.; Moldovan, S.; Nakouri, K.; Thuriot-Roukos, J.; Wojcieszak, R.; Thybaut, J. W.; Virginie, M.; Khodakov, A. Y. Efficient Promoters and Reaction Paths in the CO 2 Hydrogenation to Light Olefins over Zirconia-Supported Iron Catalysts. *ACS Catal.* **2022**, 3211–3225. https://doi.org/10.1021/acscatal.1c05648.

(7) Li, Z.; Wang, J.; Qu, Y.; Liu, H.; Tang, C.; Miao, S.; Feng, Z.; An, H.; Li, C. Highly Selective Conversion of Carbon Dioxide to Lower Olefins. *ACS Catal.* **2017**, *7* (12), 8544–8548. https://doi.org/10.1021/acscatal.7b03251.

(8) Tada, S.; Ochiai, N.; Kinoshita, H.; Yoshida, M.; Shimada, N.; Joutsuka, T.; Nishijima, M.; Honma, T.; Yamauchi, N.; Kobayashi, Y.; Iyoki, K. Active Sites on $Zn_xZr_{1-x}O_{2-x}$ Solid Solution Catalysts for CO_2-to-Methanol Hydrogenation. *ACS Catal.* **2022**, *12* (13), 7748–7759. https://doi.org/10.1021/acscatal.2c01996.

(9) Jia, X.; Sun, K.; Wang, J.; Shen, C.; Liu, C. jun. Selective Hydrogenation of CO_2 to Methanol over Ni/In_2O_3 Catalyst. *J. Energy Chem.* **2020**, *50*, 409–415. https://doi.org/10.1016/j.jechem.2020.03.083.

(10) Lee, S. M.; Park, K. H.; Kim, S. S.; Kwon, D. W.; Hong, S. C. Effect of the Mn Oxidation State and Lattice Oxygen in Mn-Based TiO_2 Catalysts on the Low-Temperature Selective Catalytic Reduction of NO by NH_3. *J. Air Waste Manag. Assoc.* **2012**, *62* (9), 1085–1092. https://doi.org/10.1080/10962247.2012.696532.

(11) Chen, J.; Wang, X.; Wu, D.; Zhang, J.; Ma, Q.; Gao, X.; Lai, X.; Xia, H.; Fan, S.; Zhao, T. S. Hydrogenation of CO2 to Light Olefins on CuZnZr@(Zn-)SAPO-34 Catalysts: Strategy for Product Distribution. *Fuel* **2019**, *239*, 44–52. https://doi.org/10.1016/j.fuel.2018.10.148.

(12) Briend, M.; Vomscheid, R.; Peltre, M. J.; Man, P. P.; Barthomeuf, D. Influence of the Choice of the Template on the Short- and Long-Term Stability of SAPO-34 Zeolite. *J. Phys. Chem.* **1995**, *99* (20), 8270–8276. https://doi.org/10.1021/j100020a060.

(13) Kong, C.; Zhu, J.; Liu, S.; Wang, Y. SAPO-34 with a Low Acidity Outer Layer by Epitaxial Growth and Its Improved MTO Performance. *RSC Adv.* **2017**, *7* (63), 39889–39898. https://doi.org/10.1039/C7RA06488H.

(14) Marchese, L.; Frache, A.; Gianotti, E.; Martra, G.; Causà, M.; Coluccia, S. ALPO-34 and SAPO-34 Synthesized by Using Morpholine as Templating Agent. FTIR and FT-Raman Studies of the Host–Guest and Guest–Guest Interactions within the Zeolitic Framework. *Microporous Mesoporous Mater.* **1999**, *30* (1), 145–153. https://doi.org/10.1016/S1387-1811(99)00023-2.

(15) Sedighi, M.; Mohammadi, M. CO_2 Hydrogenation to Light Olefins over Cu-CeO_2/SAPO-34 Catalysts: Product Distribution and Optimization. *J. CO_2 Util.* **2020**, *35*, 236–244. https://doi.org/10.1016/j.jcou.2019.10.002.

(16) Shen, W.; Li, X.; Wei, Y.; Tian, P.; Deng, F.; Han, X.; Bao, X. A Study of the Acidity of SAPO-34 by Solid-State NMR Spectroscopy. *Microporous Mesoporous Mater.* **2012**, *158*, 19–25. https://doi.org/10.1016/j.micromeso.2012.03.013.

(17) Wang, D.; Yang, M.; Zhang, W.; Fan, D.; Tian, P.; Liu, Z. Hollow Nanocrystals of Silicoaluminophosphate Molecular Sieves Synthesized by an Aminothermal Co-Templating Strategy. *CrystEngComm* **2016**, *18* (6), 1000–1008. https://doi.org/10.1039/C5CE01798J.

(18) Li, Z.; Martínez-Triguero, J.; Concepción, P.; Yu, J.; Corma, A. Methanol to Olefins: Activity and Stability of Nanosized SAPO-34 Molecular Sieves and Control of Selectivity by Silicon Distribution. *Phys. Chem. Chem. Phys.* **2013**, *15* (35), 14670. https://doi.org/10.1039/c3cp52247d.

(19) Yang, L.; Wang, C.; Zhang, L.; Dai, W.; Chu, Y.; Xu, J.; Wu, G.; Gao, M.; Liu, W.; Xu, Z.; Wang, P.; Guan, N.; Dyballa, M.; Ye, M.; Deng, F.; Fan, W.; Li, L. Stabilizing the Framework of SAPO-34 Zeolite toward Long-Term Methanol-to-Olefins Conversion. *Nat. Commun.* **2021**, *12* (1). https://doi.org/10.1038/s41467-021-24403-2.

(20) Fu, G.; Nazar, L. F.; Bain, A. D. Aging Processes of Alumina Sol-Gels: Characterization of New Aluminum Polyoxycations by Aluminum-27 NMR Spectroscopy. *Chem. Mater.* **1991**, *3* (4), 602–610. https://doi.org/10.1021/cm00016a009.

(21) Hiradate, S. Speciation of Aluminum in Soil Environments: Application of NMR Technique. *Soil Sci. Plant Nutr.* **2004**, *50* (3), 303–314. https://doi.org/10.1080/00380768.2004.10408483.

(22) Smart, S. E.; Vaughn, J.; Pappas, I.; Pan, L. Controlled Step-Wise Isomerization of the Keggin-Type Al13 and Determination of the γ-Al13 Structure. *Chem. Commun.* **2013**, *49* (97), 11352. https://doi.org/10.1039/c3cc44844d.

(23) Ashtekar, S.; Chilukuri, S. V. V.; Chakrabarty, D. K. Small-Pore Molecular Sieves SAPO-34 and SAPO-44 with Chabazite Structure: A Study of Silicon Incorporation. *J. Phys. Chem.* **1994**, *98* (18), 4878–4883. https://doi.org/10.1021/j100069a018.

(24) Li, G.; Jiao, F.; Pan, X.; Li, N.; Miao, D.; Li, L.; Bao, X. Role of SAPO-18 Acidity in Direct Syngas Conversion to Light Olefins. *ACS Catal.* **2020**, *10* (21), 12370–12375. https://doi.org/10.1021/acscatal.0c03257.

(25) Su, J.; Zhou, H.; Liu, S.; Wang, C.; Jiao, W.; Wang, Y.; Liu, C.; Ye, Y.; Zhang, L.; Zhao, Y.; Liu, H.; Wang, D.; Yang, W.; Xie, Z.; He, M. Syngas to Light Olefins Conversion with High Olefin/Paraffin Ratio Using ZnCrOx /AlPO-18 Bifunctional Catalysts. *Nat. Commun.* **2019**, *10* (1). https://doi.org/10.1038/s41467-019-09336-1.

(26) Ortner, N.; Zhao, D.; Mena, H.; Weiß, J.; Lund, H.; Bartling, S.; Wohlrab, S.; Armbruster, U.; Kondratenko, E. V. Revealing Origins of Methanol Selectivity Loss in CO_2 Hydrogenation over CuZn-Containing Catalysts. *ACS Catal.* **2023**, *13* (1), 60–71. https://doi.org/10.1021/acscatal.2c04480.

(27) Barrios, A. J.; Gu, B.; Luo, Y.; Peron, D. V.; Chernavskii, P. A.; Virginie, M.; Wojcieszak, R.; Thybaut, J. W.; Ordomsky, V. V.; Khodakov, A. Y. Identification of Efficient Promoters and Selectivity Trends in High Temperature Fischer-Tropsch Synthesis over Supported Iron Catalysts. *Appl. Catal. B Environ.* **2020**, *273*, 119028. https://doi.org/10.1016/j.apcatb.2020.119028.

(28) Morgan, K.; Maguire, N.; Fushimi, R.; Gleaves, J. T.; Goguet, A.; Harold, M. P.; Kondratenko, E. V.; Menon, U.; Schuurman, Y.; Yablonsky, G. S. Forty Years of Temporal Analysis of Products. *Catal. Sci. Technol.* **2017**, *7* (12), 2416–2439. https://doi.org/10.1039/C7CY00678K.

(29) Dent, A. L.; Kokes, R. J. Hydrogenation of Ethylene by Zinc Oxide. I. Role of Slow Hydrogen Chemisorption. *J. Phys. Chem.* **1969**, *73* (11), 3772–3780. https://doi.org/10.1021/j100845a035.

(30) Oikawa, H.; Shibata, Y.; Inazu, K.; Iwase, Y.; Murai, K.; Hyodo, S.; Kobayashi, G.; Baba, T. Highly Selective Conversion of Ethene to Propene over SAPO-34 as a Solid Acid Catalyst. *Appl. Catal. Gen.* **2006**, *312*, 181–185. https://doi.org/10.1016/j.apcata.2006.06.045.

(31) Palčić, A.; Ordomsky, V. V.; Qin, Z.; Georgieva, V.; Valtchev, V. Tuning Zeolite Properties for a Highly Efficient Synthesis of Propylene from Methanol. *Chem. - Eur. J.* **2018**, *24* (50), 13136–13149. https://doi.org/10.1002/chem.201803136.

(32) Wang, P.; Yang, D.; Hu, J.; Xu, J.; Lu, G. Synthesis of SAPO-34 with Small and Tunable Crystallite Size by Two-Step Hydrothermal Crystallization and Its Catalytic Performance for MTO Reaction. *Catal. Today* **2013**, *212*, 62.e1-62.e8. https://doi.org/10.1016/j.cattod.2012.08.027.

(33) Bakhtiar, S. U. H.; Wang, X.; Ali, S.; Yuan, F.; Li, Z.; Zhu, Y. CTAB-Assisted Size Controlled Synthesis of SAPO-34 and Its Contribution toward MTO Performance. *Dalton Trans.* **2018**, *47* (29), 9861–9870. https://doi.org/10.1039/C8DT01811A.

(34) Hajfarajollah, H.; Askari, S.; Halladj, R. Effects of Micro and Nano-Sized SAPO-34 and SAPO-5 Catalysts on the Conversion of Methanol to Light Olefins. *React. Kinet. Mech. Catal.* **2014**, *111* (2), 723–736. https://doi.org/10.1007/s11144-013-0650-6.

(35) Plessow, P. N.; Smith, A.; Tischer, S.; Studt, F. Identification of the Reaction Sequence of the MTO Initiation Mechanism Using Ab Initio-Based Kinetics. *J. Am. Chem. Soc.* **2019**, *141* (14), 5908–5915. https://doi.org/10.1021/jacs.9b00585.

(36) Zhang, P.; Ma, L.; Meng, F.; Wang, L.; Zhang, R.; Yang, G.; Li, Z. Boosting CO_2 Hydrogenation Performance for Light Olefin Synthesis over GaZrOx Combined with

SAPO-34. *Appl. Catal. B Environ.* **2022**, *305*. https://doi.org/10.1016/j.apcatb.2021.121042.

(37) Li, Y.; Wang, M.; Liu, S.; Wu, F.; Zhang, Q.; Zhang, S.; Cheng, K.; Wang, Y. Distance for Communication between Metal and Acid Sites for Syngas Conversion. *ACS Catal.* **2022**, *12* (15), 8793–8801. https://doi.org/10.1021/acscatal.2c02125.

Chapter 5

Silver Metallic Nanoparticles for Direct Conversion of Carbon Monoxide to Light Olefins over Bifunctional Catalysts

5.1. Introduction

The LO production from CO_2 hydrogenation reduces the dependence on fossil fuels, improving resource utilization, and contributing to the development of more efficient and environmentally friendly industrial technologies. In addition to CO_2, a possible sustainable feedstock is CO. In fact, the CO hydrogenation to LO employs syngas produced from gasification of renewable feedstocks such as biomass and waste or even from CO_2, by the reverse water gas shift reaction (RWGS)[1]. Developing more efficient processes for the conversion of CO to light olefins could lead to energy savings and reduce environmental footprint compared to conventional methods of olefin production. The latter are often endothermic, require high operating temperatures and high energy consumption.

As already mentioned in the previous chapters of this thesis, Fischer Tropsch synthesis is a possible pathway to produce LO from syngas[2–4], but the light olefin selectivity is limited to about 60% by an Anderson-Schulz-Flory polymerization kinetics. The alternative proposed in this chapter is the methanol-mediated CO hydrogenation to LO. Like in the case of CO_2 hydrogenation, bifunctional catalysts made of a high temperature methanol synthesis component and a methanol-to olefin zeolite active phase are used in this process[5,6]. The selectivity to LO of OX-ZEO process is usually higher than that of Fischer-Tropsch reaction and generally ranges between 60 and 80%.

In the bifunctional catalyst, the most common zeolite phase is SAPO-34,[5,7–12] while the catalytic phase for methanol synthesis typically involves mixed oxides such as Zn-Cr, ZnO-ZrO_2[5], $ZrCeZnO_x$[10], $ZnAlO_x$[8], Mn-Ga[9,12]. Interestingly, metal-based methanol synthesis catalysts have not been reported for use in the tandem synthesis of LO from syngas. Indeed, metal catalysts for methanol synthesis such as copper or palladium systems, usually operate at a lower temperature of 200-250°C. They are not suited for methanol synthesis at higher temperatures, because of strong hydrogenation activity leading to the production of methane and other light hydrocarbons.

Ag/ZrO_2 systems have been earlier proposed for the CO_2 hydrogenation to MeOH[13,14] and methyl formate[15], while they usually exhibit somewhat lower activity at the conventional conditions of methanol synthesis. In this work, we uncovered a high LO selectivity in CO hydrogenation on bifunctional catalysts, containing silver metallic nanoparticles supported over zirconia and SAPO-34 zeolite.

5.2. Results and discussion

5.2.1. CO hydrogenation over silver hybrid catalysts at steady state conditions

The hybrid catalysts were prepared by mechanical mixing of zirconia supported silver nanoparticles and zeolite. CO hydrogenation over the hybrid zirconia supported silver SAPO-34 zeolite catalysts at 350-400°C results in the production of CO_2, methane, light olefins (LO: ethylene, propylene and butylene), light paraffins (LP: ethane, propane, butane), and C_5^+ species (mostly pentene/pentane) and water. The catalysts were tested under the same conditions (375 °C, 20 bar; H_2: CO=2). The catalytic performance data at steady state

conditions were typically achieved after catalyst stabilization after 30 h on stream (Table 11). The CO conversions varied a function of gas space velocities. All catalysts exhibited relatively high selectivity to CO_2 (30-40%). Water gas shift reaction in OX-ZEO process is coupled with hydrocarbon synthesis:

$$nCO+2nH_2 \rightleftharpoons (CH_2)_n + nH_2O \quad (1)$$

$$CO+H_2O \rightleftharpoons CO_2+H_2 \quad (2)$$

$$2nCO+nH_2 \rightleftharpoons (CH_2)_n+nCO_2 \quad (3)$$

That is the reason why CO_2 can be considered as the main reaction product, which is produced stoichiometrically with hydrocarbons according to Eq. (3) with a theoretically possible maximum selectivity of 50%.

The CO_2-free hydrocarbon selectivities are shown in Table 11 and Figure 58**.** High selectivity to LO in CO hydrogenation was observed over zirconia supported silver catalysts mixed with SAPO-34. At a CO conversion of 7.8%, the LO selectivity was higher than 76% on AgZr10-S34 (1:2) accompanied by low selectivities to methane and C_{5+} hydrocarbons (entry 1, Table 11). Increase in the zeolite to zinc-zirconia catalyst ratio in the catalysts from 1:2 to 2:1 resulted in a decrease in LO selectivity from 76.4 to 57.6% at a CO conversion of 7%. (entry 2, *Table 11*). The information about zeolite crystallite sizes in S34 and S34L samples is given in Table 7 (Chapter 2). The use of a SAPO-34 zeolite with larger crystallites in AgZr10-S-34L yielded a higher CO conversion, but a reduced light olefin selectivity (entry 3, Table 11). Interestingly, an increase in CO conversion with the AgZr10-S34L (2:1) catalyst with larger SAPO-34 crystallites was achieved compared to AgZr10-S34 (2:1) at the same gas space velocity normalized by the weight of silver.

Furthermore, CO hydrogenation was performed over AgZr10 and Ag-S34, to prove the necessity of synergy of the Ag/ZrO_2 and SAPO-34 components. Ag-S34 was prepared by

impregnation of SAPO-34 with an Ag nitrate precursor and did not contain zirconia. The Ag-S34 sample was almost inactive (entry 4, Table 11), whereas AgZr10, which does not contain SAPO-34 zeolite, showed a CO conversion of 32% with a CO_2-free selectivity to CH_4 of 98% (**entry 5,** *Table 11*). A negligible olefin production was observed on AgZr10. It is known that silver catalysts exhibit[13,14,16] higher selectivity to methanol at lower temperature. Higher methane selectivity observed on AgZr10 can be due to multistep hydrogenation of CO and intermediate methanol to methane at higher reaction temperatures.

Table 11: Catalytic performance in CO hydrogenation (375 °C, 20 bar, H_2: CO=2) at steady state.

Entry	Catalyst	WHSV (NL g_{cat}^{-1} h^{-1})	WHSV(Ag) (NL g_{Ag}^{-1} h^{-1})*	X CO (%)	S CO_2 (%)	CO_2-free selectivity (%)			
						CH_4	LO	LP	C_5+
1	AgZr10-S34 (1:2)	0.6	18	7.8	40.8	5.6	76.4	16.1	1.9
2	AgZr10-S34 (2:1)	1.6	24	7.2	33.1	31.0	57.6	9.3	2.1
3	AgZr10-S34L (1:2)	0.6	18	17.7	40.1	7.5	36.0	52.1	4.4
4	Ag-S34	1.6	48	0.0		-	-	-	-
5	AgZr10	4.8	48	32.6	11.4	98.5	1.0	0.0	0.5
6	ZrO_2-S34	1.6	-	1.5	25.5	0.0	91.9	7.1	1.0
7	AgNPZr1-S34	1.6	480	1.8	67.7	1.7	87.1	9.6	1.6
8	AgNPZr12-S34	0.6	19	1.3	41.2	4.9	62.5	32.5	1.0
9	ZnZrOx-S34	4.8	-	7.4	32.9	11.7	60.8	25.8	1.7
		1.6	-	18.9	33.6	16.3	67.0	15.4	1.3

Notice: X CO is the CO conversion; S CO_2 is the selectivity to CO_2;
AgZr10-S34L is the zirconia supported silver-zeolite catalyst with large S-34 crystallites;
AgNPZrX-S34 is the zirconia supported silver nanoparticles with different Ag content mixed with SAPO-34 zeolite;
AgZr10 is the zirconia supported silver catalyst;
Ag-S34 corresponds to silver deposited over SAPO-34.
* Gas space velocity was calculated based on silver amount. WHSV(Ag)= gas flow rate (L/h)/m_{Ag} (g)

As expected, without silver, ZrO_2-S34 showed very low activity in CO hydrogenation with a CO conversion less than 2% (entry 6, *Table 11*). No CO conversion was observed on SAPO-34 zeolite. At low conversion of 1.8%, the catalyst prepared from silver nanoparticles supported on zirconia and mixed with SAPO-34 (AgNPZr1-S34, **entry 7,** *Table 11*) exhibited a high LO selectivity of 87%.

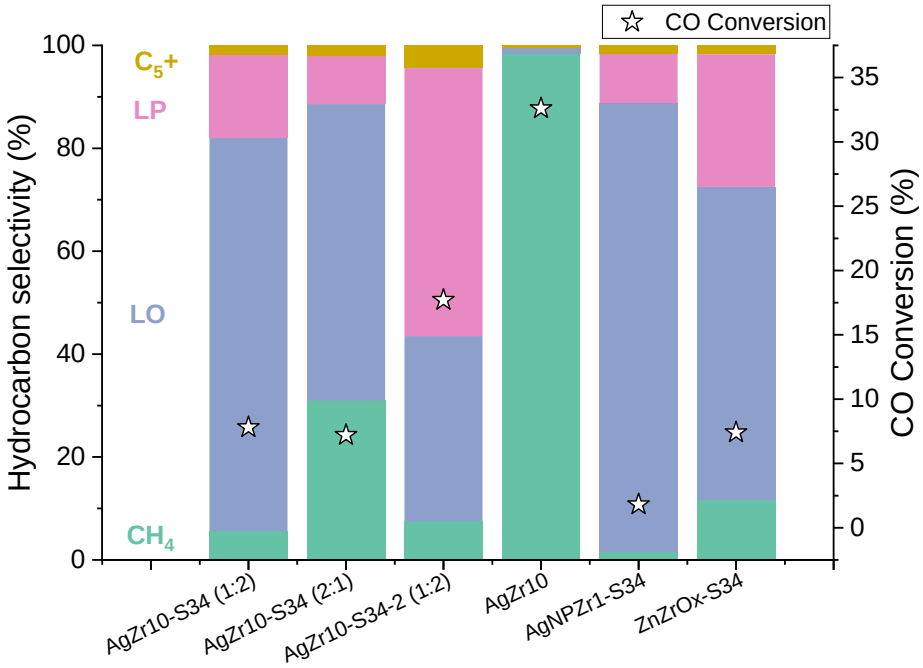

Figure 58: Steady state selectivities and CO conversion for different catalysts. Conditions: 375 °C; 20 bar; 4.8-0.6 NL g_{cat}^{-1} h^{-1}.

The silver-based bi-functional catalysts were compared to a reference bifunctional catalyst[4,5] for OX-ZEO process, $ZnZrO_x$-S34 (entry 9, Table 11 and Figure 58). $ZnZrO_x$-S34 was composed by a 13 mol% ZnO solid solution in ZrO_2, mixed with the same SAPO-34 zeolite as the one used for making the AgZr10-S34 catalyst. Interestingly, at the same conversion level, on AgZr10-S34. the CO_2-free selectivity to LO was slightly higher (78% versus 63%), while the selectivities towards CH_4 and LP were lower compared to $ZnZrO_x$-S34 (Figure 59).

An increase in the reaction temperature from 375 to 500°C resulted in higher CO conversion over AgZr10-S34, which coincided with a decrease in the LO selectivity and a simultaneous increase in the selectivity to LP (Figure 60).

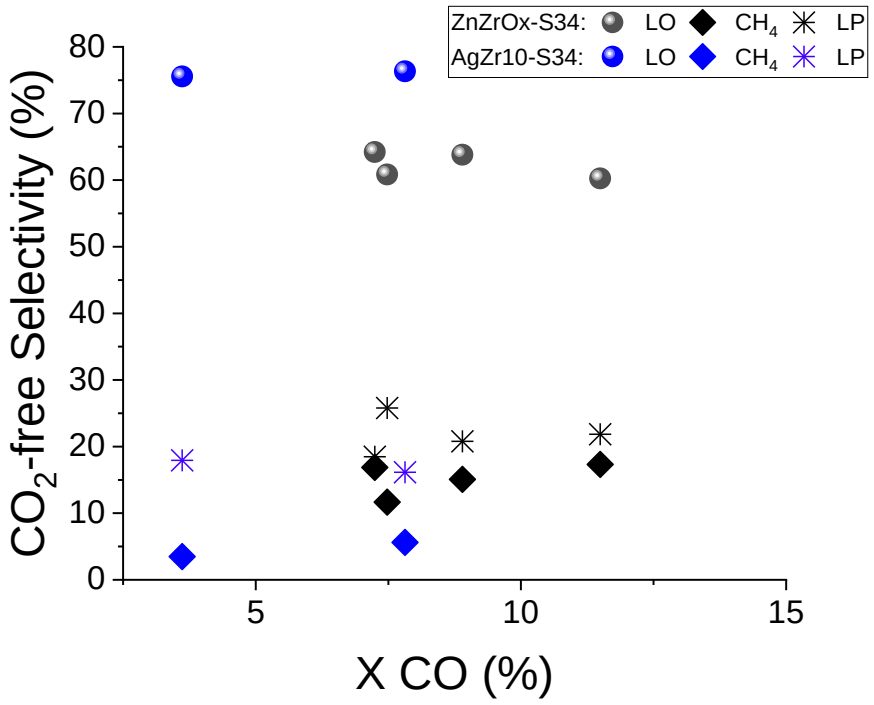

Figure 59: Selectivity-conversion curve: AgZr10-S34 compared to ZnZrOx-S34.

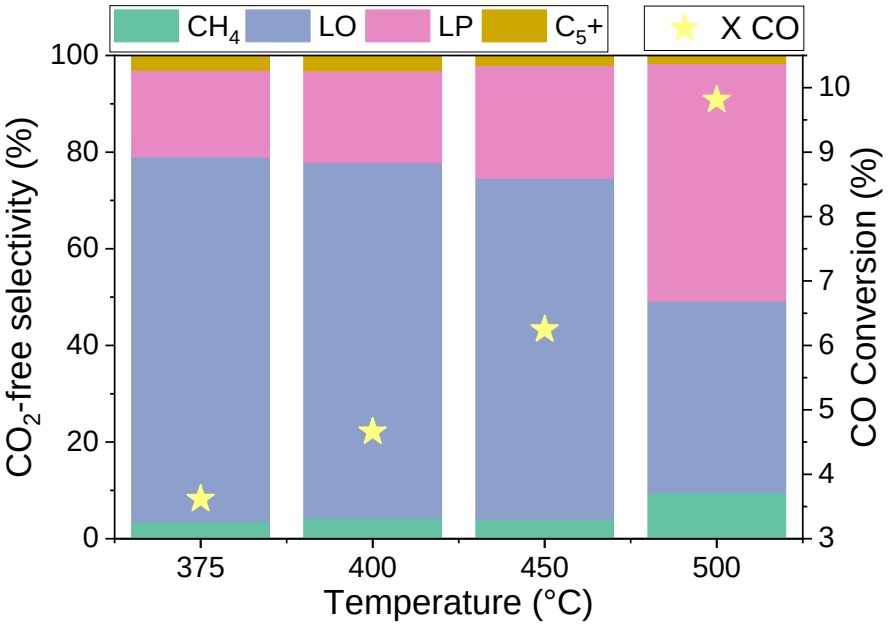

Figure 60: Effect of temperature on catalysis. AgZr10-S34. .Conditions: 20 bar; 1.6 NL g_{cat}^{-1} h^{-1}

5.2.2. Transient behaviour of the AgZr-S34 catalyst

Interestingly, before reaching the steady state performance, the conversion and selectivity of the AgZr10-S34 catalysts evolves with the time of stream (Figure 61). The evolution of performance was observed over AgZr10-S34 with smaller and larger zeolite crystallites. In particular, the CO conversion drops doing the first hours of reaction. The selectivity to LO steadily increases on both catalysts (Figure 61a and b), while the selectivity to LP drops. The methane selectivity remains low during the whole catalytic tests. After an initial drop from 45 % to 40%, the CO_2 selectivity remained constant all along the reaction. At the same conversion level, higher LO selectivity was observed on the catalysts containing smaller zeolite crystallite sizes. This observation is consistent with the results reported in Chapter 4, emphasizing the role of zeolite crystallite sizes in obtaining light olefin selectivity from CO_2 hydrogenation. After 180 h of TOS, a selectivity of 78% to LO was achieved over AgZr10-S34 with smaller crystallite sizes (Figure 61a**)**, while a quasi-steady selectivity of 40% was detected on AgZr10-S34L (Figure 61b). Similar evolution of the catalyst performance with time on stream was observed at the initial CO conversion of 22% and 6.8% conversions (Figure 62a) on AgZr10-S34 with smaller crystallite sizes. Interestingly, a much rapid stabilization of conversion and selectivity was observed on AgNP12-S34 catalyst prepared by deposition of relatively large sliver nanoparticles (10-20 nm) on zirconia (Figure 62b). The evolution of the catalytic performance with the reaction time suggests that the structure of AgZr10 -S34 catalysts changes during the reaction.

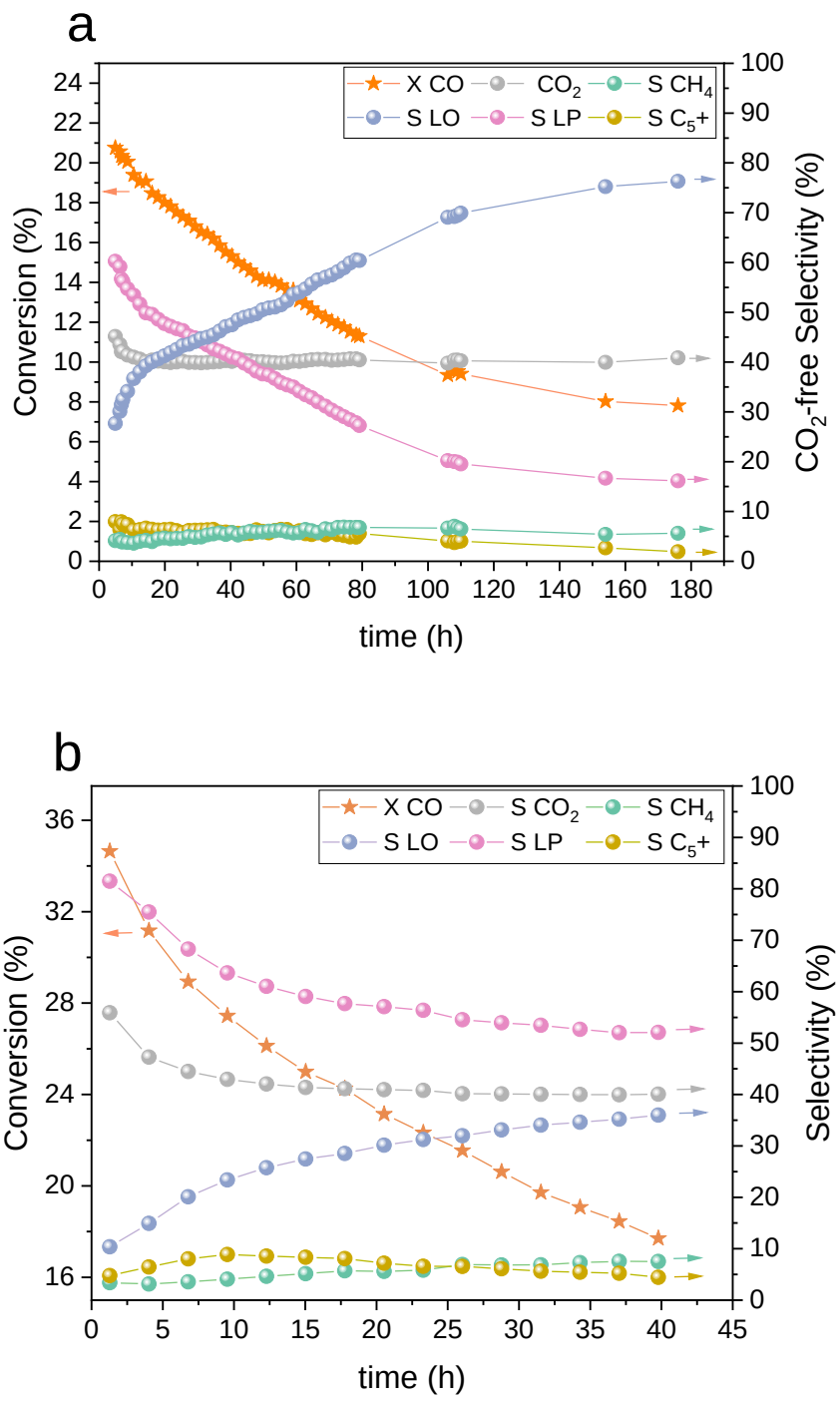

Figure 61: Selectivity CO-free and CO and conversion versus time on stream for S-34 small and larger crystals at high conversion. a) AgZr10-S34; b) AgZr10-S34L. Conditions: 375 °C; 20 bar; 0.6 NL g_{cat}^{-1} h^{-1}.

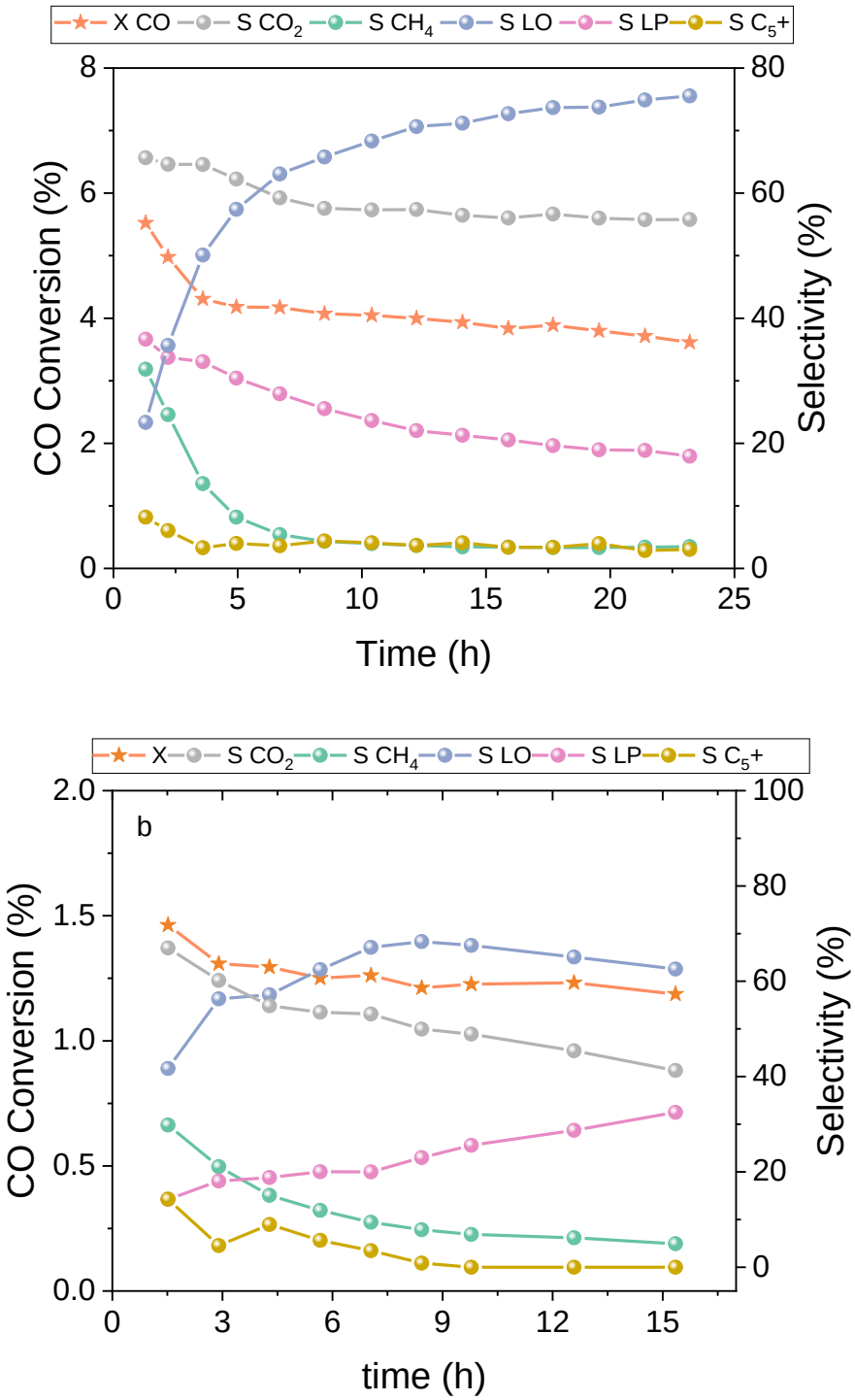

Figure 62: CO conversion, CO selectivity and CO-free hydrocarbon selectivity versus time on stream for AgZr10-S34 catalysts with S-34 small crystallites at 375 °C; 20 bar; 1.6 NL g_{cat}^{-1} h^{-1}(a) and for AgNPZr12-S34 catalyst at 375 °C; 20 bar; 0.6 NL g_{cat}^{-1} h^{-1} (b)

5.2.3. Catalyst structure

To better understand the nature of active sites in CO hydrogenation and modification of catalyst structure during the reaction, the fresh and spent AgZr10-S34 samples were analyzed by a combination of techniques.

The STEM-HAADF and STEM-EDX images of the AgZr10-S34 samples are shown in Figure 63, Figure 64, and Figure 65. The presence of Ag nanoparticles on ZrO_2 in both fresh and used catalysts was then confirmed by STEM-EDX (Figure 63 b,c,d and *Figure 64*). The AgZr10 component(Figure 63a), and the fresh AgZr10-S34 sample (Figure 63 b,c,d) showed very small Ag nanoparticles. The calculation of average silver nanoparticle size from histogram gives a value of 2 nm (Figure 63d). On the contrary, in the spent AgZr10-S34 catalyst , both STEM-HAADF (Figure 63 e,f,g,h) and STEM-EDX (Figure 65) showed a partial increase of the Ag particles. Note that two main populations of particles were detected, clearly shown in Figure 63 f and g: the first one is characterized by nanoparticles with average size of 2nm, and the second one shows an average sizes of 5-6 nm (Figure 63f). Hence, after performing the CO hydrogenation reaction, the smaller nanoparticles probably sintered to form bigger particles. In addition, the high-resolution observation of silver nanoparticles showed that the spent AgZr10-S34 catalyst showed the presence of large polycrystalline nanoparticles constituted several smaller silver crystallites (Figure 63h). This evidence agrees with the idea of nanoparticle sintering. As a result, the increase in selectivity towards LO during the CO hydrogenation coul be explained considering the reduction of Ag active surface, that could prevent the secondary LO hydrogenation to produce LP.

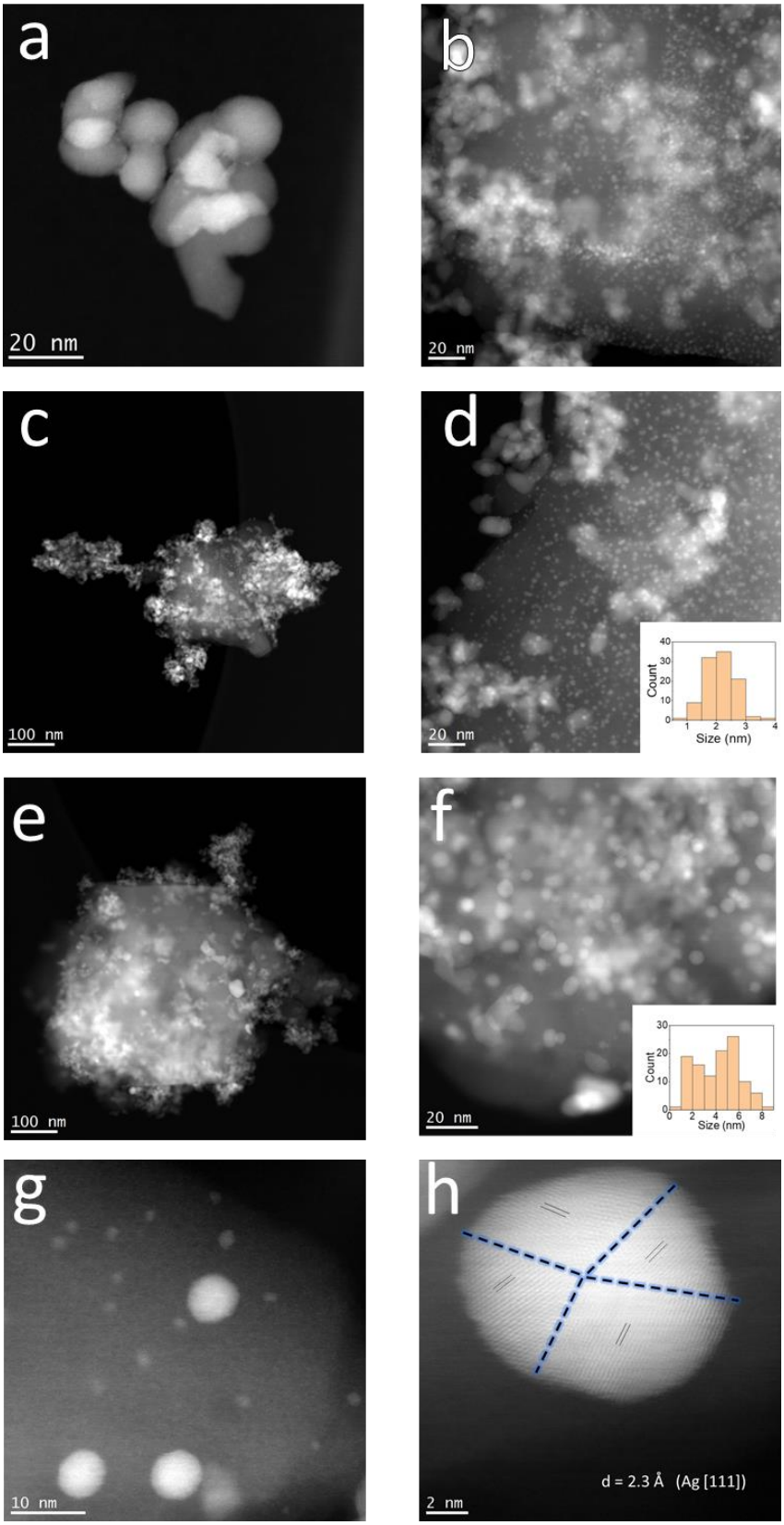

Figure 63: HAADF-STEM analysis of AgZr10 component (a), and the fresh (b-d) and spent (e-h) AgZr10-S34 catalysts (b-h). Figure h shows an example of a polycrystalline nanoparticle in the AgZr10-S34 spent catalyst.

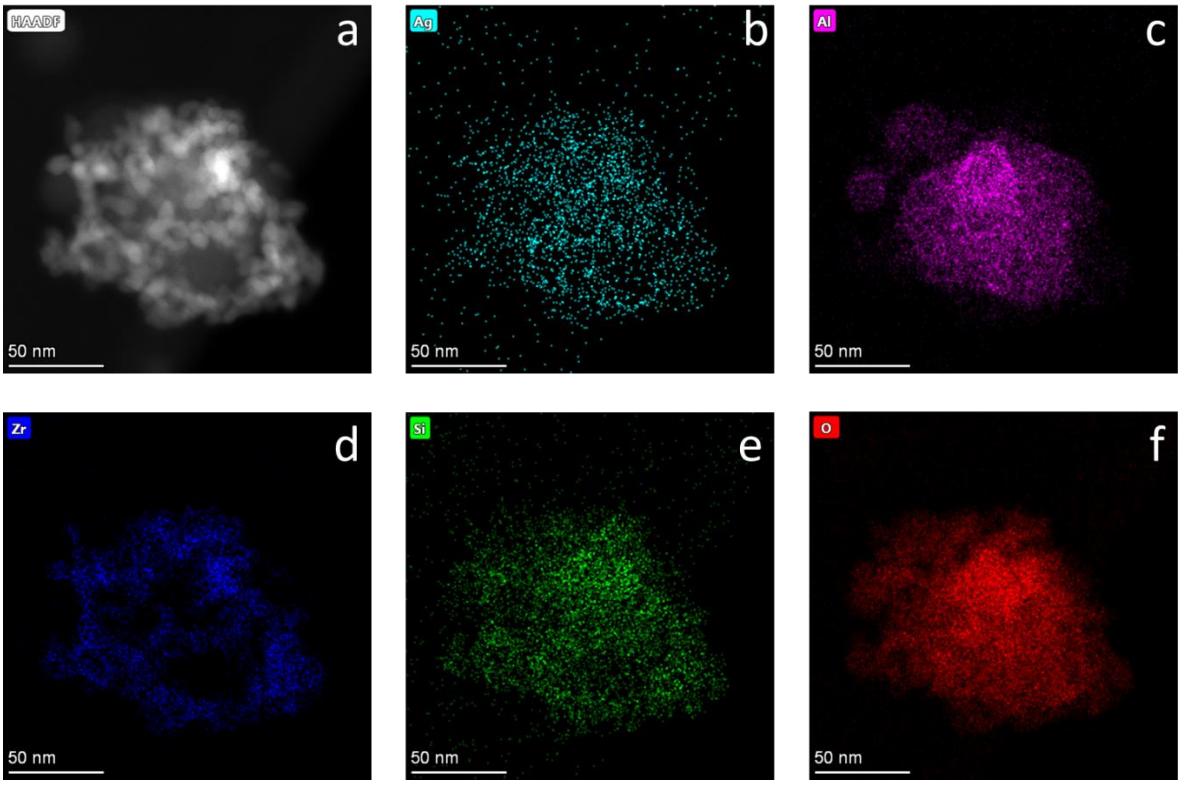

Figure 64: STEM-EDX mapping of the fresh AgZr10-S34 catalyst. a) HAADF-STEM; b) Ag map; c) Al map; d) Zr map; e) Si map; f) O map.

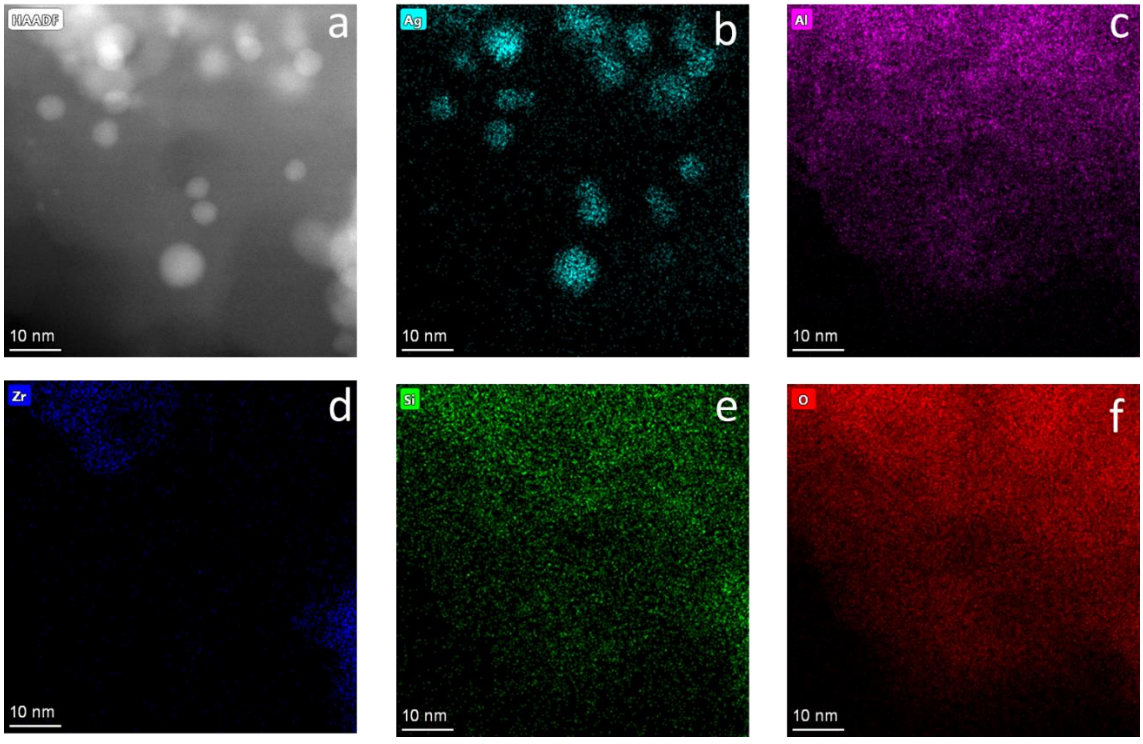

Figure 65: STEM-EDX mapping of the spent AgZr10-S34 catalyst. a) HAADF-STEM; b) Ag map; c) Al map; d) Zr map; e) Si map; f) O map.

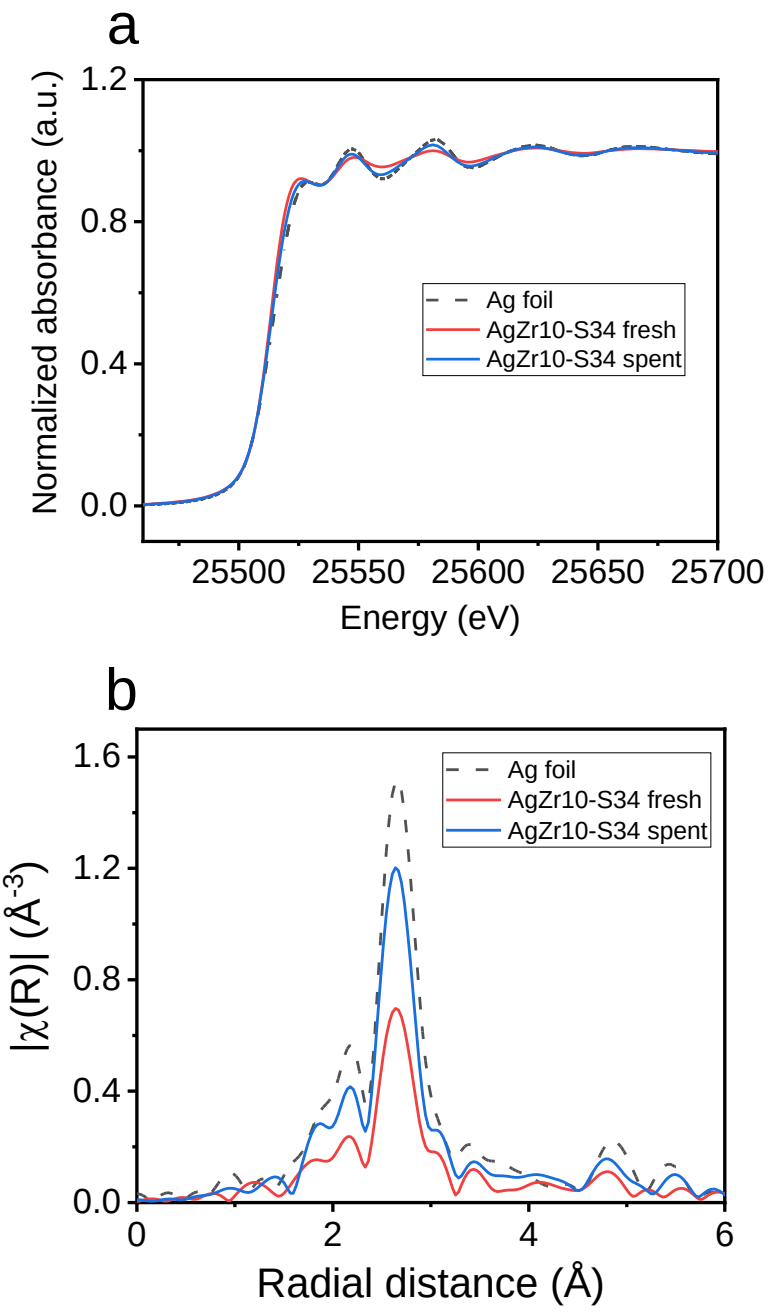

Figure 66: XANES (a) and FT EXAFS (b) for fresh and spent silver catalysts.

Figure 66a compares the Ag K-edge XANES spectra of the fresh and spent AgZr10-S34 samples with an Ag-foil reference sample. The XANES spectra of both fresh and spent silver catalysts are almost identical to that of metallic foils. This indicates that silver is the metallic phase in the catalysts before and after reaction. No silver oxidation occurs. Figure 66b shows the Fourier transform (FT) EXAFS moduli of the metal silver foil and catalyst samples.

The intense peak at 2.6 Å is assigned to the first shell Ag-Ag coordination in silver metallic phase. Note that the intensity of this peak is higher in the spent AgZr10-S34 catalyst compared to the fresh counterpart. The increase in the intensity of FT EXAFS peak corresponds to the increase in silver coordination number in silver nanoparticles which can be due to silver sintering. The EXAFS results are consistent with STEM-HAADF data also showing an increase in silver nanoparticle size in CO hydrogenation.

Interestingly, no modification of the catalyst morphology at micron scale was observed by SEM (Figure 67). SEM images of both fresh and spent AgZr10-S34 catalysts showed the presence of cubic SAPO-34 crystallites in interaction with the zirconia phase. It can also be suggested that silver cations may migrate within the SAPO-34 zeolite and become localized in its cationic sites. It is known that CO adsorption over Ag^{+} ions results in a very characteristic peak at 2150-2180 cm^{-1} corresponding to $Ag^{+}CO$ complexes[17,18]. Metallic silver does not adsorb CO. No FTIR peaks related to CO adsorption were observed in the spent AgZr10-S34 sample (Figure 68), indicating no migration of cationic silver inside SAPO-3 channels.

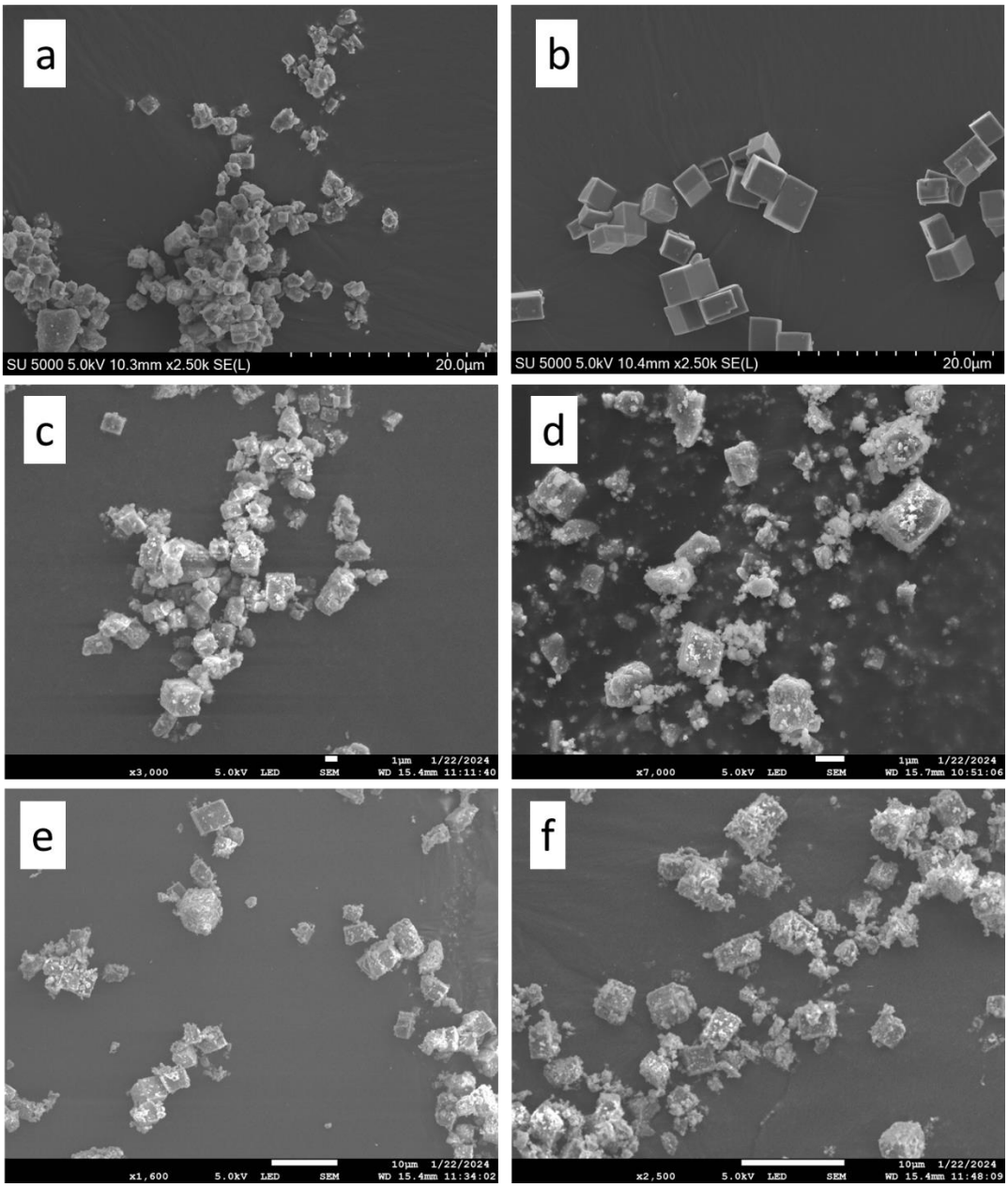

Figure 67: SEM of zeolite used to prepare the bifunctional catalysts, and fresh and spent catalysts. a)S34; b)S34L; c) AgZr10-S34 fresh; d) AgZr10-S34 spent; e) AgZr10-S34L fresh; f) AgZr10-S34L spent.

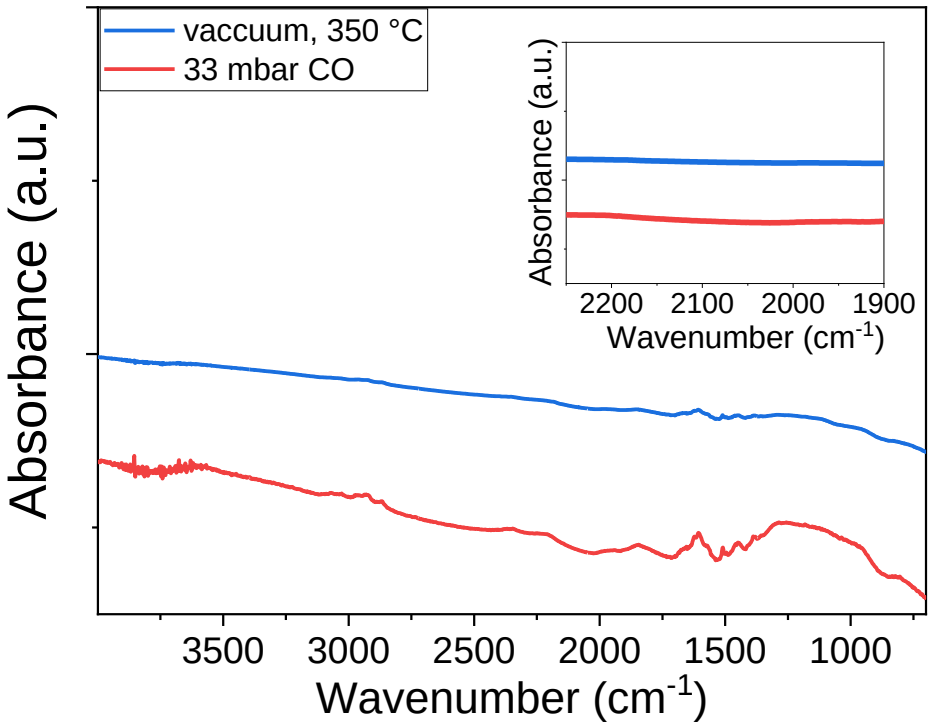

Figure 68: CO FTIR spectra on spent AgZr10-S34, after treatment at 350 °C under vacuum to remove adsorbed water (red), and after a CO dose of 33 mbar (blue).

TGA curves for the fresh and spent catalysts are shown in Figure 70. The TGA profiles of both the fresh catalyst catalysts exhibit a decrease in the sample weight occurring at about 100°C. In agreement with previous reports, this decrease in the sample weight could be related to the water desorption from the catalysts. In addition, the first weight decreases peaks, the TGA profile of the spent catalysts showed a high temperature peaks at 580°C which can be attributed to removal of carbon species. In particular, they were attributed to the hydrocarbon pool species that are formed during the MTO step[19,20] of the LO synthesis, within the zeolite cages.

Furthermore, the AgZr10, S34, and the fresh and spent AgZr10-S34 samples were analyzed by XRD to evaluate the structure of the catalyst before and after reaction (*Figure 69*). As expected, the fresh and spent AgZr10-S34 samples showed the presence of monoclinic ZrO_2, SAPO-34 and Ag. The diffraction pattern of the S34 sample showed the chabazite structure

typical of the SAPO-34 zeolite. The XRD patterns also display relatively sharp peaks attributed to metallic silver. These peaks are related to bigger Ag agglomerates that we do not consider as relevant for the reaction. Note that small silver nanoparticles detected by STEM with the sizes of a few nanometers are difficult to detect by XRD. The AgZr10 sample showed the presence of monoclinic ZrO_2, and four signals at 38°, 44°, 65° and 78°, typical of metallic Ag. Some modification of intensity of XRD peaks attributed to SAPO-34 was observed during the reaction. These reversible modifications of XRD patterns correspond to expansion of zeolite unit cell previously observed [21,22] in SAPO-34 during MTO process. They were attributed to carbon deposition within the zeolite framework. Indeed, carbon species on the spent catalysts were observed by TGA (Figure 70). Calcination of spent AgZr10-S34 catalyst in air results in compete restoration of initial peak intensity.

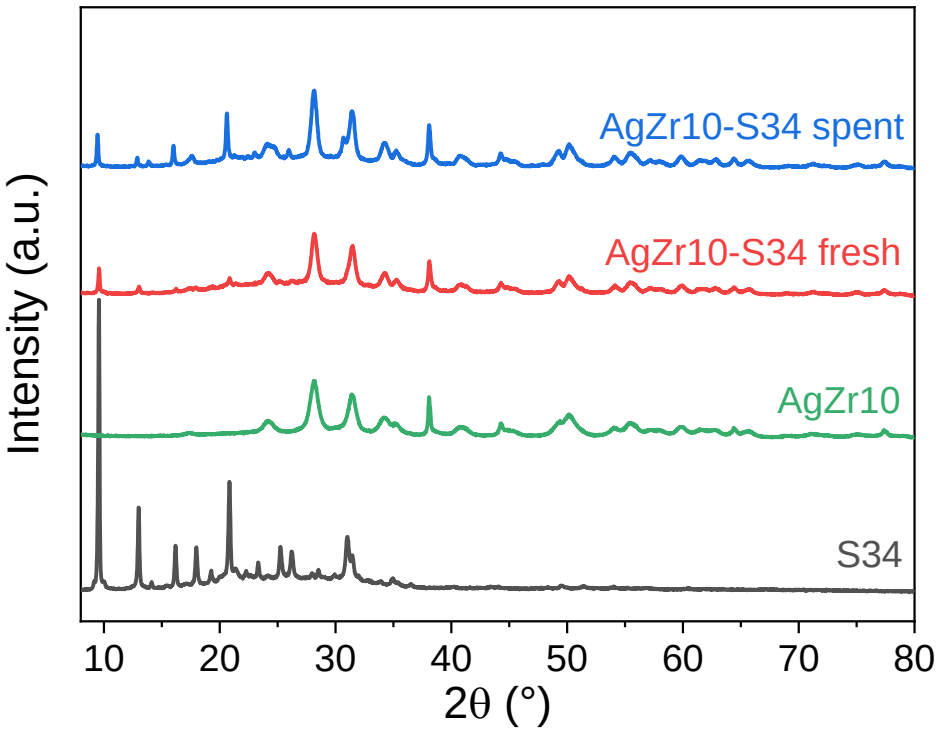

Figure 69: XRD of the S34 zeolite; the AgZr10 component, and the fresh and spent AgZr10-S34 catalysts.

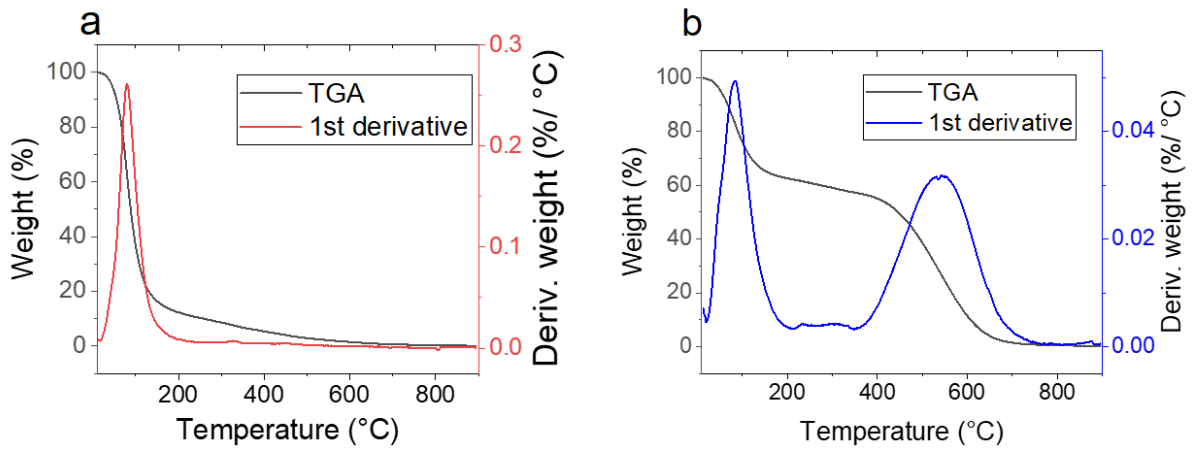

Figure 70: TGA of fresh (a) and spent (b) Ag/Zr10-S-34 catalysts.

5.3. Conclusions

In conclusion, we have found that a bifunctional catalyst prepared integrating supported silver metallic nanoparticles, instead of the typically used oxide catalysts, along with SAPO-34 responsible for the MTO process, is active in the tandem CO hydrogenation to LO. Moreover, it can achieve higher selectivity in the direct synthesis of light olefins from syngas compared to a typical OX-ZEO catalyst. The selectivity for light olefins in fact can exceed 75% with a CO conversion of 8% at 375°C, surpassing the results obtained at the same conversion with $ZnZrO_x$-S34.

During the reaction, the catalysts undergo a structure modification, resulting in a significant increase in light olefin selectivity. This modification consists in the optimization of silver nanoparticle sizes, which in turn influences the hydrogenation activity of the catalysts.

5.4. References

(1) Daza, Y. A.; Kuhn, J. N. CO_2 Conversion by Reverse Water Gas Shift Catalysis: Comparison of Catalysts, Mechanisms and Their Consequences for CO_2 Conversion to Liquid Fuels. *RSC Adv.* **2016**, *6* (55), 49675–49691. https://doi.org/10.1039/C6RA05414E.

(2) Galvis, H. M. T.; Jong, K. P. D. Catalysts for Production of Lower Olefins from Synthesis Gas: A Review. *ACS Catal.* **2013**, *3* (9), 2130–2149. https://doi.org/10.1021/cs4003436.

(3) Barrios, A. J.; Gu, B.; Luo, Y.; Peron, D. V.; Chernavskii, P. A.; Virginie, M.; Wojcieszak, R.; Thybaut, J. W.; Ordomsky, V. V.; Khodakov, A. Y. Identification of Efficient Promoters and Selectivity Trends in High Temperature Fischer-Tropsch Synthesis over Supported Iron Catalysts. *Appl. Catal. B Environ.* **2020**, *273*, 119028. https://doi.org/10.1016/j.apcatb.2020.119028.

(4) Zhou, W.; Cheng, K.; Kang, J.; Zhou, C.; Subramanian, V.; Zhang, Q.; Wang, Y. New Horizon in C1 Chemistry: Breaking the Selectivity Limitation in Transformation of Syngas and Hydrogenation of CO_2 into Hydrocarbon Chemicals and Fuels. *Chem. Soc. Rev.* **2019**, *48* (12), 3193–3228. https://doi.org/10.1039/c8cs00502h.

(5) Cheng, K.; Gu, B.; Liu, X.; Kang, J.; Zhang, Q.; Wang, Y. Direct and Highly Selective Conversion of Synthesis Gas into Lower Olefins: Design of a Bifunctional Catalyst Combining Methanol Synthesis and Carbon-Carbon Coupling. *Angew. Chem.* **2016**, *128* (15), 4803–4806. https://doi.org/10.1002/ange.201601208.

(6) Jiao, F.; Li, J.; Pan, X.; Xiao, J.; Li, H.; Ma, H.; Wei, M.; Pan, Y.; Zhou, Z.; Li, M.; Miao, S.; Li, J.; Zhu, Y.; Xiao, D.; He, T.; Yang, J.; Qi, F.; Fu, Q.; Bao, X. Selective Conversion of Syngas to Light Olefins. *Science* **2016**, *351* (6277), 1065–1068. https://doi.org/10.1126/science.aaf1835.

(7) Yu, Y.; Xu, Y.; Cheng, D. G.; Chen, Y.; Chen, F.; Lu, X.; Huang, Y.; Ni, S. Transformation of Syngas to Light Hydrocarbons over Bifunctional CuO-ZnO/SAPO-

34 Catalysts: The Effect of Preparation Methods. *React. Kinet. Mech. Catal.* **2014**, *112* (2), 489–497. https://doi.org/10.1007/s11144-014-0707-1.

(8) Wang, M.; Kang, J.; Xiong, X.; Zhang, F.; Cheng, K.; Zhang, Q.; Wang, Y. Effect of Zeolite Topology on the Hydrocarbon Distribution over Bifunctional ZnAlO/SAPO Catalysts in Syngas Conversion. *Catal. Today* **2021**, *371*, 85–92. https://doi.org/10.1016/j.cattod.2020.07.076.

(9) Yang, G.; Meng, F.; Zhang, P.; Yang, L.; Li, Z. Effects of Preparation Method and Precipitant on Mn-Ga Oxide in Combination with SAPO-34 for Syngas Conversion into Light Olefins. *New J. Chem.* **2021**, *45* (18), 7967–7976. https://doi.org/10.1039/d1nj00443c.

(10) Meng, F.; Li, X.; Zhang, P.; Yang, L.; Yang, G.; Ma, P.; Li, Z. Highly Active Ternary Oxide ZrCeZnOx Combined with SAPO-34 Zeolite for Direct Conversion of Syngas into Light Olefins. *Catal. Today* **2021**, *368*, 118–125. https://doi.org/10.1016/j.cattod.2020.03.023.

(11) Liu, Z.; Ni, Y.; Hu, Z.; Fu, Y.; Fang, X.; Jiang, Q.; Chen, Z.; Zhu, W.; Liu, Z. Insights into Effects of ZrO2 Crystal Phase on Syngas-to-Olefin Conversion over ZnO/ZrO_2 and SAPO-34 Composite Catalysts. *Chin. J. Catal.* **2022**, *43* (3), 877–884. https://doi.org/10.1016/S1872-2067(21)63908-6.

(12) Zhang, P.; Meng, F.; Yang, L.; Yang, G.; Liang, X.; Li, Z. Syngas to Olefins over a CrMnGa/SAPO-34 Bifunctional Catalyst: Effect of Cr and Cr/Mn Ratio. *Ind. Eng. Chem. Res.* **2021**, *60* (36), 13214–13222. https://doi.org/10.1021/acs.iecr.1c02150.

(13) Grabowski, R.; Słoczyński, J.; Śliwa, M.; Mucha, D.; Socha, R. P.; Lachowska, M.; Skrzypek, J. Influence of Polymorphic ZrO_2 Phases and the Silver Electronic State on the Activity of Ag/ZrO2 Catalysts in the Hydrogenation of CO_2 to Methanol. *ACS Catal.* **2011**, *1* (4), 266–278. https://doi.org/10.1021/cs100033v.

(14) Baikera, A.; Kilob, M.; Maciejewskiq, M.; Menzia, S.; Wokaunb, A. *HYDROGENATION OF C02 OVER COPPER, SILVER AND GOLD/ZIRCONIA CATALYSTS: COMPARATIVE STUDY OF CATALYST PROPERTIES AND REACTION PATHWAYS*; p 43.

(15) Corral-Pérez, J. J.; Copéret, C.; Urakawa, A. Lewis Acidic Supports Promote the Selective Hydrogenation of Carbon Dioxide to Methyl Formate in the Presence of Methanol over Ag Catalysts. *J. Catal.* **2019**, *380*, 153–160. https://doi.org/10.1016/j.jcat.2019.10.013.

(16) Köppel, R. A.; Stöcker, C.; Baiker, A. Copper- and Silver–Zirconia Aerogels: Preparation, Structural Properties and Catalytic Behavior in Methanol Synthesis from Carbon Dioxide. *J. Catal.* **1998**, *179* (2), 515–527. https://doi.org/10.1006/jcat.1998.2252.

(17) Bolis, V.; Bordiga, S.; Palomino, G. T.; Zecchina, A.; Lamberti, C. Calorimetric and Spectroscopic Study of the Coordinative Unsaturation of Copper(I) and Silver(I) Cations in ZSM-5 Zeolite. *Thermochim. Acta* **2001**, *379* (1–2), 131–145. https://doi.org/10.1016/S0040-6031(01)00612-8.

(18) Tarach, K.; Góra-Marek, K.; Chrzan, M.; Walas, S. Quantification of Silver Sites in Zeolites: Carbon Monoxide Sorption Monitored by IR Spectroscopy. *J. Phys. Chem. C* **2014**, *118* (41), 23751–23760. https://doi.org/10.1021/jp506820v.

(19) Yang, M.; Fan, D.; Wei, Y.; Tian, P.; Liu, Z. Recent Progress in Methanol-to-Olefins (MTO) Catalysts. *Adv. Mater.* **2019**, *31* (50), 1902181. https://doi.org/10.1002/adma.201902181.

(20) Sun, X.; Mueller, S.; Liu, Y.; Shi, H.; Haller, G. L.; Sanchez-Sanchez, M.; Van Veen, A. C.; Lercher, J. A. On Reaction Pathways in the Conversion of Methanol to Hydrocarbons on HZSM-5. *J. Catal.* **2014**, *317*, 185–197. https://doi.org/10.1016/j.jcat.2014.06.017.

(21) Wragg, D. S.; Johnsen, R. E.; Balasundaram, M.; Norby, P.; Fjellvåg, H.; Grønvold, A.; Fuglerud, T.; Hafizovic, J.; Vistad, Ø. B.; Akporiaye, D. SAPO-34 Methanol-to-Olefin Catalysts under Working Conditions: A Combined in Situ Powder X-Ray Diffraction, Mass Spectrometry and Raman Study. *J. Catal.* **2009**, *268* (2), 290–296. https://doi.org/10.1016/j.jcat.2009.09.027.

(22) Wragg, D. S.; Akporiaye, D.; Fjellvåg, H. Direct Observation of Catalyst Behaviour under Real Working Conditions with X-Ray Diffraction: Comparing SAPO-18 and SAPO-34 Methanol to Olefin Catalysts. *J. Catal.* **2011**, *279* (2), 397–402. https://doi.org/10.1016/j.jcat.2011.02.011.

General Conclusions

The findings of this thesis have significant implications for the field of sustainable chemical production. In fact, this work is focused in advancing the understanding of MeOH and light olefins production from CO_2 and CO. These products are applied as platform molecules in a vast array of processes. MeOH is a versatile chemical that serves as a feedstock for various industrial applications and as a fuel. Light olefins, such as ethylene and propylene, are essential building blocks in the petrochemical industry. The development of more sustainable processes is fundamental for the reduction of CO_2 emissions in the production of these high-demand commodities. The methanol-mediated conversion of CO_2 to light olefins represents a possible solution for this goal. The hydrogenation of CO to methanol followed by MTO conversion has many similarities with the CO_2-based process, and offers an alternative pathway for producing light olefins. Not to mention that CO_2 can be converted to CO by RWGS, and generally CO is the main byproduct in the methanol-mediated CO_2 hydrogenation to LO.

The development of efficient catalytic processes for converting CO_2 and CO into value-added chemicals addresses both environmental and economic challenges. By utilizing CO_2 as a feedstock, these processes contribute to the reduction of greenhouse gas emissions and support the transition to a circular carbon economy. Furthermore, the production of methanol and light olefins from CO_2 and CO offers a sustainable alternative to traditional petrochemical processes, reducing reliance on fossil-based resources. One sector that can benefit from these reactions to reduce its oil-dependency is the aviation sector. In fact, these reactions can be integrated in SAF production pathways.

SAF are aviation fuels whose employment allow to reduce carbon emissions. Currently they are produced from biomass-derived feedstocks, and the carbon emission reduction is related to an indirect CO_2 utilization. A problem associated to biofuels is that to meet the 2050

goals of carbon neutrality, the production of SAF needs to increase significantly, and the biomass availability is not sufficient to allow a sufficient SAF supply. For this reason, new pathways that allow the direct CO_2 conversion to SAF should be developed. One possible approach is Power-to-SAF, which involves the use of renewable electricity in water electrolysis to produce hydrogen, and uses the latter to convert CO_2.

The CO_x conversion to methanol and light olefins products can be integrated in Power-to-SAF technologies. In fact, these species can act as intermediates for producing jet-fuel range hydrocarbons. This possibility is studied by the European Project TAKE-OFF, which aims to develop a technology that produces SAF through the methanol-mediated CO_2 hydrogenation to light olefins, followed by the light olefin oligomerization and hydrogenation. Within this project, the CO_2 conversion to LO is carried out either indirectly, consisting of a first CO_2 conversion to MeOH followed by MTO, or directly, in which the two reactions are coupled thanks to the in-situ production of MeOH. For all the reasons mentioned above, advancements in understanding the CO_2 hydrogenation to methanol, and the methanol-mediated CO_x hydrogenation are highly valuable. With this in mind, the research presented in this thesis aimed to study these reactions by combining catalyst design and mechanistic studies.

Catalyst design

This work focused on enhancing product selectivity in three different reactions through catalyst design. For the conversion of CO_2 to methanol (MeOH), the study aimed to improve the commercial Cu-ZnO-Al_2O_3 (CZA) catalyst, which is widely used in industrial MeOH production. By incorporating halogens through the decomposition of halobenzene precursors, it was found that bromine could increase selectivity by 10%, while chlorine and iodine had

minimal impact. The concentration of bromine on the catalyst surface also played a crucial role in its activity.

In the case of the methanol-mediated CO_2 hydrogenation to LO, various metal oxides were mixed to SAPO-34 to prepare bifunctional catalyst to explore their potential influence in the selectivity to LO. Nonetheless, their impact on LO selectivity was excluded as their primary role was found to be controlling CO_2 conversion and selectivity to MeOH/CO. The modification of the properties of the zeolite allowed to influence the LO selectivity. It was observed that crystal size and acidity were key factors to improve selectivity.

This research also proposed the development of an Ag-based bifunctional catalyst specifically designed for CO hydrogenation to LO. Traditionally, noble metal catalysts are not favored for tandem LO production due to their high hydrogenation activity. However, this study demonstrated that with proper optimization, an Ag-based catalyst could effectively facilitate methanol-mediated CO hydrogenation to LO, obtaining high selectivity.

Mechanistic insights

This research integrated catalyst design with mechanistic studies to better understand the side reaction that affect the product selectivity, and how to modify the catalyst to avoid them.

The investigation on the CO_2 hydrogenation to methanol revealed the role of methanol decomposition in increasing CO production at higher conversions. This was done by studying the correlation between selectivity and conversion, along with conducting parallel kinetic studies. The enhancement in selectivity due to bromine deposition was attributed to the selective poisoning of active sites responsible for CO production, with the concentration of bromine on the surface being critical to not poison all the types of active site.

In case of the methanol-mediated CO_2 hydrogenation to LO, the analysis of the selectivity-conversion correlation showed that LO selectivity is influenced by total hydrocarbon yield, rather than directly by CO_2 conversion. Higher hydrocarbon yields were found to reduce LO selectivity due to secondary hydrogenation processes. Thanks to ethylene hydrogenation model reaction, it was revealed that the metal oxide components is not active in secondary hydrogenation of LO to LP when CO_2 and water are present in the system. Hence it was confirmed that the metal oxide does not play a role Nonetheless, this component influences the total CO_2 conversion and the selectivity to CO.

Furthermore, for the tandem CO hydrogenation to LO the analysis of the selectivity variation with time, coupled with catalyst characterization, allowed to identify a structure-dependent nature of this reaction over Ag-based catalyst. Particle size significantly impacted product selectivity . Ag-based catalysts, such as AgZr10-S34, achieved higher LO selectivity compared to ZnZrOx-S34. Overall, this study represents a pioneering effort to develop a new family of catalysts using noble metals instead of metal oxides, offering significant advancements in catalyst design and optimization.

Perspectives

This thesis presents new perspectives on the catalytic conversion of CO_2 and CO into methanol and light olefins. By optimizing catalysts, developing novel systems, and gaining a deeper understanding of reaction mechanisms, the research identifies new strategies for improve catalyst performance. Moreover, open questions and challenges are still present for the indirect and direct CO_2 hydrogenation to light olefins via methanol processes.

From the catalyst development point of view, three research directions can be suggested. First, the halogen selective poisoning of the catalytic sites responsible for CO production can be further explored, and extended to other catalyst types to study a possible improvement of the selectivity to MeOH. Alternative poisons can also be explored, and this strategy could be extended to bifunctional catalysts for the methanol-mediated CO_2 hydrogenation to LO. Moreover, this work suggests the different nature of active sites for MeOH synthesis, RWGS and MeOH decomposition. The clarification of the nature of these three active sites might allow to eliminate the ones related to CO production directly by tuning the catalyst synthesis, avoiding post synthesis treatments that can poison also the methanol synthesis sites.

Second, LO selectivity can be improved by designing bifunctional catalyst composed by small zeolite crystallites. A possibility could be the use of embryonic/hierarchical zeolites, which allow to minimize the residence time of produced olefins inside the zeolite, possibly preventing secondary hydrogenation reactions. Moreover, new bifunctional catalysts should be developed to reduce the selectivity to CO in the methanol-mediated LO synthesis, and hence increase the carbon efficiency of the process.

Last but not least, the silver-based bifunctional catalysts should be further studied to attempt to achieve better performance. A necessary improvement would be to study of the

catalyst pre-treatment to reduce the activation time needed to obtain bigger Ag particles. Moreover, the effect of the support on the catalyst performance should be studied, along with the impact of promotion. While this research provided evidence of the activity of Ag, it is not excluded that other noble metals can be employed in this reaction, by carefully tuning the particle size or selectively poisonings the most active hydrogenation sites to avoid secondary LO reactions.

The knowledge on the methanol-mediated light olefin production could be also extended with engineering and techno-economical studies. An important open question concerns which pathway among the direct and indirect methanol-mediated synthesis of light olefins is more viable from an economical and environmental point of view.

In the direct approach, CO_2 is transformed into light olefins in a single step. This method might simplify the process and reduce costs, but it requires significant advancements in catalyst development to achieve the desired selectivity and yield. Currently, while CO recycling might be avoided in the indirect pathway, in the direct approach this solution is necessary to improve carbon efficiency. In fact, in the indirect route one can employ selective catalysts for the MeOH synthesis, while all the available bifunctional catalysts produce significant amounts of CO. This is due to the fact that the reaction conditions are not optimal for MeOH synthesis, and RWGS is more favorable.

The indirect process benefits from higher TRL technologies and offers greater flexibility. The main advantage is the possibility to employ the optimal conditions for both MeOH synthesis and MTO. At the same time, it can be potentially costlier and more energy-intensive. Each step requires its own set of catalysts, separation processes, and energy inputs which might lead to higher operational and capital expenditures, and higher carbon footprint.

The clarification of these doubts would significantly help the development of the technology. Moreover, these considerations can be extended also to the TAKE-OFF technology, as the most viable configuration should be employed to minimize costs and life-cycle emissions related to SAF production.

Acknowledgements

Completing this PhD thesis has been a journey filled with challenges, and it would not have been possible without the support, guidance, and encouragement of many people. I am profoundly grateful to all who have contributed to this work and to my personal development.

First and foremost, I would like to express my deepest gratitude to my supervisor, Dr. Vitaly Ordomsky. Vitaly, your passion and enthusiasm have been a constant source of motivation. Your encouragement and constructive challenges pushed me to achieve my best. Moreover, my thesis would not have been possible without Dr. Andrei Khodakov. Andrei, your vast expertise, coupled with your sense of humor, has made my research work both enlightening and enjoyable. Your guidance and insightful feedback have been invaluable.

I am also grateful to Pr. Anne-Cécile Roger, Dr. Stephane Loridant, Pr. Michiel Dusselier and Dr. Lawien Zubeir, for accepting to participate to my thesis defense and for the time taken to evaluate my thesis.

I gratefully acknowledge the financial support provided by the H2020 European Project TAKE-OFF, without which this research would not have been possible. I also deeply acknowledge all the partners of the project. I really enjoyed our discussions, and I have learnt a lot from your different expertise. Taking part in this project has been instrumental in shaping my career goals.

A heartfelt thank you goes to my colleagues at UCCS and Centrale Lille. The time spent inside and outside the laboratory, and the mutual support, have been a boost of joy and motivation. In particular, my deep gratitude goes to Dr. Sergei Chernyak, who helped me in so many ways, and kept doing it even after changing job, and to Dr. Deizi Peron and Dr. Yong Zhou, whose help during my first year of PhD was fundamental.

I would like to acknowledge all the participants and collaborators who contributed to the works presented in this thesis: Kang Cheng, Yuri G. Kolyagin, Evgenii V. Kondratenko, Vita A. Kondratenko, Maya Marinova, Jean-Charles Morin, Olga V. Safonova, Olena Vovk.

I am thankful to the administrative and technical staff at UCCS and Centrale Lille for their assistance in managing the logistical aspects of my research. I would like to thank as well Pardis Simon, Olivier Gardoll, Svetlana Heyte, Joëlle Thuriot-Roukos and all the staff of the Realcat platform.

On a personal note, I owe an immense debt of gratitude to my family and friends, for the constant support during this PhD rollercoaster, and for filling my life with love and joy.

List of publications

Publications presented in this thesis:

Chernyak, S. A.; **Corda, M.**; Dath, J.-P.; Ordomsky, V. V.; Khodakov, A. Y. Light Olefin Synthesis from a Diversity of Renewable and Fossil Feedstocks: State-of the-Art and Outlook. Chem. Soc. Rev. 2022, 51 (18), 7994–8044. https://doi.org/10.1039/D1CS01036K.

Chernyak, S. A.; **Corda, M.**; Marinova, M.; Safonova, O. V.; Kondratenko, V. A.; Kondratenko, E. V.; Kolyagin, Y. G.; Cheng, K.; Ordomsky, V. V.; Khodakov, A. Y. Decisive Influence of SAPO-34 Zeolite on Light Olefin Selectivity in Methanol-Meditated CO_2 Hydrogenation over Metal Oxide-Zeolite Catalysts. ACS Catal. 2023, 13 (22), 14627–14638. https://doi.org/10.1021/acscatal.3c03759.

Corda M., Chernyak S, Marinova M., Morin J.C., Trentesaux M., Kondratenko V.A., Kondratenko E.V., Ordomsky V.V., Khodakov A.Y. Selective CO2 hydrogenation to methanol by halogen deposition over a Cu-based catalyst. In preparation.

Corda M., Vovk O., Marinova M., Ordomsky V.V., Khodakov A.Y. Silver Metallic Nanoparticles for Direct Conversion of Carbon Monoxide to Light Olefins over Bifunctional Catalysts. In preparation.

Other contributions:

Dong, C.; Marinova, M.; Tayeb, K. B.; Safonova, O. V.; Zhou, Y.; Hu, D.; Chernyak, S.; **Corda, M.**; Zaffran, J.; Khodakov, A. Y.; Ordomsky, V. V. Direct Photocatalytic Synthesis of Acetic Acid from Methane and CO at Ambient Temperature Using Water as Oxidant. J. Am. Chem. Soc. 2023, 145 (2), 1185–1193. https://doi.org/10.1021/jacs.2c10840.

Zhou, Y.; Sadia Traore, A.; Peron, D. V.; Barrios, A. J.; Chernyak, S. A.; **Corda, M.**; Safonova, O. V.; Iulian Dugulan, A.; Ersen, O.; Virginie, M.; Ordomsky, V. V.; Khodakov, A. Y. Promotion Effects of Alkali Metals on Iron Molybdate Catalysts for CO_2 Catalytic Hydrogenation. J. Energy Chem. 2023, 85, 291–300. https://doi.org/10.1016/j.jechem.2023.06.019.

Fellenberg, A. K.; Addad, A.; Chernyak, S. A.; Zhou, Y.; **Corda, M.**; De Souza, D. O.; Safonova, O. V.; Martin-Diaconescu, V.; Ordomsky, V. V.; Ji, G.; Khodakov, A. Y. Covalent Organic Frameworks for Design of Ruthenium Catalysts with High Single-Atom Site Density for CO_2 Hydrogenation into Formic Acid. Cell Rep. Phys. Sci. 2024, 5 (4), 101926. https://doi.org/10.1016/j.xcrp.2024.101926.

Oral presentations at international conferences:

Chernyak, S. A.; **Corda, M. (Speaker)**; Marinova, M.; Safonova, O. V.; Kondratenko, V. A.; Kondratenko, E. V.; Kolyagin, Y. G.; Cheng, K.; Ordomsky, V. V.; Khodakov, A. Y. , Role of metal oxide and zeolite in the direct CO2 hydrogenation to light olefins over bifunctional catalysts, 15th European Congress on Catalysts (Europacat), August 2023, Prague, Czech Republic.

Corda, M. (Speaker); Chernyak, S. A.; Marinova, M.; Ordomsky, V. V.; Khodakov, A. Y., CO_2 hydrogenation to methanol over halogen-promoted CuO-ZnO-Al2O3 catalysts, 13th Natural Gas Conversion Symposium (NGCS13), April 2024, Xiamen, China

Catalyst Design and Mechanistic Insights into COx Hydrogenation to Methanol and Light Olefins

Abstract

The increasing concentration of atmospheric CO_2 presents significant environmental challenges and emphasizes the urgency for sustainable chemical processes. One promising approach to address this issues is the catalytic conversion of CO_2 into value-added chemicals, such as methanol and light olefins. This thesis focuses on the catalyst development for the methanol synthesis and the methanol-mediated light olefin synthesis from CO_2. Moreover, the methanol-mediated CO hydrogenation to light olefins is also studied: CO can be considered as an alternative to CO_2, as it can be produced by the Reverse Water Gas Shift reaction. The work reported in this thesis provides new insights into catalyst design for the COx hydrogenation to methanol or light olefins, suggesting new strategies to improve product selectivity. Additionally, the thesis advances the understanding of mechanistic aspects of these reactions. For the CO_2 hydrogenation to methanol, the commercial $CuO\text{-}ZnO\text{-}Al_2O_3$ catalyst was promoted with halogens (Br, Cl, I), to improve selectivity to methanol. It was observed that Br allowed to improve the selectivity of 10 % compared to the pristine catalyst. A kinetic analysis showed that Br caused the suppression of the Reverse Water Gas Shift reaction and of the methanol decomposition reaction, both responsible of the parallel production of CO. For the methanol-mediated CO_2 hydrogenation to light olefins, a series of bifunctional catalysts based on oxides of Zn, In, Mn, Cr, or Ga and different SAPO-34 zeolites were studied. The analysis of the selectivity-conversion correlations allowed to elucidate the functions of each catalyst component. It was uncovered that the selectivity to LO within hydrocarbon fractions depended ultimately on the zeolite component and decreased as a function of hydrocarbon yield. The metal-oxide catalyst component was responsible for the CO_2 conversion, overall hydrocarbon and CO selectivity. The SAPO-34 morphology and acidity were identified as major descriptors of the CO-free LO selectivity in the CO_2 hydrogenation over bifunctional catalysts. Finally, for the methanol-mediated synthesis of light olefins from syngas, this work studied the activity of a bifunctional catalyst composed by supported silver nanoparticles mixed with SAPO-34 zeolite. The resulting catalysts exhibited higher selectivity to light olefins compared to a conventional oxide-zeolite catalyst. It was observed that the reaction is structure-sensitive, and the silver particle size influences the selectivity to light olefins.

Keywords: CO_2 hydrogenation; CO hydrogenation; heterogeneous catalysis; methanol; light olefins.

Conception de Catalyseurs et Compréhension Mécanistique de l'Hydrogénation de COx en Méthanol et Oléfines Légères

Resumé

L'augmentation de la concentration de CO_2 atmosphérique présente des défis environnementaux significatifs et souligne l'urgence de développer des procédés chimiques durables. Une approche prometteuse pour aborder ces problèmes est la conversion catalytique du CO_2 en produits chimiques à valeur ajoutée, tels que le méthanol et les oléfines légères. Cette thèse se concentre sur le développement de catalyseurs pour la synthèse de méthanol et la synthèse d'oléfines légères à partir de CO_2 par médiation de méthanol. De plus, l'hydrogénation du CO médiée par le méthanol en oléfines légères est également étudiée: le CO peut être considéré comme une alternative au CO_2, car il peut être produit par la réaction du gaz à l'eau inverse. Les travaux rapportés dans cette thèse fournissent de nouvelles perspectives sur la conception de catalyseurs pour l'hydrogénation de CO_x en méthanol ou en oléfines légères, en suggérant de nouvelles stratégies pour améliorer la sélectivité des produits. De plus, la thèse fait progresser la compréhension des aspects mécanistiques de ces réactions. Pour l'hydrogénation du CO_2 en méthanol, le catalyseur commercial $CuO\text{-}ZnO\text{-}Al_2O_3$ a été promu avec des halogènes (Br, Cl, I) pour améliorer la sélectivité au méthanol. Il a été observé que le Br permettait d'améliorer la sélectivité de 10 % par rapport au catalyseur initial. Une analyse cinétique a montré que le Br entraînait la suppression de la réaction de conversion inverse de l'eau en gaz et de la réaction de décomposition du méthanol, toutes deux responsables de la production parallèle de CO. Pour l'hydrogénation du CO_2 en oléfines légères médiée par le méthanol, une série de catalyseurs bifonctionnels basés sur des oxydes de Zn, In, Mn, Cr ou Ga et différents zéolithes SAPO-34 a été étudiée. L'analyse des corrélations sélectivité-conversion a permis d'élucider les fonctions de chaque composant du catalyseur. Il a été découvert que la sélectivité aux oléfines légères au sein des fractions d'hydrocarbures dépendait finalement du composant zéolithique et diminuait en fonction du rendement en hydrocarbures. Le composant catalyseur à base d'oxyde métallique était responsable de la conversion du CO_2, de la sélectivité globale aux hydrocarbures et au CO. La morphologie et l'acidité du SAPO-34 ont été identifiées comme des descripteurs majeurs de la sélectivité aux oléfines légères sans CO dans l'hydrogénation du CO_2 sur des catalyseurs bifonctionnels. Enfin, pour la synthèse d'oléfines légères médiée par le méthanol à partir de gaz de synthèse, ce travail a étudié l'activité d'un catalyseur bifonctionnel composé de nanoparticules d'argent supportées mélangées à la zéolithe SAPO-34. Les catalyseurs résultants ont montré une sélectivité plus élevée aux oléfines légères par rapport à un catalyseur conventionnel oxyde-zéolithe. Il a été observé que la réaction est sensible à la structure, et la taille des particules d'argent influence la sélectivité aux oléfines légères.

Mots clés : hydrogénation du CO_2 ; hydrogénation du CO ; catalyse hétérogène ; oléfines légères.